Curso 2011/12
CIENCIAS Y TECNOLOGÍAS/30
I.S.B.N.: 978-84-15910-30-5

CHRISTOPH KUCKEIN

Study of the Magnetic Structure of Active Region Filaments

Directores
VALENTÍN MARTÍNEZ PILLET
REBECA CENTENO ELLIOTT

SERVICIO DE PUBLICACIONES
UNIVERSIDAD DE LA LAGUNA

SOPORTES AUDIOVISUALES E INFORMÁTICOS
Serie Tesis Doctorales

Examination date: July 2012.
Thesis supervisors:
Dr. Valentín Martínez Pillet & Dr. Rebeca Centeno Elliott

ISBN: xx-xxx-xxxx-x
Depósito legal: TF-xxxx/2012

Some of the material included in this document has been already published in *Astronomy and Astrophysics* and *The Astrophysical Journal.*
Parte del material incluido en este documento ya ha sido publicado en *Astronomy* & *Astrophysics* y *The Astrophysical Journal.*

Resumen

El objetivo de esta tesis es el estudio de la estructura magnética de filamentos solares en regiones activas (RAs) y esclarecer su formación y evolución. Mientras que se han observado en numerosas ocasiones (y con diferentes resoluciones espaciales) filamentos fuera de RAs y sobre el limbo solar, el número de observaciones de filamentos en RAs es realmente escaso en la literatura. Los filamentos en RAs son fenómenos importantes que pueden dar lugar a eyecciones de masa coronal (EMC) cuyo material puede ser expulsado hacia el espacio con velocidades muy grandes pudiendo afectar a la Tierra. Las EMC están asociadas con cambios globales del campo magnético en la corona.

En base a estos objetivos, se han estudiado en detalle datos espectropolarimétricos de los cuatro perfiles de Stokes en la región espectral de 10830 Å. Las observaciones fueron tomadas en julio de 2005 con el polarímetro TIP en la VTT en Tenerife. Se realizaron observaciones de un filamento en una RA. El filamento se encontraba sobre la línea de inversión de polaridad (LIP) perteneciente a una RA que se encontraba en su fase de decaimiento. La región espectral de 10830 Å ofrece la ventaja de disponer de varias líneas espectrales relevantes que se pueden observar de manera simultánea. Entre estas líneas se encuentra el triplete cromosférico de helio, una línea fotosférica de silicio y dos líneas telúricas. Durante la campaña de observación se tomaron dos mapas el 3 de julio y siete mapas y una serie temporal el 5 de julio. Estos datos se han preparado cuidadosamente para ser analizados mediante diferentes códigos de inversión. Como resultado de las inversiones de los cuatro parámetros de Stokes (I, Q, U, V) del triplete de He I 10830 Å se han obtenido los valores del campo magnético más fuertes jamás registrados (600-700 G).

El siguiente paso consistió en determinar la estructura magnética, en el sistema de referencia local del Sol, en la cromosfera. Para ello fue necesario resolver la ambigüedad de los 180°. Existen varios métodos para solucionar este problema. En esta tesis se usó la herramienta AZAM (Lites et al., 1995). Las imágenes de helio permitieron distinguir dos áreas diferentes del filamento: (1) un área que presenta un filamento con forma alargada y grosor fino que corresponde al eje principal del filamento y (2) un área donde el filamento aparece difuso y extenso. Desde el punto de vista magnético, la primera parte presenta líneas de campo alargadas (paralelas) al eje del filamento mientras que en la segunda parte las líneas de campo pasan gradualmente de ser paralelas al eje a una configuración de polaridad normal.

Para entender la estructura magnética global del filamento se incluyó en el análisis la línea de Si I 10827 Å, la cual nos proporcionó la distribución magnética en la fotosfera. Dicha estructura presenta las siguientes características: (1) debajo del eje del filamento la configuración de polaridad es inversa, (2) debajo del filamento difuso se observan penumbras huérfanas y poros. Las líneas de campo en estas estructuras son alargadas y paralelas a la LIP.

Es de destacar que, por primera vez, se obtiene en un filamento de una RA el vector del campo magnético simultáneamente en la cromosfera y fotosfera. Del análisis del vector del campo magnético se dedujo que el filamento es soportado por líneas de campo con forma de hélice. El eje principal de la hélice se encuentra, en una parte del filamento en la cromosfera mientras que en la otra en la fotosfera. El eje en la fotosfera da lugar a la creación de penumbras huérfanas. Para confirmar la estructura magnética propuesta, se

realizaron extrapolaciones del campo magnético bajo la aproximación no lineal y libre de fuerzas. Como novedad, al disponer de magnetogramas vectoriales en dos alturas diferentes, estas extrapolaciones se pudieron realizar desde la fotosfera y también desde la cromosfera. Las líneas de campo obtenidas en ambas extrapolaciones son consistentes entre ellas y además confirmaron la estructura magnética propuesta con forma de hélice. Al disponer de magnetogramas vectoriales en dos diferentes alturas se pudo estimar la altura de formación promedio de He I 10830 Å, que resultó ser, en nuestras observaciones, de unos 1.4 Mm por encima de la superficie solar. Además, hemos propuesto un nuevo método para resolver la ambigüedad de los 180° usando extrapolaciones desde la fotosfera en combinación con el vector del campo magnético en la cromosfera. La solución obtenida a través de este método concuerda con la obtenida usando AZAM.

Una vez obtenida la estructura magnética del filamento, pasamos a explicar cómo se ha formado éste. Para ello se estudiaron las velocidades a lo largo de la línea de visión, es decir, los desplazamientos Doppler de la línea espectral. Las velocidades se calibraron en una escala absoluta usando las líneas telúricas y corrigiendo los movimientos orbitales Sol-Tierra y el corrimiento al rojo gravitacional. Se calculó una nueva longitud de onda (10832.108 Å) para la línea telúrica más próxima a la componente roja del triplete de He I 10830 Å. Se usaron diferentes estrategias de inversión para determinar el movimiento de las líneas de campo transversales. De nuevo el filamento se puede dividir en dos áreas que se comportan de manera diferente: (1) los campos transversales correspondientes al filamento que se encuentra muy bajo en la atmósfera solar presentan en promedio movimientos ascendentes en la fotosfera y parches ascendentes en la cromosfera. Interpretamos esto como un ascenso global de toda la hélice. (2) La otra parte del filamento muestra, el primer día de observación, movimientos ascendentes en ambas alturas. Dos días más tarde, en la fotosfera se siguen viendo movimientos promedios ascendentes pero con velocidades más lentas. En cambio, en la cromosfera, el eje del filamento muestra movimientos descendentes. Interpretamos este resultado como una detención en el ascenso del filamento. El estudio de las velocidades a lo largo de la línea de visión en la cromosfera revelaron velocidades con sentido descendente omnipresentes en toda la fácula. Estas velocidades son del orden de $\sim 1.6\,\mathrm{km\,s^{-1}}$. Se encuentran agrupaciones localizadas de velocidades supersónicas con sentido descendente a lo largo de la LIP. Estas velocidades están asociadas con campos cuya orientación es predominantemente a lo largo de la línea de visión. Especulamos que estas velocidades podrían ser la manifestación fotosférica de las velocidades faculares omnipresentes o debidas a material que cae de la hélice durante su ascenso en la atmósfera solar.

La historia evolutiva que proponemos para este filamento en una RA corresponde a la emergencia de líneas de campo helicoidales desde debajo de la fotosfera. No se han encontrado velocidades descendentes de los campos transversales en la fotosfera, lo cual descarta varios modelos de formación de filamentos para nuestro caso en particular. Los resultados presentados en esta tesis no son compatibles con modelos de formación de filamentos que generan la hélice magnética mediante procesos de reconexión en la corona. En nuestro caso detectamos la hélice en la misma fotosfera.

Summary

The aim of this thesis is to study the magnetic structure of active region (AR) filaments and shed light on their formation and evolution. While quiescent filaments have been regularly observed (with different spatial resolutions) above the solar limb, the number of AR filament observations on the disk is extremely scarce in the literature. AR Filaments are important phenomena that may lead to violent coronal mass ejections (CMEs), with material being expelled into space at great velocities which can affect the space weather near Earth. These events are associated to a global change in the coronal magnetic field.

Throughout this thesis, full Stokes spectropolarimetric data sets in the 10830 Å spectral region acquired on July 2005 with the Tenerife Infrared Polarimeter (TIP), at the Vacuum Tower Telescope in Tenerife, have been thoroughly analyzed. The object under study was an AR filament that lay above the polarity inversion line and belonged to an AR which was in its decaying phase. The advantage of the 10830 Å spectral region is that it comprises a photospheric silicon line, a chromospheric helium triplet and two telluric lines. From this observing campaign, two maps on July 3 and seven maps and one time series on July 5 were obtained. The data sets were carefully prepared for their analysis with different spectral line inversion codes. From the inversions of the four Stokes profiles of the He I 10830 Å triplet, the strongest magnetic fields ever measured in AR filaments (600-700 G) were inferred.

After doing the spectral line inversion we needed to determine the magnetic structure, in the local solar frame of reference, in the chromosphere. Therefore, the 180° ambiguity had to be solved. There are several methods to solve this issue. For this thesis we chose the AZAM utility (Lites et al., 1995). The slit-reconstructed helium images showed that the filament was divided in two parts: (1) an elongated and thin shaped filament which was identified as the main axis (or spine) of the filament and (2) a more diffuse filament which represented the top part of a lower-lying filament. From a magnetic point of view, the first part showed sheared field lines along the spine, while in the second part, the field gradually changed into a normal polarity configuration.

To understand the global magnetic field structure of this AR filament we also used the magnetic information encoded in the photospheric Si I 10827 Å line. The analysis confirmed that below the filament, two different parts could still be distinguished: (1) below the spine, the magnetic field had an inverse polarity configuration and (2) below the diffuse filament, the photosphere presented orphan penumbrae (penumbral-like structures without an umbra) and pores that showed sheared field lines along the polarity inversion line (PIL).

These data sets provided unprecedented simultaneous multi-height information of the vector magnetic field in an AR filament. The filament was supported by a flux rope whose main axis lies in the chromosphere, for one part of the filament, while surprisingly was extremely low-lying (in the photosphere) on the other end, thus generating the orphan penumbrae that we observed. For an independent confirmation of the proposed magnetic structure, non-linear force-free (NLFF) field extrapolations were carried out. Since from our observations the information of the vector magnetic field was available at two heights (usually only the photospheric vector magnetogram is available), the extrapolations were carried out twice, first using the photospheric magnetogram and then using the chromospheric one as the boundary layer. Both extrapolations yielded consistent magnetic field lines and confirmed the flux rope topology of the filament. Moreover, having simultaneous

information at two heights, one can determine from the extrapolations the formation height of the He I 10830 Å triplet, which in these data sets yielded ~ 1.4 Mm above the solar surface. In addition, it was proposed that two-layer extrapolations could be used as a method to solve the 180° ambiguity. The solution obtained from the AZAM utility was confirmed by this method.

Once the magnetic structure of this AR filament was reliably inferred, there was still uncertainty about how it was formed. In order to get a better insight to this process, line-of-sight (LOS) velocities, i.e., Doppler shifts, were determined on an absolute scale to study the global motion of the filament. The orbital motions and the gravity shift was taken into account to calibrate the velocities. A new wavelength was inferred for the telluric line (10832.108 Å) next to the red component of the He I 10830 Å triplet. Using different inversion methods, the motions of the transverse magnetic field lines were inferred. Again, the two parts of the filament behaved in a different manner: (1) the low-lying part had transverse field lines that on average moved upwards in the photosphere and had upflow patches in the chromosphere. This was interpreted as a global rise of the flux rope. (2) The other part of the filament showed on the first day, upward motions of its transverse fields, that were consistent on both heights. Two days later, upflows were still inferred in the photosphere (although with slower velocities) but downflows were detected in the spine (chromosphere). This was interpreted as a halt in the rise of the filament. Furthermore, the study of the LOS velocities in the chromosphere revealed that the filament was surrounded by an ubiquitous downflow in the faculae of $\sim 1.6\,\mathrm{km\,s^{-1}}$ on average. Localized photospheric supersonic downflows along the PIL, associated to a predominantly longitudinal component of the magnetic field, might be the photospheric manifestation of the ubiquitous facular downflow or a result of mass drainage during the emergence process of the flux rope.

All in all, the proposed evolutionary scenario for this AR filament corresponds to the emergence of a flux rope from below the photosphere. No large scale downflows of the transverse fields in the photosphere were detected, ruling out several filament formation models for this particular case / scenario. Moreover, the results presented in this thesis were not compatible with filament formation models that generate the flux rope through magnetic reconnection in the corona, because there was already evidence of the flux rope in the photosphere.

Contents

1

Introduction

Solar filaments (or prominences) have been a puzzling topic in solar physics for many centuries. Many excellent reviews have been written about this topic, e.g., Tandberg-Hanssen (1974); Hirayama (1985); Leroy (1989); Tandberg-Hanssen (1995); Demoulin (1998); Paletou and Aulanier (2003); López Ariste and Aulanier (2007); Labrosse et al. (2010); Mackay et al. (2010). Filaments have been seen above the solar limb and at almost every latitude and longitude all over the disk. The magnetic field strength and orientation inside filaments has been inferred. Several models that explain the formation mechanism and the balance of forces of these structures have been developed in the last decades. But still, many new questions have arisen recently owing to the spectacular improvement of instruments, telescopes, and numerical simulations.

This thesis will focus on some of these new (and sometimes old but not yet answered) questions. The magnetic properties inside and below active region filaments, together with the line-of-sight velocities, will be analyzed in order to understand the formation, evolution and plasma support mechanisms that give rise to these mysterious structures.

1.1 What are solar filaments or prominences?

Tadashi Hirayama (1985) wrote: “Prominences are fascinating objects, abundant in variety, beautiful, and above all mysterious”.

The term filament refers to large magnetic structures filled with plasma seen in the chromosphere or corona of the Sun. Filaments on the solar disk appear as dark, elongated structures with lengths of 60–600 Megameters (Tandberg-Hanssen, 1995). Filaments appear dark against the bright solar disk because they are cooler than their surroundings and produce strong absorption signatures in certain spectral lines. However, filaments can also show up in emission when observed above the solar limb, when their structure is seen against the black background of the sky. In this observing geometry they are referred to as prominences. Nevertheless, both terms, filament or prominence, are often used interchangeably in the literature.

Filaments always lie between opposite polarities of the magnetic field, i.e., along the so-called polarity inversion line (PIL) (Babcock and Babcock, 1955). The PIL can be easily identified in a magnetogram as the gray area between the negative (black) and positive (white) magnetic polarities, where the longitudinal magnetic field is absent.

Generally speaking, filaments may be divided into two groups: quiescent (QS) and active region (AR) filaments. The latter are located inside active regions or very close to sunspots. They lie lower in the solar atmosphere (e.g., Martin, 1973; Low, 1996; Lites, 2005) and harbor stronger magnetic fields than the QS ones (e.g., Hirayama, 1985). On the other hand, quiescent filaments (not associated to ARs) are typically much larger and more stable than AR ones. They are embedded high in the corona and have lifetimes of up to several months. It is also worth mentioning a third type of filaments: the polar crown (PC) filaments (e.g., Cartledge et al., 1996). As their name suggests, they are found at high latitudes and usually form a ring (or crown) around the pole. The PIL is therefore East-West oriented and the overlying filament is very stable.

1.1.1 Brief historical background

Interpreted in 1851 as "clouds in the solar atmosphere", prominences have been observed since the 13th century. For centuries, these phenomena were only seen during eclipses. It was not until 1868, when Janssen, and independently Lockyer (1868) and Huggins (1868), measured emission lines of a prominence above the solar limb in the daylight. Later, Zirin and Severny (1961) made the first measurements of the magnetic field in prominences using polarimetric techniques. Over the past decades, the Zeeman and Hanle effects (see Sect. 1.4.1) have been somewhat routinely used to infer their magnetic properties, and such measurements have led to the development of new prominence models. The filament formation models will be described below in Sect. 1.3. See Tandberg-Hanssen (1995, 1998) for an extensive review of the history of prominences.

1.2 Filament observations

1.2.1 Spectral lines

Finding chromospheric spectral lines that are neither too faint nor too broad, and have measurable polarization signatures is not an easy task. Among the most popular chromospheric spectral lines for the study of filaments are the Hα line at 6563 Å, the He I 10830 Å triplet, the D$_3$ line of He I at 5876 Å, the three Ca II lines in the 8542 Å spectral region, the Ca II H line at 3968 Å and the Ca II K line at 3934 Å. However, it is also crucial to study the photosphere below filaments. This is often achieved by using the two Fe I lines at 6301.5 and 6302.5 Å or the Si I line at 10827 Å. The spectral range around the helium 10830 Å triplet offers a unique opportunity to study simultaneously the chromosphere and the photosphere.

Several difficulties arise when observing magnetic fields in the chromosphere. Harvey and Hall (1971) describe some of them: (1) the chromosphere is an inhomogeneous layer whose structure has to be taken into account when interpreting magnetograms and (2) some chromospheric lines are blended by photospheric lines which affects the final magnetic field measurements. Besides, the chromosphere changes very fast and hence requires high spatial and temporal resolution for its analysis. Another complication appears due to the presence of scattering-polarization (and its modification through the Hanle effect). Chromospheric

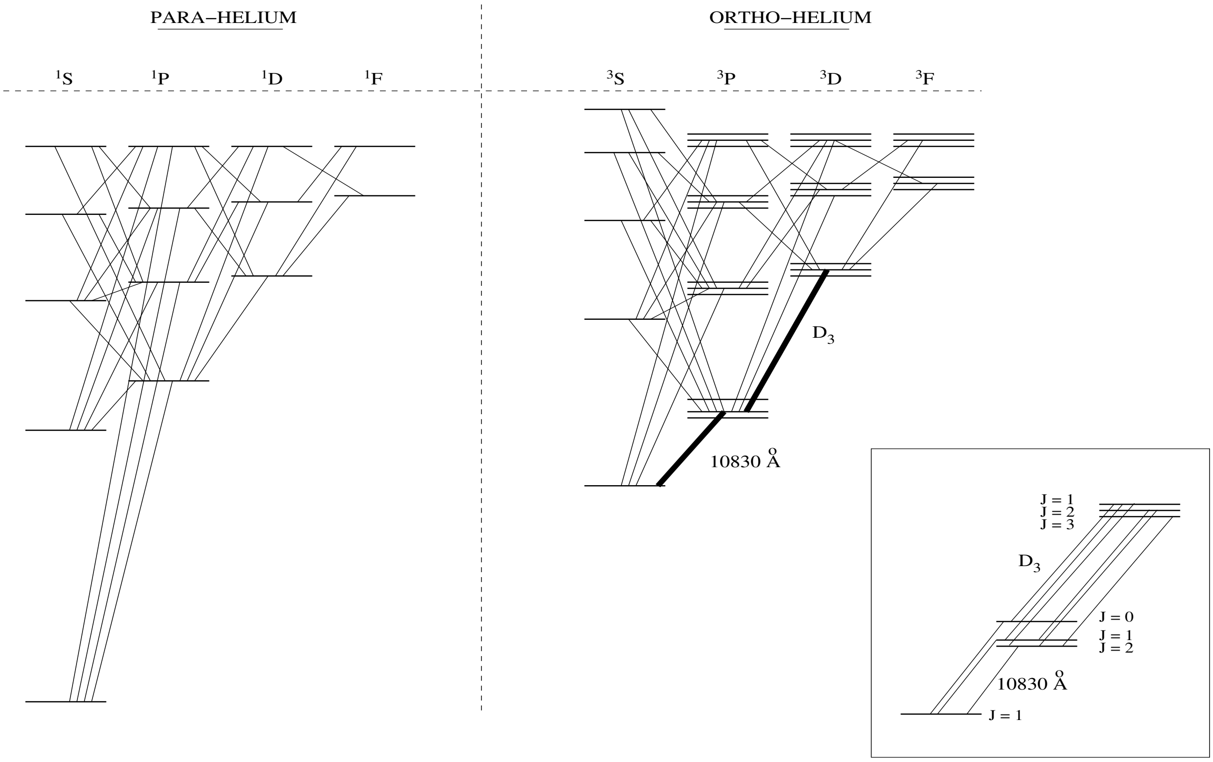

Figure 1.1 Grotrian diagram of the energy levels of the neutral helium atom. The *lower righthand* panel shows the detailed splitting of the 10830 Å triplet and D_3 line. This figure is from Centeno et al. (2008).

magnetic fields are weaker and therefore the polarization signals are fainter and harder to measure.

Since this thesis is almost completely based on He I 10830 Å and Si I 10827 Å observations, a more detailed analysis of these transitions will be presented in the next subsections.

He I 10830 Å triplet

The 10830 Å triplet of neutral helium is a set of transitions that take place between the energy levels 1s2s $^3\mathrm{S}_1$ — 1s2p $^3\mathrm{P}_{0,1,2}$ (see Fig. 1.1), the lower level (^{3}S) being a metastable one. Two spectral features arise from this triplet system, a "blue" and a "red" component, owing to their wavelengths. The blue component at 10829.09 Å arises from the 2s $^3\mathrm{S}_1$ — 2p $^3\mathrm{P}_0$ transition, while the red component at $\sim$ 10830.3 Å is in fact a blend of two lines, that originate from the $^3\mathrm{P}_1$ and $^3\mathrm{P}_2$ levels, respectively. The wavelengths shown in Table 1.1 were taken from the NIST[1] database. Other relevant atomic parameters, such as the effective Landé factor (g_{eff}) – defined by Landi Degl'Innocenti (1982) as a parameter which is used to characterize the Zeeman response of the line to a given value of the magnetic field strength – are also listed in Table 1.1.

---

[1] National Institute of Standards and Technology; http://www.nist.gov/pml/data/asd.cfm .

λ^* (Å)	Lower Term	Upper Term	$g_{\mathrm{eff}}^{\dagger}$	Relative Strength†	$\log gf^{\ddagger}$
10829.091	^{3}S$_1$	^{3}P$_0$	2.00	0.111	−0.745
10830.250	^{3}S$_1$	^{3}P$_1$	1.75	0.333	−0.268
10830.340	^{3}S$_1$	^{3}P$_2$	1.25	0.556	−0.047

Table 1.1 Atomic data of the He I 10830 Å transitions. The parameters were taken from (∗) the NIST database, (†) Socas-Navarro et al. (2004), and (‡) VALD (Kupka et al., 1999).

Helium 10830 Å is formed only in the high chromosphere without contribution from the photosphere (Avrett et al., 1994). It is a suitable candidate to infer magnetic fields in filaments. Figure 1.1 shows the Grotrian diagram of the energy levels of He I. There are two sets of levels, one of singlets and one of triples. Under normal chromospheric conditions of temperature and density, the majority of the helium population sits in the ground state of He I. Transitions between singlets and triplets are forbidden in the electric dipole approximation. This scenario results in a poor population of the ^{3}S metastable level of the triplet system that cannot explain the strong absorption features of the He I 10830 Å triplet in some areas of the solar disk. In order to produce the above-mentioned He I 10830 Å absorption, the metastable 1s2s ^{3}S$_1$ level needs to be populated. One way to do this is by means of photoionization and further recombination processes of the helium atom. The incoming extreme ultraviolet (EUV) radiation of the corona is proposed to cause the ionization of the helium atoms (Goldberg, 1939; Hirayama, 1971; Zirin, 1975; Centeno et al., 2008). Then, the recombination of He II with the free electrons takes place and both singlets and triplets systems are populated.

Collisional excitation is an alternative mechanism to populate the He I 10830 Å triplet levels in the chromosphere (Athay and Johnson, 1960). The ionization of these helium atoms is produced by mixing them with higher temperature electrons (Jordan, 1975). A mixing procedure was proposed later by Shine et al. (1975): their numerical simulations show that *diffusion* (concentration and thermal diffusion) can significantly enhance the He I and He II resonance lines. Furthermore, in agreement with observations, they claim that the diffusion effect happens more in active regions (high pressure) and less in coronal holes (low pressure).

Milkey et al. (1973) proposed that both of the above-mentioned mechanisms take place when producing the He I lines. In lower temperature regions of the chromosphere the EUV radiation photoionizes the He I atoms which afterwards recombine with free electrons. In high temperature regions the collisions dominate. This hypothesis makes sense since the formation height of He I 10830 Å lies between 1500 and 2000 km, but is also observed in high-lying quiescent filaments (tens of megameters), which indicates that He I is present at different heights, i.e., at different temperatures. Andretta and Jones (1997) also favor a mixed, two-layer formation model of the helium lines over a mere photoionization-recombination mechanism.

Si I 10827 Å line

The photospheric Si I 10827 Å line is a magnetically sensitive line and an excellent candidate to study the vector magnetic field and Doppler velocities in the photosphere underneath active region filaments, as already pointed out, for example, by Lites et al. (1985). In addition, its closeness in spectral distance to the chromospheric He I 10830 Å triplet makes this line extremely useful to study both atmospheric layers at the same time.

λ^* (Å)	Lower Term	Upper Term	$g_{\rm eff}^{\dagger}$	Excitation Potential†	$\log gf^{\dagger}$	$\alpha^{\ddagger}$	$\sigma^{\ddagger}$ (cm^2)
10827.089	^{3}P$_2$	^{3}P$_2$	1.5	4.954	0.363	0.231	2.0412×10^{-14}

Table 1.2 Atomic data of the Si I 10827 Å transition. The parameters were taken from (∗) the NIST database, (†) Borrero et al. (2003), and (‡) Barklem et al. (2000). α and σ are the collisional broadening parameters, from the mechanical quantum theory of Anstee, Barklem and O'Mara.

The line originates from the transition between the 3p4s ^{3}P$_2$ and 3p4p ^{3}P$_2$ levels of the Si I atom. The atomic data for this line are presented in Table 1.2. As reported by Bard and Carlsson (2008), the Si I 10827 Å line is formed in non local thermodynamical equilibrium (NLTE). The main difference with respect to the local thermodynamical equilibrium (LTE) profile is that the NLTE profile is substantially deeper than the LTE[2] one. The authors also presented the response function of the spectral line core to velocity perturbations for two different atmospheric models. For an average quiet Sun model (Fontenla et al., 1993; Vernazza et al., 1981) the mean response height is 541 km while for sunspot umbrae (Maltby et al., 1986) it is 308 km above the solar surface.

Through the study of response functions one can infer at which height the spectral line is most sensitive to a perturbation in a given parameter. This is the approach followed by Bard and Carlsson (2008). The response function (RF) to the perturbation of a physical parameter can be calculated for any wavelength and optical depth with the SIR code (see Sect. 1.4.6). The optical depth is a function of the absorption coefficient k_λ and the density ρ. Mathematically it can be expressed as (Gray, 1992):

$$\tau = \int_0^L k_\lambda \, \rho \, dx \; . \tag{1.1}$$

When light passes through a slab of density ρ in the atmosphere, photons can be destroyed or scattered in another direction. The fraction of light loss per unit of mass due to these two processes is denoted by k_λ. The relation between the geometrical depth x and optical depth τ is show in Eq. (1.1). However, the formation height of spectral lines is often given in the τ-scale.

SIR was used in this thesis to calculate the RFs of the Si I line (in LTE conditions) to the magnetic field in a penumbral model atmosphere (del Toro Iniesta et al., 1994). The calculation yielded an average formation height of the Si I 10827 Å line of $\log \tau_{5000} = -2$ (where τ_{5000} is the optical depth at the continuum wavelength of 5000 Å). This value also agrees with the height of the maximum of the RF to velocity perturbations. Hence, this silicon line is formed in the upper photosphere.

---

[2] Spectral lines formed in LTE conditions have their transitions balanced between the involved levels (the number of emitted and absorbed photons is the same). In LTE conditions the population of the levels depends only on the temperature and the transition rates are affected by the density (e.g., Zirin, 1988).

1.2.2 Observations in the past

A considerable amount of literature has been published on prominence observations. In the second half of the 19th century, however, the works published were related to the position of the prominences on the Sun, as well as their morphology and their heights above the solar surface (e.g., Secchi, 1872; Tupman, 1872). With the development of spectroheliographs, that are able to generate monochromatic solar images at a specific wavelength (e.g., Hale and Ellerman, 1903), it was possible to observe them on the solar disk. The relevant observations for the purpose of this thesis began with the introduction of polarimetric measurements as a technique to study the magnetic fields on the Sun. By observing bipolar magnetic regions with a magnetograph, Babcock and Babcock (1955) concluded that filaments appear above and along the polarity inversion line or around the borders of bipolar magnetic regions.

Rust (1967) used a magnetograph, that measured the Hα emission line, to determine the LOS magnetic field strength ($B_{\rm LOS}$) in almost 100 quiescent prominences. From the observed Zeeman displacement, the author inferred the polarity and longitudinal (projected along the line-of-sight) magnetic field strength. Three years later, Tandberg-Hanssen (1970) presented the $B_{\rm LOS}$ in 135 quiescent prominences using a magnetograph that measured the Zeeman effect in several lines: Hα, He I (4471 Å and D$_3$ at 5876 Å), Na I (D$_1$ at 5889 Å, D$_2$ at 5896 Å), and Mg I (5184 Å). Leroy et al. (1977) suggested that the observed polarization in the He I D$_3$ line of a sample of 60 QS prominences was due to the Hanle effect (see also Sect. 1.4.2 and Sahal-Brechot et al., 1977; Trujillo Bueno et al., 2002, for additional information about the Hanle effect method to infer vector magnetic fields in prominences). One year later, with the help of this theory, Leroy (1978) inferred the magnetic field orientation in QS prominences. The author showed that the magnetic fields above polarity inversion lines of active regions are frequently parallel to the long axis of prominences. This study provided, for the first time, information of the orientation of the transverse magnetic field relative to the body of the prominence. However, this information was only inferred using Stokes Q and U. An attempt to obtain the complete vector magnetic field in prominences, i.e., the three components of the vector, was carried out by Bommier et al. (1981). For this purpose the authors proposed two methods: (1) using two lines sensitive, but with different responses, to the Hanle effect and (2) measuring simultaneously the longitudinal Zeeman effect and the Hanle effect in a single line.

The observations of linear polarization in prominences that followed, mainly in the He I D$_3$ line, were interpreted using the Hanle effect to infer the strength and orientation of the magnetic field, e.g., Leroy et al. (1983); Athay et al. (1983); Querfeld et al. (1985). The next observational aim was to match the vector magnetic field (which was not straightforward to infer owing to instrumental limitations and ambiguity problems that always arise from polarimetric measurements) with the theoretical models of prominences (see Sect. 1.3). Longitudinal magnetographs, which are sensitive to the longitudinal Zeeman effect, do not provide information of the transverse magnetic fields, which dominate inside prominences. Therefore, linear polarization measurements interpreted with the Hanle effect provide valuable information on the magnetic field orientation with respect to the polarity inversion line. Leroy et al. (1984) distinguished between two groups of prominences according to their transverse field orientation: (1) prominences found below 30 Mm in height with transverse magnetic fields that point from the positive photospheric polarity towards negative

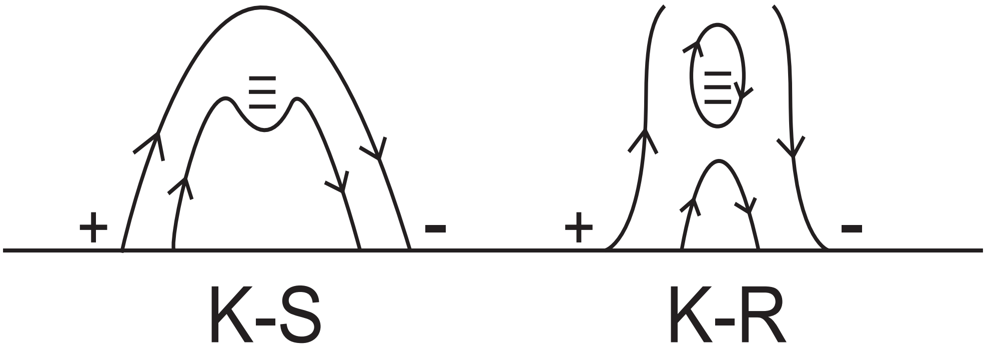

Figure 1.2 Cartoon representing the magnetic field configuration of the filament support models from Kippenhahn and Schlüter (1957) (K–S) and Kuperus and Raadu (1974) (K–R).

one; (2) prominences located above 30 Mm that have the most probable vector magnetic field pointing from the negative photospheric polarity to the positive one. This important statistical result validated both models that were available at that time: the Kippenhahn and Schlüter (1957) model and the Kuperus and Raadu (1974) and Pneuman (1983) models.

Before getting into details regarding these two models, two crucial concepts, which will appear throughout this thesis, have to be defined. On the one hand, transverse magnetic fields pointing from a positive photospheric polarity towards a negative one are said to be in a *normal polarity* (NP) configuration, resembling what a potential field[3] solution would look like. On the other hand, transverse magnetic fields pointing from negative to positive polarity are said to be in *inverse polarity* (IP) configuration. These definitions are in agreement with the ones found in the literature. Why are these two definitions so important? Mainly because either one or the other configuration is responsible for different filament support models. The Kippenhahn and Schlüter (1957) model, identified as K–S on the left side of Fig. 1.2, supports the filament with horizontal magnetic fields that have a NP configuration and so-called dipped field lines (upward concavity) where plasma can be allocated. On the other hand, the Kuperus and Raadu (1974) model, K–R, shown on the right side of Fig. 1.2, has field lines in an IP configuration, i.e., non-potential solution. Hirayama (1985) described the measurement of the angle between the vector magnetic field and the long axis of the prominence as “one of the most important problems of the magnetic field measurements”.

Apart from Leroy’s study on the orientation of the transverse fields in prominences, not many observational studies were published in the late 80’s. Another study by Bommier et al. (1994) showed that 12 QS prominences, from a total of 14, presented an IP configuration.

By the end of the 90’s, Lin et al. (1998) carried out the first full Stokes spectropolarimetric measurement of a QS filament using the He I 10830 Å triplet (see Fig. 1.3). Having Stokes I, Q, U, and V would provide new clues for the study of the magnetic field in filaments. The authors demonstrated the potential of He I 10830 Å polarimetry as an ideal

---

[3] The potential field is a current-free field that corresponds to a minimum magnetic-energy configuration (Priest, 2000). Such a field has field lines that ideally represent an arching loop configuration with loops that start from the positive polarity and end at the negative one.

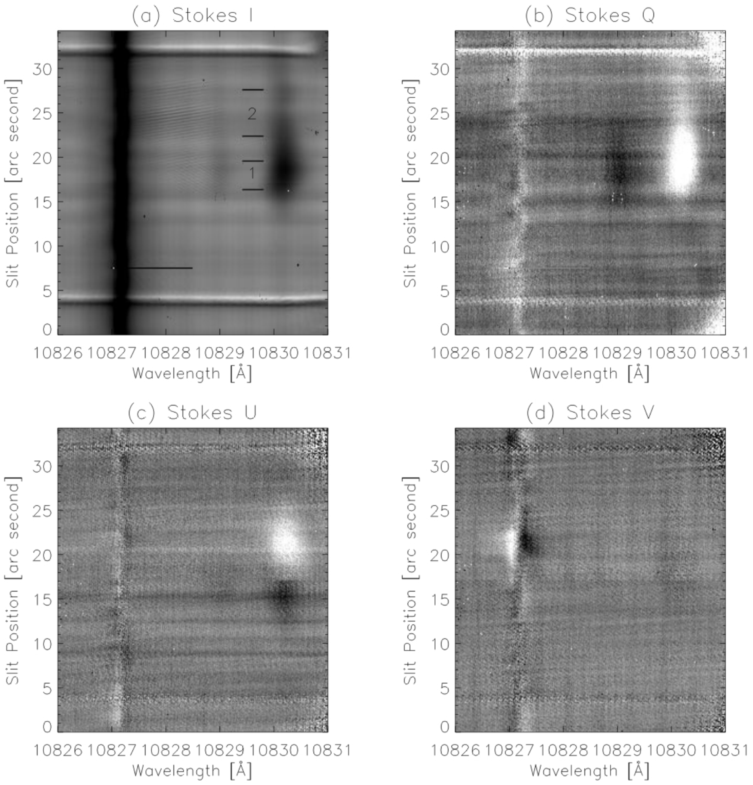

Figure 1.3 The first full Stokes polarization measurements of a QS filament using the He I 10830 Å triplet. The spectral direction is plotted along the x-axis while the y-axis represents the spatial direction along the spectrograph slit. This figure appears in Lin et al. (1998).

candidate to infer the magnetic field in filaments. This triplet had been used by other authors to study, for example, Doppler line shifts in QS filaments, using the nearby telluric lines in the spectra for their calibration (Yi et al., 1991).

The era of high resolution *full* Stokes spectropolarimetry brought us new observations of prominences and filaments with high spectral and spatial resolution. Paletou et al. (2001) pioneered observations of quiescent prominences with the THEMIS telescope located in Tenerife (Spain). The authors used the multi-line spectropolarimetric (MTR) observing mode to carry out full Stokes He I D_3 observations. Interestingly, clear Zeeman-like signatures were detected in Stokes V in some parts of the prominence. The detection of the Zeeman effect implies the presence of stronger magnetic fields than those found in the Hanle effect dominated measurements (see Sect.1.4.2). Hence, the magnetic field strength in prominences might be stronger than expected, between 30–45 G are the values for the longitudinal component reported by Paletou et al. (2001). On the contrary, Trujillo Bueno et al. (2002) detected polarized light in the He I 10830 Å triplet in a QS filament, located at disk center. The polarization signals were entirely ascribed to atomic level polarization and its modification through the Hanle effect. This result favors weaker magnetic fields in filaments since this effect is sensitive to weaker fields (≤ 100 G; Stenflo, 2002) than the Zeeman effect and to magnetic fields that are very inclined with respect to the solar radial direction, i.e., horizontal fields. Using spectropolarimetric observations, the first vector magnetic field maps of a prominence were presented by Casini et al. (2003). The authors showed 2D maps of the magnetic field strength, inclination, and azimuth inside a QS prominence. The inferred magnetic fields of the above-mentioned works together with other works are listed in the summary Table 1.4 which appears in Sect.1.4.7.

Several spectropolarimetric studies, in filaments and prominences, using different spectral lines have been published since then. The main aim of these works was to shed some light on the strength, inclination and azimuth of the magnetic field, which were inferred using either the Hanle or the Zeeman effect (or both), e.g., López Ariste et al. (2005, 2006); Merenda et al. (2006); Ramelli et al. (2006); Sasso et al. (2007); Guo et al. (2010).

Hα observations

Special attention should be given to the Hα 6563 Å observations, which nicely map prominences and filaments in the chromosphere. Many observations of this line have been carried out in the past. Since the Hα spectrum is polarized (Lyot, 1937), it was originally used to study the magnetic field strength in prominences (e.g., Rust, 1967; Malville, 1968; Tandberg-Hanssen, 1970). Nowadays, it is mainly used to study their morphology (e.g., Malherbe et al., 1983), fine structure and evolution (e.g., Mein and Mein, 1991; Lin et al., 2005), and Doppler shifts (e.g., Schmieder et al., 1991, 2010).

As already discovered using other spectral lines, the filaments seen in Hα are also located above polarity inversion lines (Smith and Ramsey, 1967). They usually appear to be composed of a *spine* and *barbs*. Martin (1998) defined the spine as the horizontal fine structure along the long axis of the filament and the barbs as extensions along the sides of the filament, protruding from the spine. Several Hα observations from the 60's were afterwards used to establish conditions for filament formation. Smith (1968) investigated chromospheric fibrils around PILs. He found that the fibrils tended to align with what would become the long axis of the filament before it formed, i.e., parallel to the polarity inversion line (see the upper panels in Fig. 1.4). Later, Foukal (1971) described, based on Hα images, a progressive scenario starting from chromospheric fibrils until the filament was finally formed. The author concluded that filaments were formed in *filament channels*. However, Martin (1990) highlighted that a filament channel does not necessarily have a filament above it.

Filtergrams and movies of Hα have shown that the small scale structure of filaments is far from being static. The small scale elements are highly dynamic and have lifetimes of the order of minutes (Engvold, 1976). As reported by Zirker and Koutchmy (1990), prominences are made of very narrow, optically-thin *threads*. Schmieder et al. (1991) concluded the same for filaments. In that work, the threads seen in Hα images are close to one another and are constantly "squeezed" towards the filament axis. Impressive high-resolution Hα observations taken with the ground based Swedish Solar Telescope (SST; Scharmer et al., 2003) and the Dutch Open Telescope (DOT; Rutten et al., 2004) at La Palma (Spain) have revealed very small fine-scale threads (see Fig. 1.5) in filaments with widths of $\leq 0.3''$ (Lin et al., 2005). These threads have a large range of line-of-sight velocities. Using Hα images from the Big Bear Solar Observatory, Chae et al. (2007) found some threads at rest or slowly moving,

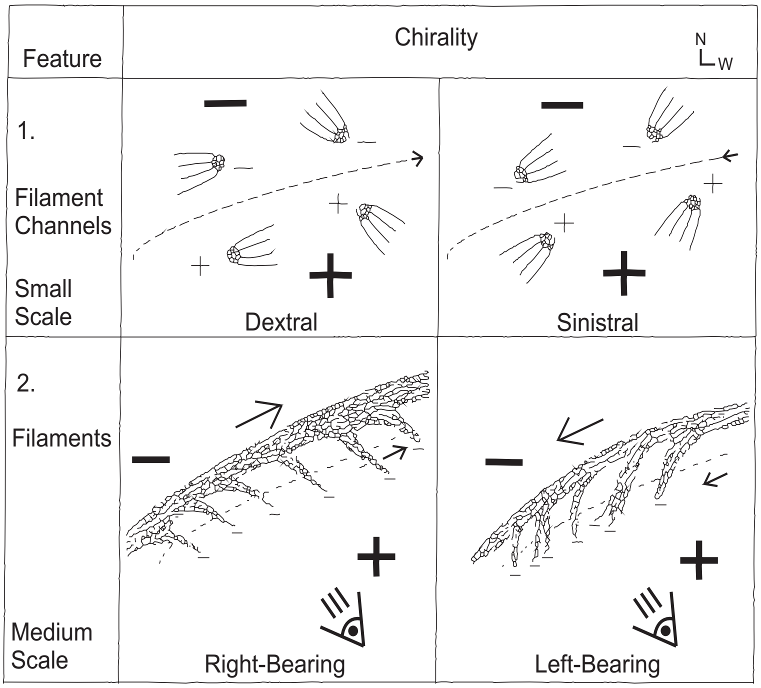

Figure 1.4 Upper row: Hα fibrils aligned with the PIL forming a filament channel. Lower row: relation between the direction of the barbs that extend from the filament and the global polarities found on each site of the filament. This figure originally appears in Martin (1998).

whilst others moved horizontally with speeds up to $\sim 30\,\mathrm{km\,s^{-1}}$. Even horizontal flows in opposite directions inside the spine or inside barbs have been detected (Zirker et al., 1998). These opposite flows are called *counter-streaming*. Swaying motions of filament threads using Hα Dopplergrams were also observed by Lin et al. (2009).

From Hα images a chirality (handedness) property for filaments and filament channels has been inferred (Martin et al., 1994). As a result, when filaments are seen from their positive polarity side, one can find two types: right-bearing and left-bearing filaments. In the former type, the barbs extend from the spine and point to the right, while in the left-bearing filaments the barbs point to the left (see lower panels in Fig. 1.4). Martin et al. (1994) found a correlation between the magnetic field direction along the axis of the filament and the right/left-bearing barbs. The magnetic field points (big arrow in Fig 1.4) to the right (dextral) in right-bearing filaments and to the left (sinistral) in left-bearing filaments. Based on these findings, Martin et al. (2008) developed the chiral method and its application to solve the 180° ambiguity[4] of the magnetic field orientation. The chiral method requires the identification of the chirality of the filament, for example using Hα images, and knowledge of the polarity, for instance, through magnetograms. Therefore, with the available ground based and space-borne telescopes it is an easy and fast method which should be taken into account when solving the 180° ambiguity.

To sum it up, Hα images have substantially improved our knowledge regarding filaments

---

[4] This term will be explained in detail in Sect. 1.4.3.

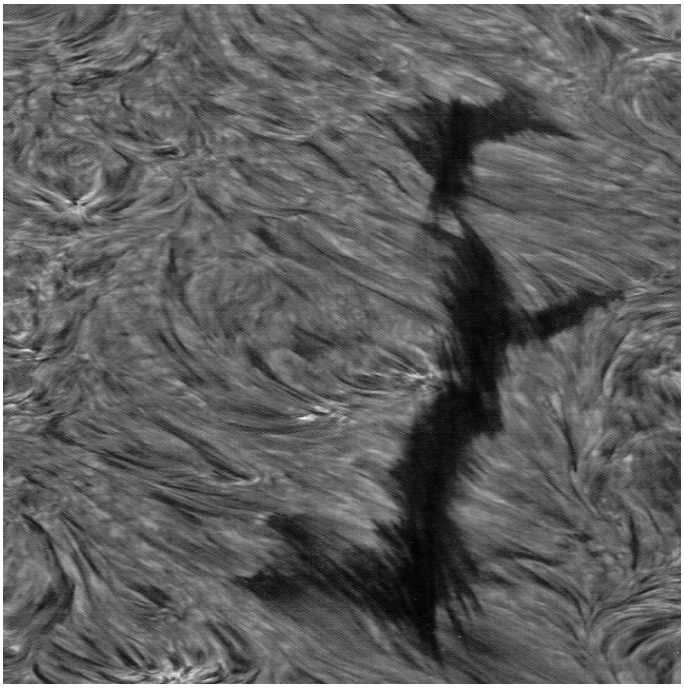

Figure 1.5 High-resolution Hα image showing a filament observed with the DOT. The spine represents the long axis of the filament and barbs extend from the spine towards its right and its left. The filament is made of thin threads. Fibrils are seen around the filament. This image appears in Heinzel and Anzer (2006).

and prominences. Furthermore, they are and excellent tool to complement spectropolarimetric measurements.

1.3 Filament magnetic structure models

From the previous sections it can be easily deduced that filaments are embedded in magnetic fields. But, how is the plasma sustained in the corona against gravity? Several filament support and formation models have been developed by different authors in order to explain the observed filaments/prominences. However, this issue has not been solved yet and the community is strongly divided between supporters of one of two models. Since one of the main aims of this thesis is to improve our knowledge of active region filament formation (through new observations), the most important models will be briefly reviewed below.

1.3.1 K–S versus K–R models

Kippenhahn and Schlüter (1957) presented a simple 2D stationary support model for filaments (K–S model). This model agreed with the observations at the time (e.g., Thompson and Billings, 1967; Rust, 1967). According to the results of Babcock and Babcock (1955) filaments were always found above polarity inversion lines; the magnetic structure presented by K–S corresponded to horizontal magnetic field lines which were able to support the plasma. These field lines emerged vertically from the photospheric positive polarity plage, then became horizontal (slightly "dipped") when crossing the PIL, and then plunged vertically into the photospheric negative polarity, as seen in Fig. 1.2. In Sect. 1.2.2 we mentioned that this magnetic configuration is known as a normal polarity (NP) configuration (i.e., the field lines point from the positive towards the negative photospheric polarity). To balance gravity, there is an upward force produced by magnetic tension. Moreover, the magnetic pressure gradient (with height) provides a transverse force that compresses the plasma (Priest, 2000).

A suitable inverse polarity (IP) configuration model was presented by Kuperus and Raadu (1974), hereafter K–R model (see also Anzer, 1989; Tandberg-Hanssen, 1995; Priest, 2000). In their work, magnetic reconnection[5] is triggered by the proximity of oppositely directed vertical magnetic field lines. The resulting magnetic configuration leads to an IP field that can support prominence plasma (see Fig. 1.2). The authors propose a vertical upward Lorentz force ($F_{\uparrow}$) generated by a current I. This current induces photospheric surface currents that avoid a downward movement of the field lines into de convection zone. K–R propose a second, downward, Lorentz force ($F_{\downarrow}$) induced by the previously generated horizontal magnetic field. The sum of both Lorentz forces has to be $F_{\uparrow} + F_{\downarrow} > 0$ in order to support the prominence against gravity.

1.3.2 Sheared arcade models

The work published by Antiochos et al. (1994) provided a new 3D model able to support the plasma inside prominences (see Fig. 1.6a). A mandatory condition imposed on their model was the presence of dips in the resulting structure. The model is based on a 3D magnetic field connected to a dipole located below the photosphere. The footpoints of a flux tube, anchored at both sides of the PIL, move parallel to the PIL in different directions. As reported by Klimchuk (1990), footpoint shearing motions imposed upon force-free flux tubes produce an upward expansion of the field lines, i.e., the field lines rise. The authors point out that a dip naturally arises due to the differential expansion along the field line. The sheared field lines seen in Fig. 1.6a reach higher altitudes the further away they are ($y \sim \pm 1$) from their initial position ($y = 0$). Therefore, the midpoint of the field lines appear to hang lower in the atmosphere, thus forming dips. The dipped field lines are free of twist, or only slightly twisted when a gradient of the shear is present. Owing to the shear, the resulting S-shaped field line presents an IP configuration almost everywhere where dips have formed, although the authors also note the presence of a NP configuration in the low-lying field lines. From this model it is clear that dips (i.e., concave upward field lines) are not formed as a consequence of the weight of the filament plasma. This is usually the case since the plasma beta, i.e., the ratio of gas pressure to magnetic pressure ($\beta = 2\mu P/B^2$; where μ is the magnetic permeability), is low ($\beta \ll 1$) at coronal heights. However, caution has to be taken because Anzer and Heinzel (2007) estimated beta values in QS prominences that were larger than unity. Under such circumstances, the gravitational force cannot be neglected and dips may form due to the weight of the prominence's mass.

In the sheared arcade model presented by Aulanier et al. (2002), most of the dips have

---

[5] Magnetic reconnection releases magnetic energy and produces a rearrangement of the magnetic field lines.

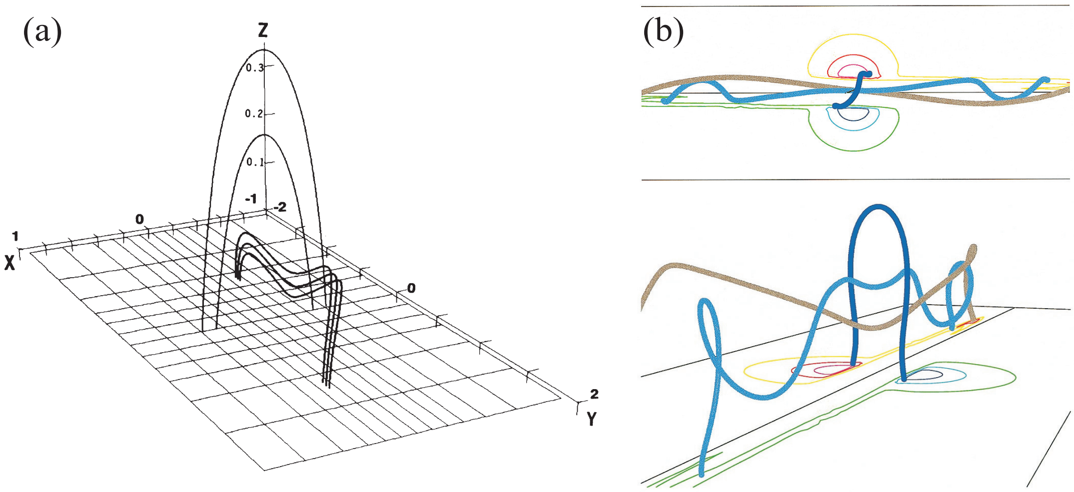

Figure 1.6 Two different filament formation models are shown. a) Plot taken from Antiochos et al. (1994). Their model show sheared magnetic field lines that lie underneath an unsheared coronal arcade which is centered at the dipole system. b) Top and side view plots from the filament formation model that appears in DeVore and Antiochos (2000). In their model, the photospheric footpoints appear heavily displaced. A helical structure (light blue line) has formed owing to reconnection processes with the above unsheared arcades. The dark gray line corresponds to the magnetic field line in the core of the filament.

formed through reconnection between the sheared field lines and the overlying potential loops. The authors mostly identified dips with an inverse polarity magnetic field configuration. However, also normal polarity dips appeared at the top of the central part and at the ends of the filament. Hence, a mixture of IP and NP configurations can coexist in the same filament. Interestingly, when the field lines are largely sheared, reconnection modifies the magnetic topology and weakly helical field lines appear.

The merging of two filaments was successfully simulated by Aulanier et al. (2006). Reconnection processes result in a stable magnetic structure that has also long sheared field lines. These field lines have dips along their length. The authors emphasize that the resulting topology differs *significantly* from that of a flux rope.

Before moving on to the next section, it is worth mentioning that an IP configuration does not always imply the presence of twisted field lines, as seen in the model of Antiochos et al. (1994).

1.3.3 Flux rope models

Nowadays, flux ropes are believed to be the magnetic structure responsible for supporting the filament's plasma (especially in AR filaments). Flux rope is defined as a group of helical flux tubes. In the past, many works have found a dominating IP configuration of the field lines in the filament (see Sect.1.2.2). Therefore, the solution which comes up naturally is a helical structure of the field lines.

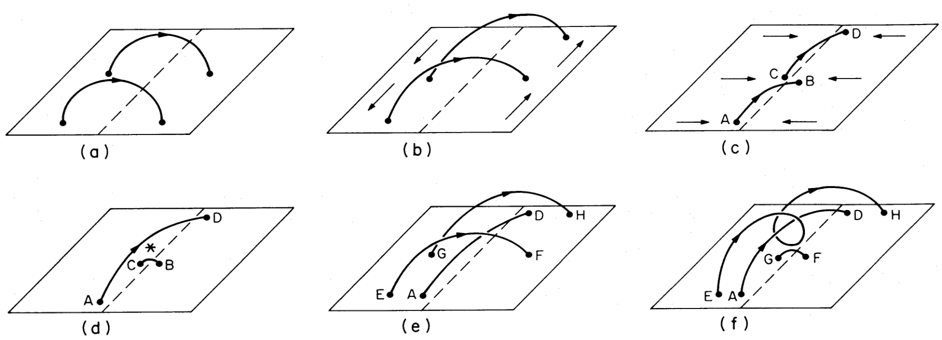

Figure 1.7 The flux rope formation model by van Ballegooijen and Martens (1989) is shown. The initial configuration in panel a) has potential field lines (solid lines) that cross the PIL (dashed line). Shearing motions and convergence towards the PIL in panels b) and c) trigger magnetic reconnection and finally, in panel f), generate a flux rope. Note that as a byproduct, small loops, points G and F in panel f), that are perpendicular to the PIL have appeared and submerge below the photosphere.

Pneuman (1983) suggested a filament formation model with helical field lines. The proposed magnetic structure is formed due to the distention of a photospheric bipolar region upwards into the corona. Magnetic reconnection can take place where vertical field lines with opposite polarity meet. If the field is sheared along the PIL, twisted field lines are the result of this reconnection. These field lines have an IP configuration and sit above low-lying potential-like arcades which are perpendicular to the PIL. Then, through condensation of the gas that is found inside the flux rope, the authors explain how the material gathers at the bottom of the rope. They emphasize that the actual filament only occupies the bottom part of the helix. Demoulin and Priest (1989) proposed that the prominence structure, after condensation, is able to generate a NP configuration at greater heights. This is only possible if the plasma that sits in the bottom of the helical structure deforms the field lines, pulling them down and consequently decreasing the magnetic pressure. As a result, dips with a NP configuration can form above the helix. This model has therefore an IP configuration at the bottom of the helix and a NP configuration at the top.

A clear step-by-step description of the formation of the twisted magnetic field lines that support filaments was presented by van Ballegooijen and Martens (1989) and is shown in Fig. 1.7. This model, although very similar to the one of Pneuman (1983), has been a major reference source for filament and prominence studies. The authors constructed their model based on the assumption that magnetic flux disappears from the solar photosphere by the submergence of magnetic loops (after reconnection). The resulting helical structure, i.e., a flux rope, results from a potential field that is sheared along the PIL and whose footpoints then experience motions converging towards the PIL; this structure eventually reconnects with other sheared field lines shaping into a flux rope (see Fig. 1.7a-f). As a byproduct of the magnetic reconnection, small loops ($\leq 900\,\mathrm{km}$; G and F points in Fig. 1.7f) are formed in the photosphere, perpendicularly oriented with respect to the PIL, which submerge below the photosphere. This is also found in a more recent model by van Ballegooijen and Mackay (2007). According to these models, flux ropes are formed in the chromosphere or corona.

The numerical simulations presented by DeVore and Antiochos (2000) produce helical

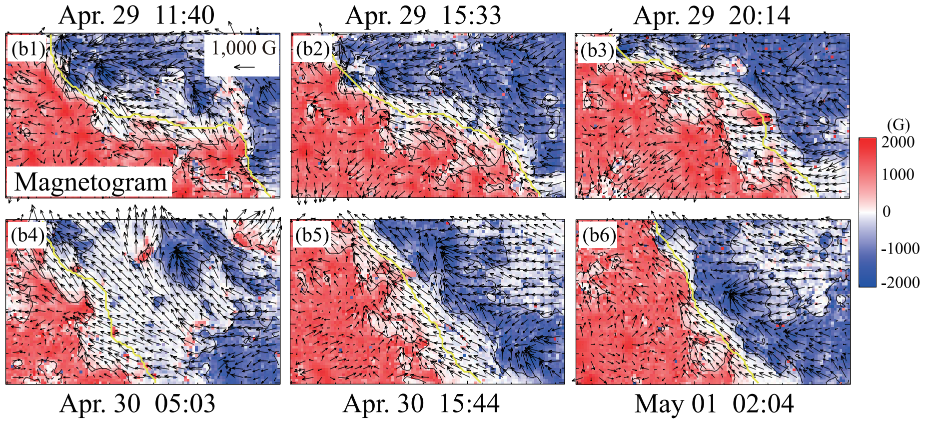

Figure 1.8 Photospheric vector magnetogram time series below an AR filament. The yellow line shows the PIL. The black arrows represent the orientation of the horizontal magnetic field. The arrows slightly change from a NP configuration into an IP configuration. This figure is adapted from Okamoto et al. (2008).

field lines surrounding the core field of the filament (see Fig. 1.6b). However, only reconnection between the highly sheared magnetic field lines and the overlying (unsheared) arcades is necessary to produce them. No converging flows are needed in this model. Furthermore, reconnection only takes place in the corona. Therefore, coronal arcades are indispensable in this model (otherwise no flux rope can be built up). In the flux rope model developed by Amari et al. (1999), the twist is built up by swirling motions in the photosphere, around the PIL. While shearing flows have been measured parallel to the PIL (although it is unclear if they are large enough, e.g., Low, 1996), no systematic converging flows towards the PIL have been found (Hindman et al., 2006; Lites et al., 2010).

Several other flux rope filament formation models can be found in the literature. For instance, the model by Priest et al. (1989) presents twisting motions, produced by the Coriolis force, that are able to create dips. Another model proposed by Rust and Kumar (1994) shows the bodily elevation from the chromosphere of horizontal flux ropes that contain the prominence's plasma. According to Low and Hundhausen (1995), the filament sits in a superposition of two magnetic flux systems: the first one connects opposite polarities and the second one is a flux rope that lies above the former one, along the PIL. Furthermore, models that use linear force-free field equations can also be found (e.g., Aulanier and Demoulin, 1998).

Flux rope emergence from below the photosphere

From an observational point of view, a new scenario of filament formation has been proposed. Lites et al. (1995) and Lites and Low (1997) proposed the emergence of twisted magnetic field lines through the photosphere, at the PIL of a δ-sunspot, into the corona. At the same time, a filament seen in Hα started to form above the PIL. Recently, observations carried out with the Solar Optical Telescope (SOT) on board Hinode, were interpreted by Okamoto et al. (2008, 2009) as an emerging flux rope from below the photosphere. A more diffuse pre-existent filament was seen along the PIL before the Hinode observations took place. The spectropolarimeter provided full Stokes profiles of the photospheric Fe I lines. The sequence of inferred photospheric vector magnetograms, see Fig. 1.8, shows field lines that change from a NP into an IP configuration in a time range of ∼ 1 day. The change from a NP into an IP configuration *in the photosphere* suggests the emergence of a flux rope along the PIL. The authors argue that the emerging flux rope reconnects with the magnetic field lines of the overlying filament and consequently stabilizes the whole structure for the next days. The flux rope emergence scenario has been supported by few new observations so far (Lites, 2005; Lites et al., 2010; Xu et al., 2012). Recently, from simultaneous observations in the photosphere and chromosphere, Xu et al. (2012) have inferred a helical structure supporting the filament's plasma. Moreover, since the chromospheric Doppler shifts inferred from the He I 10830 Å triplet show upflows, the authors conclude that the flux rope is rising.

The rise of flux ropes from the convection zone (CZ) into the corona has been simulated numerically by many authors (e.g., Fan, 2001; Archontis et al., 2004; Magara, 2004; Manchester et al., 2004; Murray et al., 2006; Martínez-Sykora et al., 2008; Cheung et al., 2008; Fan, 2009; Yelles Chaouche et al., 2009; MacTaggart and Hood, 2010). However, severe problems appear during the emergence process. It is widely accepted that the flux rope rises through the CZ owing to *magnetic buoyancy*, i.e., the flux rope is lighter than its surroundings (Parker, 1955). Once it reaches the photosphere, density and pressure decrease sharply with height (see Fig. 1 in Archontis et al., 2004). The flux rope evolves into an Ω-shaped rope that barely crosses the photosphere, but its body stops rising just before reaching the surface (e.g., Manchester et al., 2004) or slightly above it (MacTaggart and Hood, 2010). In the latter work, the trapped flux rope (lying just above the photosphere) expands laterally producing a broadening of the polarity inversion line. The broadening and subsequent narrowing of the width of the PIL is known as the "sliding doors" effect, a term first mentioned (and observed) by Okamoto et al. (2008). The larger the twist of the flux rope and the stronger the field, the more flux moves from the photosphere into the chromosphere (Martínez-Sykora et al., 2008). Although the body of the flux rope cannot rise to higher layers, the expansion of the magnetic field lines due to secondary buoyancy instability reaches coronal heights, as shown by Martínez-Sykora et al. (2008) and MacTaggart and Hood (2010). Such an instability is generated owing to the decreasing magnetic field strength with height (Priest, 2000). The expanding field lines might reconnect with the overlying coronal magnetic field. Finally, reconnection below and above the formed flux rope eventually leads to a runaway situation where the flux rope completely erupts (e.g., Archontis and Török, 2008), producing, for instance, a coronal mass ejection (CME).

1.3.4 Extrapolations

Magnetic fields in the photosphere and chromosphere can be inferred through different techniques. But, to get a global picture of how the field lines look like in a particular solar region, extrapolation techniques are needed. Moreover, magnetic field measurements in the corona are extremely difficult. Therefore, a first approach can be achieved through magnetic field extrapolations (see Gary, 1989; Priest, 2000; Wiegelmann, 2004; Neukirch, 2005, and references therein for a complete review on extrapolations).

How do extrapolations work? In order to reconstruct the magnetic field in the solar atmosphere, this method uses as its main assumption that the plasma β is small, i.e., the magnetic pressure is much higher than the plasma gas pressure, in the corona. As a consequence, the magnetic field is close to being force-free. In addition, it is imposed that coronal magnetic fields are in equilibrium ($\partial/\partial t \approx 0$) and plasma flows can be neglected. Hence, the ideal magnetohydrodynamic (MHD) equations relevant for the extrapolations are reduced to:

$$\vec{j} \times \vec{B} = 0 \ , \tag{1.2}$$

$$\nabla \times \vec{B} = \mu_0 \vec{j} \ , \tag{1.3}$$

$$\nabla \cdot \vec{B} = 0 \ , \tag{1.4}$$

$\vec{j}$ being the current density, μ_0 the vacuum permeability and $\vec{B}$ the magnetic field. From Eq. 1.2, it is clear that the current density is parallel to $\vec{B}$, hence

$$\mu_0 \vec{j} = \alpha \vec{B} \ , \tag{1.5}$$

where α, the so-called force-free parameter, is a function of position but remains constant along each field line. It gives information of the level of twist of the field line. Equation 1.3 can be then rewritten as follows

$$\nabla \times \vec{B} = \alpha \vec{B} \ . \tag{1.6}$$

Depending on the value of α, we can distinguish among three different types of force-free field extrapolations: potential ($\alpha = 0$), linear force-free (LFF; α is constant and has a unique value for all field lines), and non-linear force-free (NLFF; α varies from field line to field line but is constant along each field line).

There is no doubt that NLFF field extrapolations show more realistic results than the other two types (Schrijver et al., 2006). However, it is not always possible to perform such extrapolations. The photospheric magnetic field measurements are taken as a boundary condition for the extrapolation code. NLFF field extrapolations require the three components of the magnetic field (B_x, B_y, and B_z), while the LFF field method only requires a longitudinal magnetogram (B_z or B_{LOS}).

Yan et al. (2001) obtained for the first time a flux rope structure from NLFF field extrapolations of the magnetic field of an active region. Recently, a few works have presented the magnetic structure of active region filaments inferred from NLFF field extrapolations starting from the photosphere (e.g., Guo et al., 2010; Canou and Amari, 2010; Jing et al., 2010). Interestingly, all these works clearly detect a flux rope topology sustaining the filament. However, Guo et al. (2010) also found a sheared arcade structure in a different section of the same filament (see Fig. 6 of their work). Dips, where the plasma is located, are found in the extrapolated magnetic structure. The field strength inside the filament was found to be large, between 200–400 G (Jing et al., 2010) and 700 G (Guo et al., 2010). These results favor the flux rope models but cannot clarify the origin of the twisted field lines (emergence versus reconnection above the photosphere).

1.4 Magnetic field measurements

In this section we will describe the techniques to infer magnetic fields from polarimetric measurements. A brief overview of the inversion codes used in this thesis is presented as well as a summary of the literature on the inferred magnetic fields in filaments and prominences.

1.4.1 Polarimetry

Light has an electromagnetic (EM) nature. This means that it can be represented by an electric and a magnetic field vectors that oscillate perpendicular to each other and perpendicular to the direction of propagation. If the electric field vector of a group of EM waves oscillates in an organized way we say that the light is *polarized*. Mathematically, an electric field vector in the x-y plane can be separated into the following two components:

$$E_x = E_1 \cos(\omega t - \phi_1) \quad , \qquad\qquad E_y = E_2 \cos(\omega t - \phi_2) \quad , \tag{1.7}$$

where E_1 and E_2 are constants representing the amplitude of the wave, ω is the angular frequency, t is the time coordinate and ϕ_1 and ϕ_2 are the phases of each component. The amplitudes of the wave (E_1,E_2) together with the phase difference between E_x and E_y, i.e., $\phi_1 - \phi_2$, describe the polarization state of the wave: linear, circular or elliptical. For instance, when both phases have the same value ($\phi_1 = \phi_2$), the electric field vector $\vec{E}$ follows a straight line in the x-y plane, the light beam is linearly polarized. The circular polarization state (a circle is traced out by the electric field vector in the x-y plane) is achieved when the components have their phases shifted by $\pi/2$ (or $3\pi/2$), i.e., $\phi_1 - \phi_2 = \pm 90°$, and their amplitudes are the same ($E_1 = E_2$). If none of the previous cases apply, the light is elliptically polarized.

However, rather than an individual monochromatic light beam, what we really observe is the superposition of many wave packets. Since the electric field vector cannot be directly measured, George Stokes introduced the Stokes parameters (I, Q, U, V), which are averages of the amplitudes and phases of $\vec{E}$:

$$\begin{aligned} I &= < E_1^2 + E_2^2 > \ , & Q &= < E_1^2 - E_2^2 > \ , \\ U &= < 2E_1E_2\cos(\phi_1 - \phi_2) > \ , & V &= < 2E_1E_2\sin(\phi_1 - \phi_2) > . \end{aligned} \tag{1.8}$$

The advantage of these parameters is that a polarimeter, installed at the telescope, is able to measure linear combinations of time *averages* of the four Stokes parameters. From Eqs. (1.8) it can be deduced that Stokes I is the total intensity and Stokes Q is the intensity difference between horizontal and vertical *linear* polarizations. Stokes U gives information about the intensity difference between *linear* polarization at +45° and −45° and Stokes V allows us to distinguish between right or left-handed *circular* polarization (see also the book and review by del Toro Iniesta, 2003; Trujillo Bueno, 2006, and references therein). A basic characteristic of the Stokes parameters is that they obey the following equation:

$$I^2 \geq Q^2 + U^2 + V^2 \ . \tag{1.9}$$

It is thus possible to measure I although $Q = U = V = 0$. This naturally leads to the case of incoming radiation that is unpolarized (also known as *natural* light).

A polarimeter is an instrument that can measure linear combinations of the Stokes I, Q, U, and V parameters. Several polarimeters that can measure the full Stokes vector have been built in the past, for example, the Advanced Stokes Polarimeter (ASP; Elmore et al., 1992),the Zurich Imaging Polarimeter (ZIMPOL; Povel, 1998), the La Palma Stokes Polarimeter and the Tenerife Infrared Polarimeter (LPSP and TIP; Mártinez Pillet et al., 1999). Two fundamental components of a polarimeter are the polarizer and the retarder (e.g., Landi Degl'Innocenti, 1992; del Toro Iniesta, 2003). When the light beam arrives at the *polarizer*, only the component of the electric field vector oscillating along a particular axis will pass through it. If the electric vector oscillates perpendicular to that axis, the polarizer is completely opaque to that light. Therefore, a desired polarization state of the incoming light beam (e.g., linear at 90°) can be selected. On the other hand, a *retarder* divides the incident beam into two orthogonal components and shifts the phase of one of them with respect to the other. As a consequence, the polarization state can be modified. Once the radiation goes through the retarder and polarizer (see the scheme in Fig. 2 by Landi Degl'Innocenti, 1992), the output beam $I_{out}(\alpha, \phi)$ is a linear combination of the four Stokes parameters, where α is the angle of the transparent axis of the polarizer with respect to an arbitrary reference axis and ϕ is the phase shift introduced by the retarder. Several variations of α and ϕ yield different measurements of $I_{out}(\alpha, \phi)$. A combination of the obtained $I_{out}(\alpha, \phi)$ leads to the determination of the Stokes parameters. In particular, Stokes Q, U, and V are calculated combining several $I_{out}(\alpha, \phi)$ measurements.

1.4.2 The generation of polarized light

"Polarization is produced when the spatial symmetry is broken in the physical process that generates the radiation that we observe", by Stenflo (2002). Electric or magnetic fields, anisotropic radiation or scattering, are elements that can break the symmetry.

Zeeman effect

The Zeeman effect can split a degenerated atomic energy level of an element into different sublevels due to the presence of a magnetic field B. The radiation resulting from transitions to and from these new sublevels is polarized. The energy level of an atom with angular momentum J, can split into $2J + 1$ magnetic sublevels with magnetic quantum number M. The following theory of the Zeeman effect is valid for "weak" magnetic fields, in the sense that the Russel-Saunders or LS coupling is a valid approximation to describe the state of the atom (see e.g., Stix, 2002; del Toro Iniesta, 2003). Then, the energy shift, and hence the resulting wavelength displacement $\Delta\lambda$ of these sublevels, is proportional to the effective Landé factor ($g_{\rm eff}$; a combination of the quantum numbers J, L and S) of the transition and the magnetic field strength (see e.g., Landi Degl'Innocenti, 1992):

$$\Delta\lambda = \frac{e}{4\pi c m_{\rm e}} g_{\rm eff} \lambda_0^2 B \simeq 4.67 \times 10^{-13} g_{\rm eff} \lambda_0^2 B \ , \tag{1.10}$$

with λ_0 in Å units and B in Gauss units. It is clear from Eq. (1.10) that the greater the value of $g_{\rm eff}$, λ_0 or B, the larger the wavelength displacement. Given the selection rules for

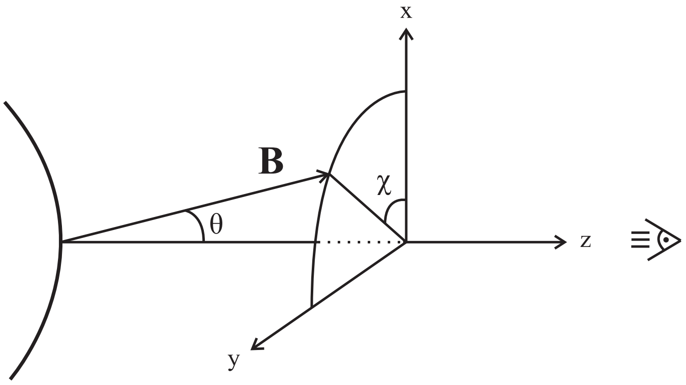

Figure 1.9 The vector magnetic field $\vec{B}$ projected onto the local frame of reference is shown. The angle θ is the inclination of $\vec{B}$ with respect to the LOS. In the plane perpendicular to the LOS, the angle between the reference axis (vertical axis) and $\vec{B}$ is called the azimuth angle χ.

electric dipole transitions:

$$\Delta M = M_{\mathrm{u}} - M_{\mathrm{l}} = 0, \pm 1 \ , \tag{1.11}$$

where M_{u} (M_{l}) is the magnetic quantum number of the upper (lower) level, the transitions that fulfill the condition $\Delta M = 0$ are called π transitions and the ones that fulfill $\Delta M = \pm 1$ are known as σ transitions. It is important to note that the π component is not displaced in wavelength, while the σ components are shifted symmetrically to the red (σ_{r}; $\Delta M = +1$) and blue (σ_{b}; $\Delta M = -1$) of the original wavelength. The subscripts "r" and "b" stand for red and blue due to their shift in wavelength with respect to the central wavelength λ_0. When the magnetic field $\vec{B}$ is oriented parallel to the observer's line-of-sight (LOS), only the σ transitions of the spectral line are seen and are circularly polarized while no π transitions are seen (longitudinal Zeeman effect). The circular polarization spectrum shows two antisymmetric lobes (see e.g., Fig. 1 in Trujillo Bueno, 2006). Longitudinal magnetograms are based on this effect and are extremely useful to obtain 2D images of the Sun showing the longitudinal component of $\vec{B}$. When $\vec{B}$ is perpendicular to the LOS, both π and σ components can be measured and represent linearly polarized light (transverse Zeeman effect). The linear polarization spectrum shows one central lobe (π component) and two symmetric lobes placed on each side (σ_{b} and σ_{r}). However, usually $\vec{B}$ is neither completely longitudinal nor transverse with respect to the LOS and therefore has an arbitrary inclination (θ) and azimuth (χ) which can be inferred studying the Stokes profiles $I(\lambda), Q(\lambda), U(\lambda)$, and $V(\lambda)$.

Radiative transfer equation

In order to interpret the observed Stokes profiles, the polarized radiative transfer equation (RTE) is needed. The solution to this partial differential equation gives the Stokes parameters as a function of a series of physical quantities used to describe the medium through which the light travels. Given the Stokes vector $\vec{I} = (I, Q, U, V)^{\mathrm{t}}$ ("t" meaning transpose), the polarized RTE can be written as follows

$$\frac{d}{d\tau_{\mathrm{c}}}\vec{I}=\mathbb{K}(\vec{I}-\vec{S}) \ , \tag{1.12}$$

where τ_{c} is the optical depth measured in the continuum, $\mathbb{K}$ is the propagation matrix of the light and $\vec{S}$ is the source function, defined as the ratio of emission to absorption (Gray, 1992). The propagation matrix $\mathbb{K}$ is written as the addition of three matrices: the absorption matrix and the symmetrical and antisymmetrical components of the matrix (see Landi Degl'Innocenti, 1992). Under the approximation of Local Thermodynamic Equilibrium (LTE), the source function equals the Planck function, $\vec{S}=(B_T,0,0,0)^{\mathrm{t}}$. Equation (1.12) can be extensively written as (Landi Degl'Innocenti, 1992):

$$\frac{d}{d\tau_{\mathrm{c}}}\begin{pmatrix} I \\ Q \\ U \\ V \end{pmatrix} = \begin{pmatrix} \eta_I & \eta_Q & \eta_U & \eta_V \\ \eta_Q & \eta_I & \rho_V & -\rho_U \\ \eta_U & -\rho_V & \eta_I & \rho_Q \\ \eta_V & \rho_U & -\rho_Q & \eta_I \end{pmatrix} \begin{pmatrix} I-B_T \\ Q \\ U \\ V \end{pmatrix} . \tag{1.13}$$

The coefficients of the propagation matrix $\mathbb{K}$ can be expressed as follows:

$$\eta_I = 1+\frac{\eta_0}{2}\left[\phi_{\mathrm{p}}\sin^2\theta+\frac{\phi_{\mathrm{b}}+\phi_{\mathrm{r}}}{2}(1+\cos^2\theta)\right] \ , \tag{1.14}$$

$$\eta_Q = \frac{\eta_0}{2}\left[\phi_{\mathrm{p}}-\frac{\phi_{\mathrm{b}}+\phi_{\mathrm{r}}}{2}\right]\sin^2\theta\cos 2\chi \ , \tag{1.15}$$

$$\eta_U = \frac{\eta_0}{2}\left[\phi_{\mathrm{p}}-\frac{\phi_{\mathrm{b}}+\phi_{\mathrm{r}}}{2}\right]\sin^2\theta\sin 2\chi \ , \tag{1.16}$$

$$\eta_V = \frac{\eta_0}{2}\left[\phi_{\mathrm{r}}-\phi_{\mathrm{b}}\right]\cos\theta \ , \tag{1.17}$$

$$\rho_Q = \frac{\eta_0}{2}\left[\psi_{\mathrm{p}}-\frac{\psi_{\mathrm{b}}+\psi_{\mathrm{r}}}{2}\right]\sin^2\theta\cos 2\chi \ , \tag{1.18}$$

$$\rho_U = \frac{\eta_0}{2}\left[\psi_{\mathrm{p}}-\frac{\psi_{\mathrm{b}}+\psi_{\mathrm{r}}}{2}\right]\sin^2\theta\sin 2\chi \ , \tag{1.19}$$

$$\rho_V = \frac{\eta_0}{2}\left[\psi_{\mathrm{r}}-\psi_{\mathrm{b}}\right]\cos\theta \ . \tag{1.20}$$

The absorption profiles $\phi_{\mathrm{p,b,r}}$ are a superposition of as many Voigt profiles as π, σ_{b}, and σ_{r} Zeeman components are generated between the splitted upper J_{u} and lower J_{l} levels. The ϕ profiles are centered at the main (unshifted) wavelength λ_0 of the line transition (for the π components) or are shifted by $\pm\Delta\lambda$ (from Eq. 1.10) with respect to λ_0 (for the σ_{b} and σ_{r} components). $\psi_{\mathrm{p,r,b}}$ are the dispersion profiles which include, for example, effects produced by microscopic velocity fields (Landi Degl'Innocenti and Landolfi, 2004). η_0 is the ratio between the absorption coefficient in the line center and the absorption coefficient of the continuum. The angles θ and χ are used to describe the orientation of the vector magnetic field $\vec{B}$. θ is the *inclination* angle between $\vec{B}$ and the line-of-sight (see Fig. 1.9). χ is the *azimuth* angle that $\vec{B}$ forms, when projected onto the plane of the sky (perpendicular to the LOS), with respect to an arbitrary reference axis.

The solution of the polarized RTE is a complex problem. Therefore, several approximations can be taken to solve it. One of them is the well-known weak field solution. This approach is satisfied when the wavelength displacement $\Delta\lambda$ from Eq. (1.10) is much smaller than the Doppler width of the spectral line:

$$g_{\text{eff}} \frac{\Delta\lambda}{\Delta\lambda_{\text{D}}} \ll 1 \ , \tag{1.21}$$

where $\Delta\lambda_{\text{D}}$ is the Doppler width defined as:

$$\Delta\lambda_{\text{D}} = \lambda_0 \frac{\omega_{\text{T}}}{c} \ , \tag{1.22}$$

ω_{T} being the thermal velocity (a Maxwellian distribution of velocities), c the speed of light and λ_0 the wavelength of the transition.

For instance, a magnetograph (see Sect. 2.3.1) is based on the above-mentioned approach.

Paschen-Back effect

The aforementioned theory of the Zeeman effect is only valid for "relatively weak" magnetic fields so that the LS coupling is an appropriate description to define the state of an atom. However, in the "strong" magnetic field regime, the orbital angular momentum $\vec{L}$ and the spin $\vec{S}$ are almost decoupled (Socas-Navarro et al., 2004). In such a case, the splitting of a particular J level produced by the magnetic field is comparable to the energy separation between different J levels (Landi Degl'Innocenti and Landolfi, 2004). Therefore, the spin-orbit interaction represents a further perturbation that has to be taken into account and which increases the difficulty to solve the Hamiltonian H. When this happens we are in the so-called *complete* Paschen-Back regime. The *incomplete* Paschen-Back effect regime is defined as the transition region between the weak (Zeeman effect regime) and the strong magnetic field regimes. For instance, for the He I 10830 Å triplet the incomplete Paschen-Back effect regime lies between 400 and 1500 G (Socas-Navarro et al., 2004). Since this effect has a visible impact on the Stokes profiles generated in the solar atmosphere, it has to be taken into account when interpreting these spectral lines.

Atomic level polarization

In the absence of magnetic field, there is no splitting of the magnetic energy levels, and the π and σ components of a transition lie at the same wavelength. As a consequence, the emergent polarization signals cancel out. However, polarization can still be produced due to population imbalances among magnetic sublevels of the same J level (Trujillo Bueno et al., 2002; Trujillo Bueno, 2006). Given the upper and lower levels of a two-level atom, $J_{\text{u}} = 0$ and $J_{\text{l}} = 1$, respectively, if the sublevels of J_{l} ($M_{\text{l}} = 0, \pm 1$) are not equally populated and, for instance, $M_{\text{l}} = 0$ is less populated than $M_{\text{l}} = \pm 1$, then there will be more σ than π transitions between $J_{\text{l}} \rightarrow J_{\text{u}}$. Hence, linear polarization is induced through a *selective absorption* of polarization components. The same happens when the upper level has unbalanced populations among sublevels and *selective emission* is generated, e.g., between $J_{\text{u}} = 1 \rightarrow J_{\text{l}} = 0$.

How do the population imbalances generate? If an atom is not isotropically illuminated, say, for example, owing to a preferred direction of the radiation that comes from the solar surface, then population imbalances can occur. In the above-mentioned example, a unidirectional and unpolarized radiation beam, does not induce π transitions between the $J_{\rm l}$ and $J_{\rm u}$ levels. As a consequence, only the σ transitions populate the upper $M_{\rm u} = \pm 1$ sublevels. Anisotropic radiation is a rather common phenomenon that happens in the solar atmosphere.

Hanle effect

Atomic level polarization can be generated in the absence of magnetic fields. Nevertheless, in the presence of a magnetic field *inclined* with respect to the axis of symmetry of the radiation beam, the Hanle effect produces a modification of the atomic level polarization, a rotation of the polarization plane, and therefore a modification of the pre-existent polarization signal (see e.g., Trujillo Bueno, 2001, 2006, for a review on this topic). In the case of filaments that are at a considerable height above the photosphere, the radiation from below illuminates anisotropically the material inside them, producing atomic level polarization. In addition, the presence of a weak field (weak in the sense that $\vec{B}$ is not strong enough to produce a visible Zeeman splitting) can induce the Hanle effect. There is a critical magnetic field strength required in order to produce a modification of the linear polarization signal via the Hanle effect (Trujillo Bueno, 2006):

$$B = \frac{1.137 \times 10^{-7}}{t_{\rm life}\ g_{\rm eff}} \ , \tag{1.23}$$

where $t_{\rm life}$ is the life time of the level. Remembering Eq. (1.10), $(g_{\rm eff} B)$ represented the Zeeman splitting. If $g_{\rm eff} B \gg 1/t_{\rm life}$, then we are in the Hanle saturated regime. Eq. (1.23) is only valid if the atom is excited by radiative transitions (not due to collisions of any kind). As reported by Stenflo (2002), depending on the atomic levels involved in a specific transition, the critical magnetic field for the Hanle effect lies between 1–100 G (transitions between excited states) or even much lower, around 0.01–1 G (transitions between the ground and excited states). It is therefore clear that the Hanle effect is an important diagnostic tool to study structures that involve weak fields in the solar atmosphere.

1.4.3 The 180° ambiguity

From polarimetric observations it is possible to infer the vector magnetic field $\vec{B}$. However, in the context of the Zeeman effect, there is not a unique solution for the component of $\vec{B}$ that is perpendicular to the LOS. Let us call this component $B_\perp$. In a Cartesian coordinate system, if z is chosen along the line-of-sight, $\vec{B}$ can be projected onto the three axes: B_x, B_y (perpendicular to the LOS; $B_\perp$), and B_z (along the LOS; $B_\|$). The following equations can be written for each component of $\vec{B}$ (see Fig. 1.9):

$$\begin{aligned} B_x &= |B| \sin\theta \cos\chi \ , && (1.24) \\ B_y &= |B| \sin\theta \sin\chi \ , && (1.25) \\ B_z &= |B| \cos\theta \ , && (1.26) \end{aligned}$$

with θ being the inclination of $\vec{B}$ with respect to the line-of-sight and χ the azimuth angle in the plane perpendicular to it. These angles are inferred from the Stokes profiles. Take as an example the weak field regime (see Sect. 1.4.2), where Stokes $Q(\lambda)$ and $U(\lambda)$ are proportional to (Landi Degl'Innocenti and Landolfi, 2004)

$$Q(\lambda) \propto \sin^2\theta \cos 2\chi \ , \tag{1.27}$$

$$U(\lambda) \propto \sin^2\theta \sin 2\chi \ . \tag{1.28}$$

The azimuth angle can be easily obtained dividing both equations (Auer et al., 1977):

$$\tan 2\chi = \frac{U(\lambda)}{Q(\lambda)} \ . \tag{1.29}$$

From Eqs. (1.27) and (1.28) it is straightforward to see that a 180° rotation of the azimuth angle in the plane perpendicular to the LOS, yields the same Stokes $Q(\lambda)$ and $U(\lambda)$ profiles. For that reason, the vector magnetic field cannot be fully determined without solving this 180° ambiguity.

Unfortunately there is no easy way to solve this problem. However, several methods have been used to address this issue (see Metcalf et al., 2006, for a complete review on this issue). Among others: the "Minimum Energy" method (e.g., Metcalf, 1994), the "Uniform Shear" method (Moon et al., 2003), the "Structure Minimization" method (Georgoulis et al., 2004), the "Chiral" method (Martin et al., 2008) and the AZAM utility (see Appendix A in Lites et al., 1995). A description of each of them is far beyond the scope of this thesis. Nevertheless, a brief description of the AZAM utility will be presented below since that code was applied to the data of this thesis.

The AZAM utility

Originally developed to solve the 180° ambiguity from Advanced Stokes Polarimeter data, the AZAM code (e.g., Lites et al., 1995; Metcalf et al., 2006) has been adapted for its use with the Tenerife Infrared Polarimeter data sets. AZAM is an interactive tool written in the IDL programming language that has to be applied on the inferred magnetic field inclination or azimuth maps. It is mainly aimed at resolving the azimuth ambiguity interactively but it also has advanced displaying features for the data sets.

AZAM has several initial guess solutions to solve the ambiguity, among others, the closest to potential field solution, a whole-map smoothing to minimize the discontinuities, or an up-and-down solution – the closest to LOS solution of the vector magnetic field– as a first approach. After a first disambiguation attempt, further fine tuning of the azimuth solution is required. One can then select a small arbitrary box (ranging from 1×1 to 16×16 pixels) in the field of view. It is important that the azimuths of the pixels inside this initial box do not differ too much, to meet the continuity requirement of the AZAM code. Then, the user interactively drags the box across the FOV in order to smooth out magnetic field discontinuities. It should be mentioned that it is not an easy task to smooth out the magnetic field solution. Naturally, the stronger the magnetic fields the more reliable are the inclinations and azimuths inferred from the observations and the better AZAM works with the provided maps. One typically begins to smooth out the maps starting from structures where the orientation of the vector magnetic field is constrained by the context. For this reason, unipolar sunspots are perfect candidates since the polarity can be easily inferred from longitudinal magnetograms. When such structures are not available, like in our case, the determination of the correct azimuth is more complicated and, as stated by Lites et al. (1995): “the resolution of the azimuth ambiguity remains somewhat of an art”. However, each solution should of course have a physical meaning within the global picture of the magnetic field that surrounds the region under study.

Another advantage of the AZAM utility is that it directly projects the inclination and azimuth angles onto the solar frame of reference (not on the observer’s frame). Therefore, the resulting vector magnetic field components B_z ($B_{\|}$) and B_x and B_y ($B_{\perp}$) correspond to field lines along the solar radius and parallel to the solar surface, respectively.

1.4.4 Techniques to infer the magnetic field strength: Inversion codes

The atmospheric conditions where polarized light is generated cannot be directly measured. One way to infer the physical conditions that take place in the solar atmosphere is to interpret the Stokes profiles of spectral lines. Understanding the observations can then lead to the creation of model atmospheres that satisfy the observed conditions. However, the relation between the observations and the model parameters is a non-linear problem.

In a simplified way, an inversion code (IC) generates synthetic Stokes profiles $\vec{I}^{\mathrm{syn}}(\lambda)$ and compares them with the observed ones $\vec{I}^{\mathrm{obs}}(\lambda)$. To that end, the IC uses a predefined atmospheric model as an initial guess. The atmospheric model has a set of free parameters which will be modified iteratively by the code in order to achieve the best fit between the synthetic and the observed Stokes profiles. The goodness of this fit is given by the merit function χ^2 (e.g., Ruiz Cobo and del Toro Iniesta, 1992; del Toro Iniesta, 2003):

$$\chi^2 = \frac{1}{\nu} \sum_{s=1}^{4} \sum_{i=1}^{q} \left[I_s^{\mathrm{obs}}(\lambda_i) - I_s^{\mathrm{syn}}(\lambda_i) \right]^2 \omega_{si}^2 \, , \tag{1.30}$$

where ν is the number of degrees of freedom (the difference between the number of observables and free parameters), s samples the four Stokes parameters, q samples through the wavelength range and the ω parameter represents the relative weight of the Stokes profiles. The IC modifies the free parameters searching for the global minimum of the χ^2 function. In order to minimize χ^2, the most common algorithm used by the available ICs is the Levenberg-Marquardt method (*Numerical recipes;* Press et al., 1986) used for least-square curve fitting, although several other methods exist. A negative feature of this method is that it can get trapped quite easily in local minima of the merit function (see e.g., Asensio Ramos et al., 2008) but ICs have ways to avoid this.

Every particular IC uses its own set of free parameters, although many are common among them. An initial set of parameters is needed in order to produce the first synthetic profiles (which then are iteratively changed in order to minimize χ^2) and compare them with the observed ones. Therefore, it is necessary to estimate the initial atmospheric conditions to run the IC. Obviously this is not an easy step since this information is exactly what we are trying to retrieve from the inversions. One can find several atmospheric models

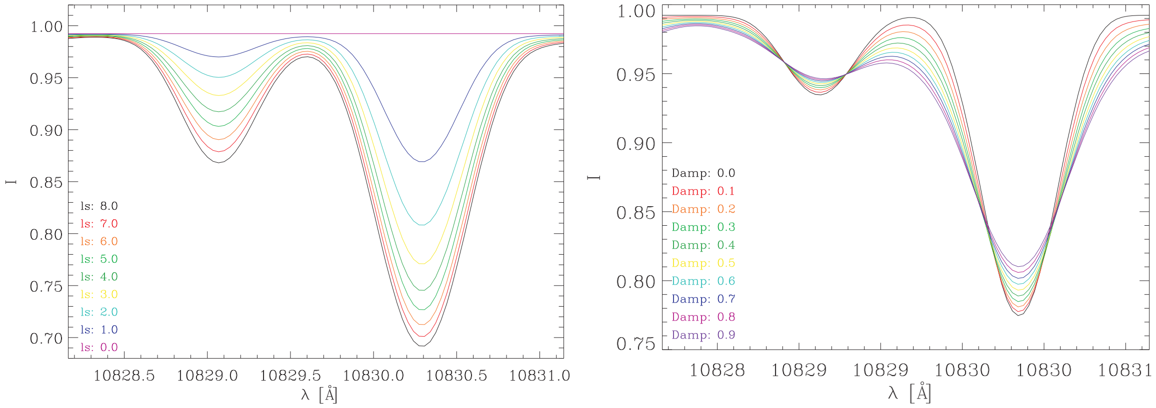

Figure 1.10 Synthetic Stokes I profiles from the inversion code MELANIE. The color-coded lines show how the variation of the line strength (left) and the damping parameter (right) affects the resulting spectral line profile. The following parameters were fixed and used for both plots: $B = 875\,\mathrm{G}$, $\theta = 85°$, $\chi = 58°$, $\Delta\lambda_{\mathrm{D}} = 163\,\mathrm{m\AA}$, $S_0 = 0.6$, $S_1 = 0.4$, and macroturbulence $= 6\,\mathrm{km\,s^{-1}}$. In particular, the lefthand figure has a line strength range of $\eta_0 \in [0.0, 8.0]$, damping $a = 0.12$, and LOS velocity $v_{\mathrm{LOS}} = 0\,\mathrm{km\,s^{-1}}$. The righthand figure has a changing damping parameter between $a \in [0.0, 0.9]$, $\eta_0 = 2.76$, and $v_{\mathrm{LOS}} = 1.58\,\mathrm{km\,s^{-1}}$ (redshift).

for different solar phenomena in the literature: e.g., sunspot umbrae model (Maltby et al., 1986), average quiet Sun model (Vernazza et al., 1981), and penumbral model (del Toro Iniesta et al., 1994), that can be used as initial guesses for the IC.

Another fundamental ingredient that needs to be introduced into the IC is the atomic data of the involved line transitions. Parameters such as the rest wavelength, the quantum numbers, the logarithm of the oscillator strength times the multiplicity of the lower level ($\log(gf)$), and the excitation potential are needed by some ICs.

Depending on the level of physical complexity, several inversion codes are available to the solar community (see the reviews by Socas-Navarro, 2001; Asensio Ramos et al., 2012). The simplest (but widely used) ICs are based on the Milne-Eddington (ME) approximation (see explanation below): VFISV (Borrero et al., 2011) developed for the Helioseismic and Magnetic Imager (HMI), MERLIN (Lites et al., 2007), HELIX (Lagg et al., 2004), MELANIE (Socas-Navarro, 2001), etc. More complex codes that assume LTE and include a depth stratification, e.g., SIR (Ruiz Cobo and del Toro Iniesta, 1992), or are able to deal with NLTE spectral lines, e.g., NICOLE (Socas-Navarro et al., 2000) and SIR (see Sect. 3), have also been developed. It is also worth mentioning the inversion code HAZEL (Asensio Ramos et al., 2008), which takes into account the atomic level polarization produced by anisotropic illumination and its modification through the Hanle effect.

While Levenberg-Marquardt minimization is the most common inversion tool, others, such as the principal component analysis (e.g., López Ariste, 2002), see Sect. 2.3.3, are able to carry out the same task without using least-square fitting techniques.

Milne-Eddington atmosphere

The Milne-Eddington approximation assumes that the relevant physical quantities of the atmosphere are constant with height, with the exception of the source function S that depends linearly on the optical depth (e.g., Landi Degl'Innocenti, 1992; del Toro Iniesta, 2003):

$$\vec{S}(\tau) = \vec{S}_0 + \vec{S}_1\tau = (S_0 + S_1\tau)(1,0,0,0)^{\mathrm{t}} \ . \tag{1.31}$$

Based on this assumption, an analytical solution of the polarized RTE (Eq. 1.12), referred to as the Unno-Rachkovsky solution, can be found. As a result of this, the Stokes profiles are given as a function of wavelength and a set of nine parameters:

- Vector magnetic field parameters: B, θ, and χ.
- Line strength or line core to continuum absorption coefficient ratio η_0 (see Sect. 1.4.2).
- Doppler width of the line $\Delta\lambda_{\mathrm{D}}$.
- Damping parameter a.
- Line-of-sight velocity v_{LOS}.
- Source function and its gradient S_0 and S_1.

In order to understand how η_0 and a affect the resulting Stokes profiles, a test synthesis of Stokes I with different values of these parameters was performed, see Fig. 1.10 (the other parameters were fixed, see the caption in this figure). Variations of η_0 are mainly responsible for the depth of the line while variations of a lead to smoother line profiles with shallower line cores and extended wings.

The need to describe the presence of *turbulence* is somehow "mysterious" because its nature in stellar atmospheres is not well understood. Nevertheless, it is a necessary parameter of ICs. As defined by Rosseland, turbulence comprises motions of gas that can be of large scale compared to atomic dimensions and of small scale when compared to the size of the star. Turbulence affects the spectral line profiles mainly producing line broadening (Gray, 1992; Asplund et al., 2000). Furthermore, Gray (1992) defines *microturbulence* as the motions of turbulent elements smaller than the mean free path (MFP) of the photon and *macroturbulence* as turbulent motions of scales that are larger than the MFP. Asplund et al. (2000) found in their simulations that micro and macroturbulence are produced by the photospheric granular velocity field and temperature inhomogeneities.

Although many ICs are based on the ME approximation, the simple assumption that the observed radiation is generated at a constant height in the solar atmosphere is unrealistic. A clear proof of this are the observed Stokes V profile asymmetries presumably originated by gradients of the velocity and magnetic fields along the LOS (see e.g., Landolfi and Landi Degl'Innocenti, 1996; Balasubramaniam et al., 1997; López Ariste, 2002; Sainz Dalda et al., 2012). Therefore, ME inversions are a good tool to retrieve physical quantities of the analyzed Stokes profiles as a first approach, but they have certain limitations that have to be taken into account.

1.4.5 Inversion code: MELANIE

The **M**ilne-**E**ddington **L**ine **A**nalysis using a **N**umerical **I**nversion **E**ngine (MELANIE) inversion code was developed by H. Socas Navarro. MELANIE is based on the aforementioned ME approach and is able to interpret the Stokes profiles only in the Zeeman effect regime. It can be used either in synthesis or inversion mode.

The IC requires a "grid" file that defines the spectral region under study, the starting wavelength in Å units, the sampling (mÅ px^{-1}), and the number of wavelength points. For instance, the He I 10830 Å spectral region, for a particular map, had a starting wavelength of 10828.245 Å, a sampling of 33.1 mÅ px^{-1}, and the profiles comprised 86 points. The former two values slightly change among different maps (changes of the order of ∼mÅ) because the wavelength calibration is carried out individually for each map. Furthermore, this file needs the atomic parameters, such as the quantum numbers S, L, and J, for the lower and upper levels and the relative strength of the lines (see Table 1.1).

The relative weighting of Stokes I, Q, U, and V can be customized for the inversion. We did not use a unique set of weights for all of the 10830 Å data sets analyzed in this thesis but, typically, Stokes Q and U were weighted more than I and V because their profiles were weaker. Also, MELANIE has the possibility to fix any parameter to an arbitrary value. The Stokes profiles have to be normalized to the local (pixel-by-pixel) continuum intensity before providing them to the IC: $I/I_\mathrm{c}, Q/I_\mathrm{c}, U/I_\mathrm{c}$, and V/I_c.

An initial guess for the model atmosphere is given in a different file, and it has to contain values for the following eleven parameters: the magnetic field B and its inclination θ and azimuth χ, the line strength, η_0, the Doppler width, $\Delta\lambda_\mathrm{D}$, the damping parameter, a, the LOS velocity, v_LOS, the source function and its gradient, S_0 and S_1, the macroturbulence, v_mac, and the stray-light fraction, α. These values are constant with optical depth.

The term "stray light" refers to scattered photons that contribute to the observed spectra but are actually not coming from the object under study. There is not only one source for these photons. It is rather a mix of light that scatters in the Earth's atmosphere and inside the instrument (see e.g., Martinez Pillet, 1992; Chae et al., 1998; Asensio Ramos and Manso Sainz, 2011; Beck et al., 2011, and references therein). Stray-light contamination is taken into account by adding a mean intensity profile to the Stokes I synthesized by the IC. This scattered light profile is calculated by averaging several pixels that are far away from magnetic structures in the observed map. Nevertheless, Asensio Ramos and Manso Sainz (2011) recommend computing the stray-light profile as an average over the whole field of view (FOV).

1.4.6 Inversion code: SIR

The **S**tokes **I**nversions based on **R**esponse functions (SIR) code is a more complex inversion code than MELANIE. The main advantage of SIR is that it uses a depth stratification of the physical parameters of the model atmosphere. Hence, contrary to a ME atmosphere, all parameters change with the optical depth. This makes this code more time-consuming, but at the same time the resulting atmosphere is more realistic since gradients along the LOS are permitted. SIR handles spectral lines that are formed in LTE conditions and assumes hydrostatic equilibrium. The code has also the possibility to introduce constant

NLTE coefficients (LTE departure or so-called β coefficients). The polarization signal is interpreted in the Zeeman effect regime.

In synthesis mode, through the calculation of response functions, given an atmospheric model one can study the sensitivity of the emergent Stokes profiles to a particular physical parameter as a function of height (optical depth) and wavelength. This was performed in this thesis for the Si I 10827 Å line and will be commented in Sect. 3.3. As explained by Ruiz Cobo and del Toro Iniesta (1992), RFs tell us how the observed spectrum changes due to modifications of the physical parameters of a given model atmosphere. Therefore, RFs are the derivatives of the merit function (χ^2) with respect to the free parameters. SIR computes the RFs to all the atmospheric parameters once in each iteration. The main goal of the inversion is the minimization of χ^2, which translates into a good agreement between the synthetic and observed Stokes profiles and hence to a good resulting model atmosphere.

The model atmosphere has a set of ten depth-dependent parameters that vary with respect to the logarithm of the continuum optical depth at 5000 Å: temperature, T, electron pressure, P_{e^-}, microturbulent velocity, v_{mic}, the magnetic field parameters B, θ, and χ, the LOS velocity, v_{LOS}, the geometrical height, x, the gas pressure, P_{g}, and the density, ρ. In addition, three depth-independent parameters, that globally change for each pixel, are needed: macroturbulent velocity, v_{mac}, stray light, α, and the filling factor, f. Out of these ten parameters, due to the hydrostatic equilibrium constraint, only the following six are independent: T, v_{mic}, the magnetic field parameters B, θ, and χ, and v_{LOS}.

It is worth pointing out why one commonly uses either α or f as free parameters instead of both. Assuming that, in a given pixel, the observed Stokes I_{px} is the sum of a magnetic (m) and a non-magnetic (nm) contribution, just because our instrument is not resolving the smallest spatial scales:

$$I_{\mathrm{px}} = f I_{\mathrm{px}}^{\mathrm{m}} + (1-f) I_{\mathrm{px}}^{\mathrm{nm}} \ . \tag{1.32}$$

Furthermore, it is widely assumed that the measured Stokes I_{obs} is contaminated by light from the surroundings (stray light) and one can write:

$$I_{\mathrm{obs}} = \alpha I_{\mathrm{s}} + (1-\alpha) I_{\mathrm{px}} \ , \tag{1.33}$$

where α is the stray-light parameter. If one further assumes that $I_{\mathrm{px}}^{\mathrm{nm}} = I_{\mathrm{s}}$, it is trivial to show that

$$I_{\mathrm{obs}} = \beta I_{\mathrm{s}} + (1-\beta) I_{\mathrm{px}}^{\mathrm{m}} \ , \tag{1.34}$$

being $\beta = f(1-\alpha)$. The fact that α and f appear in this equation as a product makes it impossible to decouple both parameters.

The perturbations of the physical parameters are not computed for each optical depth. The user has to choose a set of *nodes* (selected grid points along the LOS) for each parameter (and each iteration cycle) where the perturbations are calculated. The perturbations of the remaining grid points are obtained by interpolating the values computed at the nodes. As a result, fewer free parameters have to be solved in the RTE. It is not easy to decide the adequate number of nodes for all parameters. There is no established rule for selecting the number of nodes but generally one tries to use as few as possible, in other words, less freedom of the inversion code while at the same time obtaining an adequate χ^2 result. However, once the IC is guided into the right direction, the next cycles usually have slightly more nodes in order to “fine tune” the χ^2 minimization. Examples of typical values of the amount of nodes for three cycles that have been used in this thesis are given in Table 1.3.

Inversion type	Nodes						
	T	P_{e^-}	$v_{\rm mic}$	B	θ	χ	$v_{\rm LOS}$
Standard	2,3,4	–	1,1,1	2,2,3	2,2,3	1,1,1	2,3,3
Two-comp	2,3,4	–	1,1,1	2,2,2	1,1,1	1,1,1	2,2,2
	$-1^{\star}$	–	1,1,1	2,2,2	1,1,1	1,1,1	2,2,2

Table 1.3 Example of the number of nodes used for each parameter throughout the three cycles of a SIR inversion. The number of nodes in each cycle is separated by a comma. The first column identifies the type of inversions that were carried out: standard (all Stokes profiles are equally weighted; $\omega_{I,Q,U,V} = 1$) and two-component inversions (using two atmospheric models). See Sect. 5.3 for a more extensive explanation of the different inversion schemes.
$\star$ The ”-1” node means that the temperature is coupled between both atmospheric models.

In our case, the P_{e^-} cannot be reliably inferred since the spectral profiles do not provide enough information (more than one ion is required to infer P_{e^-}; Landi Degl’Innocenti and Landolfi, 1982). That is the reason why in Table 1.3 no nodes were used for this parameter. The atomic data required by SIR for the Si I 10827 Å line appear in Table 1.2. The abundance of Si I, defined as $12 + \log[\mathrm{Si}]/[\mathrm{H}]$, was taken from Thevenin (1989) who gives 7.5.

The observed Stokes profiles that will be used by SIR ideally need to be normalized to the continuum of the quiet Sun at disk center. However, usually the region under study is not located at disk center. While flat-field images can be used for this purpose, in our case we could not reliably verify that they were taken, as usual, at disk center. Another drawback, but less important than the above mentioned one, is that small changes of the atmospheric conditions between the data and the flat-field images can occur. Therefore, the continuum was determined for each map out of an average of pixels that are far away from magnetic regions. Slit reconstructed images centered at wavelengths where Stokes Q, U, and V have their maximum signal can be used to find “quiet” Sun regions. From the non-magnetic regions (where Q, U, and V were negligible), the average value of the continuum $I_{\rm c}$ was inferred. Then, the four Stokes profiles were divided by $I_{\rm c}$.

1.4.7 Magnetic field strength in filaments

The literature on inferred magnetic field strengths in prominences and filaments is reviewed in this section. The first measurements provided only the LOS component of the field strength ($B_{\rm LOS}$) via the longitudinal Zeeman effect (e.g., Zirin and Severny, 1961). Harvey and Tandberg-Hanssen (1968) showed in their study that the longitudinal magnetic field strength in prominences, inferred using the Zeeman effect, yielded consistent values when different spectral lines, such as He I D_3, Hα, and Hβ, were used. Later, the Hanle effect provided new measurements and opened the possibility to measure the total field strength (B) in prominences (e.g., Sahal-Brechot et al., 1977; Leroy, 1977) and to retrieve the complete magnetic field vector (Bommier et al., 1981). A combination of both, the Zeeman and Hanle effects, yields the most reliable values. For instance, Casini et al. (2003) applied PCA to the four Stokes profiles recorded at a QS prominence obtaining values between 10–20 G for the field strengths, although selected points reached values up to 70 G.

It is worth noticing that from an observational point of view, Leroy et al. (1983) found that the magnetic field strength in QS prominences increased with height. The authors inferred a vertical gradient of $0.5 \times 10^{-4}\,\mathrm{G\,km^{-1}}$, which is consistent with the vertical gradient of the horizontal field strength previously found ($10^{-4}\,\mathrm{G\,km^{-1}}$) by Rust (1967). Extrapolation models (with constant α) have also found gradients of the magnetic field of 0.1–1.5 $\times 10^{-4}\,\mathrm{G\,km^{-1}}$ in filaments (Aulanier and Démoulin, 2003).

A list of magnetic field measurements of prominences and filaments, before the year 2009, is given in Table 1.4. The following columns are shown in the table: B_{LOS} (longitudinal magnetic field strength), B (total magnetic field strength), Type (where the prominence / filament was observed), Line (the spectral lines used for the inference of the field strength), Method (either Zeeman or Hanle effect, or both), and the bibliographic reference.

B_{LOS} (G)	B (G)	Type	Line	Method	Reference
~ 200	–	AR prom.	Hβ	Zeeman	Zirin and Severny (1961)
25–50	–	QS prom.	Hβ	Zeeman	
5	–	QS prom.	Hα	Zeeman	Rust (1967)
8–60	–	Sunspot prom.	Hα	Zeeman	
80 ± 6	–	Active prom.	Hα	Zeeman	Malville (1968)
200 ± 100	–	AR prom.	?	Zeeman	Harvey (1969)
7.3	–	QS prom.	Hα	Zeeman	Tandberg-Hanssen (1970)
≤ 136	–	Limb prom.	Not specified	Zeeman	T-H and Malville (1974)
4.5 ± 3.4	0–10	QS prom.	He I D$_3$	Zeeman & Hanle	Leroy (1977)
11.1–12.3	–	QS prom.	He I D$_3$,Hβ	Zeeman	Kim et al. (1982)
–	8	PC prom.	He I D$_3$	Hanle	Leroy et al. (1983)
–	6–27	Prom.	He I D$_3$	Hanle	Athay et al. (1983)
–	6–60	QS prom.	He I D$_3$	Hanle	Querfeld et al. (1985)
8–20	–	Prom.	He I D$_3$,Hα,Hβ	Zeeman	Nikolsky et al. (1984)
75-180	–	Active prom.	Ca II 8542	Zeeman	Wiehr and Stellmacher (1991)
30–45	–	QS prom.	He I D$_3$	Zeeman	Paletou et al. (2001)
–	20	QS fil.	He I 10830	Hanle	Trujillo Bueno et al. (2002)
–	10–20	QS prom.	He I D$_3$	Zeeman & Hanle	Casini et al. (2003)
–	~ 30	PC prom.	He I 10830	Zeeman & Hanle	Merenda et al. (2006)

Table 1.4 Magnetic field strength measurements in prominences and filaments. Abbreviations: AR (active region), QS (quiet Sun), PC (polar crown). The sunspot prominences are described by Rust (1967) as QS prominences near sunspots.

To summarize, the inferred magnetic fields in QS filaments / prominences reach values up to 60 G. For AR prominences, the longitudinal component (along the LOS) of the magnetic field presents values in the range of 75-200 G.

1.5 State of purpose of the thesis

The main scientific driver for the work developed in this thesis was to analyze, through observations, the magnetic structure in solar active region filaments and how AR filaments are formed. Since filaments are always detected above polarity inversion lines, it is also crucial to study the magnetic structure in the photosphere to get a global picture of the formation scenario.

Filament formation, evolution and their disappearance are important issues in solar physics that are currently being widely debated. The disappearance of a filament may lead to violent coronal mass ejections (CMEs), with material being expelled into space at great velocities, and it is associated with a global change in the coronal magnetic field topology. CMEs are explosive events that occur in the solar atmosphere and which immediately affect the space weather near Earth. To study the formation of AR filaments, it is necessary to understand how the magnetic field behaves in these kind of structures. As seen in Table 1.4, there seems to be a gap in the available magnetic field strength measurements in AR filaments. Several authors (e.g., Tandberg-Hanssen and Malville, 1974) have argued that there is an upper limit of the LOS component of the field strength ($B_{\rm LOS}$) in prominences. This upper limit is around 200 G and has to be further confirmed by new observations.

The following objectives have been achieved:

i) Inference of the magnetic field strength from the AR filament data of July 2005. Comparison of the inferred values with new AR filament observations.

ii) Analysis of the vector magnetic field in the AR filament and in the underlying photosphere. Projection of the vector magnetic field onto the local solar frame of reference. Resolution of the 180° ambiguity.

iii) Representation of the global magnetic structure of the AR along the PIL using different visualization tools and techniques.

iv) Study of the evolution of the AR filament. Determination of the absolute line-of-sight velocities with high accuracy. Analysis of the dynamics of the magnetic fields inferred from the He I 10830 Å triplet and the Si I 10827 Å line inversions.

v) Combination of all the inferred properties in a consistent scenario of the structure and evolution of the observed AR filament.

vi) Comparison of this scenario with the properties of filaments expected from different models.

2

Magnetic field strength of active region filaments

The first part of this thesis is dedicated to the inference of the magnetic field strength inside an active region filament using spectropolarimetric data sets of the He I 10830 Å triplet. The data were acquired on July 2005 with the Tenerife Infrared Polarimeter at the Vacuum Tower Telescope, Tenerife, Spain. A compact active region was found near disk center (see Fig. 2.1). By closer inspection, the AR was extremely compact at the polarity inversion line, i.e., the opposite polarities were very close together (almost touching each other). The AR emerged a couple of weeks before on the rear side of the Sun. A filament was clearly detected on top of the polarity inversion line. A careful analysis of the Stokes profiles, using three different techniques, yielded consistent values of the magnetic field strength inside this AR filament.

The article presented in this chapter was published with the title "Magnetic field strength of active region filaments", in Astronomy & Astrophysics, volumen 501, pages 1113–1121, year 2009.

Abstract: We study the vector magnetic field of a filament observed over a compact active region neutral line. Spectropolarimetric data acquired with TIP-II (VTT, Tenerife, Spain) of the 10830 Å spectral region provide full Stokes vectors that were analyzed using three different methods: magnetograph analysis, Milne-Eddington inversions, and PCA-based atomic polarization inversions. The inferred magnetic field strengths in the filament are around 600–700 G by all these three methods. Longitudinal fields are found in the range of 100–200 G whereas the transverse components become dominant, with fields as high as 500–600 G. We find strong transverse fields near the neutral line also at photospheric levels.

Our analysis indicates that strong (higher than 500 G, but below kG) transverse magnetic fields are present in active region filaments. This corresponds to the highest field strengths reliably measured in these structures. The profiles of the helium 10830 Å lines

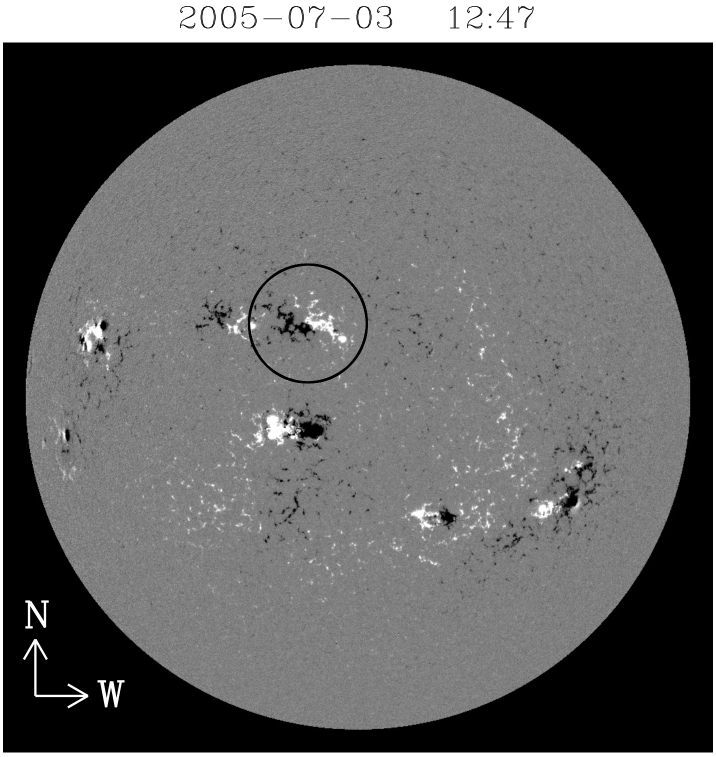

Figure 2.1 *SOHO*/MDI photospheric full-disk line-of-sight magnetogram saturated at ±300 G. White represents positive and black negative polarity. The black circle is centered at active region NOAA 10781.

observed in this active region filament are dominated by the Zeeman effect.

A&A 501, 1113–1121 (2009)
DOI: 10.1051/0004-6361/200911800
© ESO 2009

Astronomy & Astrophysics

Magnetic field strength of active region filaments

C. Kuckein[1], R. Centeno[2], V. Martínez Pillet[1], R. Casini[2], R. Manso Sainz[1], and T. Shimizu[3]

[1] Instituto de Astrofísica de Canarias, vía Láctea s/n, 38205 La Laguna, Tenerife, Spain
e-mail: `ckuckein@iac.es`
[2] High Altitude Observatory (NCAR), Boulder, CO 80301, USA
[3] Institute of Space and Astronautical Science, JAXA, Sagamihara, Kanagawa 229-8510, Japan

Received 5 February 2009 / Accepted 28 April 2009

ABSTRACT

Aims. We study the vector magnetic field of a filament observed over a compact active region neutral line.

Methods. Spectropolarimetric data acquired with TIP-II (VTT, Tenerife, Spain) of the 10 830 Å spectral region provide full Stokes vectors that were analyzed using three different methods: magnetograph analysis, Milne-Eddington inversions, and PCA-based atomic polarization inversions.

Results. The inferred magnetic field strengths in the filament are around 600–700 G by all these three methods. Longitudinal fields are found in the range of 100–200 G whereas the transverse components become dominant, with fields as high as 500–600 G. We find strong transverse fields near the neutral line also at photospheric levels.

Conclusions. Our analysis indicates that strong (higher than 500 G, but below kG) transverse magnetic fields are present in active region filaments. This corresponds to the highest field strengths reliably measured in these structures. The profiles of the helium 10 830 Å lines observed in this active region filament are dominated by the Zeeman effect.

Key words. Sun: filaments – Sun: photosphere – Sun: chromosphere – Sun: magnetic fields – techniques: polarimetric

1. Introduction

The magnetic field strength of active region (AR) filaments has long remained poorly known or understood. The situation for quiescent filaments is notably more satisfactory since the early measurements back in the 70s (see, e.g., the review by López Ariste & Aulanier 2007). Field strengths measured in quiescent structures, mostly using the Hanle effect on the linear polarization of He D$_3$ at 5876 Å (e.g., Sahal-Brechot et al. 1977), were found to be in the range of 3–15 G (Leroy et al. 1983; see also the review by Anzer & Heinzel 2007). However, more recent measurements, which also took circular polarization into account, consistently show a tendency towards stronger field strengths. For example, the He 10 830 Å investigation of Trujillo Bueno et al. (2002) and the He D$_3$ of Casini et al. (2003) found, respectively, field strengths of 20–40 G and 10–20 G (with field strengths up to 80 G in the latter set of observations). With similar techniques, using carefully inverted observations of the He 10 830 Å lines, Merenda et al. (2006) find field strengths of about 30 G. Other recent works that also obtained relatively strong filament magnetic fields as compared with older measurements are Paletou et al. (2001) and Wiehr & Bianda (2003). Of particular interest are the high field strength areas revealed by Zeeman-dominated Stokes V profiles in conjunction with scattering dominated Q and U linear polarization signals obtained by Casini et al. (2003), showing how important it is to use all four Stokes parameters for a proper determination of the field strength in prominences.

Well-established properties of AR filaments are their systematically stronger field strengths as compared to their quiescent counterparts, and they lie lower in the atmosphere (see, e.g., Aulanier & Démoulin 2003). Zeeman observations, using coronagraphs, provided field strengths for AR prominences in the range of 50–200 G (Tandberg-Hanssen & Malville 1974, and references therein). However, the intrinsic difficulties of observing such low-lying structures near the limb and the use of Hα magnetography render these results somewhat questionable (see López Ariste et al. 2005, for the problems associated with using a Zeeman-based formulation of the measurements made in Hα). Perhaps the most relevant modern estimate of the field strength in AR prominences has been provided by Wiehr & Stellmacher (1991), who measured the longitudinal magnetic field using the Stokes I and V profiles of the Ca IR triplet, finding a value of 150 G, compatible with previous measurements. It is important for the discussion presented in our paper to note that, in that observational study, linear polarization signals (Q and U) were not included. The only measurements of strong magnetic fields using an He 10 830 Å full Stokes vector that we are aware of belong to a multicomponent flaring active region and reached values of ≈380 G (see Sasso et al. 2007).

Because measurements are scarce, we are still far from having a complete picture of the field strengths that permeate solar filaments. Some progress has come from using photospheric distributions of (mostly longitudinal) fields that are extrapolated into the corona (usually using models of constant-α force-free field). The study by Aulanier & Démoulin (2003) is of particular relevance to the present work. According to these authors, the field strength of filaments found from the extrapolations is about 3 G for the quiescent case, 40 G for active filaments (called "plage case" in their work) and 15 G for intermediate cases. The typical height in the atmosphere of a filament base ranges from 20 to 10 Mm, or even lower, as one moves from quiescent to AR structures. These authors also find positive field gradients with height that result in values of 0.1–1 G Mm^{-1}, i.e., stronger fields are higher up in the atmosphere. If these gradients are used to extrapolate down into the photosphere, the fields there would be very similar to those found some Mm up in the corona. For example a 10 Mm-height active filament with 100 G in the corona would have no less than 90 G close to the photosphere. The argument could also be turned around to start from the fields measured near the photosphere, close to AR neutral lines (NLs), and infer what the fields could be high in the corona. In the case of kG-strong plage fields, with high density areal filling factors (that can reach up to 50%; Martínez Pillet et al. 1997), one could expect fields of several hundred Gauss within the filaments. Indeed, Aulanier & Démoulin (1998, 2003) provide arguments supporting a relationship between the photospheric fields at the base of the filament and the filament fields up in the corona. They conclude that the stronger the photospheric fields at the base of the filament, the stronger the field in the filament itself. Similarly, the separation of the two opposite polarity regions scales inversely with the field strength of the filament, the latter being greater whenever the two polarities are closer together. Dense (highly packed) fields in the photosphere correspond indeed to the photospheric configuration found below AR filaments as observed recently by Lites (2005) and Okamoto et al. (2008). In both cases, they find opposite polarity "abutted" plage fields at the NL, with sheared horizontal fields in the hecto-Gauss range and relatively high filling factors. These abutted field configurations seem to also correspond with low-lying filaments structures. Lites (2005) comments that the height of the filaments on top of the abutted plage fields is no more than 2.5 Mm. Thus, high density (i.e., large filling factor) horizontal plage fields near AR NLs, together with the inferences from theoretical modeling (Aulanier & Démoulin 1998, 2003), would indicate that fields of several hundred Gauss can be expected in low-lying AR filaments.

Given the observation that energetic coronal mass ejections (CMEs) are often associated with AR filament eruptions (see, e.g., Manchester et al. 2008; and Low 2001, for a review), it is highly desirable to develop diagnostic tools for direct measurements of the AR filament magnetic field and its evolution, from its emergence (see Okamoto et al. 2008) to the erupting phase. In this work, we present a clear diagnostic tool of how this can be achieved using full Stokes polarimetry of the He I 10 830 Å lines.

2. Observations

The observations described in this paper were carried out at the German Vacuum Tower Telescope (VTT, Tenerife, Spain) on the 3rd and the 5th of July, 2005, using the Tenerife Infrared Polarimeter (TIP-II, Collados et al. 2007). TIP-II allows to measure the full Stokes vector (almost) simultaneously for all the pixels along the spectrograph slit. The slit ($0\farcs5$ wide and $35''$ long) was placed over the target, a filament lying over the NL of active region NOAA 10781 situated close to disk center (at coordinates N13-W4 around $\mu = 0.97$ on July 3rd and at N13-W29 or $\mu = 0.92$ on July 5th) with the help of context Hα and continuum images. The Hα frames showed the filament lying always on top of bright plage regions visible immediately to either side of the absorption feature. It is likely that the results presented in this paper particularly apply to such an "active" filament configuration. SOHO/MDI (Scherrer et al. 1995) magnetograms and continuum frames have been used to follow the evolution of the active region as it crossed the visible surface. The active region was identified to be in its slow decay mode, encompassing a round symmetric leader sunspot and a follower, spotless, plage region. At the location of the NL, sporadic pore-like formations and penumbral-like configurations (with no evident radially symmetric link to an umbral or pore structure as normal penumbra or partial penumbrae do) were seen, especially on the 5th of July data-sets. Pores near the NL with both polarities are identified and the penumbral-like region seems to correspond to field lines connecting them. The NL was oriented in the N-E direction and showed a very compact configuration, with the two polarities always remaining in close contact. The leader sunspot became invisible on the 6th of July after decreasing in size while approaching the west solar limb.

Two observing strategies were used to map the NL region. Several spatial scans that covered the whole AR were carried out in the course of the 3 days, and one time series (with the slit fixed over the filament) was taken on July 5th. This data-set was averaged in time in order to improve the signal-to-noise (S/N) ratio of the spectral profiles. The pixel size along the slit was $0\farcs17$ and the scanning step (in the case of the rasters) was $0\farcs3$ per step. The exposure time per slit position was 8 seconds. The adaptive optics system (KAOS, von der Lühe et al. 2003) was locked on nearby pores during all the runs, substantially improving the image quality of the observations carried out during relatively poor seeing conditions, and providing a final estimated spatial resolution of $\sim 1''$. Flat-field and dark current corrections were performed for all the data-sets and, in order to compensate for the telescope instrumental polarization, we also carried out the standard polarimetric calibration (Collados 1999; Collados 2003) for this instrument.

The observed spectral range spanned from 10 825 to 10 836 Å, with a spectral sampling of ~11.1 mÅ px^{-1}. However, a 3px binning in the spectral domain was applied to all the data to increase the S/N while still preserving subcritical sampling. The 10 830 Å spectral region is a powerful diagnostic window of the solar atmospheric properties since it contains valuable information coming simultaneously from the photosphere (carried by the Si I line at 10 827 Å) and the chromosphere (encoded in the He I 10 830 Å triplet). This He multiplet originates between a lower term 2^3S_1 and an upper term $2^3P_{2,1,0}$. Thus, it comprised three spectral lines, namely a "blue" component at 10 829.09 Å ($J_L = 1 \rightarrow J_U = 0$) and a "red" component at ~10 830.3 Å that results from the remaining two transitions ($J_L = 1 \rightarrow J_U = 1, 2$), which appear completely blended at typical solar atmospheric temperatures. This multiplet is formed in the high chromosphere (Avrett et al. 1994) with no contribution from photospheric levels, and serves as a unique diagnostic tool for chromospheric magnetic fields. In filament structures, the height of formation of this multiplet corresponds to the height of the opaque material inside them, which might well correspond to typical coronal heights.

2.1. Predominance of Zeeman-like signatures in AR filament He I 10 830 Å Stokes profiles

The most striking finding encountered during the analysis of the data from this campaign was the ubiquitous presence of Zeeman-like signatures in the Stokes Q and U profiles of the He I lines in the AR filament (see Fig. 1). Recent observations of this triplet carried out with the same instrument (Trujillo Bueno et al. 2002) have shown quiescent filament Stokes profiles

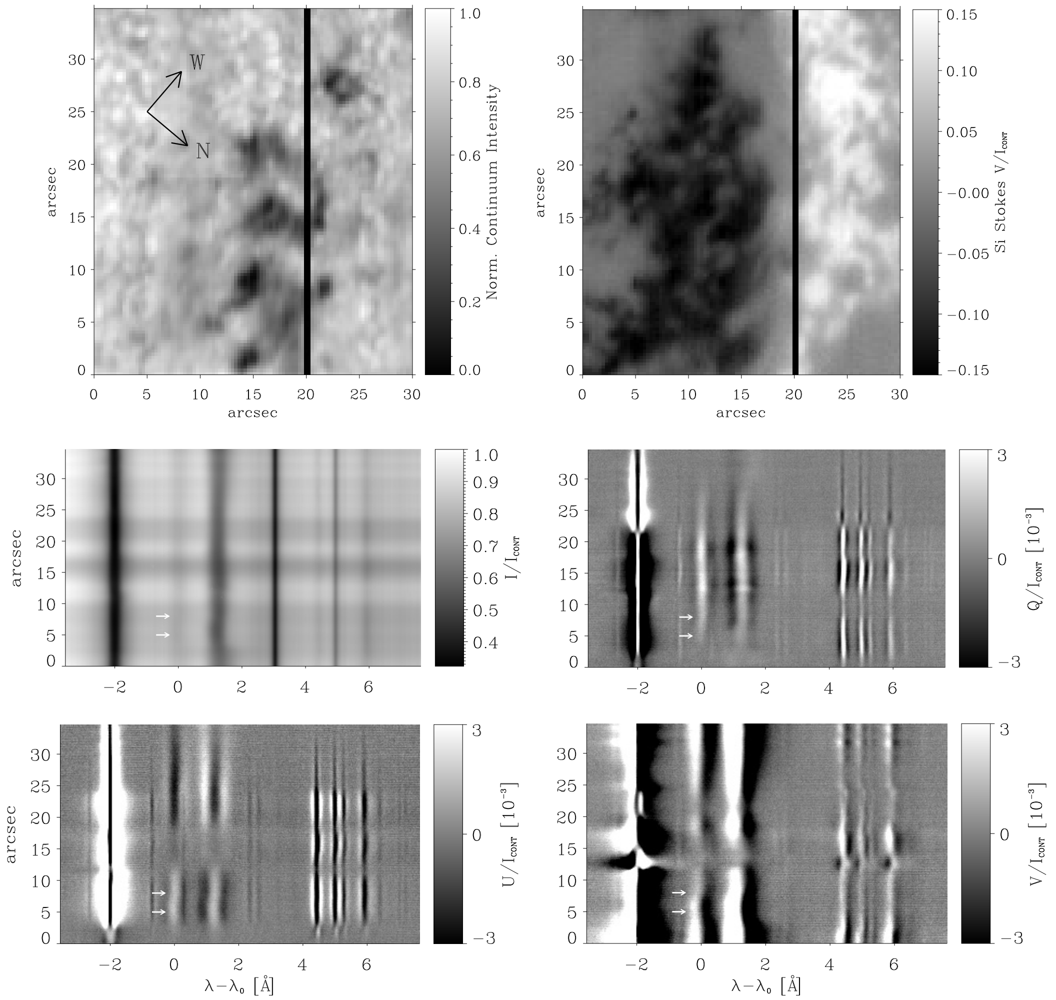

Fig. 1. *Top left*: slit reconstructed continuum intensity map centered at the NL where the pores and penumbral-like formations can be identified. The location of the slit for the time series map is displayed. *Top right*: Si Stokes *V* map normalized to the continuum intensity. *Bottom*: Stokes profiles observed at the slit position indicated in the *top* images and averaged over the time series (comprising 100 scans). The gray scale bar only applies to the polarization signals. The Zeeman-like signature of Stokes *Q* and *U* are evident in this picture (He lines are centered at 0 and 1.2 Å approximately. The zero in the wavelength scale corresponds to 10 829.09 Å). The arrows indicate the position of the presented Stokes profiles in Figs. 3 and 4.

dominated by atomic level polarization (and its modification through the Hanle effect). These forward-scattering signatures (see Fig. 4 of Trujillo Bueno et al. 2002) correspond to one-lobe profiles that are positive for the red component of the He triplet and negative for the blue one (in the positive Stokes *Q* reference system) due, respectively, to selective emission and absorption processes induced by the anisotropic illumination of the He atoms. However, in the present case, the Stokes *Q* and *U* signals of the blue and red components of the multiplet, exhibit the usual three-lobe profile that is expected from the Zeeman effect (right panel of Fig. 1). While some influence of atomic polarization in these profiles cannot be ruled out a priory, it is clear that an explanation of their shapes should rely mainly on the Zeeman and Paschen-Back effects. This fact, interesting in itself, will be briefly discussed below (Sect. 3.3).

The continuum frame in the top panel of Fig. 1 was reconstructed from the various slit scan positions (thus reflecting the real spatial resolution of the data) of a map centered at the NL. This data-set was taken on the 5th of July, 2005. The presence of pores and penumbral-like structures is evident in this frame and their location corresponds to the NL. Right after this map, a time series with the slit fixed over the NL was performed in order to produce high S/N Stokes profiles. The bottom four panels of Fig. 1 correspond to the Stokes parameters obtained after averaging over the full time series (100 scans), which resulted in a S/N of about 4000. The inversions performed later in this work were carried out on the spectral profiles extracted from this time-averaged data-set. The location of the NL had to be guessed in real-time during the observations. The chosen slit position for the time series is represented by a vertical black line in the continuum frame of Fig. 1. Posterior analysis has shown that this location was a few arcsec off at one side of the actual NL, and that the slit would have been more correctly placed at $x = 18''$ (referred to the abscissa coordinates in the continuum panel) instead of at $x = 20''$. Nevertheless, indications of polarity changes along the slit in the Si line (evident around $y = 13''$ in the Stokes V map of the same figure) show that we were not very far away from it.

Inspection of the profiles at other slit locations, and of similar maps taken on the 3rd of July, consistently exhibited Zeeman-dominated linear polarization signals in those regions where the He line showed strong absorption features. However, in regions with weak He absorption (typically near the boundaries of the filament), we often find linear profiles dominated by scattering polarization signatures, similar to those observed by Trujillo Bueno et al. (2002). This indicates that, in general, the profiles obtained in AR filaments can have significant contributions from various competing physical processes: the atomic level polarization due to the anisotropic illumination of the He atoms, the modification of these population imbalances induced by the presence of a magnetic field inclined with respect to the axis of symmetry (Hanle effect), and the Zeeman splitting characteristic of strong magnetic fields. A detailed study with these physical ingredients for all the maps observed at this NL is beyond the scope of this paper. In the present work, we concentrate on the implications of the clear Zeeman-dominated signatures observed almost everywhere in this filament.

One point is worth mentioning after a simple visual inspection of Fig. 1. A comparison of the signs displayed by the linear polarization profiles of the He and Si lines shows that the orientation of the vector magnetic field is different in the filament than in the underlying photosphere. In the Stokes Q frame, the He 3-lobed profiles have the same sign all along the slit whereas the Si line (and all the other smaller photospheric features at redder wavelengths) exhibits a change in sign around $y = 23''$. Conversely, in the Stokes U frame, the photospheric signals have a 3-lobed sign distribution that remains constant almost all along the spatial domain while the He lines now show a sign reversal near the middle of the slit. An analysis based on the formula for the azimuth angle by Auer et al. (1977) gives an estimate of this difference between the azimuths inferred from the Si and He lines. Around $y = 5''$ we obtain values of the azimuth which differ in ~50°. This readily shows that the 10 830 Å spectral region has a great potential to diagnose the orientation of the magnetic field from the photosphere all the way up to the filament. We postpone this study to a future paper.

3. Vector magnetic field near the AR neutral line

Several analyses with various levels of complexity have been performed on the reduced data. The first approach was a simple magnetograph-like analysis based on the assumption of the weak-field approximation as formulated below. This method was applied to all the points in one of the maps obtained during the campaign. We subsequently performed an analysis of the high S/N spectral profiles obtained from the averaged time series with a Milne-Eddington (ME) code and later with a more sophisticated inversion procedure based on principal component analysis (PCA) of a statistically generated database of spectral profiles that account for the physics of atomic level polarization and the Hanle effect. All these different methods consistently yield transverse field strengths in the filament well above 500 G.

3.1. Magnetograph analysis

Typical Doppler widths for the red He line are in the range of 200–300 mÅ. The Landé factors are 1.75 and 1.25 for the $J_L = 1 \rightarrow J_U = 1$ and the $J_L = 1 \rightarrow J_U = 2$ transitions, respectively. If the transitions are weighted with their line strengths, an average Landé factor of $g_{\rm eff}$ =1.42 for the red component of the helium multiplet is obtained. This Landé factor translates the above Doppler widths to field strengths in the range of 2000–3000 G, which is much stronger than the fields we expect for AR filaments. Together with the assumption that the observed signals are due to the Zeeman effect, these large Doppler widths justify the use of the well-known weak field approximation (see, e.g., Landi Degl'Innocenti 1992) as a first approach to infer the magnetic field from the data. In this approximation, the relation between the longitudinal field strength and Stokes V profile is given by:

$$V_{\rm o} = f V_{\rm m} = -fCB\cos\theta \frac{{\rm d}I_{\rm m}}{{\rm d}\lambda}\,. \tag{1}$$

The subscript "o" stands for the observed profile, while "m" represents the profile generated in the magnetic component that fills a fraction f of the resolution element; B is the field strength, θ the angle between the line-of-sight (LOS) and the magnetic field direction and C the constant $4.67 \times 10^{-13} g_{\rm eff} \lambda_{\rm o}^2$ (which forces the wavelength to be expressed in Å and the field strength in G). The observed Stokes I profile is given by:

$$I_{\rm o} = fI_{\rm m} + (1-f)I_{\rm nm} \tag{2}$$

with the subscript "nm" referring to the non-magnetic component. The last factor in the right-hand-side of Eq. (1) is the derivative of $I_{\rm m}$ with respect to the wavelength. However, observations only provide the compound profile $I_{\rm o}$, product of the coexistence of magnetic and non-magnetic components in the same resolution element. The present He analysis benefits from the fact that the non-magnetic areas of the Sun display a very weak He absorption, so the derivative of the Stokes $I_{\rm nm}$ profile with respect to λ can be neglected (we note that, in non-magnetic regions, ${\rm d}I_{\rm nm}/{\rm d}\lambda$ is found to peak at one order of magnitude smaller values than ${\rm d}I_{\rm m}/{\rm d}\lambda$ as observed in the filament). This nicely eliminates any dependence of the inferred longitudinal field on the unknown filling factor. Following this argument of ignoring the derivative of the $I_{\rm nm}$ profile with respect to wavelength, the longitudinal field is directly inferred as

$$B_{\parallel} = B\cos\theta = -\frac{1}{C}\frac{V_{\rm o}(\lambda)}{\frac{{\rm d}I_{\rm o}}{{\rm d}\lambda}(\lambda)}\,. \tag{3}$$

The λ dependence in the last ratio is written explicitly to emphasize that each point within the profile provides an estimate of the longitudinal field. Thus, the way to solve Eq. (3) is through a least-square fit to all the observed points within the profile.

For transverse fields, a similar equation applies including the quadratic dependence of the linear polarization signals on the transverse component of the field and the second derivative of the Stokes I profile with respect to λ. A similar argument gives:

$$B_{\perp}^2 = B^2\sin^2\theta = \frac{4}{C^2}\frac{\sqrt{Q_{\rm o}^2(\lambda_{\rm o}) + U_{\rm o}^2(\lambda_{\rm o})}}{\frac{d^2 I_{\rm o}}{d\lambda^2}(\lambda_{\rm o})}\,. \tag{4}$$

Like in the equation for the longitudinal field, the filling factor (of a non-magnetic component) is absent. On the other hand, and in contrast to Eq. (3), the right hand side of Eq. (4) must be computed at the central wavelength, $\lambda_{\rm o}$, as this equation can only

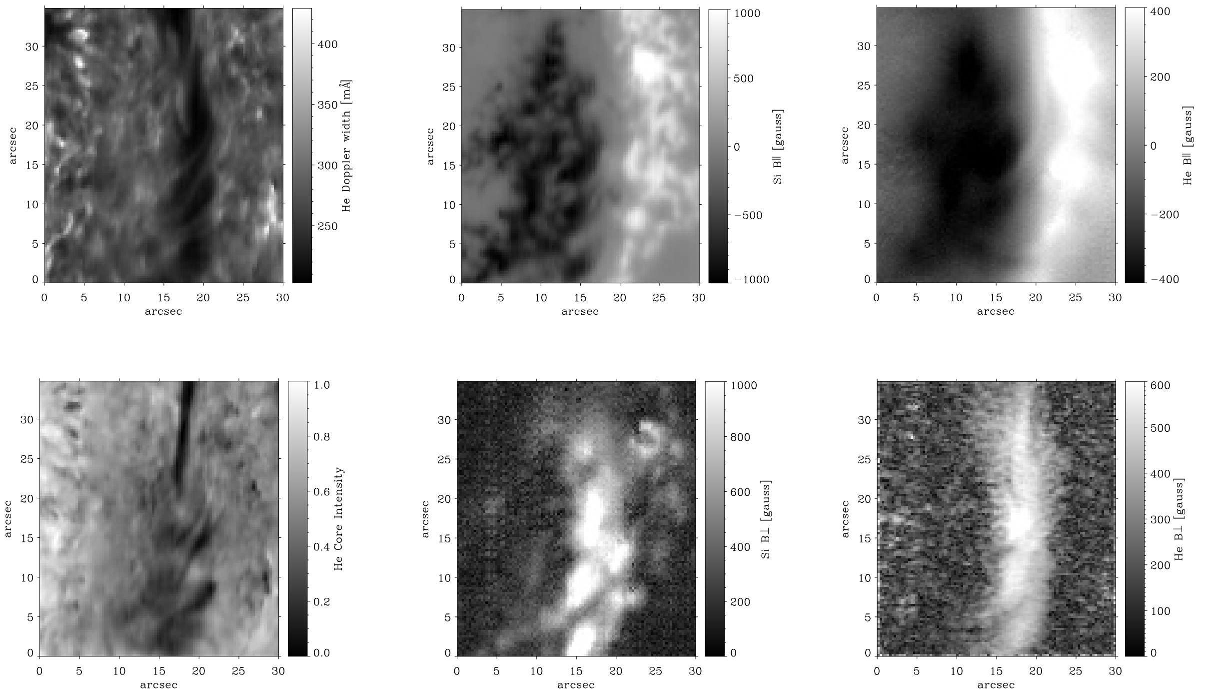

Fig. 2. *From left to right and top to bottom*: He Doppler width, Si LOS magnetic field, He LOS magnetic field, He core intensity, Si transverse magnetic field and He transverse magnetic field. The corresponding continuum intensity frame can be seen in the *top* panel of Fig. 1.

be formally derived there (Landi Degl'Innocenti 1992). Having only one wavelength point to compute the transverse fields prevents the use of a least square approach, unlike in the case of the longitudinal field equation. This, in turn, complicates the determination of the transverse component because the Stokes Q and U signals are often found to be at, or close to, the noise level. The quadratic average of the linear polarization signals in Eq. (4) hinders any possible noise reduction and generates a veil of noise-induced transverse fields that proves problematic in the use of this equation in many cases. This is particularly true for the He line, whose second derivative of the (broad) Stokes I_o profile is very small. This derivative in the denominator in Equation (4) results in values of the noise-induced transverse fields as high as 300–400 G, only slightly lower than the actual values measured in the filament region. Note that this 300–400 G noise level corresponds to a S/N of 1000 in the map in Fig. 2, whereas in Fig. 1 the S/N is four times higher.

Thus, and in order to obtain high S/N maps of the chromospheric transverse fields, we averaged the unsigned Q and U signals over three wavelengths, the central wavelength and two wavelengths at 278 mÅ on each side of line center, corresponding approximately to the locations of the peak signals in the linear polarization profiles, so

$$\sqrt{Q_o^2(\lambda_o)+U_o^2(\lambda_o)} \approx \sqrt{\bar{Q}_o^2+\bar{U}_o^2}, \qquad (5)$$

where $\bar{Q}_o$ and $\bar{U}_o$ are the averaged linear polarization signals over these three wavelength points. We emphasize that this approach reduces the noise level considerably while at the same time preserves the distribution of transverse fields already present when directly applying Eq. (4). The results obtained from this approach have been validated by the ME inversions presented in the next section.

A similar approach was followed with the Si line to obtain the photospheric magnetic field. The Landé factor for this line is 1.5. The spectral profiles arising from this transition are broad enough to partly justify the application of the weak-field approximation. However, like for any other photospheric line, the vector-magnetograph data obtained with this method have to be interpreted with caution. In particular, the results for this line are affected by filling factor effects as is the case for commonly used photospheric magnetograph data. For the Si line, the exact formulation of Eq. (4) was used. The intrinsically greater photospheric magnetic field strengths together with the fact that the Si Stokes I profile has a sizeable second derivative, makes the determination of $B_\perp$ less affected by noise when using only the central wavelength point of the linear polarization profiles for its determination.

Lastly, the Stokes I profiles of both He and Si were fitted with Gaussian functions from which the line center, line width and strength were inferred. In the case of the He , this approach proved very useful to identify the location of the filament above the NL.

The results from this approach are presented in Fig. 2 for the map observed on the 5th of July. The He Doppler width and line core frames show that the line becomes deeper and narrower inside the filament. This could be an indication of the presence of a denser and cooler plasma than in its immediate plage surroundings. These frames also reveal that the filament has a highly twisted topology, with filamentary threads running at almost 45 degrees from the direction defined by the NL. This becomes evident when compared to the Si and He LOS magnetograms. The twist in the filament is more obvious in the bottom half of the frames than in the top part, where a more diffuse linear topology is observed. These twisted signatures could be clearly seen in the observations from the 5th of July, while they were hardly visible in the maps obtained two days earlier. The Si LOS magnetogram shows that the separation between the two polarities is less than 5″ at photospheric levels when the magnetogram is scaled at ±1000 G. A tighter scaling with a smaller threshold would provide a much narrower NL channel. In the He LOS magnetograms, with a scaling of ±400 G, the channel is practically absent, showing how intense the plage surrounding this AR filament was. A thread-like structure in the longitudinal component running parallel to the direction of the twist (i.e. at 45 degrees from the NL) in the mid range of the frame is observed. Note that the AR is 22 degrees off disk center so horizontal threads in the filament can give rise to sizeable Stokes V signals. The intrinsic LOS magnetic field strength at the NL (we stress that no filling factor effect is included in these estimates) is typically 100 G for each of the two polarities (in agreement with older measurements of AR filaments that did not include transverse field measurements). The neighboring plage displays an intrinsic longitudinal field strength of 200–400 G. If we assume an intrinsic photospheric field strength in the plage of 1400 G (see Martínez Pillet et al. 1997), this would indicate a filling factor of about 20% in this layer.

In both, the photospheric and chromospheric magnetograms, the region where the longitudinal field becomes weaker corresponds to the region with very strong transverse fields. The somewhat wider photospheric NL channel corresponds to a wider photospheric area occupied with strong transverse fields, while the transverse fields in the chromosphere fill a narrower region. These transverse fields seem to follow the structures observed in the He line core frame: a more linear topology in the top part and a twisted formation in the bottom half. What becomes readily surprising is the magnitude of the transverse fields observed in the chromosphere (and to the extent that the weak field approximation is valid, in the photosphere as well). The photosphere shows fields in the range of up to kG in the region between abscissae $x = 15''$ to $x = 20''$ in the frames of Fig. 2. This area shows penumbral-like structures and pores in the white light image. It is clear that these orphan penumbral-like regions are magnetically linked to the main body of the AR filament and correspond to horizontal field lines at the photospheric surface. The transverse fields derived from the Si line undoubtedly show the twist configuration similar to that observed in the He lines. In the chromosphere, the transverse fields are also strong. The present analysis yields transverse fields with strengths in the range of 500–600 G, strongly concentrated in the narrow NL channel. Note that this region, at best, a few arcsec wide, is below the low resolutions of old observations. These high transverse magnetic fields are well above most, if not all, of past field strength measurements in AR filaments.

The various maps for the observations on the 3rd of July support the hypothesis that an AR filament corresponds to a narrow channel characterized with strong (~500 G) transverse fields. There is a clear spatial correlation between strong absorption signatures in He (measured by the line core intensities), and narrow (or "abutted") plage regions with strong transverse fields in the chromosphere. A complete description of all these maps is postponed to a future paper. But it is interesting to point out the following main differences with the map of Fig. 2: the absence of evident twisted threads, the absence of penumbral-like regions in white-light maps, weaker and more diffuse transverse fields at the photosphere (not reaching kG levels) and the presence of weaker He absorption signatures in regions outside the intense NL channel that display atomic polarization signals.

3.2. Milne-Eddington inversions

The interest of the magnetograph analysis is that it is easily computed over a complete map with a very low computational effort. However, in order to validate the weak-field approximation inferences of the magnetic field strength in the filament, we carried out a Milne-Eddington (ME) inversion of the He Stokes profiles of the averaged time series. These high S/N data correspond to the location of the vertical line at $x = 20''$ in the map of Fig. 1. The inversion code we used (MELANIE; Socas-Navarro 2001) computes the Zeeman-induced Stokes spectra – in the incomplete Paschen-Back (IPB) effect regime – that emerge from a model atmosphere described by the Milne-Eddington approximation. This assumes a semi-infinite constant-property atmosphere whose source function varies linearly with optical depth, τ. This approach does not account for the atomic-level polarization induced by the anisotropic radiation pumping of the He atoms from the underlying photospheric continuum.

For magnetic fields between 400 and 1500 G the Zeeman splitting of the upper J-levels of the He triplet is comparable to their energy separation. Thus, it is crucial to compute the energy levels in the IPB regime to avoid an under-estimation of the magnetic field strength when carrying out the inversion to interpret observations (Socas-Navarro et al. 2004; Sasso et al. 2006).

The Milne-Eddington model atmosphere uses a set of eleven free parameters that the inversion code modifies in an iterative manner in order to obtain the best fits to the observed Stokes profiles. These free parameters are: the magnetic field strength (B), its inclination (θ) and azimuth (χ) angles in the reference system of the observer (the azimuth is measured with respect to the local solar radial direction), the line strength (η_0), the Doppler width ($\Delta\lambda_{\rm D}$), a damping parameter, the LOS velocity, the source function at $\tau = 0$ and its gradient, a macroturbulence factor and a stray light fraction f. An initial guess model must be provided to the code. In order to prevent the inversion scheme from getting locked into local minima, we carried out the inversions using several different initializations, in which B, θ and χ were taken from the above-described magnetograph analysis and the remaining parameters were obtained from random perturbations of reasonable pre-set values. All parameters were free except for the stray light fraction, which was set to zero (i.e., assuming a filling factor of 1; we refer to the explanation in Sect 3.1). We stress that, even if the data is contaminated with stray-light from the surroundings, using a filling factor of unity allows a direct comparison with the results given in the previous section.

Figures 3 and 4 show the results of the ME inversion of the full Stokes vector for two positions along the filament (only two fits are shown but the complete set of profiles from Fig. 1 were inverted). The excellent performance of the ME inversion tells us that there are barely any scattering polarization signatures in these profiles, and that the formation physics of the multiplet is adequately described in the IPB regime. As expected, the magnetic field strengths inferred from all the inversions are around 600–700 G with very high inclinations (~80°) with respect to the line-of-sight, thus confirming the existence of strong transverse fields in this AR filament. The exact values obtained for Fig. 3 are $B_{\parallel} = 109$ G and $B_{\perp} = 616$ G while for Fig. 4 we obtain $B_{\parallel} = 176$ G and $B_{\perp} = 602$ G. In the solar reference frame, the magnetic field vector turns out to be close to horizontal, 59° and 99° of inclination with respect to the local vertical, respectively.

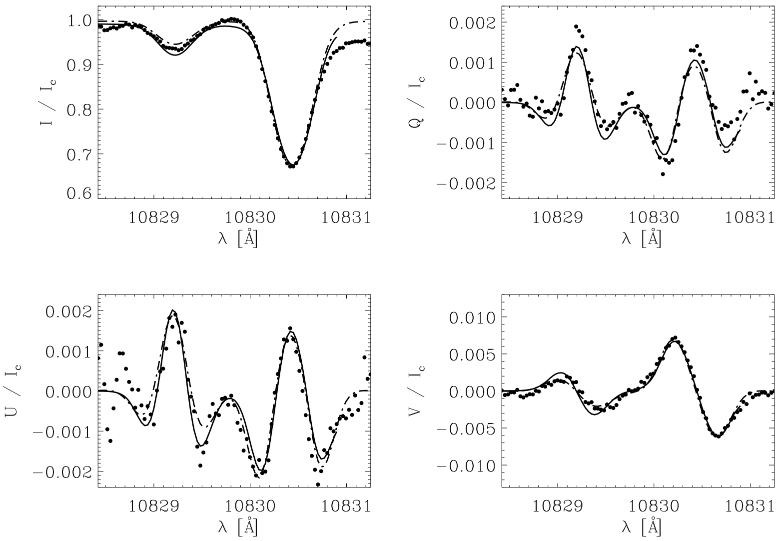

Fig. 3. Stokes profiles of the He 10 830 Å triplet at a height of 8 arcsec in Fig. 1 in the mid portion of the twisted region of the filament. The dots represent the observed profiles obtained after averaging the time series in order to achieve a higher S/N. The solid line corresponds to the best fit achieved with a Milne-Eddington inversion code that takes into account the IPB effect. The magnetic field obtained from this particular fit is B = 626 ± 10 G, θ = 80.2° ± 0.1° and χ = 174.9° ± 0.1° (the origin of azimuths being the local solar radial direction). The dot-dashed line shows the best fit obtained from an inversion in a slab model of constant properties that accounts for the joint action of scattering polarization and the Hanle Zeeman effects. This fit provided for the magnetic parameters B = 667 ± 16 G, θ = 81.1° ± 0.3° and χ = 174.8° ± 0.5°.

The magnetic field strengths derived from the weak field regime analysis are systematically under-estimated by ~100−150 G, but the retrieved inclinations and azimuths are in very good agreement with those obtained from the ME-IPB inversions. This means that the weak field approximation yields a reliable magnetic field topology and a low-end value for the field strength.

3.3. PCA-based atomic polarization inversion

The observations described above were also independently inverted using the principal component analysis (PCA) approach described by López Ariste & Casini (2002). In fact, pattern recognition techniques are particularly well suited to attack ill-defined inversion problems characterized by computationally intensive forward problems. This is exactly the case for spectropolarimetric inversions in prominences and filaments, where the Stokes profiles are often formed by the scattering of resonant radiation. The computation of the emergent polarization in such case requires the preliminary solution of the non-LTE problem of atomic-level excitation by anisotropic illumination of the plasma from the underlying photosphere. The presence of a magnetic field further modifies the ensuing atomic polarization through the Hanle effect (see, e.g. Landi Degl'Innocenti & Landolfi 2004, for a review of atomic polarization effects). This problem, which is totally by-passed in the ME approach to spectropolarimetric inversion, completely dominates the numerical computation of line polarization in radiation scattering. For this reason, pattern recognition techniques provide a very attractive strategy to Stokes inversion for radiation scattering, since the numerically intensive forward problem is solved once and for all for a comprehensive set of illumination, thermodynamic, and magnetic conditions in the plasma for the problem at hand. The goal of these techniques is thus to build universal databases of profiles that can be searched for the solution to any given Stokes inversion problem. Principal component analysis additionally provides a way of compressing database information, by reducing it to a few principal component profiles that contain all the fundamental physics of the formation of the emergent Stokes profiles (López Ariste & Casini 2002; Casini et al. 2005).

For the inversion of the observations illustrated in this paper, we created a database of 250 000 profiles, spanning all possible orientations of the magnetic field, with strengths between 0 and 2000 G. The illumination conditions were set by the radiation temperature and center-to-limb variation (CLV) profile of the photospheric radiation at 1 μm (Cox 2000), and by assuming a range of scattering heights between 0 and 0.06 $R_\odot$ (42 Mm). The LOS inclination in the database used for the inversion of the July 5, 2005, observations spanned between 20° and 30°. The thermal Doppler width and micro-turbulent velocity, responsible for the overall profile broadening, were accounted for by introducing an equivalent temperature spanning between 10^4 and 2×10^4 K. Finally, the database Stokes profiles were calculated by integrating the polarized radiation emerging from a homogeneous slab with optical depth at line center varying between 0.2 and 1.4. Very soon it was realized that such conventional scattering scenario could not fit satisfactorily the observations, unless some additional depolarizing mechanism could be accounted for to explain the surprisingly low level of atomic polarization revealed by the Zeeman-like shape of the Stokes Q and U profiles. For this reason, in the creation of the inversion database we introduced an ad-hoc weight factor for the anisotropy of the photosphere radiation, ranging between 0 and 1. Extensive inversion tests that were run over the entire filament map consistently gave anisotropy weight factors significantly smaller than unity, with a predominance of values around 0.2, thus confirming the presence of some unidentified depolarizing mechanism in the formation of the observed profiles. The possible physical origin of such depolarization has been extensively discussed by Casini et al. (2009), but see also Trujillo Bueno & Asensio Ramos (2007).

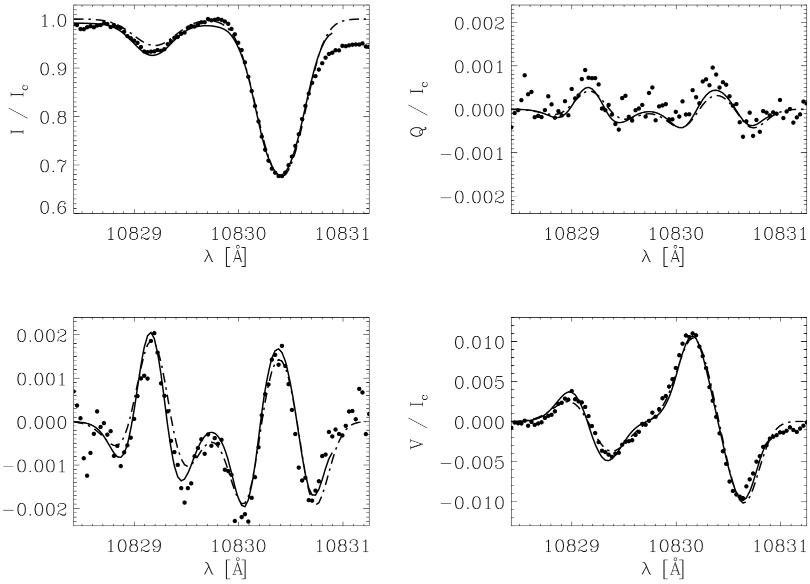

Fig. 4. Same as Fig. 3 but for a profile near the bottom portion of the twisted region of the filament (at a height of 5 arcsec). The fitted parameters for the ME case are B = 627 ± 10 G, θ = 73.7° ± 0.3° and χ = 5.7° ± 0.1°. The PCA-based algorithm including Hanle effect provided: B = 664 ± 15 G, θ = 74.9° ± 0.6° and χ = 5.1° ± 0.8°.

The results of the PCA inversion are overplotted to the ME inversions as dot-dashed lines in Figs. 3 and 4. The PCA inversion provides a magnetic field of B = 667 G in the first case and B = 664 G in the second. The inclination angles are almost the same as the ones obtained by the ME inversions, ~59° and ~99° with respect to the local vertical, respectively. The inferred magnetic field azimuths are also in very good agreement.

4. Conclusions

The He 10 830 Å lines observed in a filament at the NL of active region NOAA 10 781 exhibit linear polarization profiles dominated by the Zeeman effect. Three different independent analyses (magnetograph approximation, ME inversion and PCA inversion including atomic polarization) of the four Stokes profiles consistently support inferred field strengths in the range 600–700 G at the formation height of the helium triplet. These fields are 3 to 7 times higher than those measured heretofore in AR filaments. The field strengths found at the NL are largely horizontal with 500–600 G transverse fields. The longitudinal component is typically measured to be in the range of 100–200 G, in agreement with past measurements. It must be stressed that these previous observations of AR filaments did not include transverse field estimates. Thus, it is clear that the inclusion of the Stokes Q and U profiles in our analysis is what has allowed the detection of such strong magnetic fields in AR filaments. While the role played by the linear polarization signals was evident already from the magnetograph analysis, a further test was made with the ME inversion to prove this point. Using as input the observed I and V profiles but replacing the Stokes Q and U profiles with noisy data, the ME inversions resulted in fields strengths in the range of 100–200 G. We thus propose that the lack of full Stokes polarimetry was the main reason why past measurements did not find the high field strengths reported in this work. Note also that the spatial extent that displays such strong fields is not more than a few arcsec wide, which would be hardly visible in low resolution measurements. It is also clear that it becomes crucial to search for the signatures of these high field strengths in different spectral windows such as Hα and the Ca triplet.

A similar trend to infer higher field strengths (albeit in a lower range) is presented in modern measurements of quiescent filaments that is also ascribed to the use of full Stokes polarimetry (Casini et al. 2003). In the case of quiescent filaments, observations are dominated by atomic polarization and its modification through the Hanle effect. In the study presented here, however, the linear polarization profiles are dominated by the Zeeman effect as long as the profiles are coming from the regions of strong helium absorption. The reason why atomic polarization signatures are almost absent from these profiles is not yet well understood. On the one hand, the observed high field strengths are approaching the values where the Zeeman effect dominates over atomic level polarization (Trujillo Bueno & Asensio Ramos 2007), but even at this high field strengths, one would have expected a clearer atomic polarization signature. On the other hand, some mechanism to reduce the anisotropy of the radiation field could be present. For example, Trujillo Bueno & Asensio Ramos (2007) suggested that, if the radiation comes from a high opacity region, the isotropy of the radiation field will be such that a much reduced atomic polarization would be induced. A more recent proposal by Casini et al. (2009) suggests that the presence of a randomly oriented field entangled with the main filament field, and of a similar magnitude, could also explain the absence of atomic polarization signatures in these profiles. It is interesting to note that the ad-hoc anisotropy weight factor introduced in the PCA inversions was found to be in the range 0.1–0.5 over the filament region, with a predominant value of 0.2. Although the various atomic processes generating polarization signals cannot be cleanly separated, this persisting value of 0.2 is evidence of their presence in our profiles (note that a weight factor of 1 corresponds to an anisotropic illumination described by the standard CLV of the photospheric radiation field). We also stress that the reason for the absence of atomic level polarization signatures is not simply due to what is commonly referred to as a Van-Vleck configuration of the vector field. For example, whereas the profiles inverted in Fig. 3 give an inclination (with respect to the local vertical) close to the Van-Vleck angle (59°; Van-Vleck angle corresponds to $\sim$55°), those in Fig. 4 yield an inclination very far from it (99°).

What is the origin of these strong transverse fields? This question relates directly to the problem of filament formation and mass loading. Two basic scenarios are commonly used to explain how these structures are formed: photospheric (shearing) motions and flux emergence (see the recent review by Lites 2008). The first one uses photospheric plasma flows that move, tangle and reconnect the field lines of an already emerged active region to form the filament directly in the corona. These processes include in one way or another some form of magnetic cancellation and reconnection that provides a source for mass upload of the filament. In this scenario, the presence of such strong magnetic fields must be related to the existence of a dense plage configuration at the NL and the low gradients inferred by Aulanier & Démoulin (2003) for their model of AR filaments. Our observations pose the question of how filament field strengths in the range of 600–700 G may be generated in this scenario from a surrounding "abutted" plage that has a longitudinal field of no more than 400 G at the height of formation of the helium lines. The emergence of a flux rope from below the photosphere scenario has recently received strong support from the observations of Okamoto et al. (2008). If the flux ropes are formed below the surface, the answer to the observed field strengths could be related to the balance between buoyancy forces and gravity acting over the flux system. Although this balance is not yet fully understood, it is clear that the stronger the fields the easier is for the flux system to emerge into the corona and carry a significant amount of trapped photospheric mass (Archontis et al. 2004). Note that the photospheric transverse fields observed at the NL are also very strong (including pore-like structures) and could represent the bottom part of the flux rope system once emerged into the atmosphere.

It remains to be studied whether the observed strong transverse field strengths presented in this paper are common to all AR filaments or only to those surrounded by exceptionally dense plages. An extension of the present study to other ARs with different degrees of activity is mandatory.

Acknowledgements. Based on observations made with the VTT operated on the island of Tenerife by the KIS in the Spanish Observatorio del Teide of the Instituto de Astrofísica de Canarias. This research has been supported by the Spanish Ministry of Science and Innovation (MICINN) under the project ESP2006-13030-C06-01. The National Center for Atmospheric Research (NCAR) is sponsored by the National Science Foundation. Help received by C. Kuckein during his stay at HAO/NCAR is gratefully acknowledged. R. Manso Sainz has been partially supported by the MICINN through project AYA2007-63881. H. Socas-Navarro helped with the implementation of the MELANIE code and with the interpretation of the obtained results. Comments on the manuscript by B. C. Low and J. Trujillo Bueno are gratefully acknowledged.

References

Anzer, U., & Heinzel, P. 2007, A&A, 467, 1285
Archontis, V., Moreno-Insertis, F., Galsgaard, K., Hood, A., & O'Shea, E. 2004, A&A, 426, 1047
Auer, L. H., House, L. L., & Heasley, J. N. 1977, Sol. Phys., 55, 47
Aulanier, G., & Démoulin, P. 1998, A&A, 329, 1125
Aulanier, G., & Démoulin, P. 2003, A&A, 402, 769
Avrett, E. H., Fontenla, J. M., & Loeser, R. 1994, Infrared Solar Physics, 154, 35
Casini, R., López Ariste, A., Tomczyk, S., & Lites, B. W. 2003, ApJ, 598, L67
Casini, R., Bevilacqua, R., & López Ariste, A. 2005, ApJ, 622, 1265
Casini, R., Manso Sainz, R., & Low, B. C. 2009, ApJ, in preparation
Collados, M. 1999, Third Advances in Solar Physics Euroconference: Magnetic Fields and Oscillations, ed. B. Schmieder, A. Hofmann, & J. Staude (San Francisco: ASP), 184, 3
Collados, M. 2003, in Polarimetry in Astronomy, ed. by S. Fineschi, Proc. SPIE, 4843, 55
Collados, M., Lagg, A., Díaz Garcí A., J. J., et al. 2007, in The Physics of Chromospheric Plasmas, ed. P. Heinzel, I. Dorotovič, & R. J. Rutten, ASP Conf. Ser., 368, 611
Cox, A.N. 2000, Allen's astrophysical quantities, 4th edn. (Springer)
Landi Degl'Innocenti, E. 1992, Solar Observations: Techniques and Interpretation, ed. F. Sánchez, M. Collados, & M. Vázquez (Cambridge Univ. Press), 73
Landi Degl'Innocenti, E., & Landolfi, M. 2004, Astrophysics and Space Science Library, Polarization in Spectral Lines (Kluwer), 307
Leroy, J. L., Bommier, V., & Sahal-Brechot, S. 1983, Sol. Phys., 83, 135
Lites, B. W. 2005, ApJ, 622, 1275
Lites, B. W. 2008, Space Sci. Rev., 10.1007, 156
López Ariste, A., & Aulanier, G. 2007, in Coimbra Solar Physics Meeting on the Physics of Chromospheric Plasmas, ed. P. Heinzel, I. Dorotovic, & R. J. Rutten, ASP Conf. Ser., 368, 291
López Ariste, A., & Casini, R., 2002, ApJ, 575, 529
López Ariste, A., Casini, R., Paletou F., et al. 2005, ApJ, 621, L145
Low, B. C. 2001, J. Geophys. Res., 106, 25141
Manchester, W. B., IV, Vourlidas, A., Toth, G., et al. 2008, ApJ, 684, 1448
Martínez Pillet, V., Lites, B. W., & Skumanich, A. 1997, ApJ, 474, 810
Merenda, L., Trujillo Bueno, J., Landi Degl'Innocenti, E., & Collados, M. 2006, ApJ, 642, 554
Okamoto, T. J., Tsuneta, S., Lites, B. W., et al. 2008, ApJ, 673, L215
Paletou, F., López Ariste, A., Bommier, V., & Semel, M. 2001, A&A, 375, L39
Sahal-Brechot, S., Bommier, V., & Leroy, J. L. 1977, A&A, 59, 223
Sasso, C., Lagg, A., & Solanki, S. K. 2006, A&A, 456, 367
Sasso, C., Lagg, A., Solanki, S. K., Aznar Cuadrado, R., & Collados, M. 2007, in The Physics of Chromospheric Plasmas, ed. P. Heinzel, I. Dorotovič, & R. J. Rutten, ASP Conf. Ser., 368, 467
Scherrer, P. H., Bogart, R. S., Bush, R. I., et al. 1995, Sol. Phys., 162, 129
Socas-Navarro, H. 2001, Advanced Solar Polarimetry – Theory, Observation, and Instrumentation, 236, 487
Socas-Navarro, H., Trujillo Bueno, J., & Landi Degl'Innocenti, E. 2004, ApJ, 612, 1175
Trujillo Bueno, J., & Asensio Ramos, A. 2007, ApJ, 655, 642
Trujillo Bueno, J., Landi Degl'Innocenti, E., Collados, M., Merenda, L., & Manso Sainz, R. 2002, Nature, 415, 403
Tandberg-Hanssen, E., & Malville, J. M. 1974, Sol. Phys., 39, 107
von der Lühe, O., Soltau, D., Berkefeld, T., & Schelenz, T. 2003, Proc. SPIE, 4853, 187
Wiehr, E., & Bianda, M. 2003, A&A, 404, L25
Wiehr, E., & Stellmacher, G. 1991, A&A, 247, 379

3

An active region filament studied simultaneously in the chromosphere and photosphere. I. Magnetic structure

In Chapter 2, the magnetic field strength inside an AR filament was inferred. In this chapter, the magnetic field topology that results from the He I 10830 Å and Si I 10827 Å inversions will be addressed. The silicon inversions have been carried out with the SIR code and the AZAM utility was used to solve the 180° ambiguity and to project the vector magnetic field onto the local solar frame of reference.

The article presented in this chapter was published with the title "An active region filament studied simultaneously in the chromosphere and photosphere. I. Magnetic structure", in Astronomy & Astrophysics, volume 539, A131, pages 1–15, year 2012.

Abstract: A thorough multiwavelength, multiheight study of the vector magnetic field in a compact active region filament (NOAA 10781) on 2005 July 3 and 5 is presented. We suggest an evolutionary scenario for this filament. Two different inversion codes were used to analyze the full Stokes vectors acquired with the Tenerife Infrared Polarimeter (TIP-II) in a spectral range that comprises the chromospheric He I 10830 Å multiplet and the photospheric Si I 10827 Å line. In addition, we used *SOHO*/MDI magnetograms, as well as BBSO and *TRACE* images, to study the evolution of the filament and its active region (AR). High-resolution images of the Dutch Open Telescope were also used. An active region filament (formed before our observing run) was detected in the chromospheric helium absorption images on July 3. The chromospheric vector magnetic field in this portion of the filament was strongly sheared (parallel to the filament axis), whereas the photospheric field lines underneath had an inverse polarity configuration. From July 3 to July 5, an opening and closing of the polarities on either side of the polarity inversion line (PIL) was recorded, resembling the recently discovered process of the sliding door effect seen by Hinode. This is confirmed with both TIP-II and *SOHO*/MDI data. During this time, a newly created region that contained pores and orphan penumbrae at the PIL was observed. On July 5, a normal polarity configuration was inferred from the chromospheric spectra, while strongly

sheared field lines aligned with the PIL were found in the photosphere. In this same data set, the spine of the filament is also observed in a different portion of the FOV and is clearly mapped by the silicon line core. The inferred vector magnetic fields of the filament suggest a flux rope topology. Furthermore, the observations indicate that the filament is divided in two parts, one which lies in the chromosphere and another one that stays trapped in the photosphere. Therefore, only the top of the helical structure is seen by the helium lines. The pores and orphan penumbrae at the PIL appear to be the photospheric counterpart of the extremely low-lying filament. We suggest that orphan penumbrae are formed in very narrow PILs of compact ARs and are the photospheric manifestation of flux ropes in the photosphere.

A&A 539, A131 (2012)
DOI: 10.1051/0004-6361/201117675
© ESO 2012

Astronomy & Astrophysics

An active region filament studied simultaneously in the chromosphere and photosphere

I. Magnetic structure

C. Kuckein[1,2], V. Martínez Pillet[1], and R. Centeno[3]

[1] Instituto de Astrofísica de Canarias, vía Láctea s/n, 38205 La Laguna, Tenerife, Spain
e-mail: `ckuckein@iac.es`
[2] Departamento de Astrofísica, Universidad de La Laguna, 38206 La Laguna, Tenerife, Spain
[3] High Altitude Observatory (NCAR), Boulder, CO 80301, USA

Received 9 July 2011 / Accepted 2 December 2011

ABSTRACT

Aims. A thorough multiwavelength, multiheight study of the vector magnetic field in a compact active region filament (NOAA 10781) on 2005 July 3 and 5 is presented. We suggest an evolutionary scenario for this filament.

Methods. Two different inversion codes were used to analyze the full Stokes vectors acquired with the Tenerife Infrared Polarimeter (TIP-II) in a spectral range that comprises the chromospheric He 10 830 Å multiplet and the photospheric Si 10 827 Å line. In addition, we used SOHO/MDI magnetograms, as well as BBSO and TRACE images, to study the evolution of the filament and its active region (AR). High-resolution images of the Dutch Open Telescope were also used.

Results. An active region filament (formed before our observing run) was detected in the chromospheric helium absorption images on July 3. The chromospheric vector magnetic field in this portion of the filament was strongly sheared (parallel to the filament axis), whereas the photospheric field lines underneath had an inverse polarity configuration. From July 3 to July 5, an opening and closing of the polarities on either side of the polarity inversion line (PIL) was recorded, resembling the recently discovered process of the sliding door effect seen by Hinode. This is confirmed with both TIP-II and SOHO/MDI data. During this time, a newly created region that contained pores and orphan penumbrae at the PIL was observed. On July 5, a normal polarity configuration was inferred from the chromospheric spectra, while strongly sheared field lines aligned with the PIL were found in the photosphere. In this same data set, the spine of the filament is also observed in a different portion of the field of view and is clearly mapped by the silicon line core.

Conclusions. The inferred vector magnetic fields of the filament suggest a flux rope topology. Furthermore, the observations indicate that the filament is divided in two parts, one which lies in the chromosphere and another one that stays trapped in the photosphere. Therefore, only the top of the helical structure is seen by the helium lines. The pores and orphan penumbrae at the PIL appear to be the photospheric counterpart of the extremely low-lying filament. We suggest that orphan penumbrae are formed in very narrow PILs of compact ARs and are the photospheric manifestation of flux ropes in the photosphere.

Key words. Sun: filaments, prominences – Sun: chromosphere – Sun: photosphere – Sun: magnetic topology – techniques: polarimetric

1. Introduction

Solar filaments, also called prominences when observed in emission outside the disk, are elongated structures formed of dense plasma, which lies above polarity inversion lines (PILs) of the photospheric magnetic field (Babcock & Babcock 1955) and has a lower temperature than its surroundings. A functional definition of the PIL would be an imaginary line that separates two close areas of opposite polarity. On disk filaments are readily identifiable in the quiet Sun (quiescent filaments) and in active regions (active region filaments) when observed using common chromospheric wavelengths, e.g., the He 10 830 Å multiplet and the Hα 6563 Å line. The magnetic field plays a major role in their formation, stability, and evolution. As a result, spectropolarimetric observations at different heights of the atmosphere combined with high angular resolution images are needed to obtain an overall picture of the physical processes that take place in filaments. The magnetic field strength and its orientation can be inferred using appropriate diagnostic techniques that are able to interpret the Zeeman effect, as well as scattering polarization and its modification through the Hanle effect (Tandberg-Hanssen 1995, and references therein). Although many line-of-sight (LOS) observations have been carried out in the past decades, it is important to emphasize the need for full-Stokes measurements in order to have complete information of the vector magnetic field.

According to observational studies, the magnetic field topology under active region (AR) filaments has sheared or twisted field lines along the PIL that can support dense plasma in magnetic dips (Lites 2005; López Ariste et al. 2006). Previous findings about prominence magnetic structure have shown models with dipped field lines in a normal (Kippenhahn & Schlüter 1957) or inverse[1] (Kuperus & Raadu 1974; Pneuman 1983) polarity configuration, the latter having a helical structure. From a

---

[1] Throughout this paper, by *inverse configuration* we mean a magnetic field vector perpendicular to the filament's axis that points from the negative to the positive polarity. This is the opposite of what one would expect in a potential field solution – where the field points from the positive to the negative side (and is referred to as normal configuration).

large sample of quiescent prominence observations, Leroy et al. (1984) found both types of configurations and a strong correlation between the magnetic field topology and the height of the prominence. On the other hand, Bommier et al. (1994) found predominantly inverse polarity configurations. However, more recent photospheric spectropolarimetric observations of AR filaments have revealed that both configurations can coexist in the same filament (Guo et al. 2010) or even evolve with time from one type to the other, as presented by Okamoto et al. (2008) from the analysis of vector magnetogram sequences.

The formation process of filaments is still a controversial issue in solar physics, so it has been widely debated. On the one hand, there is the *sheared arcade model* that, by large-scale photospheric footpoint motions (such as shear at, and convergence towards the PIL, and subsequent reconnection processes), is able to form dips and even helical structures, where plasma can be gravitationally confined (e.g., Pneuman 1983; van Ballegooijen & Martens 1989; Antiochos et al. 1994; Aulanier & Demoulin 1998; DeVore & Antiochos 2000; Martens & Zwaan 2001; Welsch et al. 2005; Karpen 2007). This model is capable of reproducing both inverse and normal polarity configurations in the same filament (Aulanier et al. 2002). However, recent observational works in a quiescent filament (Hindman et al. 2006) and along an AR filament channel (Lites et al. 2010) did not find evidence of these systematic photospheric flows that converged at the PIL and triggered reconnection processes. In our opinion, more observations are needed to support this important result.

On the other hand, the *flux rope emergence model* assumes that the twist in the field lines is already present in the convection zone before emerging into the atmosphere (e.g., Kurokawa 1987; Low 1994; Low & Hundhausen 1995; Lites 2005). The rise of twisted magnetic fields has been studied by various authors through both observations (Lites et al. 1995, 2010; Leka et al. 1996) and three-dimensional (3D) numerical simulations (e.g., Fan 2001; Archontis et al. 2004; Magara 2004; Martínez-Sykora et al. 2008; Fan 2009; Yelles Chaouche et al. 2009). Such an emerging helical flux rope scenario, combined with the presence of granular flows, is supposedly the main process of formation and maintenance of the AR filament studied by Okamoto et al. (2008, 2009). Recent nonlinear force-free field (NLFFF) extrapolations of photospheric magnetic fields underneath AR filaments (Guo et al. 2010; Canou & Amari 2010; Jing et al. 2010) have agreed that the main structure has to be a flux rope, although Guo et al. (2010) also find dipped arcade field lines in the same filament. Flux rope emergence from below the photosphere encounters severe difficulties to reach chromospheric layers and above, since it is loaded with mass (e.g., Archontis & Török 2008). Indeed, the previous work suggests that a second flux rope formed from instabilities and atmospheric reconnection is what lifts up the mass and forms the observed active region filaments.

The main difference between the sheared arcade and the emerging flux rope models is the existence of a flux concentration stuck at photospheric levels in the latter scenario. The reader is referred to the paper of Mackay et al. (2010) for a recent review of the magnetic structure of filaments.

In the past, only a few measurements have been made of the magnetic field strength in AR filaments. For instance, Kuckein et al. (2009), using the same data set as described in this paper, find a predominance of Zeeman-like signatures in the Stokes profiles. Using three different methods, they infer very strong magnetic fields in the filament (600–700 Gauss), with a dominant transverse component (with respect to the LOS).

The aim of this paper is to study the strength and topology of the magnetic field in an active region filament at photospheric and chromospheric heights simultaneously. Recently, several studies have presented analyses of the vector magnetic field in filaments or prominences from observations either in the photosphere (e.g., Lites 2005; López Ariste et al. 2006; Okamoto et al. 2008; Guo et al. 2010; Lites et al. 2010) or the chromosphere (e.g., Lin et al. 1998; Casini et al. 2003; Merenda et al. 2006; Kuckein et al. 2009), but none of them have inferred the field at both heights at the same time. The 10 830 Å spectral region, which includes a chromospheric He triplet and a photospheric Si line, offers a unique spectral window to understanding the physical processes that take place in AR filaments as already shown by Sasso et al. (2011). In this work, we focus on the overall magnetic configuration observed simultaneously in the photosphere and the chromosphere.

2. Observations

The active region filament, NOAA AR 10781, was observed on 2005 July 3 and 5 using the Tenerife Infrared Polarimeter (TIP-II, Collados et al. 2007) at the German Vacuum Tower Telescope (VTT, Tenerife, Spain). TIP-II acquires images at four different modulation states and combines them in order to measure the Stokes parameters (I, Q, U, and V) along the spectrograph slit.

The latitude and longitude of the filament region was N16-E8 (around $\mu \sim 0.95$) for the first day, and N16-W18 ($\mu \sim 0.91$) for the second. During the observations, real time Hα images and SOHO/MDI (Scherrer et al. 1995) magnetograms were used as a reference to position the slit ($0\farcs5$ wide and $35''$ long) at the center of the AR, on top of the polarity inversion line. Figure 1 shows two Big Bear Hα images from July 1 and 5 where the filament can easily be recognized. On July 1, the filament shows a more diffusive nature than on July 5, when it displays a rather compact configuration with brighter Hα emission from the plage flanking it. Scans were taken with TIP-II from E to W with the slit parallel to the PIL and step sizes of $0\farcs4$ for July 3 and $0\farcs3$ for July 5, making up at least a field of view (FOV) of $\sim 30'' \times 35''$, with a pixel size along the slit of $0\farcs17$.

The TIP-II spectral range spanned from 10 825 to 10 836 Å with an original spectral sampling of $\sim$11.04 mÅ px^{-1}. This spectral window included the photospheric Si line at 10 827 Å and the chromospheric He triplet at 10 830 Å. It also contained at least one telluric H$_2$O line, which was used for the absolute velocity calibration.

All images were corrected for flat field and dark current and was calibrated polarimetrically following standard procedures (Collados 1999, 2003). The adaptive optics system of the VTT (KAOS, von der Lühe et al. 2003) was locked on nearby pores and orphan penumbrae, i.e., penumbral-like structures not connected to any umbra (a term coined by Zirin & Wang 1991), and highly improved the observations that had changeable seeing conditions. A binning of 3 px in the spectral domain, 6 px along the slit, and 3 px along the scanning direction was carried out to improve the signal-to-noise ratio needed for the full Stokes spectral line inversions. Thus, the final spectral sampling was $\sim$33.1 mÅ px^{-1}. The spatial resolution, when the KAOS system was locked, reached $\sim 1''$. However, the binned data used for the inversions (except when stated otherwise) had a resolution of $2''$.

The He triplet comprises three spectral lines, which according to the National Institute of Standards and Technology (NIST), are the 10 829.09 Å "blue" component and the "red"

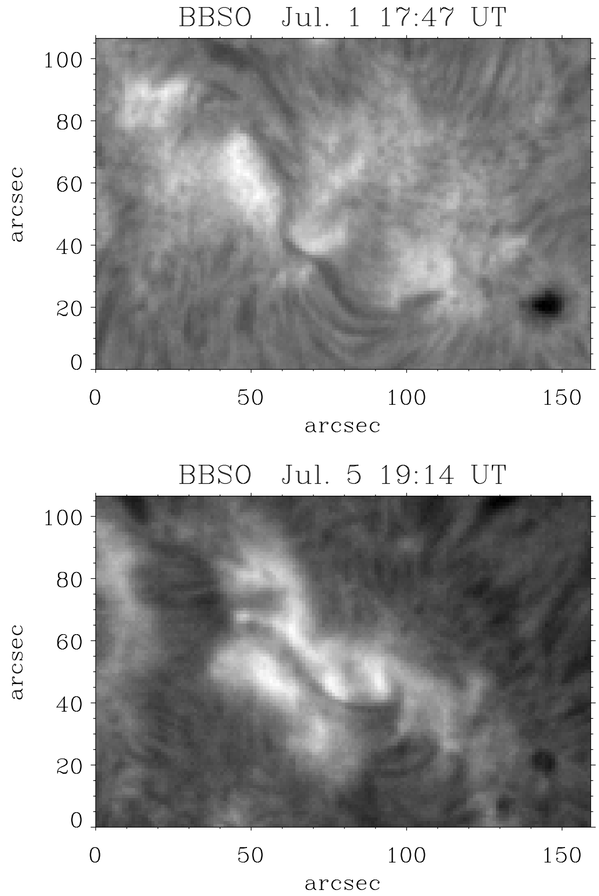

Fig. 1. Big Bear Hα image of the active region under study. The leader sunspot is seen in the bottom right corner. The filament is seen on both days, July 1 and 5. Note the more compact nature of the plage emission on the second day.

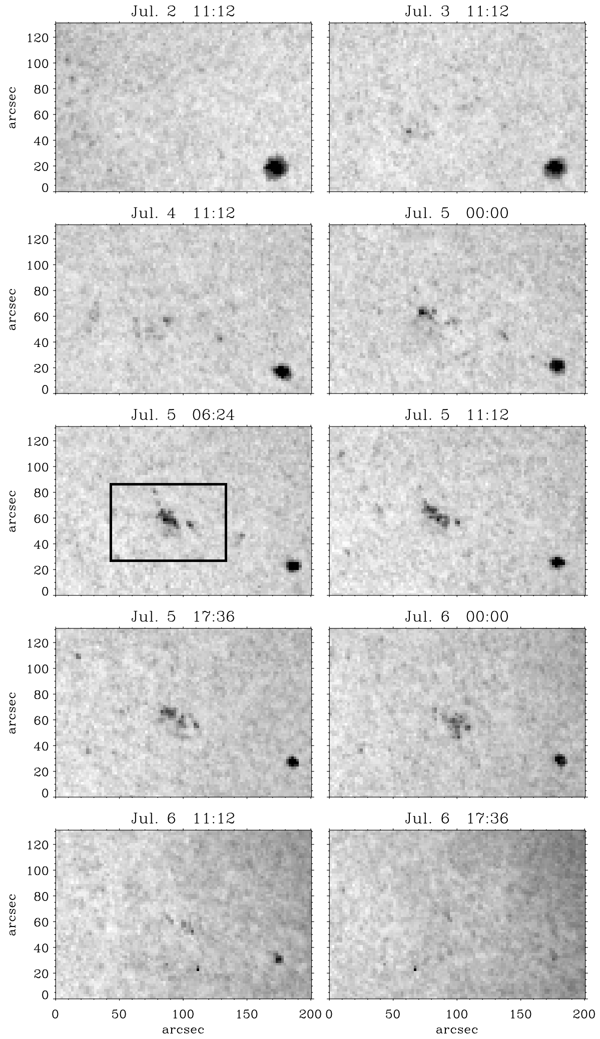

Fig. 2. Time sequence of SOHO/MDI continuum images of the whole active region NOAA 10781 between July 2 and 6 of 2005. The black box shows the size and location of the maps of Fig. 3, which have a smaller but more detailed FOV. A developed sunspot can be seen at the *bottom right* corner of the AR. Between July 2 and 3 the center of the AR was almost devoid of pores. On July 5 we increased the cadence of the sequence in order to show the quick appearance of new pores and orphan penumbrae at the PIL during that day.

components at 10 830.25 Å and 10 830.34 Å lines. The last two are blended and consequently appear as a single spectral line in the solar spectrum. The formation height of the helium triplet happens in the upper chromosphere (Avrett et al. 1994), so it is especially interesting for the study of filaments and their magnetic properties, as already proved by many authors (Lin et al. 1998; Trujillo Bueno et al. 2002; Merenda et al. 2007; Casini et al. 2009; Kuckein et al. 2009; Sasso et al. 2011). The strong photospheric Si I absorption line at 10 827.089 Å originates between the terms $^3P_2 \rightarrow {}^3P_2$ and has a Landé factor of $g_{\mathrm{eff}} = 1.5$. The combination of these lines is an excellent diagnostic tool for studying magnetic fields and their coupling between the photosphere and the chromosphere.

In this paper we also report on SOHO/MDI images that are used to understand the long-term (days) evolution of the AR in the PIL region.

2.1. Evolution of the AR (SOHO/MDI)

Active region NOAA 10781 emerged some weeks before our observing run on the rear side of the Sun. Its magnetic configuration, as seen by SOHO/MDI (see below), clearly corresponds to that of an AR that is in its decay phase, i.e., a round leader sunspot followed by facular regions of both polarities that show the latitudinal shear produced by the action of surface flows (e.g., van Ballegooijen 2008). The filament is found above the PIL in the plage region. The time sequence of continuum images of MDI between 2005 July 2 and 6 is presented in Fig. 2. Since filaments are not visible here, we expanded the FOV in order to use the AR leader sunspot, located in the lower righthand corner, as a reference. As shown in Fig. 2, it is not until July 4 that small pores start to emerge and gather together. White light images of the Transition Region and Coronal Explorer (TRACE) confirm this behavior. On July 5, we increased the cadence in Fig. 2 to show that more pores quickly emerged and orphan penumbrae formed (see black rectangle on the July 5 06:24 UT panel). Interestingly, these orphan penumbral regions act like a bridge

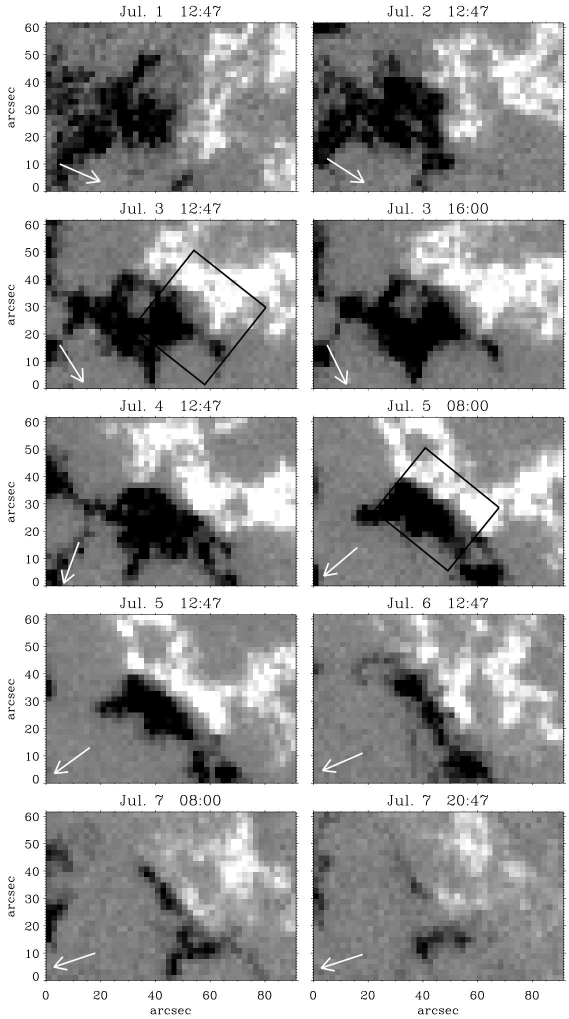

Fig. 3. SOHO/MDI line-of-sight magnetogram evolution of the compact plage between July 1 and 7 of 2005. Note that the date and time of each panel does not correspond to the panels in Fig. 2. Images are saturated at ±400 G. Solar north and west correspond to up and right, respectively. The black boxes show the approximate scanned area of TIP-II for both days. On July 3, the space between both polarities broadens in the lower part of the PIL, whereas in the following days the whole AR is more compact. The size of the panels corresponds to the black rectangle in Fig. 2. White arrows indicate the direction to disk center.

connecting different small groups of pores together. However, during July 6 the pores and orphan penumbrae disappear completely. It is also worth noting that the leading sunspot of the AR, which on July 2 had a round and rather symmetric shape, also decays away slowly over this period of time and almost vanishes by the end of July 6.

Figure 3 provides LOS magnetograms from MDI starting on 2005 July 1 until July 7. This period was chosen in order to carry out a detailed study of the magnetic morphology and evolution of the AR. The FOV is smaller and the panels show different dates and times than Fig. 2. The AR and its PIL are well defined. The *top left* image shows the two polarity regions as of July 1. On the second day, the AR became more compact and the gray area in between the two opposite polarities, i.e. the PIL, developed a winding shape that pointed approximately in the N-S direction. The next two images (from July 3) show the AR becoming even more compact, since the black and white polarities approached each other. It is important to stress that, on this day, the AR rotated counterclockwise and the PIL oriented itself at ~45° with respect to solar north. These images also reveal that from July 2 to 3, although the whole AR became more compact, the lower-right part of the PIL first broadened, then become narrower again on the next day (a process that is also seen on the upper-left part of the PIL one day later). By July 5, the PIL was highly compact with the two polarities in close contact in the scaling of the figure (±400 G). This behavior is consistent with the observations of Okamoto et al. (2008), who describe the opening and closing of the PIL region under an AR filament as a "sliding door". The authors found observational evidence for the emergence of a flux rope under that AR filament.

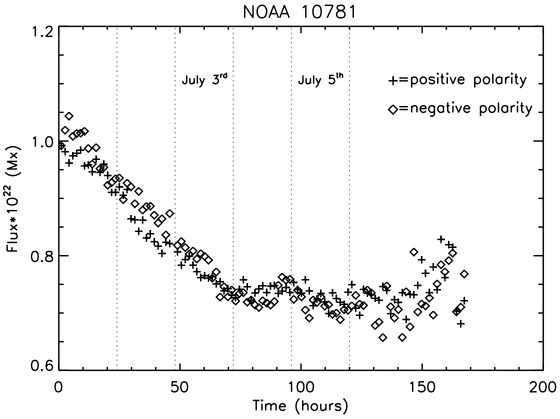

Fig. 4. Flux history curves for the positive (+) and negative (◇) polarities of AR 10781. 24-h days are separated by the vertical dotted lines.

2.2. Magnetic flux evolution of the AR

Recently, the study of AR filaments has been put in the context of the global flux history of the active region as a whole (van Ballegooijen & Mackay 2007). The seminal work of van Ballegooijen & Martens (1989) showed that flux ropes (and filaments) can be formed through successive cancellations at the PIL, transforming active region flux into flux rope field lines. This process submerges as much flux below the surface as is injected into the flux rope itself. Thus, evaluating the flux losses that occur during the last stages of an active region is important for understanding this evolutionary phase. Measurements of such flux losses in an active region by Sterling et al. (2010) yielded 2.8×10^{21} Mx day^{-1}. More recently, for a medium sized active region, Green et al. (2011) quoted a lower rate of 2.5×10^{20} Mx day^{-1}. This number agrees better with the estimate by Dalda & Martinez Pillet (2008), who find 4.8×10^{20} Mx day^{-1}. The latter authors also report on a clear relation between the cancellation events at the PIL and an outward-directed coronal activity, but they caution that the contribution of the cancellation events was four times less than the global flux decay rate. According to this study, not all flux losses could have been attributed to cancellations at the PIL, with the resolution and sensitivity of SOHO/MDI magnetograms.

Figure 4 displays the flux history curves for the positive and negative polarities of this active region. The two days when

TIP-II observations were taken are highlighted in the figure. The active region boundaries were visually selected for each SOHO/MDI map and adapted to the size changes of the AR created by the well-known flux transport processes. The magnetic flux of each pixel is multiplied by a factor $1/\cos^2(\theta)$, where θ is the heliocentric angle, to account for the LOS projection of the magnetic field (which is assumed to be vertical) and the projection effect on the pixel area. The positive flux of the active region is computed by adding the contribution of all the pixels whose flux is larger than −30 G (before multiplying by the above factor). Similarly, the negative flux of the active region is computed by adding all the pixels with fluxes below +30 G. By including pixels with fluxes in the range [−30, +30] G (which represents the peak-to-peak noise) in the computations, we ensure efficient noise cancellation. The two polarities coincide nicely in magnitude and show a similar evolution. A linear decay phase is observed during the first three days. The flux decay rate is 9.3×10^{20} Mx day^{-1}, which is intermediate in the range of values mentioned above. We do not pursue in this work whether this could have contributed to the formation of the flux rope. Magnetic-field extrapolations of some form would be needed to conduct such a study, and this is beyond the scope of this paper. After 30% of the observed initial flux is lost, the flux curves show a plateau region where no more net losses or gains are seen. The 30% fractional decrease is, of course, a lower limit since we do not observe the onset of the decay phase. This plateau region was also encountered by Dalda & Martinez Pillet (2008); however, in their study, the amount of flux lost was found to be in the range of 50−70% of the initial value.

The sliding door phenomenon was seen to occur on July 3. This date sits in the linear decay phase of the AR. However, this phase was already taking place before, and no particular slope change is seen on July 3. The appearance of the orphan penumbrae structures happens on July 4 and 5, coinciding with the flat section of the flux curve. Clearly, these processes (sliding door and orphan-penumbrae generation) cause a minimal impact on the flux curves. One way to explain this result would require that the amount of *longitudinal* flux change involved in both processes were at, or below, the noise level of the data ($\pm 0.3 \times 10^{21}$ Mx).

2.3. TIP-II observations

The first set of spatial scans were taken on 2005 July 3, centered on the filament. Two maps with a FOV of $36'' \times 35''$, which was unfortunately not large enough to cover the whole active region (see Fig. 3), were acquired with TIP-II between 13:53 and 15:01 UT. The filament is seen all along the vertical direction. Slit-reconstructed maps at different wavelengths for one of the two data sets for this day are presented in the first column of Fig. 5. The frames in this figure are located at different positions to approximately represent the alignment of their respective FOVs. The *bottom lefthand* panel shows a tight filament spine, inferred from the strong He absorption, which extends along the vertical direction. There are no big pores, but only some small magnetic features (dark patches) seen among the granulation in the continuum image on the *top left* panel of the figure. The Si line core image (in the middle row) shows dark areas with larger absorption in regions of weak longitudinal field. This line weakens in faculae, as do most photospheric lines.

The second set of spectropolarimetric data was taken on July 5 between 7:36 and 14:51 UT, Cols. 2–4 in Fig. 5. Each scan took around 20 min to complete. The acquired maps were centered on a highly interesting area with very tight opposite polarities that corresponded, in continuum image, to pores and orphan penumbrae, all located along the PIL. Note that these maps overlap with the upper half of the former map from July 3 (see black boxes in Fig. 3 to get a better notion of the FOV). The He red core intensity images in the *bottom* row of Fig. 5 still show the spine of the filament in the lower part. Moreover, the filament in the upper part appears to be more diffused and extended. One can easily distinguish dark helium threads formed on July 5 especially in the *lower righthand* panel of Fig. 5. Many authors have observed the presence of threads in filaments and prominences before (e.g., Menzel & Wolbach 1960; Engvold 1976; Lin et al. 2005, 2008; Okamoto et al. 2007). It is generally believed that dark thin features in the chromosphere near ARs trace magnetic field lines. This idea is particularly interesting when applied to threads seen in AR filaments, since it could explain the presence of magnetic dips where plasma is trapped. Nevertheless, care must be taken, since a recent paper by de La Cruz Rodríguez & Socas-Navarro (2011) proves that chromospheric fibrils mostly, but not always, trace magnetic field lines. From our maps we see that the threads observed with TIP-II change only slightly in a time range of five to six hours. This becomes apparent when closely comparing the helium maps of Cols. 2 and 4 in Fig. 5. The most prominent He threads are located above pores or orphan penumbrae. A more detailed study of the magnetic configuration of these threads is presented below in Sect. 4.2.

Strong absorption in the Si line core is present below the spine of the filament on July 5 (see Fig. 5). It is remarkable that the axis of the filament seems to lay so low in the atmosphere that even the highest layers of the photospheric silicon absorption line (at the core of the line) trace it.

2.4. DOT observations

High-resolution ($0\farcs071$/px) Hα 6563 Å images from the Dutch Open Telescope (DOT; Rutten et al. 2004) for the morning of 2005 July 5 confirm the presence of the filament, which has an inverse S-like shape and a spine in its lower part. This is also confirmed by inspection of TRACE at 171 Å images. Such an inverse S-like shape is likely to be expected in the northern hemisphere (Pevtsov et al. 2001). The *lefthand* panel of Fig. 6 shows one image of the Hα data set taken by the DOT at 8:44 UT. The filament is surrounded by a bright plage. The image reveals small arch-like structures in the upper half of the filament that are almost perpendicular to its axis and then, in the spine, stretch along it towards its center. These archs can be identified as the Hα counterpart of the He threads mentioned before. A continuum image (with a 3 Å bandpass) is shown in the *righthand* panel of Fig. 6. This image is spatially aligned with the Hα panel on the *left* and has, superimposed on it in white, the Hα-contour of the filament. It is clear that the broader part of the filament lies on top of the orphan penumbrae, in between the pores, whereas the spine in the lower part is only surrounded by weaker magnetic features (small gray patches in the continuum image).

3. Spectral line inversion and data analysis

The average signal-to-noise ratio after binning the data is about 2000. Since the polarization signals of the Si 10 827 Å line are much stronger than those of the He triplet, it is not necessary to apply the same binning to the Si Stokes profiles and suffer the corresponding loss of spatial resolution. However,

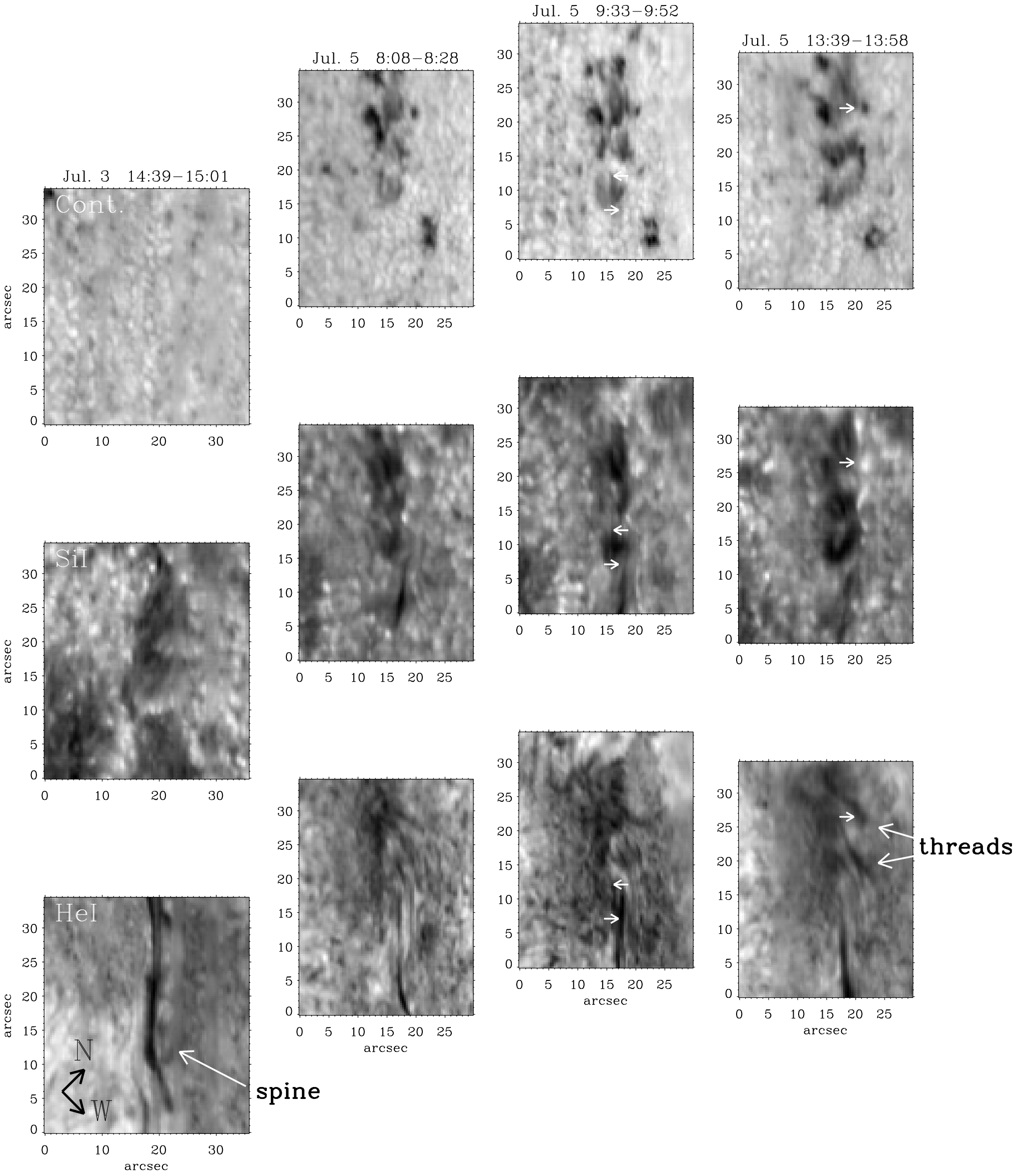

Fig. 5. From *left* to *right* slit-reconstructed images from the Tenerife Infrared Polarimeter (TIP-II) at different times. From *top* to *bottom* several wavelengths are presented that represent different layers in the atmosphere, from the photosphere to the chromosphere: continuum, Si 10 827 Å line center and He 10 830 Å red core intensities. The panels are located at different positions to approximately represent the alignment of their respective FOVs. The small white arrows indicate the position of the Stokes profiles presented in Figs. 7–9.

for a better comparison between them we use the same binning criterion for both, unless stated otherwise. Two different inversion codes were used to fit the observed Stokes profiles. Both use a nonlinear least-squares Levenberg-Marquard algorithm to minimize the differences between the observed and synthetic spectra. For the He 10 830 Å triplet a Milne–Eddington (ME) inversion code (MELANIE; Socas-Navarro 2001) that computes the Zeeman-induced Stokes spectra in the incomplete Paschen-Back (IPB) effect regime was used (see Socas-Navarro et al. 2004, for a detailed study of the effects of the IPB in the He multiplet). MELANIE does not take the atomic-level polarization due to anisotropic radiation pumping and its modification via the Hanle effect into account. Nevertheless, by comparing the output of three different techniques with different levels of physical complexity, Kuckein et al. (2009) show that the polarization signals in this AR filament are dominated by the Zeeman effect, a fact that was supported by the excellent performance of the MELANIE inversions. This code normally uses a set of eleven free parameters, which are modified to obtain the best fits to the observed Stokes profiles: magnetic field strength (B), inclination (γ), azimuth (ϕ), line strength (η_0), Doppler width ($\Delta\lambda_{\mathrm{D}}$), a damping parameter, LOS velocity (v_{LOS}), the source function at $\tau = 0$ and its gradient, macroturbulence factor and stray-light fraction ($\alpha = 1 - f$), where f is the filling factor – or fraction of the magnetic component that occupies the resolution element. MELANIE requires an initial guess for the

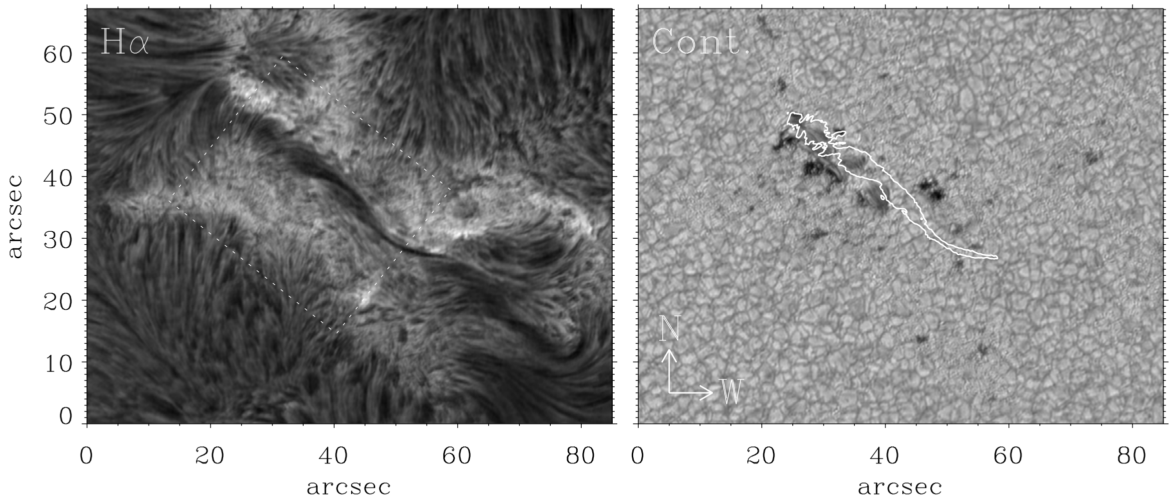

Fig. 6. Hα line core (*left*) and continuum (*right*) images from the Dutch Open Telescope taken on 2005 July 5th at 8:44 UT. The contour of the filament is superimposed upon the continuum image and shows that it partially lies on top of the orphan penumbrae, between the pores. In the *left* panel, the dashed white box indicates the approximate FOV of TIP-II for that day.

free parameters. For this purpose we carried out a magnetograph analysis and a Gaussian fit to Stokes I to obtain rough estimates for B, γ, ϕ, $\Delta\lambda_{\rm D}$ and $v_{\rm LOS}$ for each point along the slit.

For the thermodynamical parameters, several inversions of a few representative cases with random initial values, but within reasonable boundaries, were carried out. Averages of the retrieved parameters were calculated and used as initial guesses for the rest of the inversions.

Test inversions were carried out, where α was left as a free parameter, to control the fraction of a given nonmagnetic stray-light profile in the inversions. The results yielded almost no changes in the retrieved inclinations, azimuths, and LOS velocities. The inferred magnetic field strengths were greater than in the case without stray-light, but never by more than 100 G. Therefore, we finally decided to fix this parameter for the He ME inversions, setting the filling factor to 1 (i.e., $\alpha = 0$). The macroturbulence factor was also fixed to the calculated theoretical value of the spectral resolution of the data – a combination of slit, grating, and pixel resolution, which yielded 1.2 km s^{-1}. Thus, only nine free parameters were left in the MELANIE fit.

The photospheric Si 10 827 Å line was inverted using the SIR inversion code (Ruiz Cobo & del Toro Iniesta 1992) which is based on spectral line response functions (RFs) and assumes local thermodynamical equilibrium (LTE) and hydrostatic equilibrium to solve the radiative transfer equation. The advantage of using the SIR code is that a depth-dependent stratification of the physical parameters can be obtained as a function of the logarithm of the LOS continuum optical depth at 5000 Å ($\log\tau$).

We tested the effects on the inversions of using different initial model atmospheres (umbra, penumbra, and plage models), to asses their performance when reproducing the observed Stokes profiles. The penumbral model from del Toro Iniesta et al. (1994) seemed to yield the best results, which is consistent with what we see in the observations at the photosphere. However, some modifications to the model (such as assuming an initial constant magnetic field strength of 500 G and a LOS velocity of 0.1 km s^{-1}) had to be implemented.

Different initial values for the inclination and azimuth did not affect the final fit to the observed Stokes profiles. Macroturbulence was fixed to the same value as for the ME inversions. However, for the inversion of the Si line, the stray-light was initialized with 30% and left as a free parameter in the fit. Stray-light profiles for each map were computed by averaging the Stokes I of nonmagnetic areas, i.e., regions where Stokes Q, U, and V are negligible. The necessary atomic data for the Si 10 827 Å line were taken from the work of Borrero et al. (2003). In particular, the value of the logarithm of the oscillator strength times the multiplicity of the lower level that we used was $\log(gf) = 0.363$.

To have a rough idea of the formation height of silicon in order to associate an appropriate optical depth for the inferred vector magnetic field, response functions to magnetic field perturbations at various positions near or in the filament were calculated. Our atmospheric model covers heights from 1.2 up to −4.0 (in $\log\tau$ units). The highest sensitivity for both days was found to take place at $\log\tau = -2$. Thus, from this point onwards, all of the figures derived from the inversions of the Si line are referred to this height.

Figures 7–9 show the results of the MELANIE and SIR inversions of the Stokes parameters for three different positions along the filament: one in a helium dark thread, one in the spine, and one at the PIL. Each figure is made of eight plots: in the *top (bottom)* row we present the He 10 830 Å (Si 10 827 Å) observed Stokes I, Q, U, and V profiles obtained after performing the binning and the best fit achieved by the inversion code. The exact location of the selected fits is indicated by short white arrows in Figs. 5, 11, and 12 (see the captions of the figures for a detailed explanation). MELANIE does not provide the uncertainties in the retrieved atmospheric parameters. To estimate them, we used the synthetic Stokes profiles that resulted from the best fit of the model to the data. Then, several different realizations of the noise (with an amplitude of that of the noise in the observations) were added to the synthetic Stokes profiles, which were in turn inverted again. The standard deviation computed from the spread in the values of the retrieved parameters

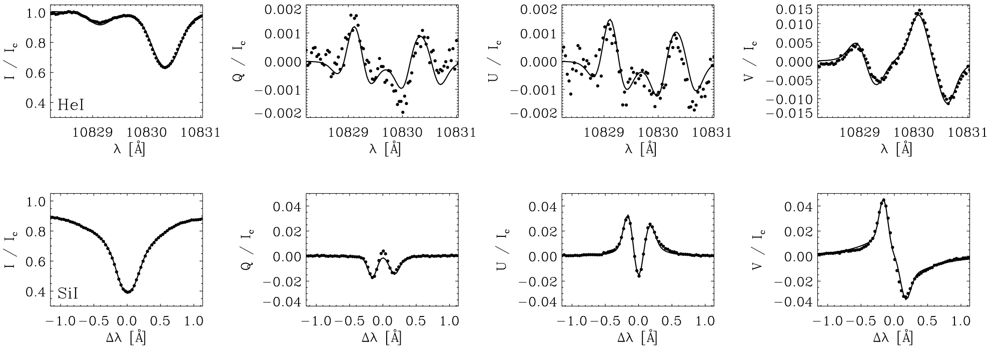

Fig. 7. Stokes profiles of the He 10 830 Å triplet (four *top* panels) and the Si 10 827 Å line (four *bottom* panels) at coordinates $x \sim 20''$ and $y \sim 26''.5$ in Fig. 5, on July 5, 13:39–13:58 UT column (see white arrows). The selected point is located inside the dark He threads. The dots represent the observed profiles which were binned in order to obtain a larger S/N. The solid line corresponds to the best fit achieved with a Milne-Eddington/LTE inversion code for the *upper/lower* panels. Stokes Q and U present the typical Zeeman-effect three-lobe signature. For helium the abscissa indicates the wavelength, while for silicon it shows the distance to the Si line core center in Angstrom units. The fit of the helium Stokes profiles provided the following magnetic parameters $B_{\rm He} = 592 \pm 31$ G, $\gamma_{\rm He} = 69.6° \pm 0.8°$, and $\phi_{\rm He} = 115.5° \pm 0.3°$, while the silicon inversion gave $B_{\rm Si} = 1185 \pm 22$ G, $\gamma_{\rm Si} = 71.7° \pm 1.1°$, and $\phi_{\rm Si} = 53.7° \pm 1.3°$. A filling factor of $f \sim 0.7$ was inferred from the SIR inversion.

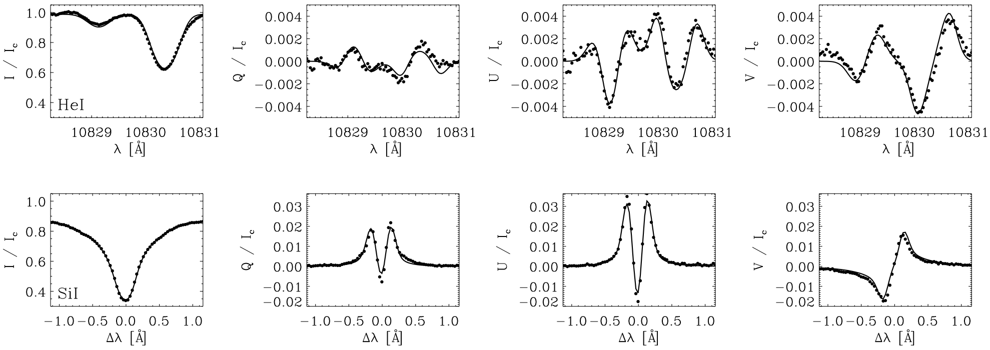

Fig. 8. Same as Fig. 7 but for coordinates $x \sim 17''$ and $y \sim 7''$ in Fig. 5, on July 5, 9:33–9:52 UT column (see white arrows pointing from *left* to *right*). These profiles belong to the spine of the filament. The magnetic field obtained from this particular fit for helium was $B_{\rm He} = 788 \pm 11$ G, $\gamma_{\rm He} = 95.0° \pm 0.2°$, and $\phi_{\rm He} = 54.3° \pm 1.1°$ and for silicon $B_{\rm Si} = 1058 \pm 26$ G, $\gamma_{\rm Si} = 99.5° \pm 0.8°$, and $\phi_{\rm Si} = 32.2° \pm 1.5°$ with a $f \sim 0.8$.

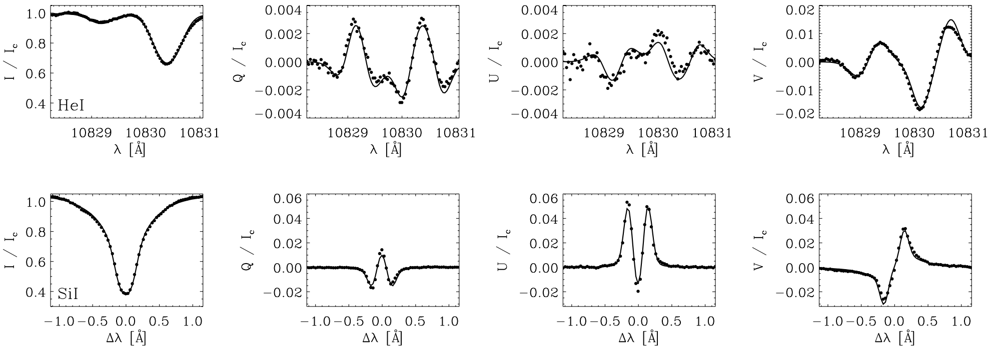

Fig. 9. Same as Fig. 7 but for coordinates $x \sim 16''$ and $y \sim 12''$, see white arrows in Fig. 5 (arrow pointing from *right* to *left*), 11, and 12, on July 5, 9:33–9:52 UT map. The Stokes profiles were observed at the polarity inversion line. The fitted parameters for the helium are $B_{\rm He} = 878 \pm 11$ G, $\gamma_{\rm He} = 109.8° \pm 0.3°$, and $\phi_{\rm He} = 76.2° \pm 1.8°$ and for the SIR case are $B_{\rm Si} = 806 \pm 21$ G, $\gamma_{\rm Si} = 99.9 \circ \pm 0.8°$, $\phi_{\rm Si} = 56.1° \pm 1.2°$, and a photospheric filling factor of $f \sim 0.8$.

provided the errors quoted in the captions of Figs. 7–9. The SIR inversions directly provide uncertainties that are proportional to the inverse of the response functions to changes in the physical parameters.

We found a very satisfactory performance of the ME inversion code when fitting the He Stokes profiles. This has already been described by Kuckein et al. (2009) who found in these data a ubiquitous presence of Zeeman-like signatures (see Stokes Q and U frames in Figs. 7–9) with no apparent contribution of atomic level polarization and its modification by the Hanle effect. The presence of strong Stokes Q and U profiles is indicative of strong transverse magnetic fields in the filament. In the photospheric Si 10 827 Å absorption line we also find strong Stokes Q and U profiles, which occasionally have larger amplitudes than the corresponding Stokes V. Consequently, a predominant horizontal field is found at photospheric heights, too.

3.1. NLTE Si I line formation

Prior to the inversions of the Si 10 827 Å line, we studied the possible impact of nonlocal thermodynamic equilibrium (NLTE) effects in the retrieved atmospheric parameters. SIR synthesizes the Stokes profiles under the assumption of local thermodynamic equilibrium. A recent study by Bard & Carlsson (2008) report that this line can be significantly affected by NLTE conditions. The authors show that the NLTE Si line core intensity is deeper than the analogous LTE result for two different model atmospheres: quiet sun (FALC model) and sunspot umbra models (SPOTM model). To study possible effects on our inversion results, we introduced the departure coefficients β (which are defined as the ratio between population densities in NLTE over LTE) from the above cited paper (kindly provided to us by Carlsson), into the SIR code. Inversions of a few selected cases were run with the β coefficients from these models (together with the LTE case), and the differences between the inferred magnetic field strength (B), inclination (γ), and azimuth (ϕ) were studied. No significant changes were found for γ and ϕ between the β and non-β inversions; however, the field strength presented some variations. Differences with an rms value of 100 G, in the spine, and of 150 G, in the diffuse filament region in the upper part of the maps, were found. We also studied the behavior of the LOS velocities taking the various options for the β coefficients into account. The rms changes found in the spine and in the orphan penumbrae were around 0.1 and 0.2 km s^{-1}, respectively.

These values are low, and similar to other errors arising from photon noise or systematics from the velocity calibration. NLTE effects of the Si 10 827 Å line are certainly non-negligible when estimating the temperature (T) stratification, which was found in our tests, but this has no impact on our purely magnetic study. In general, the temperatures above the range of $\log\tau = -0.5$ and -1.0 do depend drastically on the departure coefficients used and cannot be trusted unless a self-consistent NLTE inversion of the line is carried out. However, we emphasize that no major influence on the returned vector magnetic field and velocities was found when neglecting NLTE departure coefficients.

3.2. 180° ambiguity

Before transforming the vector magnetic field from the line-of-sight into the local solar frame of reference, we need to solve the well-known 180° ambiguity. Due to the angular dependence of Stokes Q and U with the azimuth, two configurations for the magnetic field, compatible with the measured Stokes profiles, are obtained, so the correct solution must be found by other means. Several methods for resolving the ambiguity in the azimuth can be found in the literature (Martin et al. 2008, and references therein). However, we were not able to apply them to our filament since the Hα high-resolution images clearly showed no barbs, and no sunspot was located immediately next to the filament to assure the continuity of the azimuth. Instead, we used the interactive IDL utility AZAM (Lites et al. 1995) to minimize the discontinuities between the two solutions of the azimuth on a pixel-by-pixel basis. Once we obtained the discontinuity-removed maps of the azimuth and the inclination in the local solar frame, we were left with two global solutions for each map, one of which needed to be rejected. In one of the two solutions the vector magnetic field pointed in the N-E direction (upward in Fig. 5), while in the other solution it pointed S-W (downward in the same figure). To select one or the other, we invoked the large-scale magnetic topology of the active region. Since our AR appeared during Solar Cycle 23 and was located in the northern hemisphere, the leader polarity must correspond to a magnetic field pointing outwards from the solar surface while the following polarity must contain a field that points inwards. In such a configuration, the toroidal field lines that created the AR necessarily had to point from W to E. If we now acknowledge that the leading polarity leans slightly towards the equator and the following polarity towards the pole (Joy's Law), this generates a poloidal component pointing N, which corresponds to a N-E orientation of the vector magnetic field in Fig. 5 (pointing upwards) as the most probable solution.

4. Results

4.1. Vector magnetic field analysis in and underneath the filament

Average horizontal and vertical magnetic fields in each pixel were calculated using the equations given by Landi Degl'Innocenti (1992):

$$B_{\rm vert} = f\,|\boldsymbol{B}|\,\cos\gamma, \tag{1}$$

$$B_{\rm hor} = \sqrt{f}\,|\boldsymbol{B}|\,\sin\gamma, \tag{2}$$

where f is the inferred filling factor, $|\boldsymbol{B}|$ the total field strength, and γ the inclination with respect to the local vertical. As mentioned in Sect. 3 we assumed $f = 1$ for Eqs. (1) and (2) in the case of the helium inversions. Since γ is the inclination in the local reference frame, vertical magnetic fields are radially oriented, whereas horizontal magnetic fields are parallel to the surface.

Figure 10 shows arrows denoting the horizontal magnetic field inferred from the He triplet (*upper* panel) and the Si line (*lower* panel) inversions after solving the 180° ambiguity for both days. Arrows are in black or white for a better distinction from the background. The gray-scale image in the *top* and *bottom* panels correspond, respectively, to a slit-reconstructed map of the He core intensity (for the red component) and a photospheric magnetogram (saturated at ±400 G). For July 3, the thin filament axis (or spine) lies mainly on top of the broad polarity inversion line, i.e., the gray area between opposite polarities. The photospheric vector magnetic field arrows in the *lower* panel depict an organized field with a predominantly inverse configuration at the PIL; i.e., the component of the transverse field perpendicular to the PIL tends to point from negative (black) to positive (white) polarity. Field vectors have, typically, a ~45° orientation clockwise with respect to the filament axis seen in the *upper*

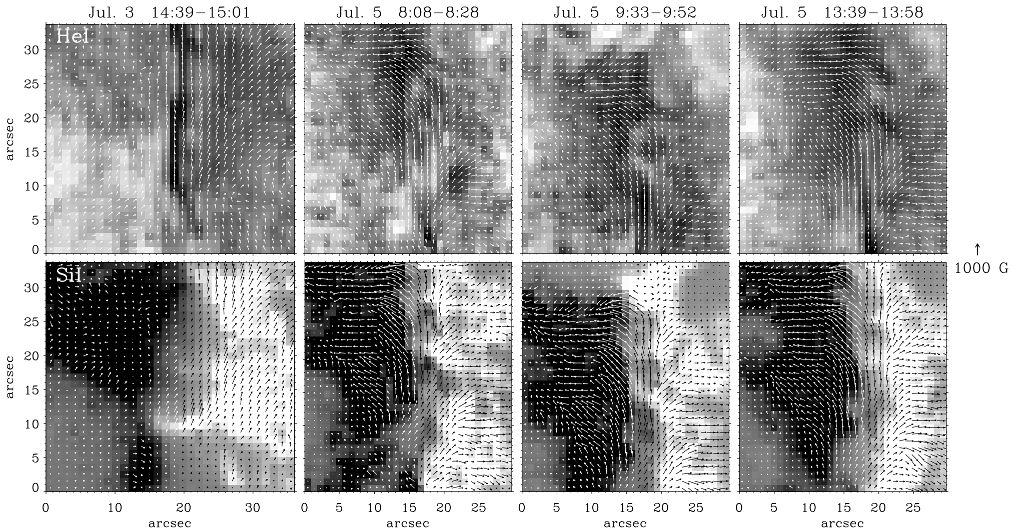

Fig. 10. *Top*: four gray-scale slit reconstructed images representing He red core intensity, increasing with time from left to right. Superimposed are white arrows indicating the horizontal magnetic fields observed with TIP-II in the He 10 830 Å multiplet after solving the 180° ambiguity. Especially in the *top right* panel the magnetic field lines are well aligned with the dark He threads. *Bottom*: background images show photospheric vertical fields $B^{\rm Si}_{\rm vert}$ observed with TIP-II in the Si 10 827 Å spectral line. The images are saturated at ±400 G to emphasize the PIL. The black and white arrows (depending on the background for a better contrast) represent the horizontal fields. The arrows are parallel to the polarity inversion line, which lies in the gray area between 15 and 20 arcsec on the x-axis and extends from the *lower* to the *upper* part of each panel.

panel. Also, the transverse magnetic fields are stronger (longer arrows) to the right (positive polarity) than to the left (negative polarity) of the PIL. The chromospheric horizontal magnetic field presented in the *upper* panel appears to be highly sheared (i.e., field lines are parallel to the PIL and to the filament axis), but also displays an inverse configuration that dominates the surroundings of the spine (main axis). It is important to emphasize here that the chromospheric fields in the filament axis or spine have a stronger shear than the photospheric ones, the latter showing a preference for an inverse configuration.

The last three columns of Fig. 10 present the vector magnetic field topology of the maps of July 5 using the same criterion as described above. The spine is also seen on this day at the bottom of the panels, but the top part is dominated by a more diffuse filament in the chromosphere and by pores and orphan penumbrae in the photosphere. In all helium images (*upper* panels), the longest arrows, i.e., larger horizontal field component, are found in the filament between 10″ and 22″ on the x-axis. This also happens at photospheric layers. This readily shows that the filament area harbors the strongest horizontal fields in the region at both heights. Changes in the vector magnetic fields through the day are almost insignificant in a five to six hour time scale. Interestingly, the field lines are aligned with the dark helium threads (top panels). This can be easily seen in the last column of Fig. 10.

The inferred chromospheric field is clearly aligned with the spine (sheared configuration) in the lower part of the images and has a slightly inverse orientation close to it. This is the same behavior as observed on July 3. The photospheric fields show a predominance of the inverse configuration over the whole spine region, which again coincides with what had been observed two days earlier. In the *upper* part of the He intensity images, above the spine, the chromospheric horizontal fields smoothly change orientation, displaying a normal configuration. This shift in orientation is complete in the top part of the figures, where the fields perpendicular to the PIL point straight from positive to negative polarity. The *bottom* panels of Fig. 10 for this day show that the photospheric horizontal fields are more aligned with the PIL, with a more sheared configuration than their chromospheric counterparts.

Thus, the filament seems to be divided in two substructures: (1) a chromospheric spine with field lines parallel to its axis and an inverse polarity configuration in the photosphere below it and (2) extensive dark helium patches or threads that show a normal polarity configuration above and, sheared field lines running along the PIL underneath, in the photosphere.

4.2. Helium threads

We performed a more detailed study of the chromospheric He threads, which appear in the *top righthand* panel of Fig. 10. The centers of two long threads are located around $[x, y] = [20'', 28'']$ and $[20'', 20'']$, hereafter thread1 (TH1) and thread2 (TH2), respectively. They extend from just above the PIL to far into the positive polarity region. According to the orientation of the field lines, which are aligned with the threads, a normal polarity configuration pointing from positive to negative is present, and therefore it is natural to consider them as simple arches anchored in one polarity and reaching over the other. We suggest that these threads act like footpoints of the filament.

The following inferred magnetic properties are consistent with this interpretation. Along thread1, between $x \in [18'', 22'']$, we found that the inclination changed from a more horizontal configuration, $\gamma_{\rm TH1} \sim 66°$, near the PIL to a more vertical one, $\gamma_{\rm TH1} \sim 35°$ farther away from it, in the positive polarity plage region. An inclination of $\gamma = 90°$ means that the field lines are parallel to the solar surface. Along with this, the horizontal fields decreased from $B^{\rm He}_{\rm hor} \sim 570$ to 360 G, whereas the total field strength remained almost constant along the structure; i.e., the vertical component of the field $B^{\rm He}_{\rm vert}$ increased. The same

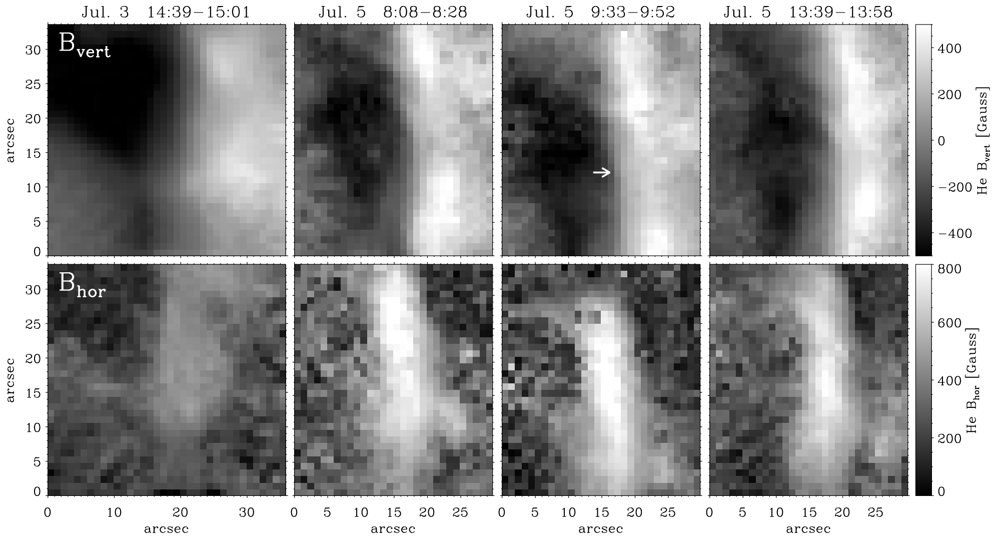

Fig. 11. The gray-scale images indicate the two components of the magnetic field strength inferred from the ME inversions of the He 10 830 Å triplet. The *upper*/*lower* four panels show the vertical ($B_{\rm vert}$)/horizontal ($B_{\rm hor}$) fields in the local frame of reference. All images in the same row have the same intensity scale. Vertical and horizontal fields are saturated at ±500 G and 800 G, respectively. Both polarities are close together and the PIL is only a few arcseconds wide in all panels. The white arrow indicates the location of the Stokes profiles shown in Fig. 9.

happened in thread2, between $x \in [19'', 22'']$: inclinations became more vertical away from the PIL, going from $\gamma_{\rm TH2} \sim 68°$ to 38°, while the horizontal fields decreased from $B^{\rm He}_{\rm hor} \sim 620$ to 360 G. These findings suggest that these threads magnetically link the chromosphere and the photosphere. The Si data also show that the fields are more vertical near the ending points of both threads. As a consequence, the threads could constitute a channel for plasma to flow down along them. Mass flows from the filament into the photosphere through these channels will be studied in the second paper of this series.

4.3. Vertical and horizontal magnetic field components

The changes in the vertical ($B_{\rm vert}$) and horizontal ($B_{\rm hor}$) magnetic fields at both heights and for both days are displayed in Figs. 11 and 12. Several properties are worth mentioning.

1. A comparison between Figs. 11 and 12 shows that the horizontal fields at the spine of the filament are stronger in the chromosphere than in the photosphere underneath. This is consistent throughout both days, along the spine on July 3 and outside the pores and orphan penumbrae (the lower half of the maps) on July 5. On average, $B^{\rm He}_{\rm hor} > B^{\rm Si}_{\rm hor}$ by ~100 G.
2. Figure 11 shows that the spine in the chromosphere has a weaker horizontal magnetic field ($B^{\rm He}_{\rm hor} \sim$ 400–500 Gauss) than the region above the orphan penumbrae observed on July 5, which reaches horizontal field strengths as high as 800 G (the region studied in detail by Kuckein et al. 2009).
3. The aforementioned chromospheric strong fields of July 5 are clearly related to the presence of pores and orphan penumbrae in the photosphere. The corresponding photospheric horizontal fields are the strongest there, too (see Fig. 5 for the exact location of the pores and orphan penumbrae). The observed $B^{\rm Si}_{\rm hor}$ in these areas is in the range of 1000–1100 G.
4. Vertical fields seem to be very similar at both heights. However, $B^{\rm He}_{\rm vert}$ appears to be weaker and have a more homogeneous distribution than $B^{\rm Si}_{\rm vert}$.

It is of interest to see the spatially widening and narrowing between opposite polarities. On July 3 there is a big gap (gray area of around 6″ wide) between positive and negative polarities in the $B^{\rm Si}_{\rm vert}$ image. Interestingly, the absence of vertical fields is better seen at photospheric heights (see *top left* panel of Fig. 12) rather than in the chromosphere. The same widening can also be seen in the MDI LOS magnetograms (see Fig. 3; starting at the second row from the *top*). Two days later, on July 5, the opposite polarities have moved closer together, forming an extremely compact active region PIL. Although only the upper half map of July 3 overlaps with the lower half of July 5, the gap is undoubtedly smaller on the second day.

4.4. Azimuth changes between the photosphere and the chromosphere

Figure 13 analyzes the differences between the azimuths inferred from the He ($\phi_{\rm He}$) and Si ($\phi_{\rm Si}$) inversions after solving the 180° ambiguity. Although only two data sets are presented, all of the other maps show very similar results. Figures 13a, b compare the photospheric and chromospheric horizontal fields for the two days. The white contours in the panels delimit the regions with predominantly horizontal magnetic fields. The adopted selection criterion defined "horizontal fields" as those having an inclination with respect to the local frame of reference in the range of $75° < \gamma_{\rm He} < 105°$. Azimuth differences[2], $\phi_{\rm He} - \phi_{\rm Si}$, in between the white contours are presented in the histograms of Figs. 13c, e, revealing that:

1. on July 3 (i.e., observing mostly the spine region) both photospheric and chromospheric fields seem to follow each

---

[2] Azimuths are always positive and measured counterclockwise.

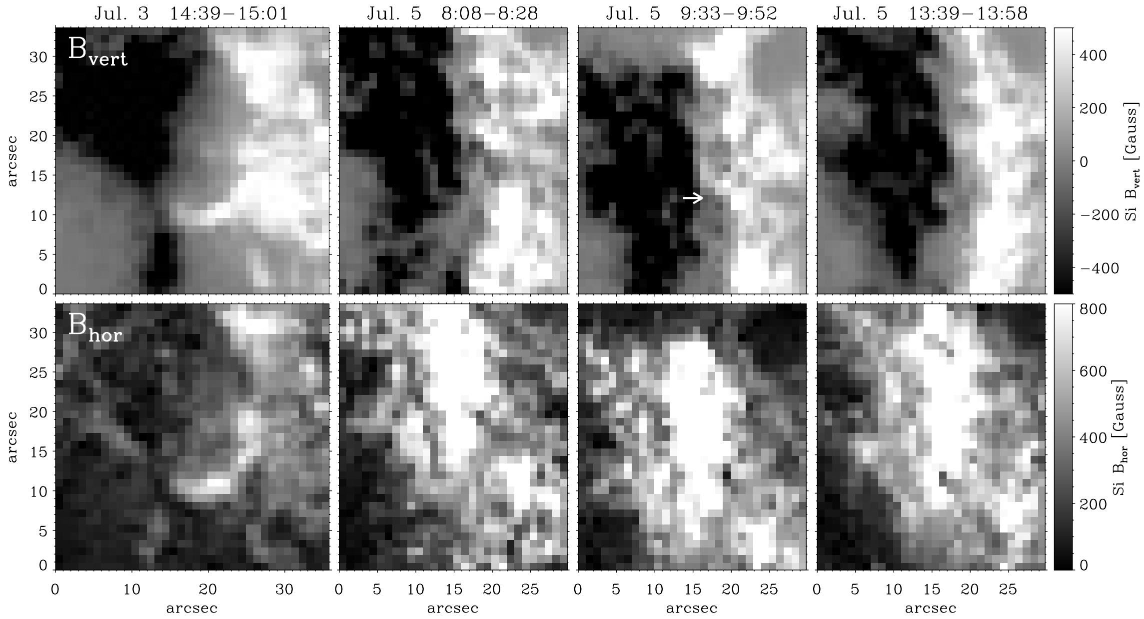

Fig. 12. Same as Fig. 11 but for the SIR inversions of the Si 10 827 Å line. On July 5, the horizontal fields are concentrated at the pores (better seen when compared to Fig. 5) and reach top values of up to 1100 G. Black (negative) and white (positive) polarities of the *top* panels are close together, indicating a very compact AR.

other, differing by only 5°–10°, with the He arrows more aligned with the filament axis (see Fig. 13d);

2. on July 5, on the other hand, it was the photospheric field that was more aligned with the PIL, and the azimuths showed a larger discrepancy, of 10°–20° on average;
3. the $\phi_{\rm He}$ angles are systematically larger than the $\phi_{\rm Si}$.

To understand why the azimuth of the chromospheric vector field always pointed in a slightly counterclockwise direction with respect to the photospheric one, we provide the inset of Fig. 13d.

On July 3, the chromospheric magnetic field was aligned with the spine, while the photospheric one displayed an inverse configuration, hence with smaller azimuth angles (angles are measured from the x-axis and increase counterclockwise). We interpret this as indicating that the field lines were wrapped around the filament axis. On July 5, the situation was reversed: the filament axis was delineated by the photospheric field lines, while the chromospheric ones showed a normal polarity configuration, thus mapping a higher part of the structure than two days earlier. Again the chromospheric azimuth angles were larger than the photospheric ones.

5. Discussion

This paper is an extensive study of the vector magnetic field at two different heights in a filament that lies on top of the polarity inversion line of an active region. This study is mostly based on TIP-II data in the 10 830 Å spectral region, but it also uses other multiwavelength data sources. Helium intensity core images clearly show the presence of a thin filament spine, which we identify with the filament axis, on top of the PIL on both days. Our observations reveal that this spine is dominated by strong homogeneous horizontal fields, typically in the range of 400−500 G in the chromosphere and 100 G smaller in the photosphere underneath. Vertical gradients of the field strength with stronger fields in the upper layers have already been observed (e.g., in polar crown prominences as shown by Leroy et al. 1983) and modeled in the past (Aulanier & Démoulin 2003) and been ascribed to the presence of dips (Anzer 1969; Demoulin & Priest 1989). The vector magnetic field in the filament spine at chromospheric heights is highly sheared (i.e., parallel to the PIL), while the photospheric vector field below the spine shows a uniformly inverse polarity. Such a configuration naturally suggests a flux rope topology. This scenario is also favored by the TRACE at 171 Å, which showed the filament with an inverse-S shape structure. Such a shape is thought to indicate the existence of an underlying flux rope (Gibson et al. 2002). This configuration of the spine, with inverse orientation in the photosphere and sheared field lines in the chromosphere, shows no significant change in the observed two-day interval. Evidence of the filament back on July 1 was presented in the BBSO Hα images (see Fig. 1). This readily shows that the process that created the filament occurred well before our observations. We tentatively identify this previously existing filament with the spine region in our observations, and remark on the fact that it showed almost no evolution during our observing campaign.

However, the PIL region was not inactive in this time lapse from the 3 to the 5 of July. MDI line-of-sight magnetograms show a widening (on July 3) and a narrowing (on July 5) of the opposite polarities of the AR. The photospheric longitudinal magnetic field obtained with TIP-II on July 3 also indicates a wide separation of both polarities compared to the more compact PILs observed on July 5. On this day, the FOV included not only the spine region, but also the newly appeared orphan penumbrae and pores. This region has a magnetic topology that is *fundamentally* different from that of the spine discussed before. The upper panels in Fig. 10 show chromospheric field lines with a normal polarity configuration (above $y \sim 15''$). The horizontal fields

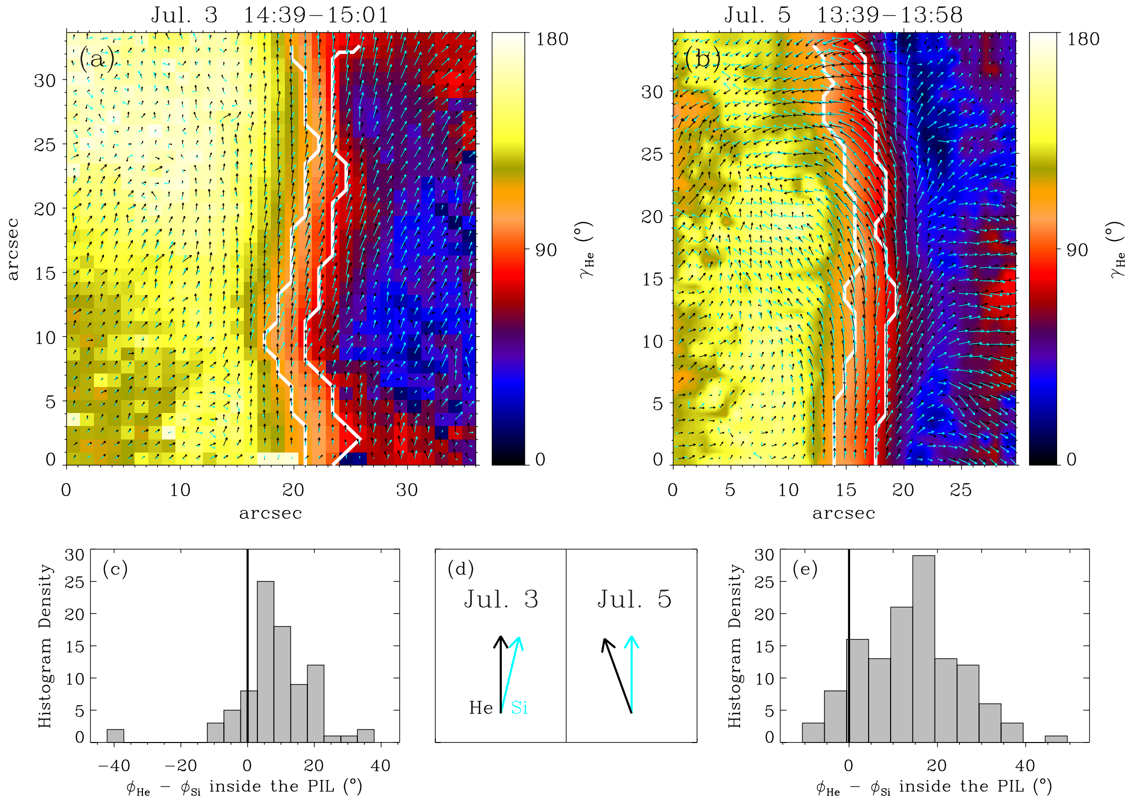

Fig. 13. **a**, **b)** Background color image shows the inclination angle $\gamma_{\rm He}$ inferred from the He inversions. Superimposed black (blue) arrows indicate the helium (silicon) horizontal fields in the local frame of reference. The white contour along the y-axis encloses horizontal fields according to the criterion of inclinations between 75° $< \gamma_{\rm He} <$ 105°. **c**, **e)** Histogram densities of the inferred azimuth differences between helium and silicon, $\phi_{\rm He} - \phi_{\rm Si}$, only for the arrows that are enclosed within the white contour in the **a)** and **b)** panels. **d)** Most common azimuth configurations between helium and silicon above $y \sim 8$ and $y \sim 12$, for July 3 and 5 respectively.

there are stronger than in the spine, reaching up to 800 G (see Kuckein et al. 2009). This normal polarity configuration suggests there are field lines that directly connect opposite polarities. On the other hand and most noticeably, in the lower panels of Fig. 10, *the photospheric field lines always point along the PIL, with a clear sheared configuration*. The strengths of these PIL-aligned fields are high, in the range of 1000–1100 G. Now, the shear is seen in the photosphere, below the chromospheric arching field lines in a normal configuration. If a flux rope above the photosphere were found in the spine region, a similar flux rope would need to be sitting underneath it, at photospheric heights. A simple potential arcade model can be excluded here since *no sheared field lines are expected in the photosphere* for such a configuration. In the scenario that we suggest, the helium Stokes profiles would be mapping the top arching field lines with a normal configuration, while the axis of the rope, with sheared fields, would be located in the denser photosphere. The field strength of the structure is high enough to generate pore-like darkenings and penumbral alignments. Moreover, as these structures become visible following the widening and closing of the PIL region, we are tempted to suggest that what we are witnessing is the emergence to the surface of a flux rope structure. Unfortunately, the limited amount of observations at our disposal and the prevailing seeing conditions prevent a study of the evolution similar to the one by Okamoto et al. (2008, 2009). However, the simultaneous observations in the chromosphere and the photosphere that we present in this paper indicate that a similar process might be at work.

There is another subtle indication that a lower lying flux rope exists in this part of the FOV observed on July 5. As stated before, the spine region displays the same configuration on both days, in agreement with a flux rope located at chromospheric heights. However, there is one difference between the Si absorption images on both days (see Fig. 5). While on July 3 the spine is not seen in the silicon core images, it does become obvious in those from July 5, suggesting that, in this case, the axis of the filament sits at lower heights. It is as if the proximity of the orphan penumbrae and pore region (interpreted here as a flux rope in the photosphere), forces the axis of the main filament to move to lower layers.

Recently, MacTaggart & Hood (2010) have studied the "sliding doors" effect through 3D magnetohydrodynamic (MHD) simulations. They report that this effect develops out of the emergence and expansion at the photosphere of a flux rope. In their simulations, the main axis of the flux bundle emerges, thanks to the magnetic buoyancy instability, to heights just slightly above the photosphere. For this area of the observed map (i.e., excluding the spine), we tentatively propose a scenario where an emerged flux rope is trapped (or slowly evolving) in the photosphere, as reported in the simulations of MacTaggart & Hood (2010). In this scenario, the observed pores and orphan penumbrae are the white-light counterparts of a flux rope trapped in the photosphere that is indeed part of the filament. To our knowledge, *this is the first observational evidence of a trapped flux rope in the photosphere*. Along with the works of Okamoto et al. (2008, 2009) and Lites et al. (2010), this work is the third example of observations of a "sliding door" and flux rope emergence scenario inside an AR filament, with almost the same time scale (~1 day).

One could argue that such an emergence process must leave a fingerprint on a flux history curve of the active region (as proposed recently by Vargas Domínguez et al. 2011). No such indication is seen in Fig. 4, neither when it emerged in the sliding door phase (on July 3), nor on July 4–5 when, at some point, the trapped flux rope emerged and generated the observed pores and orphan penumbrae system. However, it is important to point out that all these processes mainly involve *transverse* fields to which the longitudinal magnetograms from SOHO/MDI are blind. As long as the longitudinal flux involved in any of these events stays below the flux noise level in Fig. 4 (0.3×10^{21} Mx), it will remain undetectable. This can be accomplished by flux ropes that are not highly twisted (with a dominant axial flux over a poloidal component). For example, the case shown by Vargas Domínguez et al. (2011) involves a flux increase of 0.1×10^{21} Mx, which would be buried in the noise of our flux curves.

The filament formation model by van Ballegooijen & Martens (1989) and the model of active region evolution by van Ballegooijen & Mackay (2007) form, through successive reconnections above the photosphere, a twisted flux rope with a strong shear at the axis. The reconnection gives rise to two types of field lines: sheared field lines that form the axis of the helical rope and normally oriented loops below them (see Figs. 1 and 5 in van Ballegooijen & Martens 1989; van Ballegooijen & Mackay 2007, respectively). In these models, the photosphere acts as barrier to the submergence of sheared fields, which must stay in the corona once created by reconnection. However, the loops with a normal configuration must submerge below the photosphere and cross this layer at some point. This submergence is driven by tension forces pointing down and the involved spatial scales are small (900 km, see Fig. 1 in van Ballegooijen & Martens 1989). While these scales were not easily accessible to quantitative vector magnetograms in the past, the data presented in this paper achieve the needed resolution and can be used to search for evidence of these reconnected field lines. We did not find such a normally oriented component in our photospheric vector magnetic field maps. This is true not only for the inversions done with binned data, but also for the inversions done of the Si line with the original resolution (1″). Only inverse orientation (in the spine region) or sheared field lines (in the orphan penumbral region) have been detected at photospheric heights. In this sense, our observations fail to support the generation of these normal polarity submerging magnetic field lines. Another prediction of the aforementioned models is that velocity measurements must clearly show downflows in the photosphere close to the PIL, where the field lines submerge. Therefore, Doppler measurements are definitely needed to verify whether downflows or upflows of some kind are present at the base of the filaments. This will be described in Paper II of this series.

The scenario proposed in various recent works (see, e.g., Archontis & Török 2008; Mackay et al. 2010, for a review), where the original flux rope remains confined to photospheric heights and a secondary flux rope is produced after reconnection of the emerged top part of the original one, could well apply to our results. The spine region would correspond to the secondary flux rope in the chromosphere, while the orphan penumbral region would belong to the parent flux rope that stays deeper down in the denser layers. What remains unexplained by this model is the further disappearance by July 6 of the pores and orphan penumbrae observed in the SOHO/MDI continuum image (Fig. 2).

6. Conclusions

The main conclusions of the present work follow.

1. The "sliding doors" effect described by Okamoto et al. (2008) was seen in our observations during the period between July 3 and July 5. This was identified in SOHO/MDI data and in the TIP-II Si magnetograms for those days.
2. The observed AR filament can be separated into two areas. The first was observed on July 3 and shows the filament axis, or spine, in the helium-absorption images. The He data show the magnetic field (with horizontal field strengths of 400–500 G) aligned with the filament, indicating a strong sheared configuration. This region is also observed in the FOV of July 5, when portions of the spine are even seen in the silicon line core images. This would indicate that the part of the spine observed this day lies in lower layers than the portion observed two days earlier.
3. The photospheric fields for this area of the filament show an inverse configuration of the magnetic field lines that we interpret to be the bottom of a flux rope structure. Similarly, we interpret the spine seen in helium as the signature of the flux rope axis.
4. The second area corresponds to the orphan penumbrae that appear during the sliding door timeframe, and it clearly shows a different magnetic configuration. Helium observations exhibit a normal polarity configuration, whereas the silicon data show a strongly sheared region with very intense horizontal fields. This magnetic topology was interpreted as a scenario in which the chromospheric magnetic fields trace the top part of the flux rope, while the spine – or flux rope axis – is still lying in the photosphere.
5. The observed orphan penumbrae region is thus the photospheric counterpart of this active region filament. Since the spine was also seen in the silicon line, we emphasized that active region filaments can have a clear photospheric signature. In particular, it would be interesting to find out if all orphan penumbral regions observed inside active regions are related to their filaments.
6. The whole emergence process of these orphan penumbrae does not leave a clear imprint in the flux history of the active region. This was interpreted as due to the flux system being mostly transverse, with a low enough twist to not generate identifiable signals in SOHO/MDI longitudinal magnetograms.
7. We did not observe flux loops with a normal polarity configuration in the photosphere, as suggested by some filament generation models based on footpoint motions and reconnection (see van Ballegooijen & Martens 1989; van Ballegooijen & Mackay 2007). While the preexisting filament observed on July 1 in the BBSO data could have been created in the way described in these works, the configuration and the evolution described here for the period from July 3 to July 5 suggests otherwise.

The current study was limited, not only by the small FOV of TIP-II, which nowadays has a slit that is twice as long as during our observing campaign in 2005, but also by the observational gap on July 4. Magnetic field extrapolations could undoubtedly shed more light on the magnetic structure of this filament. It is now crucial to carry out more multiwavelength measurements, like the one presented in here, but with higher cadence and bigger FOVs to fit the pieces of the puzzle together, in order to fully understand the origin, evolution, and magnetic topology of AR filaments. In particular, continuous vector magnetograms of active regions, together with simultaneous imaging of the corona, should be able to prove/disprove the proposed scenario for the last stages of their evolution. The instrument suite onboard the NASA/SDO satellite is the best candidate for such a study.

Acknowledgements. We thank an anonymous referee for greatly enhancing both the scientific content of the paper and its clarity. This work has been partially funded by the Spanish Ministerio de Educación y Ciencia, through Project No. AYA2009-14105-C06-03. Financial support by the European Commission through the SOLAIRE Network (MTRN-CT-2006-035484) and help received by C. Kuckein during his stay at HAO/NCAR are gratefully acknowledged. The work was based on observations made with the VTT operated on the island of Tenerife by the KIS in the Spanish Observatorio del Teide of the Instituto de Astrofísica de Canarias. The authors thank L. Yelles Chaouche, F. Moreno-Insertis, and G. Aulanier for helpful discussions. We also thank B. Lites for extensive comments on the manuscript. The Dutch Open Telescope is operated by Utrecht University at the Spanish Observatorio del Roque de los Muchachos of the Instituto de Astrofísica de Canarias. SOHO is a project of international cooperation between ESA and NASA. The National Center for Atmospheric Research (NCAR) is sponsored by the National Science Foundation (NSF). SOLIS data used here are produced cooperatively by NSF/NSO and NASA/LWS. Data from the Big Bear Solar Observatory, New Jersey Institute of Technology, are gratefully acknowledged.

References

Antiochos, S. K., Dahlburg, R. B., & Klimchuk, J. A. 1994, ApJ, 420, L41
Anzer, U. 1969, Sol. Phys., 8, 37
Archontis, V., & Török, T. 2008, A&A, 492, L35
Archontis, V., Moreno-Insertis, F., Galsgaard, K., Hood, A., & O'Shea, E. 2004, A&A, 426, 1047
Aulanier, G., & Demoulin, P. 1998, A&A, 329, 1125
Aulanier, G., & Démoulin, P. 2003, A&A, 402, 769
Aulanier, G., DeVore, C. R., & Antiochos, S. K. 2002, ApJ, 567, L97
Avrett, E. H., Fontenla, J. M., & Loeser, R. 1994, in Infrared Solar Physics, ed. D. M. Rabin, J. T. Jefferies, & C. Lindsey, IAU Symp., 154, 35
Babcock, H. W., & Babcock, H. D. 1955, ApJ, 121, 349
Bard, S., & Carlsson, M. 2008, ApJ, 682, 1376
Bommier, V., Landi Degl'Innocenti, E., Leroy, J., & Sahal-Brechot, S. 1994, Sol. Phys., 154, 231
Borrero, J. M., Bellot Rubio, L. R., Barklem, P. S., & del Toro Iniesta, J. C. 2003, A&A, 404, 749
Canou, A., & Amari, T. 2010, ApJ, 715, 1566
Casini, R., López Ariste, A., Tomczyk, S., & Lites, B. W. 2003, ApJ, 598, L67
Casini, R., López Ariste, A., Paletou, F., & Léger, L. 2009, ApJ, 703, 114
Collados, M. 1999, in Third Advances in Solar Physics Euroconference: Magnetic Fields and Oscillations, ed. B. Schmieder, A. Hofmann, & J. Staude, ASP Conf. Ser., 184, 3
Collados, M., Lagg, A., Díaz Garcí A, J. J., et al. 2007, in The Physics of Chromospheric Plasmas, ed. P. Heinzel, I. Dorotovič, & R. J. Rutten, ASP Conf. Ser., 368, 611
Collados, M. V. 2003, in SPIE Conf. Ser., ed. S. Fineschi, 4843, 55
Dalda, A. S., & Martinez Pillet, V. M. 2008, in Subsurface and Atmospheric Influences on Solar Activity, ed. R. Howe, R. W. Komm, K. S. Balasubramaniam, & G. J. D. Petrie, ASP Conf. Ser., 383, 115
de La Cruz Rodríguez, J., & Socas-Navarro, H. 2011, A&A, 527, L8
del Toro Iniesta, J. C., Tarbell, T. D., & Ruiz Cobo, B. 1994, ApJ, 436, 400
Demoulin, P., & Priest, E. R. 1989, A&A, 214, 360
DeVore, C. R., & Antiochos, S. K. 2000, ApJ, 539, 954
Engvold, O. 1976, Sol. Phys., 49, 283
Fan, Y. 2001, ApJ, 554, L111
Fan, Y. 2009, ApJ, 697, 1529
Gibson, S. E., Fletcher, L., Del Zanna, G., et al. 2002, ApJ, 574, 1021
Green, L. M., Kliem, B., & Wallace, A. J. 2011, A&A, 526, A2
Guo, Y., Schmieder, B., Démoulin, P., et al. 2010, ApJ, 714, 343
Hindman, B. W., Haber, D. A., & Toomre, J. 2006, ApJ, 653, 725
Jing, J., Yuan, Y., Wiegelmann, T., et al. 2010, ApJ, 719, L56
Karpen, J. T. 2007, in New Solar Physics with Solar-B Mission, ed. K. Shibata, S. Nagata, & T. Sakurai, ASP Conf. Ser., 369, 525
Kippenhahn, R., & Schlüter, A. 1957, ZAp, 43, 36
Kuckein, C., Centeno, R., Martínez Pillet, V., et al. 2009, A&A, 501, 1113
Kuperus, M., & Raadu, M. A. 1974, A&A, 31, 189
Kurokawa, H. 1987, Sol. Phys., 113, 259
Landi Degl'Innocenti, E. 1992, Magnetic field measurements, ed. F. Sanchez, M. Collados, M. & Vazquez, 71
Leka, K. D., Canfield, R. C., McClymont, A. N., & van Driel-Gesztelyi, L. 1996, ApJ, 462, 547
Leroy, J. L., Bommier, V., & Sahal-Brechot, S. 1983, Sol. Phys., 83, 135
Leroy, J. L., Bommier, V., & Sahal-Brechot, S. 1984, A&A, 131, 33
Lin, H., Penn, M. J., & Kuhn, J. R. 1998, ApJ, 493, 978
Lin, Y., Engvold, O., Rouppe van der Voort, L., Wiik, J. E., & Berger, T. E. 2005, Sol. Phys., 226, 239
Lin, Y., Martin, S. F., & Engvold, O. 2008, in Subsurface and Atmospheric Influences on Solar Activity, ed. R. Howe, R. W. Komm, K. S. Balasubramaniam, & G. J. D. Petrie, ASP Conf. Ser., 383, 235
Lites, B. W. 2005, ApJ, 622, 1275
Lites, B. W., Low, B. C., Martinez Pillet, V., et al. 1995, ApJ, 446, 877
Lites, B. W., Kubo, M., Berger, T., et al. 2010, ApJ, 718, 474
López Ariste, A., Aulanier, G., Schmieder, B., & Sainz Dalda, A. 2006, A&A, 456, 725
Low, B. C. 1994, Phys. Plasmas, 1, 1684
Low, B. C., & Hundhausen, J. R. 1995, ApJ, 443, 818
Mackay, D. H., Karpen, J. T., Ballester, J. L., Schmieder, B., & Aulanier, G. 2010, Space Sci. Rev., 151, 333
MacTaggart, D., & Hood, A. W. 2010, ApJ, 716, L219
Magara, T. 2004, ApJ, 605, 480
Martens, P. C., & Zwaan, C. 2001, ApJ, 558, 872
Martin, S. F., Lin, Y., & Engvold, O. 2008, Sol. Phys., 250, 31
Martínez-Sykora, J., Hansteen, V., & Carlsson, M. 2008, ApJ, 679, 871
Menzel, D. H., & Wolbach, J. G. 1960, AJ, 65, 54
Merenda, L., Trujillo Bueno, J., Landi Degl'Innocenti, E., & Collados, M. 2006, ApJ, 642, 554
Merenda, L., Trujillo Bueno, J., & Collados, M. 2007, in The Physics of Chromospheric Plasmas, ed. P. Heinzel, I. Dorotovič, & R. J. Rutten, ASP Conf. Ser., 368, 347
Okamoto, T. J., Tsuneta, S., Berger, T. E., et al. 2007, Science, 318, 1577
Okamoto, T. J., Tsuneta, S., Lites, B. W., et al. 2008, ApJ, 673, L215
Okamoto, T. J., Tsuneta, S., Lites, B. W., et al. 2009, ApJ, 697, 913
Pevtsov, A. A., Canfield, R. C., & Latushko, S. M. 2001, ApJ, 549, L261
Pneuman, G. W. 1983, Sol. Phys., 88, 219
Ruiz Cobo, B., & del Toro Iniesta, J. C. 1992, ApJ, 398, 375
Rutten, R. J., Hammerschlag, R. H., Bettonvil, F. C. M., Sütterlin, P., & de Wijn, A. G. 2004, A&A, 413, 1183
Sasso, C., Lagg, A., & Solanki, S. K. 2011, A&A, 526, A42
Scherrer, P. H., Bogart, R. S., Bush, R. I., et al. 1995, Sol. Phys., 162, 129
Socas-Navarro, H. 2001, in Advanced Solar Polarimetry – Theory, Observation, and Instrumentation, ed. M. Sigwarth, ASP Conf. Ser., 236, 487
Socas-Navarro, H., Trujillo Bueno, J., & Landi Degl'Innocenti, E. 2004, ApJ, 612, 1175
Sterling, A. C., Chifor, C., Mason, H. E., Moore, R. L., & Young, P. R. 2010, A&A, 521, A49
Tandberg-Hanssen, E. 1995, The nature of solar prominences, Astrophys. Space Sci. Lib., 199
Trujillo Bueno, J., Landi Degl'Innocenti, E., Collados, M., Merenda, L., & Manso Sainz, R. 2002, Nature, 415, 403
van Ballegooijen, A. A. 2008, in Subsurface and Atmospheric Influences on Solar Activity, ed. R. Howe, R. W. Komm, K. S. Balasubramaniam, & G. J. D. Petrie, ASP Conf. Ser., 383, 191
van Ballegooijen, A. A., & Mackay, D. H. 2007, ApJ, 659, 1713
van Ballegooijen, A. A., & Martens, P. C. H. 1989, ApJ, 343, 971
Vargas Domínguez, S., MacTaggart, D., Green, L., van Driel-Gesztelyi, L., & Hood, A. W. 2011, Sol. Phys., 178
von der Lühe, O., Soltau, D., Berkefeld, T., & Schelenz, T. 2003, in SPIE Conf. 4853, ed. S. L. Keil, & S. V. Avakyan, 187
Welsch, B. T., DeVore, C. R., & Antiochos, S. K. 2005, ApJ, 634, 1395
Yelles Chaouche, L., Cheung, M. C. M., Solanki, S. K., Schüssler, M., & Lagg, A. 2009, A&A, 507, L53
Zirin, H., & Wang, H. 1991, Adv. Space Res., 11, 225

4

The 3D structure of an active region filament as extrapolated from photospheric and chromospheric observations

In order to confirm the proposed magnetic structure of the AR filament presented in Chapter 3, non-linear force-free field extrapolations were carried. The inferred vector magnetograms of the previous chapter were used as boundary conditions for these extrapolations.

The article presented in this chapter was published with the title "The three-dimensional structure of an active region filament as extrapolated from photospheric and chromospheric observations", in The Astrophysical Journal, volume 748, issue 1, 23, pages 1–12, year 2012.

Abstract: The three-dimensional structure of an active region filament is studied using nonlinear force-free field extrapolations based on simultaneous observations at a photospheric and a chromospheric height. To that end, we used the Si i 10827 Å line and the He i 10830 Å triplet obtained with the Tenerife Infrared Polarimeter at the Vacuum Tower Telescope (Tenerife). The two extrapolations have been carried out independently from each other and their respective spatial domains overlap in a considerable height range. This opens up new possibilities for diagnostics in addition to the usual ones obtained through a single extrapolation from, typically, a photospheric layer. Among those possibilities, this method allows the determination of an average formation height of the He i 10830 Å signal of ≈ 2 Mm above the surface of the Sun. It allows, as well, a cross-check of the obtained three-dimensional magnetic structures to verify a possible deviation from the force-free condition, especially at the photosphere. The extrapolations yield a filament formed by a twisted flux rope whose axis is located at about 1.4 Mm above the solar surface. The twisted field lines make slightly more than one turn along the filament within our field of view, which results in 0.055 turns Mm^{-1}. The convex part of the field lines (as seen from the solar surface) constitutes dips where the plasma can naturally be supported. The obtained three-dimensional magnetic structure of the filament depends on the choice of the observed horizontal magnetic field as determined from the 180° solution of the azimuth. We derive

a method to check for the correctness of the selected 180° ambiguity solution.

The Astrophysical Journal, 748:23 (12pp), 2012 March 20 doi:10.1088/0004-637X/748/1/23

THE THREE-DIMENSIONAL STRUCTURE OF AN ACTIVE REGION FILAMENT AS EXTRAPOLATED FROM PHOTOSPHERIC AND CHROMOSPHERIC OBSERVATIONS

L. Yelles Chaouche[1,2], C. Kuckein[1,2], V. Martínez Pillet[1,2], and F. Moreno-Insertis[1,2]
[1] Instituto de Astrofisica de Canarias, Via Lactea, s/n, 38205 La Laguna (Tenerife), Spain
[2] Department of Astrophysics, Universidad de La Laguna, 38206 La Laguna (Tenerife), Spain

Received 2011 November 25; accepted 2012 January 4; published 2012 March 1

ABSTRACT

The three-dimensional structure of an active region filament is studied using nonlinear force-free field extrapolations based on simultaneous observations at a photospheric and a chromospheric height. To that end, we used the Si I 10827 Å line and the He I 10830 Å triplet obtained with the Tenerife Infrared Polarimeter at the Vacuum Tower Telescope (Tenerife). The two extrapolations have been carried out independently from each other and their respective spatial domains overlap in a considerable height range. This opens up new possibilities for diagnostics in addition to the usual ones obtained through a single extrapolation from, typically, a photospheric layer. Among those possibilities, this method allows the determination of an average formation height of the He I 10830 Å signal of ≈2 Mm above the surface of the Sun. It allows, as well, a cross-check of the obtained three-dimensional magnetic structures to verify a possible deviation from the force-free condition, especially at the photosphere. The extrapolations yield a filament formed by a twisted flux rope whose axis is located at about 1.4 Mm above the solar surface. The twisted field lines make slightly more than one turn along the filament within our field of view, which results in 0.055 turns Mm^{-1}. The convex part of the field lines (as seen from the solar surface) constitutes dips where the plasma can naturally be supported. The obtained three-dimensional magnetic structure of the filament depends on the choice of the observed horizontal magnetic field as determined from the 180° solution of the azimuth. We derive a method to check for the correctness of the selected 180° ambiguity solution.

Key words: Sun: activity – Sun: filaments, prominences – Sun: magnetic topology

Online-only material: color figures

1. INTRODUCTION

Active region (AR) filaments are observed above polarity inversion lines (PILs) where the vertical component of the magnetic field changes sign, separating the two opposite polarities (Babcock & Babcock 1955). They are called filaments when observed on the solar disk and prominences when observed above the solar limb, although the two terms refer to the same phenomenon (see Demoulin 1998; Mackay et al. 2010, for a review on filaments and prominences). Filaments/prominences are formed by plasma that has been lifted up above the solar surface and is cooler and denser than its surroundings. The necessary force to sustain this plasma is of magnetic origin. Here we shall focus on AR filaments, which are characterized by a strong horizontal component of the magnetic field along the filament axis reaching several hundred gauss (Kuckein et al. 2009, 2012; Guo et al. 2010; Canou & Amari 2010; Jing et al. 2010). These filaments typically lie low above the solar surface (Lites 2005) compared with quiescent filaments.

There are two classes of models that aim to describe the magnetic structure of filaments: the sheared magnetic arcade model and the twisted flux rope (TFR) model. The former involves photospheric motions of magnetic footpoints near the PIL produced by various mechanisms such as photospheric flows, vortical motions, or the emergence of the upper part of a flux rope (Antiochos et al. 1994; DeVore & Antiochos 2000; Aulanier et al. 2002; Welsch et al. 2005; DeVore et al. 2005). The flows force the magnetic field to get reconfigured creating a variety of field configurations, as dipped field lines (Mackay et al. 2010).

The TFR model assumes that the filament is formed by a dipped flux rope where the material can naturally be located and lifted up (van Ballegooijen & Martens 1989; Leka et al. 1996; Titov & Démoulin 1999; Amari et al. 1999; Lites 2005; Lites et al. 2010). Flux emergence of a TFR to the solar atmosphere has also been numerically modeled (Magara & Longcope 2003; Fan & Gibson 2004; Archontis et al. 2004; Amari et al. 2004, 2005; Galsgaard et al. 2005; Cheung et al. 2007; Martínez-Sykora et al. 2008; Tortosa-Andreu & Moreno-Insertis 2009; Fan 2009; MacTaggart & Hood 2010). From observations, Okamoto et al. (2008, 2009) have shown that the change in the horizontal field from normal to inverse configuration can be interpreted as the signature of an emerging flux rope. This has been shown as well in three-dimensional MHD simulations of an emerging flux rope, where the spectropolarimetric signal exhibits similar changes of the horizontal field from normal to inverse (Yelles Chaouche et al. 2009a) using the same pair of Iron lines Fe I 6301 Å and Fe I 6302 Å as the ones of *Hinode* SP/SOT.

The numerical models aiming to simulate the properties of filaments assume a certain number of conditions, such as, e.g.; the mere pre-existence of a flux rope in the convection zone or in the atmosphere, the amount of twist necessary for a given flux rope to emerge into the atmosphere, its morphology and emergence velocity, etc. These assumptions and conditions can hardly be directly tested using observed magnetograms only, and it turns out to be very helpful to use extrapolations in order to get information on the observed three-dimensional magnetic field and its properties. This gives feedback to numerical models and allows them to be fine tuned.

In recent years, extrapolations have played an important role in probing AR filament properties (Guo et al. 2010; Canou & Amari 2010; Jing et al. 2010). This is due to (a) the progress in mathematical and computing techniques of

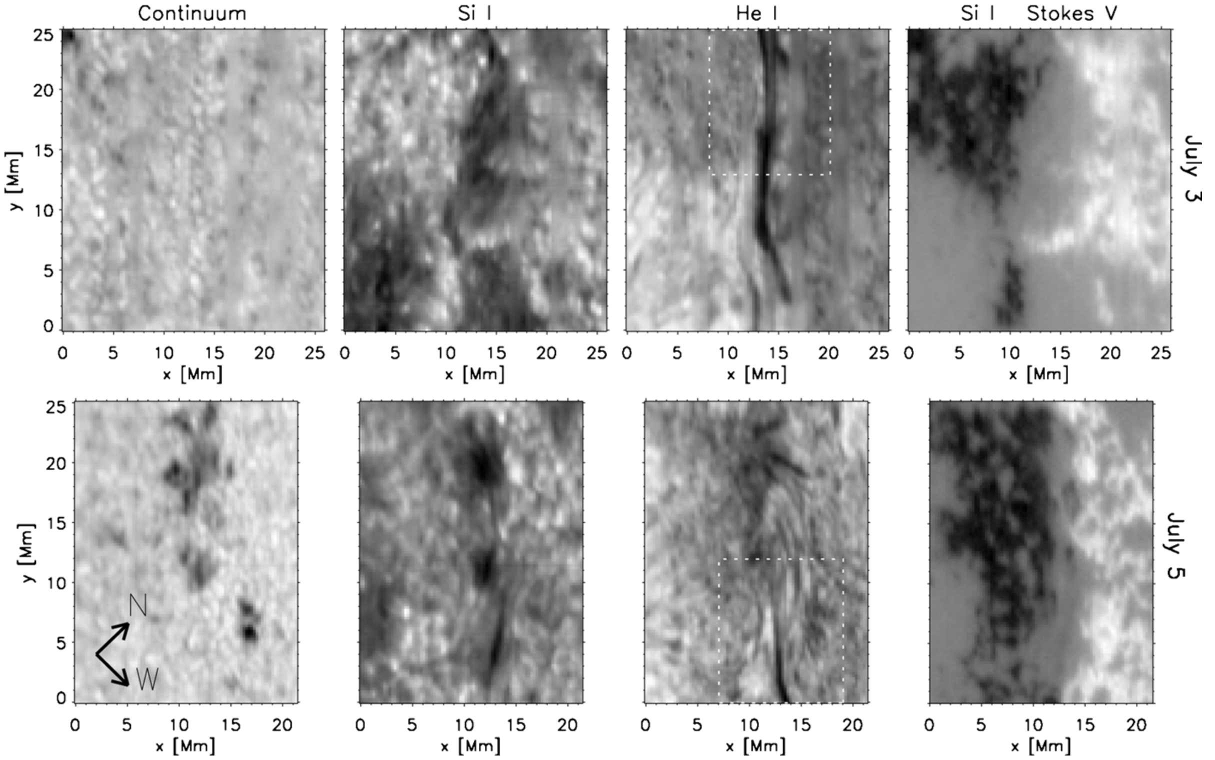

Figure 1. Two snapshots: the upper row (3rd of July); The lower row (5th of July). From left to right: continuum intensity, Si i 10827 Å line core, He i 10830 Å red core, and Stokes-*V* at −150 mÅ from Si i 10827 Å line center. As an example, the location of the spine (i.e., the filament's axis) can be seen in the upper He i panel as an elongated darkening along the *y*-axis. This can also be seen in the lower He i and Si i panels. The dashed-line rectangles indicate the approximate overlap of the filament between the two snapshots.

extrapolations (e.g., Amari et al. 1997; Wiegelmann 2004; Wiegelmann et al. 2006; Schrijver et al. 2006; Aly & Amari 2007; Metcalf et al. 2008) and (b) to the large improvement in spectropolarimetric facilities which allows the measurement of the full Stokes vector with ever higher sensitivity and resolution (e.g., SP/SOT on board *Hinode*, TIP at the VTT, THEMIS/MTR, etc.; see, e.g., López Ariste et al. 2006; Okamoto et al. 2008; Kuckein et al. 2009; Lites et al. 2010; and the review by Mackay et al. 2010 for further references.)

In the past, extrapolations of AR filaments have exclusively been computed using photospheric fields as boundary values. Knowing that the photospheric plasma is not completely force free, it is important to compare these extrapolations with ones of the same region but using chromospheric magnetic field as boundary values for the extrapolations. The plasma β in the chromosphere is usually much smaller than in the photosphere, so that the magnetic field in the former must be closer to force-free than in the latter. Simultaneous observations of the magnetic field vector at the photosphere and chromosphere (Kuckein et al. 2012; Sasso et al. 2011) offer the possibility of such a study. Based on the observations in Kuckein et al. (2012; see also Kuckein et al. 2009, 2010), we will perform extrapolations starting from the photosphere and, independently, from the chromosphere. This allows to cross check the extrapolation results and test whether the latter have been affected by, e.g., the finite plasma β and the preprocessing procedure.

We will focus here on two representative times (one for each day of observation). Then for each of them we have two snapshots: one at the photosphere using the Si i 10827 Å line and one at the chromosphere using the He i 10830 Å triplet. The time evolution of the filament over the entire observation period can be further retrieved from the paper by Kuckein et al. (2012).

2. OBSERVATIONS AND DATA ANALYSIS

In this paper, we study a filament located along the PIL of AR NOAA 10781, which was found to be in its slow decay phase when the observations were performed. The full Stokes spectropolarimetric data were acquired with the Tenerife Infrared Polarimeter (TIP-II; Collados et al. 2007) at the German Vacuum Tower Telescope (VTT, Tenerife, Spain) on 2005 July 3 and 5, at coordinates N16-E8 and N16W18, respectively. Several scans were taken with the slit ($0\farcs5$ wide and $35''$) parallel to the filament obtaining maps with a field of view (FOV) of ∼26 × 25 Mm and ∼22 × 25 Mm, for July 3 and July 5, respectively. It is important to note that the FOV was not centered on the same location on both days. However, the upper half of the map from July 3 overlaps with the lower half of the map from July 5. The observed spectral range comprises the photospheric Si i 10827 Å line and the chromospheric He i 10830 Å triplet, which allows us to simultaneously study both heights and their magnetic coupling. The reader is referred to the papers of Kuckein et al. (2009, 2012) for an extensive description of the data and the magnetic evolution of this AR filament.

Figure 1 shows slit-reconstructed maps of the two selected data sets. From left to right different wavelengths are presented: continuum, Silicon line core intensity, helium red core intensity, and Silicon Stokes-V magnetogram (at -150 mÅ from line center). The upper map was taken on 2005 July 3, between 14:39 and 15:01 and clearly shows the filament in the He I absorption panel (third panel starting from top left). The filament extends along the vertical axis and lies on top of the PIL, as shown in the upper Stokes-V panel. The lower map was observed on 2005 July 5, between 8:42 and 9:01. The spine or filament axis is still seen in the lower half of the He I panel, but above, a more diffuse filament is located on top of the pores and orphan penumbrae which have newly formed.

Two different inversion codes were used to fit the Stokes profiles. A binning in the spectral and spatial domain was applied to increase the signal-to-noise ratio. Hence, the final spectral sampling is $\sim$33.1 mÅ pixel^{-1} and the average pixel size is $\sim 1''$. For the helium 10830 Å triplet we used a Milne-Eddington inversion code (MELANIE; Socas-Navarro 2001), which computes the Zeeman-induced stokes spectra in the incomplete Paschen–Back regime (Socas-Navarro et al. 2004). In the case of the Silicon 10827 Å line we used the SIR code (Stokes Inversion based on Response functions; Ruiz Cobo & del Toro Iniesta 1992). Kuckein et al. (2012) showed that the non-local thermodynamical equilibrium (NLTE) effects of the Si I 10827 Å line reported by Bard & Carlsson (2008) do not significantly affect the inferred vector magnetic field from the SIR inversion code and therefore were not taken into account. We transformed the vector magnetic field from the line of sight (LOS) into the local solar reference frame. The 180° ambiguity was solved using the AZAM code (Lites et al. 1995). Response functions to magnetic field perturbations for the inferred atmospheres were computed at different positions inside and around the filament. An average optical depth of $\log \tau \sim -2$ for the formation height of Silicon has been obtained for both days.

3. FORCE-FREE FIELD EXTRAPOLATION

Using the photospheric or chromospheric magnetic field as boundary values, it is possible to calculate the three-dimensional magnetic field vector in the atmosphere using force-free field (FFF) extrapolations. The force-free (or zero-Lorentz force) assumption is equivalent to assuming that the electrical current $\mathbf{j}$ and the magnetic field $\mathbf{B}$ are parallel, or, using Ampère's law and cgs units:

$$\nabla \times \mathbf{B} = \frac{4\pi}{c}\mathbf{j} = \alpha\,\mathbf{B}, \tag{1}$$

where α in Equation (1) is the so-called force-free parameter and measures the level of twist of the field lines. Given that $\mathbf{B}$ is solenoidal, α must be constant along each field line. We use here nonlinear force-free extrapolations, where α is constant along each given field line but can change from one field line to another. The extrapolations are carried out using the optimization method (Wiegelmann 2004).

The observed magnetic field is not necessarily force free. This is especially the case in the photosphere where the plasma β is not small (with β the ratio of gas to magnetic pressures). For instance, $\beta \approx 1$ in the lower part of the photosphere (Yelles Chaouche et al. 2009b, from calculations using three-dimensional MHD simulations).

Schrijver et al. (2006, 2008), Metcalf et al. (2008), and De Rosa et al. (2009) have implemented a variety of tests to compute the coronal magnetic field using several nonlinear force-free field (NLFFF) extrapolation codes. The different codes were tested using analytical, numerical, and observational models. Among other conclusions, these papers have addressed the issue that the NLFFF extrapolations are sensitive to the boundary conditions (usually, photospheric vector magnetograms). These might suffer from uncertainties due to low signal-to-noise conditions, inaccuracies in the resolution of the 180° ambiguity, or more importantly from non-force-free conditions of the photospheric plasma.

In order to make the observed magnetic field maps more consistent with the force-free assumption and greatly enhance the correctness of the force-free extrapolations, it is necessary to apply some preprocessing (Wiegelmann et al. 2006; Metcalf et al. 2008). This consists of minimizing the magnetic force and torque (Aly 1989), minimizing the difference between the observed magnetic field and the preprocessed one, and applying a smoothing operator to remove the small-scale variations of the magnetic field. The preprocessing routine used here is the one developed by Wiegelmann et al. (2006). It is useful to quantify the change produced on the magnetograms by the preprocessing procedure. For that we use the usual vector correlation (Schrijver et al. 2006) between the observed vector magnetic field and the preprocessed one. It is found that for the case of the Si I 10827 Å vector magnetogram, the correlation between the original and preprocessed field is approximately 0.84. In the case of the He I 10830 Å vector magnetogram, the correlation is about 0.90 between the observed and preprocessed magnetic field. This indicates that the observed He I 10830 Å magnetic field is closer to a force-free condition than the Si I 10827 Å case.

The observed vector magnetograms have a relatively small field of view and are not isolated from the rest of the AR. This might introduce some errors in the NLFFF extrapolated model. Some authors proceed in enlarging the field of view by embedding the observed vector magnetograms in MDI maps; nevertheless this might introduce inconsistencies because the MDI magnetograms contain only the LOS component of the magnetic field, and therefore would inconsistently connect magnetic field lines throughout the NLFFF model. It is therefore safer to just use the existing vector magnetograms (after preprocessing) as lower boundary for the NLFFF extrapolations. A further test of the effect of reduced field of view on the extrapolation results is carried out in Section 4.6.

The extrapolation starts with potential lateral and top boundaries, whereas the bottom one is the preprocessed observed vector magnetogram. A description of the code can be found in Wiegelmann (2004), Schrijver et al. (2006), and Metcalf et al. (2008). The NLFFF extrapolated model is expected to be more correct in the lower central part of the computational domain (Schrijver et al. 2006).

The extrapolations are computed in a box of $33 \times 38 \times 38$ grid points in the x, y, and z directions, respectively. x and y being the horizontal directions perpendicular and parallel to the filament's axis, respectively. This yields a distance of $\approx$650 km between grid points. The same distance between grid points is used in the vertical direction.

4. RESULTS

4.1. Extrapolations Starting from the Photosphere

The vertical component of the magnetic field ($B_z^{\mathrm{Si,O}}$) inverted from the photospheric Si I 10827 Å data is plotted in Figure 2 using a color scale. The lower case "z" in $B_z^{\mathrm{Si,O}}$ refers to the vertical component of the magnetic field, while the upper case "O" and "Si" refer to the field obtained from Observations

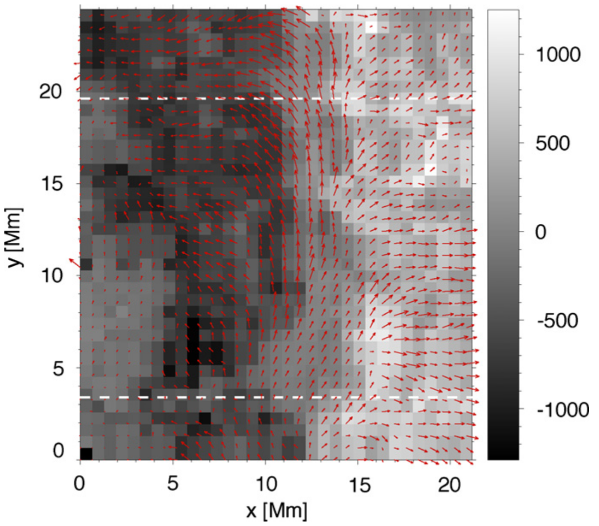

Figure 2. Background: vertical component of the magnetic field on July 5 at the photosphere ($B_z^{\mathrm{Si,O}}$). The arrows represent the horizontal component of the magnetic field. The field strength is proportional to the length of the arrows.

(A color version of this figure is available in the online journal.)

using the Si I 10827 Å line. The arrows in Figure 2 indicate the direction of the horizontal magnetic field. The length of the arrows is proportional to the horizontal field strength. In the vicinity of the PIL, some arrows point from the negative polarity to the positive one, which is called inverse configuration. A *normal configuration* is obtained when the field arrows point from the positive to the negative polarity. The inverse configuration in the PIL region suggests that the filament above is formed by a TFR.

The extrapolated magnetic field is plotted in the top panel of Figure 3 using UCAR's Vapor three-dimensional visualization package (www.vapor.ucar.edu). This three-dimensional view shows a sample of magnetic field lines in the filament region in order to outline its structure. The background map represents the vertical component of the magnetic field ($B_z^{\mathrm{Si,E}}$) at the bottom of the extrapolated cube. The upper case "E" and "Si" refer to the field obtained by extrapolations using the Si I 10827 Å line vector magnetograms as lower boundary condition. In the background map of the top panel of Figure 3, purple and blue colors correspond to $B_z^{\mathrm{Si,E}} > 0$; green and red are reserved for $B_z^{\mathrm{Si,E}} < 0$. The magnetic field forming the filament is distributed as a flux rope with dips in the lower half of the figure (i.e., with field line stretches which are convex as seen from the solar surface). This goes in the same direction as the findings of Guo et al. (2010), Canou & Amari (2010), and Jing et al. (2010).

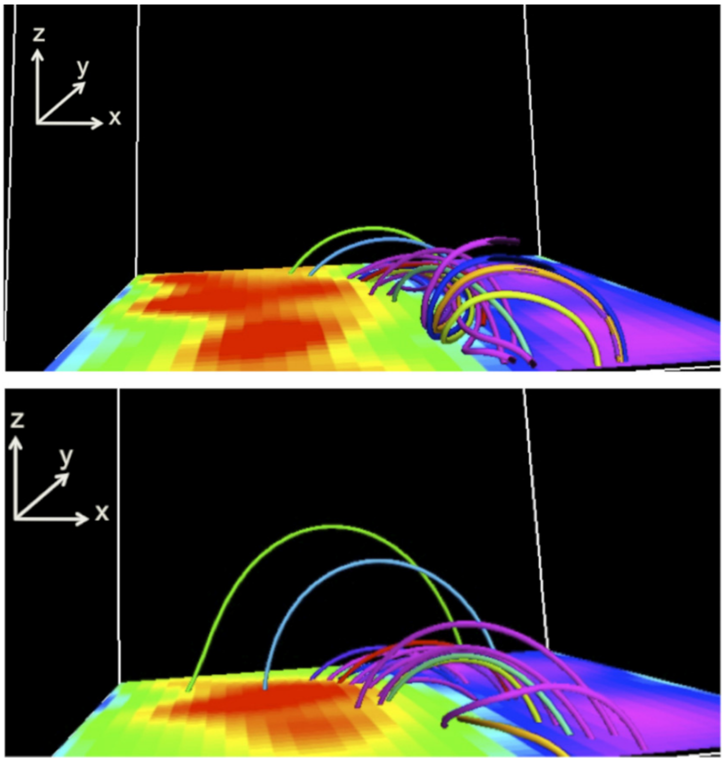

Figure 3. Top: three-dimensional view of the magnetic field of the filament on July 5. The extrapolation results are computed using the observed photospheric magnetic field as lower boundary condition. Top background image: vertical component of the magnetic field at the bottom of the extrapolation cube. Purple and blue: $B_z^{\mathrm{Si,E}} > 0$; green and red: $B_z^{\mathrm{Si,E}} < 0$ Bottom: Extrapolation results using the chromospheric magnetic field on July 5 as lower boundary condition. Bottom background image: the vertical component of the magnetic field at the bottom of the extrapolation cube $B_z^{\mathrm{He,E}}$ (same color scale as the top panel). The field lines are plotted in the filament region. The field lines that cross the lateral sides of the box are cut 2 pixels away from the boundaries to avoid plotting the part that might be affected by the lateral boundaries.

(A color version of this figure is available in the online journal.)

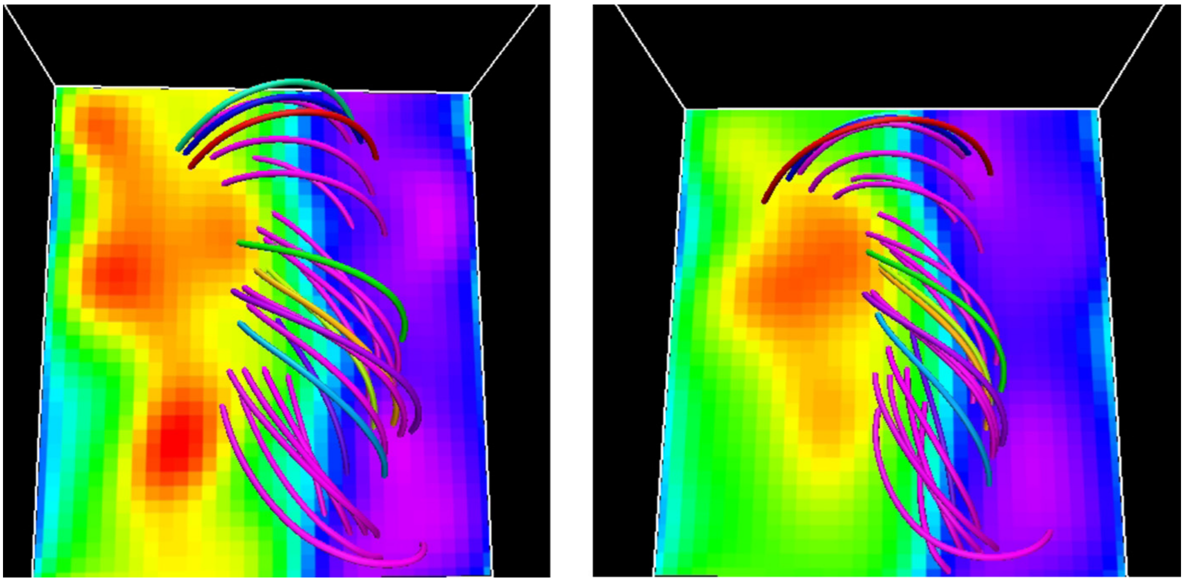

Figure 4. Left panel: field lines from the photospheric extrapolation. They are drawn above a minimum height of ≈1.6 Mm above the photosphere (to make them comparable with the chromospheric magnetic field). Right panel: magnetic field lines from the chromospheric extrapolations. They are drawn directly from the bottom of the corresponding extrapolation box (already at chromospheric height). The two sets of field lines start inside a 2 Mm deep box placed along the filament. Field lines are allowed to end outside of the starting box, but are cut if they go below it. The background images are as described in Figure 3, and the data are from July 5.

(A color version of this figure is available in the online journal.)

Bard & Carlsson (2008) have studied the properties of the Si I 10827 Å line in NLTE conditions. They have determined using empirical models that the average formation height of Si I 10827 Å is about 320 km for a sunspot umbra and about 541 km in the quiet sun. In the case of the observed filament, we expect the average height of formation to be between these two boundary values.

At this height of formation the photospheric plasma does not have small values of the plasma β. Nevertheless, there are theoretical and observational indications (Wiegelmann et al. 2010; Martínez González et al. 2010) that force-free extrapolations lead to a good retrieval of the actual magnetic field at higher atmospheric layers.

4.2. Extrapolations Starting from the Chromosphere

We have seen in the previous section that the extrapolation studies have been conducted exclusively using photospheric spectral lines. Here we would like to present an extrapolation using the helium triplet He I 10830 Å as lower boundary for the extrapolations. Chromospheric lines as H_α and He I 10830 Å have been used to identify filaments but never as boundary condition for extrapolations.

The bottom panel of Figure 3 shows a three-dimensional display of a sample of field lines at the filament region. In this case the field lines harbor some shear in the lower half of the image but with no twist. Field lines have a normal configuration (from positive to negative), except at the very central part of the filament (shown by the yellow field line) where the field lines are almost parallel to the filament axis. The bottom panel of Figure 3 suggests that the magnetic flux rope forming the filament (lower panel of Figure 3) is located below the height of formation of the He I 10830 Å triplet. We will come back to this point in detail in the next sections.

4.3. Height of Coincidence Between the Photospheric and Chromospheric Magnetic Fields

A natural question to ask when analyzing the extrapolations starting from the photosphere and the chromosphere is: do the magnetic fields from the two extrapolations agree with each other? In order to answer this question, we first plot the field lines that result from the two three-dimensional extrapolation boxes (Figure 4). The field lines start inside a 2 Mm deep box that extends along most of the filament. The field lines can develop outside of the box but will be cut if they go below it. This configuration allows selecting field lines above a suitable height in order to make it possible to compare field lines starting from the photosphere with those starting from the chromosphere.

Therefore, the field lines in the left panel of Figure 4 are all above an imaginary boundary situated at ≈1.6 Mm above the bottom of the extrapolation cube. We have tried various heights and found that ≈1.6 Mm gives a good agreement between the field lines from the photospheric extrapolations (left panel) and the ones from the chromospheric extrapolations (right panel of Figure 4), which are drawn directly from the lower chromospheric boundary. A visual inspection of both panels suggests a good agreement between the morphology of the magnetic field obtained from photospheric and chromospheric extrapolations.

To provide a quantitative comparison between the two sets of extrapolations, we compute the magnetic field strength in the photospheric extrapolation cube and look for the height where this field strength matches the observed chromospheric one. This operation is repeated along each column of the photospheric extrapolation cube. At the height (H) where the two field strengths coincide, the magnetic field components $B_x^{\mathrm{Si,C}}$, $B_y^{\mathrm{Si,C}}$, and $B_z^{\mathrm{Si,C}}$ are stored as two-dimensional arrays (the uppercase "C" stands for Coincide). For instance, the

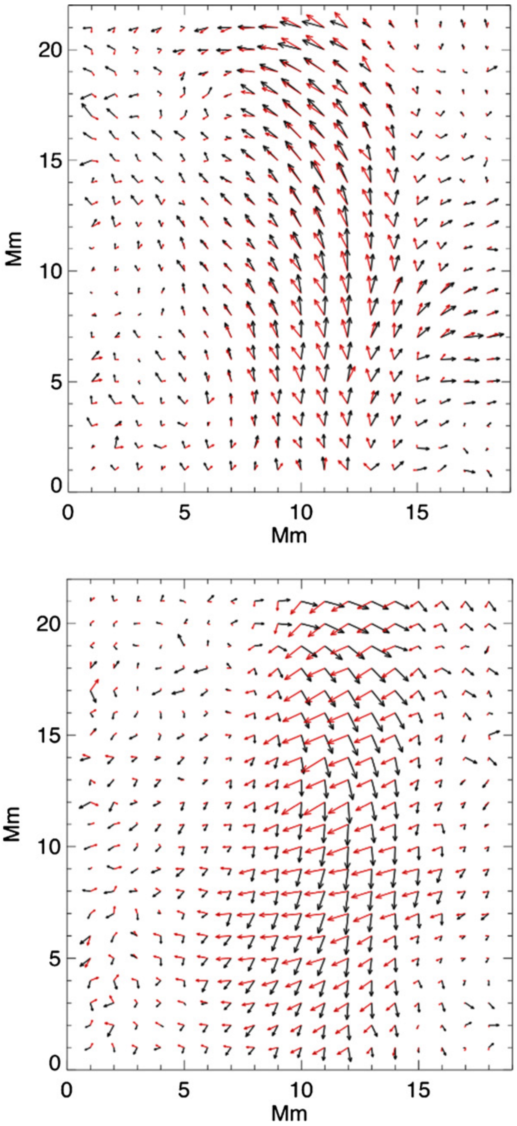

Figure 5. Red arrows: flow representation of the horizontal magnetic field from the photospheric extrapolations at the height where the extrapolated photospheric field strength matches the observed field strength in the helium vector magnetogram. Black arrows: flow representation of the observed horizontal magnetic field in the He I 10830 Å vector magnetogram. Top panel: solution obtained with the correct 180° ambiguity solution computed with the AZAM utility (Lites 2005, and references therein). Note that the solutions are obtained for both photospheric and chromospheric fields. Bottom panel: similar to the top panel but using the other solution of the 180° ambiguity. All data sets were taken on July 5.

(A color version of this figure is available in the online journal.)

horizontal magnetic field from the photospheric extrapolation ($B_x^{\mathrm{Si,C}}$, $B_y^{\mathrm{Si,C}}$) across the field of view is plotted in Figure 5 and represented by red arrows. The one from the observed helium is plotted as black arrows. The arrows length is proportional to the horizontal field strength. The top panel of Figure 5 shows a relatively good agreement between the two magnetic fields indicating that the observed magnetic field $B^{\mathrm{He,O}}$ is well matched by the extrapolated $B^{\mathrm{Si,E}}$ field especially at the filament region. This goes in favor of validating the Silicon photospheric

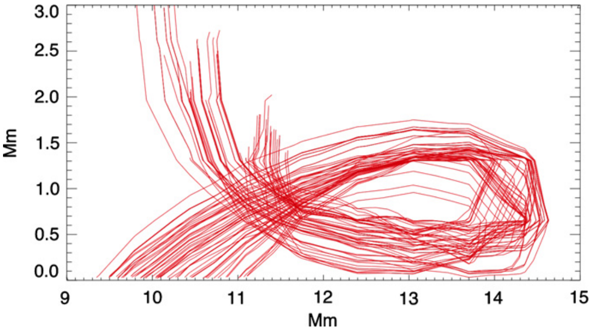

Figure 6. X–Z view of magnetic field lines having a dip of at least 650 km depth. The computations use the three-dimensional magnetic field extrapolated from the Si I 10827 Å vector magnetogram. This reveals the morphology of the flux rope with field lines making more than a full turn. In order to understand the morphology of this twisted flux rope, it is useful to look at the top panel of Figure 3 showing another perspective of the filament magnetic field lines.

(A color version of this figure is available in the online journal.)

extrapolations. The average height where $B^{\mathrm{Si,E}}$ matches $B^{\mathrm{He,O}}$ is 1.57 Mm in the filament region, with a standard deviation of 0.66 Mm. Therefore, it is possible to determine an average formation height of the He I 10830 Å triplet. This would be 1.57 Mm + the formation height of the Si I 10827 Å which leads to approximatively 2 Mm above the solar surface ($\tau = 1$).

4.4. *A Complementary Method for Solving the 180° Ambiguity*

The top panel of Figure 5 indicates that the magnetic field extrapolated from the photosphere matches well the one observed at the chromosphere. It is nevertheless interesting to redo the calculations but for the case where the observed horizontal magnetic field is taken from the solution with 180° shift of the azimuth in the LOS frame. This is done to test the coherence of the results with the other magnetic field configuration.

From the lower panel of Figure 5 it is found that, in this case, the magnetic field extrapolated from the photosphere and the one observed at the chromosphere have a quite different orientation in the horizontal plane although they have similar field strengths at the height of coincidence. This clearly discards the solution with 180° shift and provides a complementary method to test the validity of the chosen horizontal field as a result of the various routines used to solve the 180° ambiguity of the horizontal magnetic field.

4.5. *Location of the Dips Along the Filament Field Lines*

The material carried by a filament must be sustained against gravity by the magnetic curvature force associated with the dips in the field lines. Using the extrapolated magnetic field from the Si vector magnetogram, we compute all the field lines that have a dip of at least 650 km depth (equivalent to the size of one grid cell). Figure 6 indicates that such field lines with dips exhibit a twisted structure, revealing the topology of the filament's magnetic field. This X–Z view shows that the whole structure is lying relatively low. The axis of the filament is located some 1 Mm above the formation height of the Silicon line. This indicates that the axis of the TFR forming the filament is located below the formation height of the helium triplet. The lower part of the field lines in Figure 6 exhibits an inverse configuration (from negative to positive) whereas the upper part has a normal configuration. Recall that the average formation

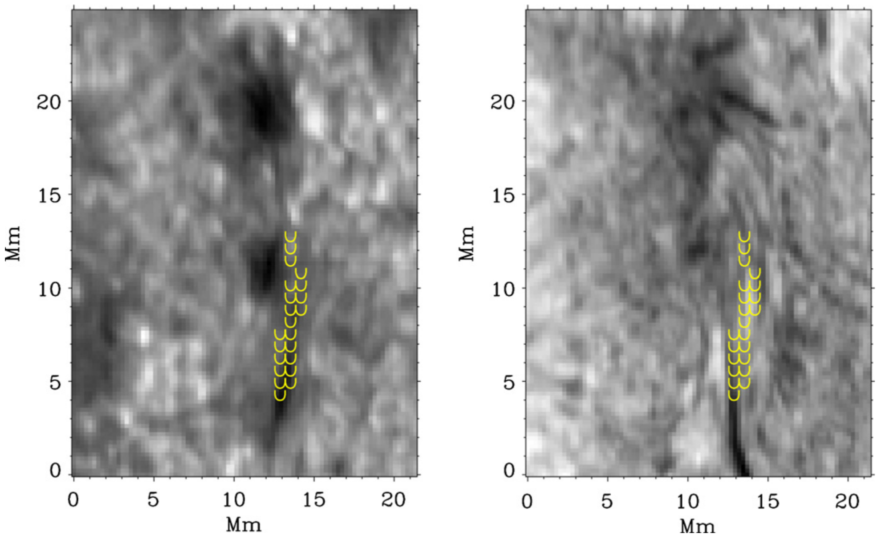

Figure 7. Location of dips (drawn in yellow "U" shapes). These dips are calculated from the photospheric extrapolations for both panels. Left panel: locations of dips on top of Si I 10827 Å line core intensity. Right panel: locations of dips on top of the red core of He I 10830 Å. The data on both panels are from July 5.

(A color version of this figure is available in the online journal.)

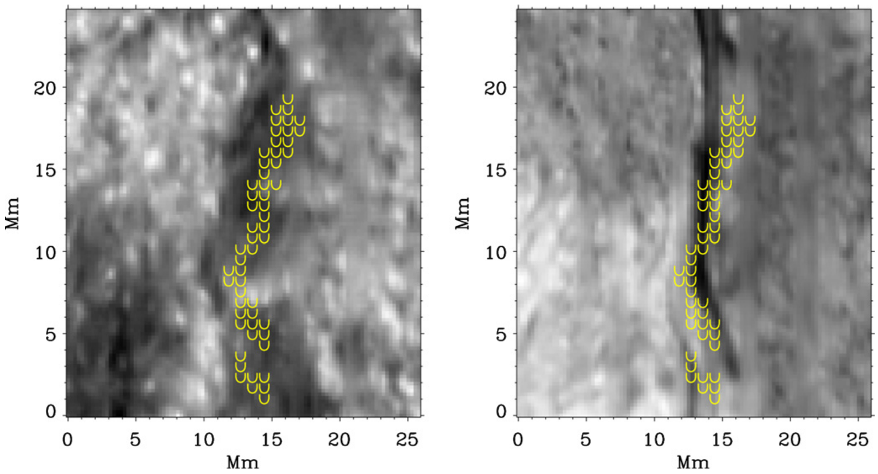

Figure 8. Similar to Figure 7 using a snapshot from July 3 (see Figure 1).

(A color version of this figure is available in the online journal.)

height of the helium triplet (Section 4.3) in the filament region is 1.57 Mm above the formation height of the Silicon line. At that height the field lines have a normal configuration. This helps in understanding the lower panel of Figure 3, where the helium extrapolations exhibit no twist, which also fits with the presence of a normal configuration magnetic field at the lower boundary of the extrapolation box. It can be seen from Figure 6 that the field lines make slightly more than one turn. These field lines extend over a horizontal distance of ≈18 Mm. This leads to ≈0.055 turns Mm^{-1}.

Following each field line in Figure 6, it is possible to calculate the location of the lowest part of the dips. These places are likely to be the preferred location where the plasma inside the filament would be gathered. Guo et al. (2010) and Canou & Amari (2010) have found a correspondence between the location of dips and the filament as observed in H_α. It is reasonable to argue that in order to build up opacity (e.g., in the H_α spectral region), filaments are filled with material that will be preferentially located in dips.

Figure 7 shows the locations of dips on top of the Si I 10827 Å line core intensity image (left panel) and the intensity image of the red core of the He I 10830 Å triplet (right panel). There is an agreement between the location of the filament and the dips, which are located in the lower half of the image where the filament has a flux rope structure. There are no dips in the upper part of the panel since the magnetic field in this region has a normal configuration with no flux rope. An even clearer case is seen in Figure 8 where we repeated the same calculations as for Figure 7 but for a snapshot taken on July 3. Note the correspondence with both line cores. This analysis also provides a further indication on the location of the filament (as the H_α spectral signature of a filament) and also allows the corroboration

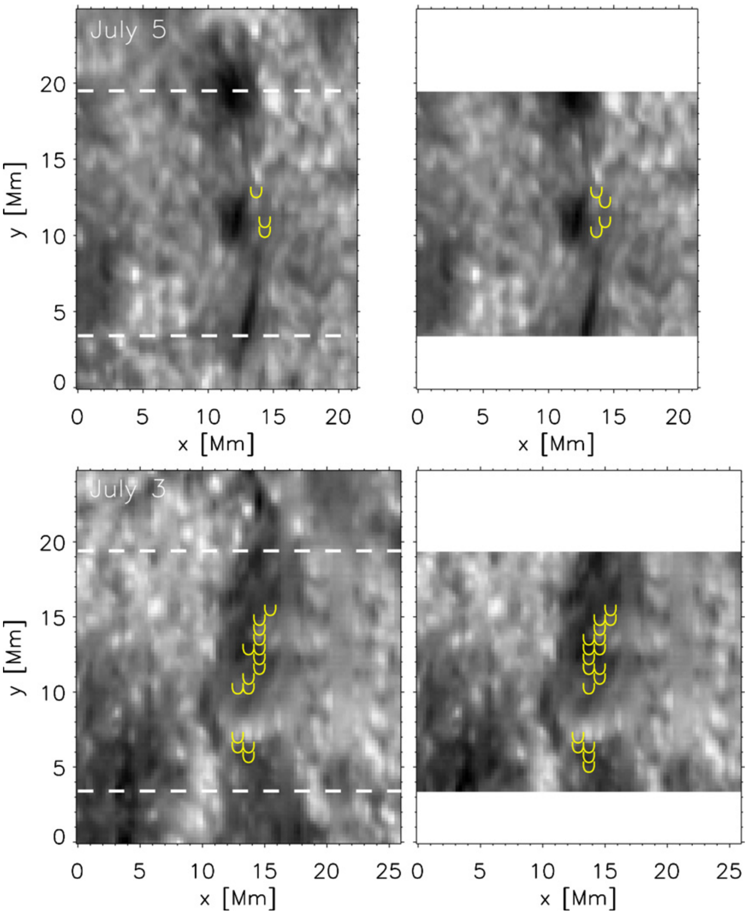

Figure 9. Location of dips calculated from the photospheric extrapolations. Top row: locations of dips on top of Si i 10827 Å line core intensity on July 5. Lower row: locations of dips on top of Si i 10827 Å line core intensity on July 3. Left column: the extrapolation of the whole field of view of Si i 10827 Å vector magnetogram is used, but the field line calculation to find the locations of dips starts from the lower dashed line until the upper dashed line. This covers a portion similar to the reduced field-of-view test. Right column: the extrapolations of the reduced field-of-view of Si i 10827 Å vector magnetogram are used (same size as displayed in the background Silicon line core image). Dips are calculated in this reduced field of view.

(A color version of this figure is available in the online journal.)

of the extrapolation results since the spectral signature of the line cores of Si i 10827 Å and He i 10830 Å is independent of the extrapolation analysis, which involves the magnetic field and the force-free condition.

4.6. Testing the Effect of the Reduced Field of View on the Extrapolations

The observations made with TIP-II have a somewhat reduced field of view. Ideally the field of view should include the whole filament or even the whole AR (in general, a flux balanced region). The fact that we use part of the filament might influence the large scale magnetic connectivity through the filament. It is very useful to make quantitative tests to clarify the effects of reduced field of view (G. Aulanier 2011, private communication). We present here a test in which we cut part of the observed filament and analyze how that affects the extrapolations. The chosen reduced field-of-view region is the one delimited by the two dashed lines in Figure 2. The resulting region is the one shown in the top-right panel of Figure 9 corresponding to July 5. Similarly, the reduced field-of-view portion for July 3 is shown in the lower-right panel of Figure 9. On these two panels we have drawn the location of dips using yellow "U" shapes. For the left column of panels in Figure 9, we used the extrapolation of the whole field of view of Si i 10827 Å vector magnetogram, but the field line calculation to find the locations of dips starts from the lower dashed line until the upper dashed line. This covers a region similar to the reduced field-of-view cases on both July 3 (bottom left) and July 5 (upper left). Figure 9 exhibits less locations of dips than the cases of Figures 7 and 8. This is primarily due to the fact that the field lines in the reduced field-of-view portion are shorter than the ones in the original full field-of-view case, and therefore there are less field lines that fulfill the criteria of having dips of 650 km depth. A comparison between the left and right panels in Figure 9 shows that they have some similarities indicating that decreasing the field of view only slightly alters the structure of the obtained filament and, more precisely, the location of dips. Figure 10 provides a closer look to the field lines forming the dips plotted in the upper panels of Figure 9. The field lines in the upper/lower panels of Figure 10 correspond to the upper left/right panels of Figure 9, respectively. The two sets of field lines are very similar indicating that the fact of reducing the field of view does not severely affect the magnetic structure

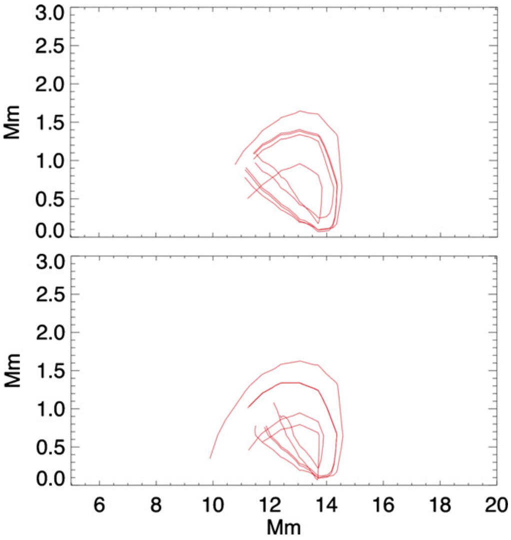

Figure 10. Lower panel: field lines with dips calculated in the extrapolation with reduced field of view corresponding to the region indicated in the upper-right panel of Figure 9. Upper panel: field lines forming dips computed from the extrapolation with the whole field of view, but calculated inside the region included between the two dashed lines in the upper-left panel of Figure 9.

(A color version of this figure is available in the online journal.)

of the extrapolated filament. Nevertheless, a more complete test of the effect of field of view on the results of extrapolation of AR filament would be useful and interesting. That would include the observation of a whole filament (ideally in an isolated and flux balanced region) and repeated extrapolations while reducing gradually the field of view. In the present work we were limited with the original field of view, therefore we could not run such a test. We intend to include a test of that sort as part of a future investigation. This test is complementary to the more complete series of tests presented in, e.g., Schrijver et al. (2006, 2008), Metcalf et al. (2008), and De Rosa et al. (2009).

4.7. Magnetic Field Increasing From the Photosphere Upward

Due to magnetohydrostatic equilibrium, the field of concentrated vertical magnetic structures usually decreases with height above the photosphere. This is a typical case in a stratified atmosphere. Nevertheless, vertical gradients of the field strength, indicating stronger fields in the upper layers, have been observed (e.g., in polar crown prominences as shown by Leroy et al. 1983) and modeled in the past (Aulanier & Démoulin 2003) and have been ascribed to the presence of dips (Anzer 1969; Demoulin & Priest 1989). Here, we would like to analyze the possibility of an upward increase of the magnetic field strength in the filament region. The upper panel of Figure 11 shows the difference between the observed field strengths of $|B|^{\mathrm{Si,O}}$ and $|B|^{\mathrm{He,O}}$. For the sake of clarity, the figure only shows negative values of those quantities. A proxy of the location of the neutral line is indicated by the contour plots of $B_z^{\mathrm{He,O}}$ (i.e., small values of $B_z^{\mathrm{He,O}}$ coincide with the neutral line location). In the central part of the figure, the values of $|B|^{\mathrm{He,O}}$ are larger than $|B|^{\mathrm{Si,O}}$, indicating that the magnetic field in the chromosphere is larger than the photospheric one, suggesting that the magnetic field has increased upward. In order to understand this phenomenon we look for the height where the extrapolated magnetic field from the photosphere reaches its maximum along each column. This height is plotted in the lower panel of Figure 11. It can be seen in the central region of the figure that the magnetic field reaches a maximum well above the photosphere, at an average height of about 1 Mm above the formation height of the Si I 10827 Å line.

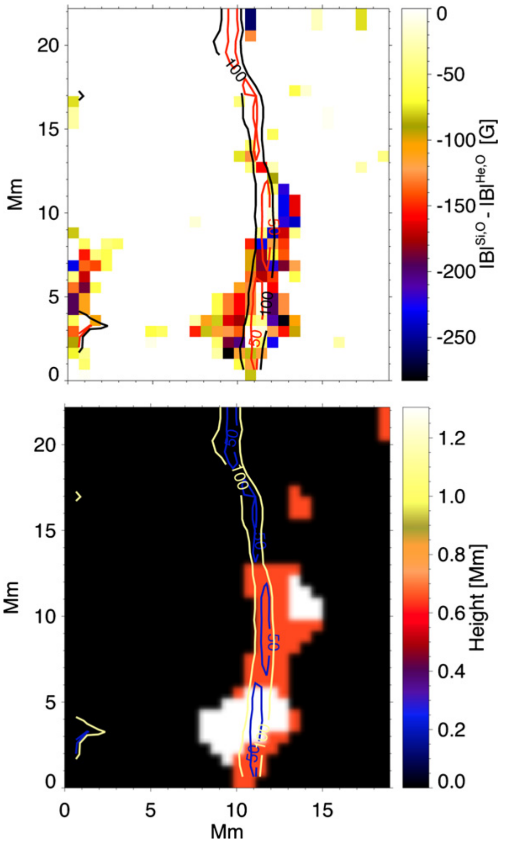

Figure 11. Upper panel: difference between the observed $|B|^{\mathrm{Si,O}}$ and $|B|^{\mathrm{He,O}}$. The positive values are clipped to 0 in order to clearly see the negative values. Lower panel: the height where the magnetic field strength from the photospheric extrapolations reaches a maximum. The data on both panels are from July 5. The location of the neutral line is approximately indicated by the contour-plots of $B_z^{\mathrm{He,O}}$ shown on both panels.

(A color version of this figure is available in the online journal.)

Figure 12 schematically explains the situation observed in those pixels where the magnetic field increases upward. First the magnetic field increases up to a maximum reached at the height H0 (plotted, in fact, in the lower panel of Figure 11), then the magnetic field decreases gradually until reaching the height of formation of the helium signal (H1) where the magnetic field is still larger than the one at the photosphere. It is also seen that there are two solutions for the height of formation of the helium signal (H1 and H2). The solution H2 is ruled out because it leads to abnormally low formation height. The H1 solution is kept and is consistent with the average height of formation of the helium signal (see Section 4.3).

The reason why the magnetic field increases lies in the fact that the corresponding part of the filament resembles the structure of a force-free flux rope. In an ideal force-free flux rope, the azimuthal component of the field yields an inward-pointing magnetic tension force, which is balanced by an increase of the magnetic pressure toward the rope axis. This leads to an increase of the magnetic field strength in the central regions of the rope.

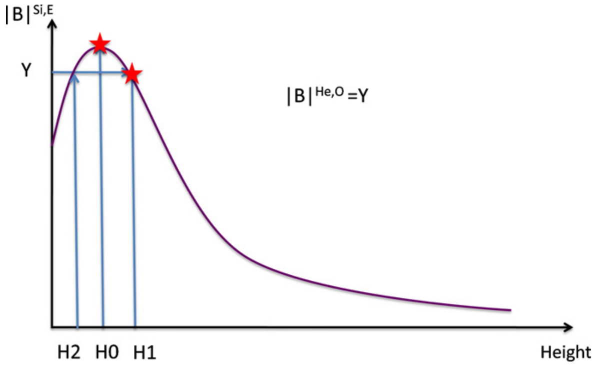

Figure 12. Schematic explanation of the situation observed in the pixels where the extrapolated magnetic field increases upward. First it increases reaching a maximum at the height "H0" plotted in the lower panel of Figure 11, then the magnetic field decreases again reaching the value of the observed chromospheric magnetic field at the height "H1".

(A color version of this figure is available in the online journal.)

4.8. *Complementary Comments on the Filament Observed on July 3*

Along the previous sections, we have used observations taken on July 3 and 5, but with some focus on the filament as observed on July 5. This has been done in order to convey a clear message and not overwhelm the reader with information about the time evolution of the filament (this time evolution will be discussed in Kuckein et al. 2012). Additionally, the filament on July 5 is very low lying (the filament's axis is located below the formation height of He I 10830 Å). This represents a peculiar and interesting case that we have chosen to address. In order to complete the picture of the actually observed filament, we will briefly describe some further features of the filament as observed on July 3.

It can be seen in Figure 8 that the line core of the Si I 10827 Å and the red core of the He I 10830 Å show a spectral signature reminiscent of the axis of the filament on July 3. The locations of dips along the filament coincide well with the line core signature (Figure 8). The filament in this case is located higher in the atmosphere and therefore imprints a clear spectral signature on both photospheric and chromospheric lines. The observed magnetic field from photospheric vector magnetograms exhibits an inverse configuration (field lines going from negative to positive polarities) in the filament region. The observed chromospheric vector magnetograms indicate that the magnetic field in the filament region has a slightly inverse configuration, with most of the field being parallel to the filament's axis. From extrapolations (Figure 13), it can be seen that the filament is formed by a TFR. This is revealed from both photospheric and chromospheric extrapolations.

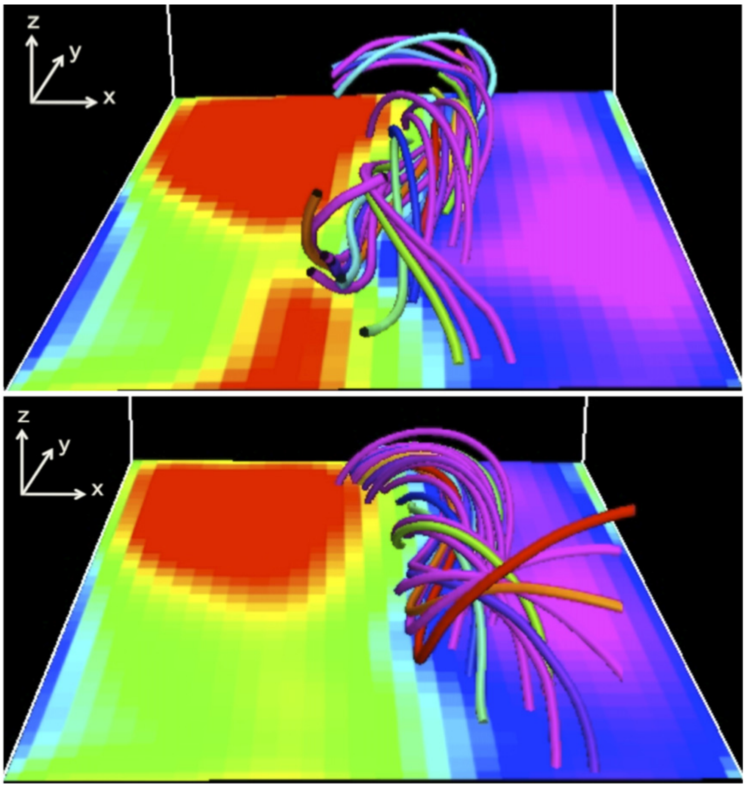

Figure 13. Top: three-dimensional view of the magnetic field of the filament on July 3. The extrapolation results use the photospheric magnetic field as lower boundary condition. The sample of field lines is plotted in the filament region to outline its structure. Top background image: vertical component of the magnetic field at the bottom of the extrapolation cube. Purple and blue: $B_z^{\mathrm{Si,E}} > 0$; green and red: $B_z^{\mathrm{Si,E}} < 0$. Bottom: extrapolation results for July 3 using the chromospheric magnetic field as lower boundary condition. Bottom background image: vertical component of the magnetic field at the bottom of the extrapolation cube $B_z^{\mathrm{He,E}}$ (same color scale as in the top panel).

(A color version of this figure is available in the online journal.)

5. DISCUSSION AND SUMMARY

This paper is dedicated to building diagnostics about an AR filament using nonlinear force-free extrapolations starting from the photosphere and the chromosphere. Extrapolations of AR filaments are usually done using the photospheric magnetic field as a lower boundary condition. This is generally convenient because the photospheric magnetic field is more accessible to observational techniques for various reasons, e.g., (1) it has a large magnetic field implying a large Zeeman splitting, (2) the photon flux coming from the photosphere is large producing a high signal-to-noise ratio, which makes it easily detectable, (3) there are many available instruments measuring photospheric field, etc. It is nevertheless interesting to probe the properties of filaments from two layers (or multi-layer if possible) since this approach provides several advantages like testing the validity of the extrapolation solutions. It also allows testing of the consistency between the extrapolations starting from the photosphere and the chromosphere. We just began to see the potential of multi-layer extrapolations, e.g., the determination of the matching height between the extrapolated photospheric field and the observed chromospheric one. This can be used as a method to determine the relative height of formation of higher-lying lines/multiplets compared to lower-lying ones. We find that the average formation height of the He I 10830 Å triplet is about 2 Mm above the surface of the Sun. Multi-layer extrapolations also provide a complementary method for testing the 180° ambiguity solutions.

The AR filament studied here harbors a TFR structure with a rather low-lying axis on July 5, where the axis is located at about 1.4 Mm above the solar surface. This height is below the formation height of the helium signal. This result is consistent with the fact that the magnetic field as observed in helium magnetograms harbors a normal configuration.

In the present study, we have essentially focused on a snapshot taken on July 5 (see Figures 1 and 2). We have also briefly discussed a snapshot observed on July 3 (Figures 1 and 12). Recall that on July 3, the filament's axis was higher located and clearly seen in the spectral signature of Si I 10827 Å and He I 10830 Å line cores. Actually, as discussed in Section 2 (observations and data analysis), the observations used here belong to a time series of snapshots covering 2005 July 3 and 5. In order to build a clear and detailed diagnostic we have essentially focused on studying one case (July 5). A more detailed analysis about the temporal evolution of the filament will be addressed at a later stage (see also Kuckein et al. 2012). Nevertheless, it is worth commenting on the other snapshots. An essential thing to mention is that snapshots observed on the same day exhibit similar properties (height of location of the filament axis, magnetic field strength, etc.). This means that the rest of the snapshots observed on July 5 have quite similar properties to the one described here, and similarly for the snapshots taken on July 3.

For the filament on July 5, we have seen that, if taken separately, the photospheric and chromospheric extrapolations would lead one to conclude that on the one hand the filament is formed by a TFR (from photospheric extrapolations), whereas on the other hand there is no TFR (from the chromospheric extrapolations). The multi-layer extrapolations helped solve this apparent discrepancy by showing that, depending on the location of the TFR, it might be seen at one layer or the other while the two extrapolations remain coherent with each other. Let us assume hypothetically that an AR filament is such that the lower part of the TFR is located at the upper chromosphere and does not extend to the photosphere. In this case, it would be seen in the chromospheric extrapolations, but the photospheric ones would not necessarily reveal it, especially since the photosphere is a relatively high plasma-β medium and therefore the surrounding magnetic field in the AR might considerably alter the magnetic field near the PIL making the horizontal component of the magnetic field harbor a normal configuration. If we would only observe the photospheric field, this would lead to finding no TFR in the filament region, whereas in fact the filament's structure is a TFR. In fact, this is true only if the electric currents present in the region are not reminiscent of a TFR, since it has been shown by Valori et al. (2010) that NLFFF extrapolations have the potential to find a TFR even if its dips are not present at the magnetogram level. Nevertheless, this hypothetical scenario highlights the usefulness of multi-layer extrapolations in helping to probe the properties of filaments and extract further information about the observed magnetic structure.

In the case studied here, the material in the dense part of the filament, along its axis, is confined inside a flux rope where the field lines are bent producing an excess of magnetic tension toward the center of the TFR. This tension is compensated by the outward oriented magnetic pressure, producing an enhancement of the magnetic field inside the TFR. This is reflected by a vertical positive gradient of the magnetic field from the photosphere up to about 1 Mm above the formation height of the Si I 10827 Å signal. In brief, the field increases from the photosphere upward in the flux rope region.

There are only few studies dealing with extrapolations of AR filaments, the most recent being from Guo et al. (2010), Canou & Amari (2010), and Jing et al. (2010). These studies picture AR filaments as TFR with the exception of Guo et al. (2010), who have shown that TFR and dipped sheared arcades can coexist in the same filament. We also find a flux rope from photospheric extrapolations, but have seen that the chromospheric extrapolations might show a different picture if the observed spectral line/multiplet is formed above the filament's axis. There is a clear necessity of further observational campaigns with the appropriate extrapolations to further clarify the properties of AR filaments and their temporal evolution. Multi-layer extrapolations would be helpful to compare the resulting three-dimensional structure of filaments with the variety of theoretical models existing in the literature (Mackay et al. 2010).

Financial support by the European Commission through the SOLAIRE Network (MTRN-CT-2006-035484) and by the Spanish Ministry of Research and Innovation through projects AYA2007-66502, AYA2007-63881, CSD2007-00050, AYA2009-14105-C06-03, and AYA2011-24808 is gratefully acknowledged.

REFERENCES

Aly, J. J. 1989, Sol. Phys., 120, 19
Aly, J. J., & Amari, T. 2007, Geophys. Astrophys. Fluid Dyn., 101, 249
Amari, T., Aly, J. J., Luciani, J. F., Boulmezaoud, T. Z., & Mikic, Z. 1997, Sol. Phys., 174, 129
Amari, T., Luciani, J. F., & Aly, J. J. 2004, ApJ, 615, L165
Amari, T., Luciani, J. F., & Aly, J. J. 2005, ApJ, 629, L37
Amari, T., Luciani, J. F., Mikic, Z., & Linker, J. 1999, ApJ, 518, L57
Antiochos, S. K., Dahlburg, R. B., & Klimchuk, J. A. 1994, ApJ, 420, L41
Anzer, U. 1969, Sol. Phys., 8, 37
Archontis, V., Moreno-Insertis, F., Galsgaard, K., Hood, A., & O'Shea, E. 2004, A&A, 426, 1047
Aulanier, G., & Démoulin, P. 2003, A&A, 402, 769
Aulanier, G., DeVore, C. R., & Antiochos, S. K. 2002, ApJ, 567, L97

Babcock, H. W., & Babcock, H. D. 1955, ApJ, 121, 349
Bard, S., & Carlsson, M. 2008, ApJ, 682, 1376
Canou, A., & Amari, T. 2010, ApJ, 715, 1566
Cheung, M. C. M., Schüssler, M., & Moreno-Insertis, F. 2007, A&A, 467, 703
Collados, M., Lagg, A., Díaz Garcí A, J. J., et al. 2007, in ASP Conf. Ser. 368, The Physics of Chromospheric Plasmas, ed. P. Heinzel, I. Dorotovič, & R. J. Rutten (San Francisco, CA: ASP), 611
De Rosa, M. L., Schrijver, C. J., Barnes, G., et al. 2009, ApJ, 696, 1780
Demoulin, P. 1998, in ASP Conf. Ser. 150, IAU Colloq. 167, New Perspectives on Solar Prominences, ed. D. F. Webb, B. Schmieder, & D. M. Rust (San Francisco, CA: ASP), 78
Demoulin, P., & Priest, E. R. 1989, A&A, 214, 360
DeVore, C. R., & Antiochos, S. K. 2000, ApJ, 539, 954
DeVore, C. R., Antiochos, S. K., & Aulanier, G. 2005, ApJ, 629, 1122
Fan, Y. 2009, ApJ, 697, 1529
Fan, Y., & Gibson, S. E. 2004, ApJ, 609, 1123
Galsgaard, K., Moreno-Insertis, F., Archontis, V., & Hood, A. 2005, ApJ, 618, L153
Guo, Y., Schmieder, B., Démoulin, P., et al. 2010, ApJ, 714, 343
Jing, J., Yuan, Y., Wiegelmann, T., et al. 2010, ApJ, 719, L56
Kuckein, C., Centeno, R., & Martínez Pillet, V. 2010, Mem. Soc. Astron. Ital., 81, 668
Kuckein, C., Centeno, R., Martínez Pillet, V., et al. 2009, A&A, 501, 1113
Kuckein, C., Martinez Pillet, V., & Centeno, R. 2012, A&A, in press (arXiv:1112.1672)
Leka, K. D., Canfield, R. C., McClymont, A. N., & van Driel-Gesztelyi, L. 1996, ApJ, 462, 547
Leroy, J. L., Bommier, V., & Sahal-Brechot, S. 1983, Sol. Phys., 83, 135
Lites, B. W. 2005, ApJ, 622, 1275
Lites, B. W., Low, B. C., Martinez Pillet, V., et al. 1995, ApJ, 446, 877
Lites, B. W., Kubo, M., Berger, T., et al. 2010, ApJ, 718, 474
López Ariste, A., Aulanier, G., Schmieder, B., & Sainz Dalda, A. 2006, A&A, 456, 725
Mackay, D. H., Karpen, J. T., Ballester, J. L., Schmieder, B., & Aulanier, G. 2010, Space Sci. Rev., 151, 333
MacTaggart, D., & Hood, A. W. 2010, ApJ, 716, L219
Magara, T., & Longcope, D. W. 2003, ApJ, 586, 630
Martínez González, M. J., Manso Sainz, R., Asensio Ramos, A., & Bellot Rubio, L. R. 2010, ApJ, 714, L94
Martínez-Sykora, J., Hansteen, V., & Carlsson, M. 2008, ApJ, 679, 871
Metcalf, T. R., De Rosa, M. L., Schrijver, C. J., et al. 2008, Sol. Phys., 247, 269
Okamoto, T. J., Tsuneta, S., Lites, B. W., et al. 2008, ApJ, 673, L215
Okamoto, T. J., Tsuneta, S., Lites, B. W., et al. 2009, ApJ, 697, 913
Ruiz Cobo, B., & del Toro Iniesta, J. C. 1992, ApJ, 398, 375
Sasso, C., Lagg, A., & Solanki, S. K. 2011, A&A, 526, A42
Schrijver, C. J., De Rosa, M. L., Metcalf, T. R., et al. 2006, Sol. Phys., 235, 161
Schrijver, C. J., De Rosa, M. L., Metcalf, T., et al. 2008, ApJ, 675, 1637
Socas-Navarro, H. 2001, in ASP Conf. Ser. 236, Advanced Solar Polarimetry—Theory, Observation, and Instrumentation, ed. M. Sigwarth (San Francisco, CA: ASP), 487
Socas-Navarro, H., Trujillo Bueno, J., & Landi Degl'Innocenti, E. 2004, ApJ, 612, 1175
Titov, V. S., & Démoulin, P. 1999, A&A, 351, 707
Tortosa-Andreu, A., & Moreno-Insertis, F. 2009, A&A, 507, 949
Valori, G., Kliem, B., Török, T., & Titov, V. S. 2010, A&A, 519, A44
van Ballegooijen, A. A., & Martens, P. C. H. 1989, ApJ, 343, 971
Welsch, B. T., DeVore, C. R., & Antiochos, S. K. 2005, ApJ, 634, 1395
Wiegelmann, T. 2004, Sol. Phys., 219, 87
Wiegelmann, T., Inhester, B., & Sakurai, T. 2006, Sol. Phys., 233, 215
Wiegelmann, T., Yelles Chaouche, L., Solanki, S. K., & Lagg, A. 2010, A&A, 511, A4
Yelles Chaouche, L., Cheung, M. C. M., Solanki, S. K., Schüssler, M., & Lagg, A. 2009a, A&A, 507, L53
Yelles Chaouche, L., Solanki, S. K., & Schüssler, M. 2009b, A&A, 504, 595

5

An active region filament studied simultaneously in the chromosphere and photosphere. II. Doppler velocities

This chapter is devoted to the study of the LOS velocities found in the AR filament. Furthermore, the analysis of the plasma motions together with the inferred magnetic structure in the previous chapters, allow us to propose a filament formation scenario. The article presented in this chapter was accepted with the title “An active region filament studied simultaneously in the chromosphere and photosphere. II. Doppler velocities”, by Astronomy & Astrophysics and is currently in press.

Abstract: Paper I presents the magnetic structure, inferred for the photosphere and the chromosphere, of a filament that developed in active region (AR) NOAA 10781, observed on 2005 July 3 and July 5. In this paper we complement those results with the velocities retrieved from Doppler shifts measured at the chromosphere and the photosphere in the AR filament area. The velocities and magnetic field parameters were inferred from full Stokes inversions of the photospheric Si I 10827 Å line and the chromospheric He I 10830 Å triplet. Various inversion methods with different numbers of atmospheric components and different weighting schemes of the Stokes profiles were used. The velocities were calibrated on an absolute scale. A ubiquitous chromospheric downflow is found in the faculae surrounding the filament, with an average velocity of $1.6\,\mathrm{km\,s^{-1}}$. The filament region, however, displays upflows in the photosphere on both days, when the linear polarization (which samples the transverse component of the fields) is given more weight in the inversions. The upflow speeds of the transverse fields in the filament region average $-0.15\,\mathrm{km\,s^{-1}}$. In the chromosphere, the situation is different for the two days of observation. On July 3, the chromospheric portion of the filament is moving upwards as a whole with a mean speed of $-0.24\,\mathrm{km\,s^{-1}}$. However, on July 5 only the section above an orphan penumbra shows localized upflow patches, while the rest of the filament is dominated by the same downflows observed elsewhere in the facular region. Photospheric supersonic downflows that last for tens of minutes are detected below the filament, close to the PIL. The observed velocity pattern in this AR

filament strongly suggests a scenario where the transverse fields are mostly dominated by upflows. The filament flux rope is seen to be emerging at all places and both heights, with a few exceptions in the chromosphere. This happens within a surrounding facular region that displays a generalized downflow in the chromosphere and localized downflows of supersonic character at the photosphere. No large scale downflow of transverse field lines is observed at the photosphere.

Astronomy & Astrophysics manuscript no. Kuckein
April 23, 2012

An active region filament studied simultaneously in the chromosphere and photosphere. II. Doppler velocities

C. Kuckein[1,2], V. Martínez Pillet[1], and R. Centeno[3]

[1] Instituto de Astrofísica de Canarias, Vía Láctea s/n, E-38205 La Laguna, Tenerife, Spain
e-mail: `ckuckein@iac.es`
[2] Departamento de Astrofísica, Universidad de La Laguna, E-38206 La Laguna, Tenerife, Spain
[3] High Altitude Observatory (NCAR), Boulder, CO 80301, USA

Received 25 January 2012 / Accepted

ABSTRACT

Context. Paper I presents the magnetic structure, inferred for the photosphere and the chromosphere, of a filament that developed in active region (AR) NOAA 10781, observed on 2005 July 3 and July 5.
Aims. In this paper we complement those results with the velocities retrieved from Doppler shifts measured at the chromosphere and the photosphere in the AR filament area.
Methods. The velocities and magnetic field parameters were inferred from full Stokes inversions of the photospheric Si I 10827 Å line and the chromospheric He I 10830 Å triplet. Various inversion methods with different numbers of atmospheric components and different weighting schemes of the Stokes profiles were used. The velocities were calibrated on an absolute scale.
Results. A ubiquitous chromospheric downflow is found in the faculae surrounding the filament, with an average velocity of 1.6 km s^{-1}. The filament region, however, displays upflows in the photosphere on both days, when the linear polarization (which samples the transverse component of the fields) is given more weight in the inversions. The upflow speeds of the transverse fields in the filament region average −0.15 km s^{-1}. In the chromosphere, the situation is different for the two days of observation. On July 3, the chromospheric portion of the filament is moving upwards as a whole with a mean speed of −0.24 km s^{-1}. However, on July 5 only the section above an orphan penumbra shows localized upflow patches, while the rest of the filament is dominated by the same downflows observed elsewhere in the facular region. Photospheric supersonic downflows that last for tens of minutes are detected below the filament, close to the PIL.
Conclusions. The observed velocity pattern in this AR filament strongly suggests a scenario where the transverse fields are mostly dominated by upflows. The filament flux rope is seen to be emerging at all places and both heights, with a few exceptions in the chromosphere. This happens within a surrounding facular region that displays a generalized downflow in the chromosphere and localized downflows of supersonic character at the photosphere. No large scale downflow of transverse field lines is observed at the photosphere.

Key words. Sun: filaments, prominences – Sun: faculae, plages – Sun: photosphere – Sun: chromosphere – Techniques: polarimetric

1. Introduction

Velocity measurements in active region (AR) filaments are extremely scarce in the literature. Most studies have been carried out only in quiescent (QS) filaments (outside ARs). However, quantifying velocities and plasma flows in filaments is a fundamental step towards understanding their formation, evolution and disappearance. Filaments are structures formed from cool dense plasma that typically lies between opposite polarities, i.e., at the polarity inversion line (PIL; Babcock & Babcock 1955), in the chromosphere or corona. Due to the temperature contrast with their surroundings, they appear as dark structures when observed on the solar disk. Filaments are called prominences if observed in emission above the limb, but both terms are often used interchangeably in the literature.

To date, there are two proposed scenarios for the formation process of filaments: the sheared arcade (SA) model and the flux rope emergence (FRE) model. Both result in very similar global structures, i.e., a flux rope that hangs above the photosphere (although the SA model combines dipped field lines and flux ropes). However, it is in the formation process of the flux ropes where the two models differ. The SA model requires shearing motions of the footpoints to form the flux rope in the corona with the aid of reconnection processes identified in the photosphere as cancellation events. On the other hand, in the FRE model the flux rope is formed deep in the convection zone (CZ) before it emerges through the surface and makes its way up into the corona. However, simulations based on buoyancy instabilities encounter difficulties when lifting up a mass-loaded flux rope from the photosphere into the corona (e.g., Murray et al. 2006; MacTaggart & Hood 2010). Kuckein et al. (2012) (hereafter Paper I) provide a more thorough discussion and additional references to these two models (see also the extensive review by Mackay et al. 2010).

Nowadays, high-resolution imaging has shown that quiescent filaments are made of smaller-scale structures (e.g., Demoulin et al. 1987; Lin et al. 2005, and references therein). Doppler measurements in these quiescent filaments (e.g., Martres et al. 1981; Schmieder et al. 2010) have revealed that a wide range of velocities coexist in the same structure. For example, the recent study by Chae et al. (2007) reported line-of-sight (LOS) velocities between ±5 km s^{-1} and ±15 km s^{-1} in the spine and in threads (respectively) of a QS filament (at coordinates N15-E26). Mein (1977) found that the axis of an AR filament (at N7-W30) was at rest, while downflows on one side and upflows on the other side were detected. Upward motions have also been detected below QS and AR filaments by Ioshpa & Obridko (1999). However, the main limitation of Doppler line shifts, and hence of the retrieved LOS velocities, is that the inferred values are position-dependent all over the solar disk. Therefore, it is hard to compare Doppler velocities measured in different filaments. In addition, a thorough calibration, i.e., setting a correct zero value for the rest wavelength, is necessary, especially when calculating photospheric velocities (below the filament) which are much smaller ($\leq 0.3\,\mathrm{km\,s^{-1}}$; Martres et al. 1976) than those found in the chromosphere and corona (see Welsch & Fisher 2012).

It is presently unclear whether there is an unequivocal way of distinguishing which of the different filament formation scenarios applies to the observed AR filament. In this paper we propose to shed some light on this topic by studying the observed Doppler velocities inside the AR filament that was analyzed in Paper I. In particular, we can ask what the expected velocity patterns (in and below the filaments) associated with these two models are. The flux rope models proposed by van Ballegooijen & Martens (1989) and van Ballegooijen & Mackay (2007) are built through successive photospheric flux cancellations driven by motions that force the field lines to converge towards the PIL. After the oppositely directed field lines are brought together, reconnection processes above the photosphere create a flux rope in the corona. The authors suggest that transverse magnetic field lines (loops which are almost perpendicular to the PIL) submerge at the PIL, and are transported downwards into the CZ as a result of the reconnection processes mentioned before (see panels d and e in Fig. 1 of van Ballegooijen & Martens 1989). The typical size of these submerging loops is small (~ 900 km), which is large enough to be detected with currently available instruments.

The prominence model presented in the work of DeVore & Antiochos (2000) does not show convergence of flux at the PIL. The helicity in the field lines is built up in the corona as a consequence of reconnection of the highly sheared field lines (twisted and stretched by the sheared displacements of the footpoints) with the overlying coronal arcade. The authors point out that the resulting magnetic structure is stable; hence, no upflows or downflows are expected in this model. However, the observed evolution of filaments suggests that they are of a non-steady nature. This calls for models with built-in evolutionary processes that allow the filament to disappear from the solar surface, transporting magnetic fields upwards or downwards through the photospheric boundary.

The first complete description of the emergence of a flux rope AR filament was presented by Okamoto et al. (2008, 2009). The authors show observational evidence of an emerging helical flux rope that apparently reconnects with the remnant magnetic field of a pre-existing filament. A Milne–Eddington (ME) inversion of the Stokes profiles observed with Hinode/SP over the region where the transverse fields of the emerging flux rope were observed yielded a mean upflow of $-0.3 \pm 0.2\,\mathrm{km\,s^{-1}}$. The ME inversion applied by these authors was able to separate the velocity of the magnetic and the non-magnetic components (see their Fig. 2). Interestingly, while the non-magnetic atmosphere showed a typical granulation pattern, upflows were systematically inferred for the *magnetic* component. Thus, in that work, the picture of the filament formation is compatible with the existence of transverse fields that are moving upwards into the chromosphere and corona. MacTaggart & Hood (2010) simulated the rise of a weakly twisted flux tube from the solar interior up into an overlying arcade in the corona. The axis of their flux rope became trapped slightly above the photosphere, while the field lines of the top of the flux rope were still able to reach coronal heights. In the same way, the 3D MHD simulations of an emerging flux rope presented by Yelles Chaouche et al. (2009) showed horizontal field lines that moved upwards with velocities of $\sim -0.67\,\mathrm{km\,s^{-1}}$. However, the authors pointed out that the emergent flux studied by Okamoto et al. (2009) was probably less buoyant than the case simulated in their work, since the observed rising speed was smaller and the modification of the granular pattern less severe than in the simulations. Interestingly, Lites et al. (2010) also found a similar pattern to that presented by Okamoto et al. (2009) in their study of the evolution of a filament channel inside an active region. The inferred magnetic structure in the filament channel corresponded to horizontal field lines elongated along the PIL (with equipartition strengths) that often (but not always) displayed upflows (see the v_{mag} panel in Fig. 5 of Lites et al. 2010). A slow continuous upward motion in active region filaments had already been observed almost three decades ago (Malherbe et al. 1983; Schmieder et al. 1985), albeit in chromospheric layers. It is thus clear that studying the behavior of transverse magnetic fields at the location of filaments (i.e., at AR PILs), is crucial to understanding their evolution (see also the discussion in Welsch & Fisher 2012). In particular, it will help to shed some light on how the magnetic structures that sustain the filaments get filled with plasma and how they eventually get rid of it, unloading most of their mass. To this end, it is crucial to obtain more data of the flows associated with filament formation and evolution.

In Paper I, we presented the magnetic structure of an AR filament, inferred from simultaneous spectropolarimetric observations in the photosphere and chromosphere. The filament seemed to be divided into two parts: (1) one section that showed a flux rope configuration which had its main axis lying in the chromosphere; and (2) another section, which was likely to have a similar magnetic structure, but whose main axis was detected in the photosphere instead. This extremely low-lying part of the filament left an imprint on the photosphere in the shape of an orphan penumbral system in the proximity of small pore associations. Paper I suggested that these features were the photospheric counterpart of the filament. However, in order to understand the formation mechanism of this AR filament, a detailed study of the Doppler velocities, in a global scenario, needs to be carried out. The present paper addresses this issue by focusing in particular on the photospheric velocities inferred from the Doppler shifts of the Si I line in order to search for systematic upflows and downflows. We also analyze the chromospheric Doppler shifts provided by the He I triplet.

2. Observations

The active region under study, NOAA AR 10781, was in its slow decay phase during our observing run in July 2005. The active region had a round leader sunspot of positive polarity and was followed by an extensive plage region that stretched towards higher latitudes. On top of the polarity inversion line (PIL), a filament with an inverse S-shape was unambiguously identified. Two spectropolarimetric maps were taken on July 3 (at latitude and longitude N16-E8, $\mu \sim 0.95$), and seven on July 5 (at N16-W18, $\mu \sim 0.91$), using the Tenerife Infrared Polarimeter (TIP-II; Collados et al. 2007) at the German Vacuum Tower Telescope (VTT) on Tenerife. In addition, a time series of ~ 19 minutes, with the slit fixed at the PIL, was acquired on July 5.

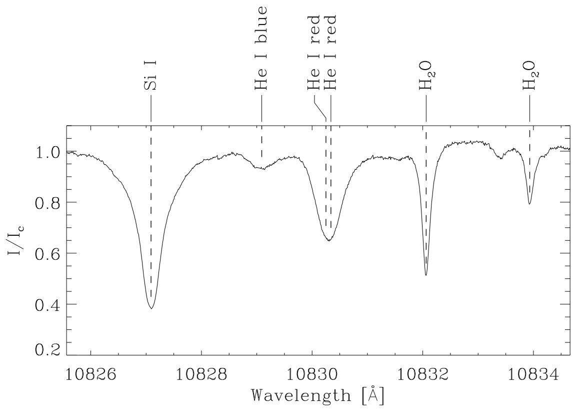

Fig. 1. Stokes *I* profile, normalized to the continuum intensity, observed by TIP-II near the polarity inversion line. The dashed vertical lines indicate the positions of the rest wavelengths for the spectral lines that are used in this work.

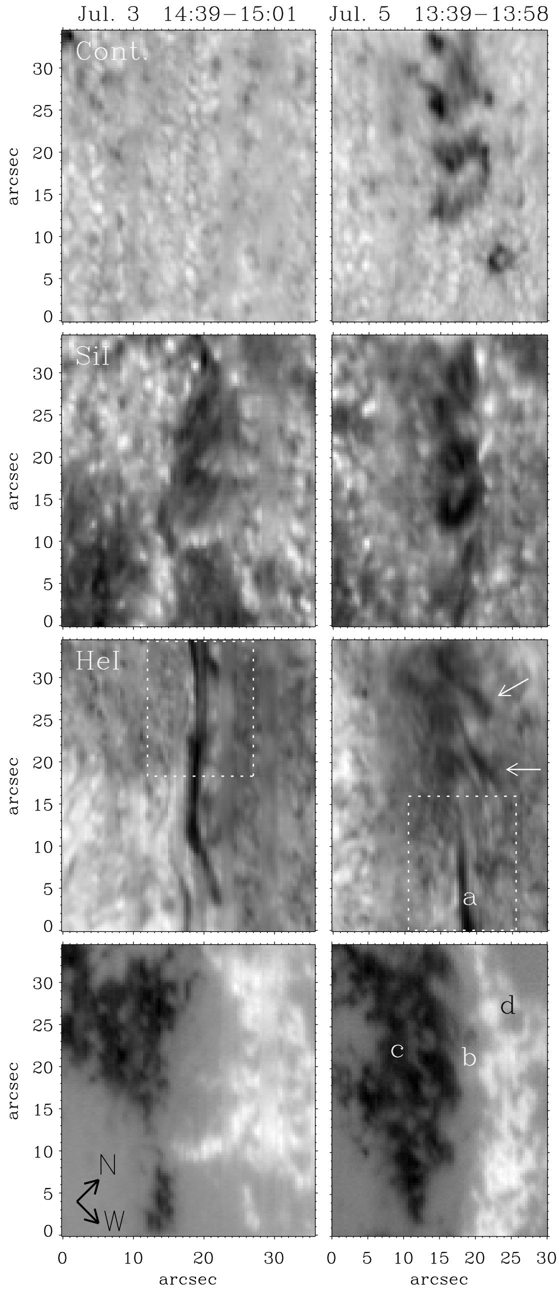

Fig. 2. TIP-II slit-reconstructed images for both days of observation. From *top* to *bottom*: continuum, Si I line core intensity, He I line core intensity (red component) and Si I Stokes *V*. The FOV was different on July 3 and July 5. We provide the dashed rectangles to show the approximate common area of the filament on both days. Characters a–d indicate the position of the Stokes profiles presented in Fig. 7. The white arrows point to high concentrations of helium with elongated shapes (thread-like structures).

The slit (0.″5 wide and 35″ long, with a pixel size of 0.″17 along the slit) was aligned with the filament and a series of spectropolarimetric maps, centered on the filament, were acquired using a scanning step size of 0.″4 or 0.″3, depending on the seeing conditions. Figure 1 shows the spectral range of the spectropolarimeter, which comprises the photospheric Si I 10827 Å line, the chromospheric He I 10830 Å triplet and two telluric H_2O lines. The helium triplet comprises a "blue" component and two blended "red" components. Table 1 provides the wavelength and the logarithm of the oscillator strength times the multiplicity of the lower level, $\log gf$, for each line. This unique spectral window allows us to study the photosphere and the chromosphere simultaneously. The seeing conditions during the observations were highly variable and the adaptive optics system of the VTT (KAOS; von der Lühe et al. 2003) helped to substantially improve the image quality. The data sets were corrected for flat field, dark current and polarimetric calibration using the standard procedures for TIP (Collados 1999, 2003).

Figure 2 shows an example, for both days, of the scanned area of the filament. From *top* to *bottom*, the slit-reconstructed images presented correspond to different wavelength bands: continuum intensity, Si I line core intensity, He I line core intensity centered at the red component and Si I line-of-sight magnetogram. On July 3, the filament had a thin elongated shape in the chromosphere (see He I panel of Fig. 2), which we interpret to be the main axis or spine of the filament. Underneath, in the photosphere, the continuum image shows no outstanding features. The FOV of July 5 was slightly different and included newly appearing pores and orphan penumbral structures in the photosphere, mainly located along the PIL and below the filament (see continuum image in the *top righthand* panel). The white dashed rectangles in Fig. 2 show the approximate portion of the filament common to both days of observation. The He I intensity image of July 5 also shows the spine of the filament in the lower (common) part of the FOV. This feature is traced by an elongated shape in the Si I line core image, indicating that the structure lies at a lower mean height than on July 3. In the upper part of the He I image, on the other hand, the filament is more diffuse and less compact, and shows a series of dark threads that are highlighted by the white arrows (see also Fig. 5 of Paper I for more TIP-II images from July 5). Since the structure of the filament is identifiable in the silicon images, Paper I concluded that the filament was extremely low-lying and was directly responsible for the orphan penumbral aggregations and pores.

The main purpose of this paper is to identify what the plasma motions associated with the filament are, both in the chromo-

Table 1. Atomic data used in this work.

Line	Wavelength (Å)	log *gf*
Si I	10827.089^a	0.363*
He I blue	10829.091^a	−0.745†
He I red	10830.250^a	−0.268†
	10830.340^a	−0.047†
H_2O (telluric)	10832.108^b	–

Notes. Wavelengths $^{(a)}$ from the NIST database $^{(b)}$ inferred in this work; see Appendix B.

References. ($\star$) Borrero et al. (2003); (†) VALD; Kupka et al. (1999)

Table 2. Examples of the line-of-sight to local solar reference frame transformation of the magnetic field inclination and azimuth. The examples were averaged over 11 (PIL) and 8 (spine) pixels, in addition to the original binning of the data (see Sect. 3.1).

			LOS frame			Solar frame	
Day	Location	Ion	γ (°)	ϕ (°)		$\gamma_\odot$ (°)	$\phi_\odot$ (°)
July 3rd	Spine	He I	101.5	93.0	→	116.1	85.3
		Si I	84.2	63.6	→	98.1	54.6
July 5th	PIL	He I	91.6	140.4	→	74.0	125.7
		Si I	88.9	114.6	→	81.2	100.0

sphere and the photosphere. In particular, we concentrate on whether the field lines are moving upwards, which would indicate an emerging process, or downwards, which would reveal a submergence phenomenon. The position on the solar disk of this active region is quite close to disk center on both days. This presents an advantage for the study of line-of-sight (LOS) velocities, which should not differ too much from the vertical velocities (measured in a local solar reference frame). For a better understanding of the inferred velocities we will distinguish between two regions in the filament: the spine area and the diffused filament area (above the orphan penumbrae), the latter being observed only on July 5. As stated in Paper I, these two areas correspond to the same filament, but observed at different heights. It is therefore helpful to study them separately.

A detailed analysis of the evolution of this AR was presented in Paper I.

3. Data analysis

To infer the physical parameters from the available sets of spectropolarimetric data we used two different inversion codes. It is important to recall that an inversion code provides full vector magnetic fields, but only the line-of-sight component of the velocity, in the observer's reference frame. Since one infers the three components of the vector magnetic field, the resulting inclinations and azimuths can be projected onto the local solar reference frame (i.e., with respect to the solar vertical, *z*, and along the solar latitude and longitude planes). However, difficulties arise when this transformation is carried out. The well-known 180° ambiguity (due to the angular dependence of Stokes *Q* and *U* with the azimuth) provides two solutions for the magnetic field, with different azimuths and inclinations when projected onto the local solar reference frame. To find the correct solution, we used the AZAM code for the disambiguation of the magnetic field vector (Lites et al. 1995) (see also Sect. 3.2 of Paper I for a more detailed explanation). Doppler shifts provide only one component of the velocity vector, the one projected along the LOS, rendering the projection onto the local solar frame impossible. Since the aim of this work is to compare the LOS velocities and their associated vector magnetic fields, for the remainder of this paper we will leave the magnetic field inclinations and azimuths in the observer's frame. As our observations were done relatively close to disk center, the distinction between the two frames is more quantitative than qualitative. In order to show the impact of using the vector magnetic field in the observer's frame instead of in the local solar frame, Table 2 provides two examples of the inclinations ($\gamma \rightarrow \gamma_\odot$) and the azimuths ($\phi \rightarrow \phi_\odot$), averaged over several pixels, in both reference frames. An inclination of $\gamma = 90°$ in the LOS frame means that the field lines are perpendicular to the LOS, while $\gamma_\odot = 90°$ means that they are parallel to the solar surface. As can be deduced from Table 2, while the exact values differ between the two frames, the horizontal or vertical nature of the field vectors is mostly preserved.

3.1. Helium 10830 Å and silicon 10827 Å inversions

Before inverting the helium spectra we carried out a 3×6 binning of the data along the scanning and slit directions, respectively, and a binning of 3 pixels in the spectral domain to increase the signal-to-noise ratio (S/N), rendering a value of ∼ 2000 for all maps. The resulting spectral sampling is ∼ 33.1 mÅ px^{-1} and the pixel size 1.2 × 1.0 arcsec^2 and 1 × 1 arcsec^2, for July 3 and 5, respectively. However, since the Si I line is much stronger than the He I triplet, the inversions of the former were carried out without any binning, the pixel size being 0.40 × 0.17 arcsec^2 and 0.30 × 0.17 arcsec^2, on July 3 and 5 respectively. This preserved the original spatial resolution at an expense of a lower S/N of ∼ 500. The binned silicon data and inversions were used solely for the purpose of Table 2.

The chromospheric He I 10830 Å triplet was inverted using a Milne–Eddington inversion code (MELANIE; Socas-Navarro 2001). This code assumes that the source function varies linearly with optical depth while the remaining semi-empirical parameters stay constant with height. MELANIE computes the Zeeman-induced Stokes profiles in the incomplete Paschen–Back (IPB) effect regime (see Socas-Navarro et al. 2004; Sasso et al. 2006, for a better understanding of the IPB effect on the Stokes profiles in the He I 10830 Å region) and has a set of nine free parameters, which are iteratively modified by the code in order to obtain the best match between the synthetic and the observed Stokes data. The macroturbulence and the filling factor, or fraction of the magnetic component occupied inside each pixel, were fixed at 1.2 km s^{-1} and $f = 1$ in the inversion, so no stray-light was used. Atomic-level polarization is not taken into account in MELANIE. However, this is not necessary for this AR filament, since Kuckein et al. (2009) proved that these He I Stokes profiles are dominated by the Zeeman effect.

The photospheric Si I 10827 Å line was inverted with the SIR code (*Stokes Inversions based on Response functions*; Ruiz Cobo & del Toro Iniesta 1992) which solves the radiative transfer equation assuming local thermodynamic equilibrium (LTE). SIR gives a depth-dependent stratification of the inferred physical parameter as a function of the logarithm of the LOS continuum optical depth at 5000 Å.

We carried out two sets of inversions for the Si I line. The first set, referred to hereafter as "standard" inversions, used a uniform weighting scheme for the four Stokes parameters: $w_{I,Q,U,V} = 1$. An average intensity profile of the non-magnetic areas of each map (regions where Stokes *Q*, *U*, and *V* had negligible values), was used as representative of the stray-light. The stray-light fraction, α, used here as a proxy for the filling factor, was left as a free parameter in the inversion. Note that in the case of helium, the line is weak in quiet regions, so the use of a magnetic filling factor does not provide any benefit. We studied the response function (RF) to velocity perturbations in several model atmospheres obtained from the inversion of the filament data, finding a consistent value of $\log\tau = -2$ for the height at which the sensitivity was the highest. The height stratification derived by the inversion code was not used since the velocities at other optical depths had larger error bars.

The Doppler shift of the stray-light profile cannot be set as a free parameter in the SIR inversion code. This extra freedom was used in the studies by Okamoto et al. (2009) and Lites et al. (2010) to separate the magnetic and non-magnetic Doppler shifts. While the latter were dominated by granulation patterns, the former provided clear indications of upflows – a crucial result that we want to investigate further in this paper. To this end, we produced a second set of SIR inversions that were able to retrieve the Doppler shifts of the magnetic component without interference from a possible shift of the stray-light profile. These inversions, referred to heretofore as the "magnetic" inversions, forced a zero-weighting ($w_I = 0$) for Stokes I, basically eliminating any sensitivity to the intensity profile, and hence to the stray-light, in the inversion procedure. Furthermore, since we were interested in the Doppler shifts of the transverse fields near the PIL, we weighted Stokes Q and U equally with $w_{Q,U} = 1$ and set the weight of Stokes V to $w_V = 0.1$. The filling factor was fixed to $f = 1$. The remaining parameters were initialized in the same way as in the "standard" silicon inversions.

Bard & Carlsson (2008) reported in their work that the Si I 10827 Å line is formed in non local thermodynamic equilibrium (NLTE) conditions. In Paper I we tested the NLTE effects on the inversions of the Si I line in the filament, using the departure coefficients, β (defined as the ratio between the population densities calculated in NLTE and LTE), reported in Bard & Carlsson (2008). We found almost negligible changes in the retrieved LOS velocities, temperature being the only parameter that was substantially affected in the upper layers. Therefore, we decided not to consider the departure coefficients for the purpose of the present work.

The reader is referred to Paper I for a more thorough description of the inversions and NLTE effects.

3.1.1. Two-component inversions

The presence of several atypical Stokes V profiles (i.e., with several highly redshifted lobes) in the Si I 10827 Å line led us to use a two-magnetic component SIR inversion for these cases (see Sect. 4.2). Therefore, we had two initial guess atmospheres. For the first one, we used the same atmospheric model as that from the previous single-component inversion, but for the second, we increased the magnetic field strength from 500 to 1500 Gauss and the velocity from 0.5 to 10 km s^{-1}. These initial conditions resulted in a good performance of the SIR code.

3.2. Wavelength calibration

The main aim of this work is to provide reliable Doppler velocities measured at the filament at both heights. In order to calibrate these velocities on an absolute scale, we had to correct them for several effects such as Earth's orbital motions and the solar gravitational redshift (see Appendix A for a complete description of the calibration). The wavelengths presented in Table 1 were all obtained from the *National Institute of Standards and Technology* (NIST) except for the one corresponding to the telluric line. The literature reports several values, with differences of the order of tens of mÅ, which are large enough to cause systematic errors in our velocity calibration. We propose a new value for the rest wavelength of this telluric line, which we inferred by calibrating flat field TIP-II data taken at disk center (see Appendix B).

4. Results

4.1. Doppler velocities

The inferred line-of-sight velocities of four representative cases (one on July 3 and three on July 5) are shown as slit-reconstructed maps in Fig. 3. Blue means upflow ($v < 0$) while red indicates downflow ($v > 0$). The pixels enclosed by the contours have LOS magnetic field inclinations between $75° \leq \gamma \leq 105°$, γ being the inclination inferred from the corresponding silicon or helium inversions. This criterion was chosen to study the velocities associated to transverse fields which, as reported in Paper I, dominate along the filament. The contours denote the area they belong to. The green contours enclose pixels with transverse field lines which lay at the orphan penumbral region whereas the black contours correspond to the spine region. Bear in mind that the FOV on July 5 only overlaps approximately with the upper half of the July 3 map (the white dashed rectangles in Fig. 2 give an idea of the common FOV). Moreover, small shifts of the FOV (in the vertical direction) between different maps of July 5 are also present.

The panels in the *upper* row of Fig. 3 correspond to the Si I 10827 Å velocities, scaled between ±1 km s^{-1}, inferred from the standard inversions, i.e., those with $w_{I,Q,U,V} = 1$. We found alternating blue and red patches in all panels, which revealed a mixture of upflows and downflows along the PIL, i.e., inside the contours. However, it is clear that on July 3, the inside of the black contour is more dominated by upflows than on July 5. On this day, there are no significant differences between the velocity patterns of the orphan penumbrae and the spine.

We now turn to the panels of the *middle* row of Fig. 3. The velocity maps correspond to the magnetic inversions as defined in Sect. 3.1 ($w_{I,Q,U,V} = 0, 1, 1, 0.1$). We therefore assume that the velocities in these panels are more likely to represent the motions of the transverse magnetic field lines (as opposed to the maps from the first row, which are more influenced by unmagnetized regions and flows along vertical field lines). The inversion code had problems in converging properly when Stokes Q and U were small, i.e., where the magnetic fields were weak or almost vertical. Nevertheless, along the PIL, the inversion code performed well and the uncertainties obtained were of the same order of magnitude as those from the standard inversions. On July 5, a comparison of the *middle* with the *upper* panels reveals that the "magnetic" Si I velocities inside the contours are globally more dominated by *blueshifts*, rather than redshifts. We interpret this result as an indication of a predominant upward motion of the transverse field lines in the photosphere, in particular inside the orphan penumbrae (green contours). Similarly, on July 3, there is more of an upward trend in the motions of the transverse fields.

The velocity maps inferred from the (binned) He I 10830 Å inversions are presented in the *lower* row of Fig. 3. Note that the color is now scaled between ±2 km s^{-1}. The first striking result are the ubiquitous red areas (indicative of downflows) that extend almost everywhere, with the exception of the region near the PIL. On July 3, an almost perfect correlation between the transverse field lines inferred from the helium inversions and the

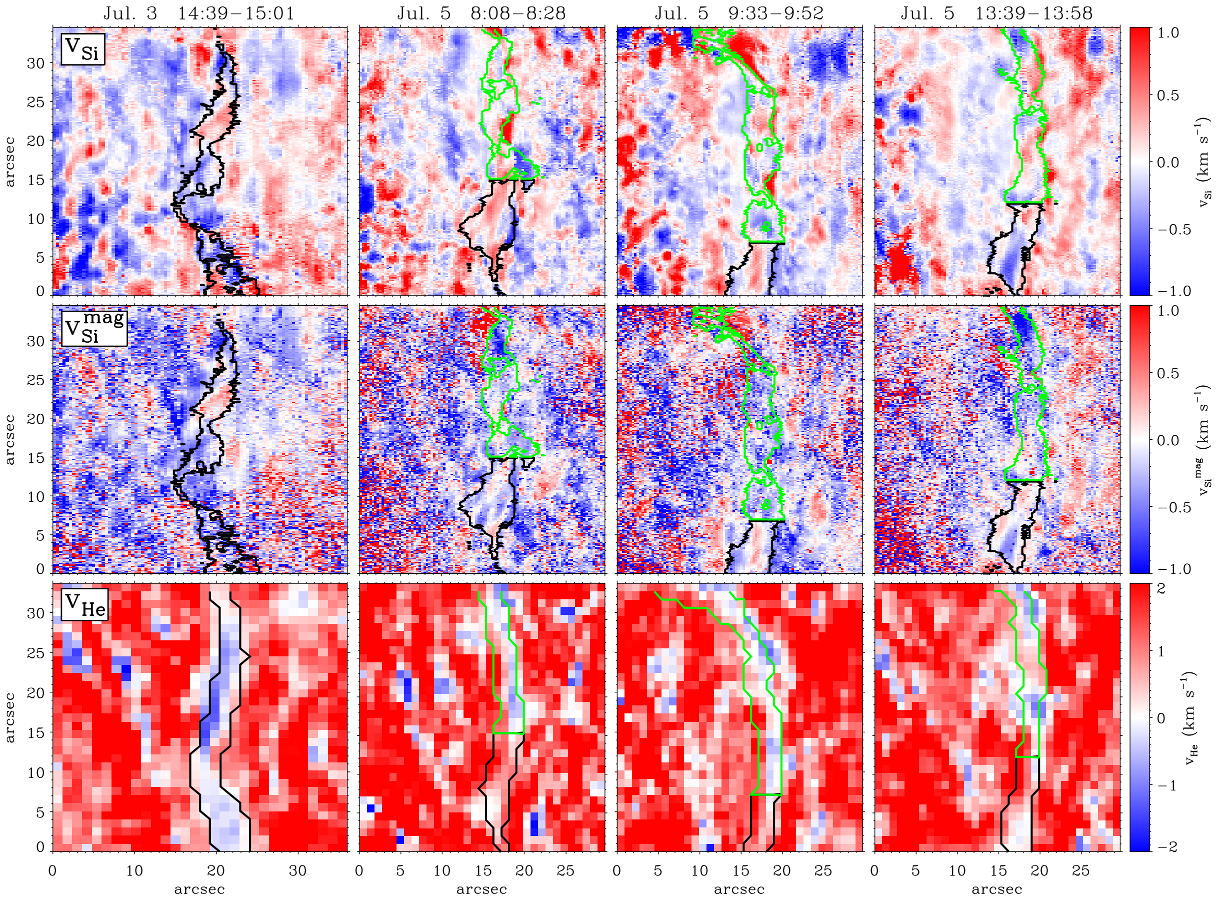

Fig. 3. Line-of-sight velocities inferred from: the Si I 10827Å full Stokes "standard" inversions (*top* row), the Si I 10827Å "magnetic" inversions (with weights: $w_I = 0$, $w_{Q,U} = 1.0$ and $w_V = 0.1$) (*middle* row) and He I 10830Å inversions (*bottom* row) at different times. Note that the color scale is saturated at [−1,1] and [−2,2] km s^{-1} for silicon and helium respectively. Pixels inside the contours have magnetic field inclinations, with respect to the LOS, between $75° \leq \gamma \leq 105°$. In the July 5 maps, the colored contours distinguish between the orphan penumbrae area (green) and the spine region (black). On July 3, only the spine of the filament was seen. Negative velocities (blue) indicate upflows while positive velocities (red) indicate downflows.

upflow areas can be seen within the black contour in the *lower lefthand* panel. Bearing in mind that on July 3 we clearly saw the filament axis in the helium core absorption map (see Fig. 2), and in Paper I we found sheared field lines parallel to its axis, one can easily deduce that the filament axis is rising in the chromosphere. Typical rising speeds are in the range [0,-1.5] km s^{-1}.

Two days later, on July 5, the spine region (black contours) hardly shows any upflows. The large-scale redshifted pattern seen elsewhere is, however, weaker. This means that, even if the filament axis was not moving upwards on July 5, it was still able to interfere with the mechanism that generates the large scale downflows (see Sect. 4.3). In the diffuse filament region (above the orphan penumbrae, marked with green contours), the velocity pattern is fundamentally different. Once again, the transverse fields near the PIL harbor clear signs of upflows. It is thus evident that, while the general trend observed in He I corresponds to a large scale downflow, the filament axis (near the PIL) is a place where the downflows are not as strong and sporadic upflow patches are also present. We will discuss this issue later, in Section 4.3.

To understand the general trends in the velocity maps of Fig. 3, a statistical study of the average velocities ($< v >$) inside the black and green contours was carried out and compiled in Table 3. The number of averaged points (#) and the standard deviation (σ) are also provided in this table. We have found the following:

1. On July 3, the mean velocities inferred from the Si I inversions at the spine (i.e., below the filament axis) show an obvious blueshift. The magnetic inversions, averaging $< v_{\rm Si}^{\rm mag} >\sim -0.150$ km s^{-1}, are more blueshifted than the standard inversions. Upflows are also found in the chromosphere ($< v_{\rm He} >\sim -0.240$ km s^{-1}).
2. For the first four maps of July 5, the spine presents an upward motion of the photospheric transverse fields (black contours) as inferred from the magnetic inversions, with typical velocities of $< v_{\rm Si}^{\rm mag} >= -0.215$ km s^{-1}. In the last three maps the velocities drop to almost zero. The standard Si I inver-

Table 3. Mean Doppler velocities ($< v >$), of all available maps for both days, calculated inside the contours, where the inferred LOS inclinations are between $75° < \gamma < 105°$, i.e., along the PIL. We distinguish between two different areas: the filament axis or spine (black contours in Fig. 3) and the orphan penumbral area (green contours). σ stands for the standard deviation and # is the number of pixels in each area selected for the study.

			Spine			Orphan penumbrae		
Day	Time range (UT)	Inversion	$< v >$ (km s^{-1})	σ (km s^{-1})	# points	$< v >$ (km s^{-1})	σ (km s^{-1})	# points
3 Jul.	13:53 – 14:14	Si	− 0.123	0.725	2097	No orphan penumbrae		
		Si$^{\rm mag}$(†)	− 0.134	0.546	1974			
		He	− 0.266	0.574	146			
3 Jul.	14:39 – 15:01	Si	− 0.010	0.542	1114	No orphan penumbrae		
		Si$^{\rm mag}$	− 0.163	0.406	1088			
		He	− 0.216	0.521	94			
5 Jul.	7:36 – 8:05	Si	− 0.011	0.424	1019	+0.086	0.383	831
		Si$^{\rm mag}$	− 0.190	0.333	1018	−0.250	0.329	825
		He	+ 0.808	0.566	42	+0.547	1.303	54
5 Jul.	8:08 – 8:28	Si	+ 0.108	0.326	870	+0.026	0.353	1009
		Si$^{\rm mag}$	− 0.144	0.263	870	−0.241	0.368	997
		He	+ 0.884	0.604	42	+0.346	0.951	59
5 Jul.	8:42 – 9:01	Si	− 0.011	0.186	780	+0.079	0.317	1127
		Si$^{\rm mag}$	− 0.237	0.288	780	−0.243	0.353	1106
		He	+ 0.954	0.564	36	+0.427	1.002	63
5 Jul.	9:02 – 9:21	Si	− 0.040	0.267	760	+0.110	0.322	1023
		Si$^{\rm mag}$	− 0.291	0.246	760	−0.229	0.336	1006
		He	+ 0.649	0.464	37	+0.183	0.622	62
5 Jul.	9:33 – 9:52	Si	+ 0.045	0.263	569	+0.021	0.332	1497
		Si$^{\rm mag}$	− 0.085	0.248	569	−0.209	0.400	1457
		He	+ 1.013	0.645	22	+0.366	0.826	102
5 Jul.	13:39 – 13:58	Si	− 0.127	0.282	755	+0.021	0.314	1292
		Si$^{\rm mag}$	− 0.063	0.248	755	−0.283	0.419	1273
		He	+ 0.779	0.960	41	+0.278	0.814	60
5 Jul.	14:31 –14:51	Si	− 0.046	0.375	618	+0.211	0.301	1257
		Si$^{\rm mag}$	+ 0.014	0.290	618	−0.099	0.427	1248
		He	+ 1.083	1.009	30	+0.271	0.558	75

Notes. (†) Velocities above 2 km s^{-1} or below -2 km s^{-1} inferred from the "magnetic" Si I inversions (and mostly due to weak Q and U signals) were excluded from the statistics. However, only very few points were affected by this filter (between 9 – 40; and 123 for the first map).

sions show, by contrast, velocities which oscillate around zero ($< v_{\rm Si} >\sim -0.012$ km s^{-1}).

3. On July 5, the chromospheric velocities at the spine are dominated by downflows in the range of $v_{\rm He} \in [0.65, 1.08]$ km s^{-1}. We note, however, that these downflows are smaller than the typical values observed elsewhere in the surrounding facular region (see Sect. 4.3).
4. At the orphan penumbrae (green contours), there is a systematic difference between the photospheric LOS velocities inferred from the "standard" and those obtained from the "magnetic" inversions of the Si I line. While the latter clearly show upflows in all maps, with values between $v_{\rm Si}^{\rm mag} \in [-0.099, -0.283]$ km s^{-1} and an average of $< v_{\rm Si}^{\rm mag} >= -0.222$ km s^{-1}, the standard inversions show slightly slower velocities, with downward motions in the range of $v_{\rm Si} \in [0.021, 0.211]$ km s^{-1}, and a mean value of $< v_{\rm Si} >= 0.079$ km s^{-1}.
5. Above the orphan penumbrae (inside the green contours) the average velocities inferred from the He I inversions show downflows in the range of $v_{\rm He} \in [0.18, 0.55]$ km s^{-1}. These downflows are weaker than those observed in the spine (see point 3 above).

4.2. Two-component Stokes V profiles at the PIL: supersonic downflows

On July 5, the day when we first observed the orphan penumbral system, we detected the presence of atypical multilobed Stokes V profiles (e.g., Fig. 4) in the Si I 10827Å line. These multilobed profiles are a clear indication of the presence of several magnetized components within the resolution element. Most of these multi-component profiles were found near the borders of the orphan penumbrae. To illustrate this, we selected one map from July 5 (taken between 13:39–13:58 UT) and marked the location of all two-component profiles with small cyan crosses (see Fig. 5). The other maps from July 5 show a similar spatial distribution of the multi-component profiles. Only points with a Stokes $V/I_{\rm c}$ signal of at least 0.01 were selected for this study. In this way, we made sure that the origin of these profiles was related to a multiple-velocity component scenario, and we were able to rule out other causes such as mixed polarities, which are also a very common occurrence in the proximity of PILs. Figure 5(a) shows a continuum intensity image. The two-component profiles are located on top of pores and orphan penumbrae, between $x \in [16'', 22'']$. The helium red component intensity map in Fig. 5(b) shows that the largest group of atypical Stokes V profiles is co-spatial with the dark He I thread located around $[x, y] = [20'', 20'']$. Only three asymmetric profiles were detected at the spine, around $[x, y] = [18\overset{''}{.}5, 3'']$. The contours in Figs. 5(b-c) correspond to the darkest areas, i.e., highest absorp-

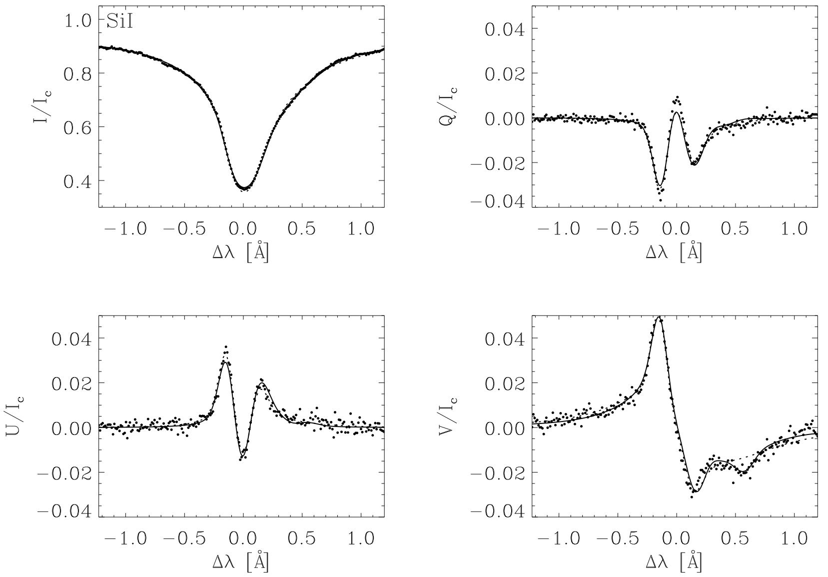

Fig. 4. From *left* to *right* and *top* to *bottom*: Stokes *I*, *Q*, *U* and *V* profiles (dots) of the Si I line normalized to the continuum, and best fits (solid line) using a two-component SIR inversion. The profiles correspond to $[x, y] = [20.''1, 19.''4]$ (area 4 in Fig. 5). The single-component fit (i.e., standard fit) is shown in the dashed lines for comparison and clearly does a worse job at fitting Stokes *V*. The physical parameters inferred from the two-component inversion are: $v_1 = 0.3 \pm 0.2\,\mathrm{km\,s^{-1}}$, $B_1 = 1001 \pm 68\,\mathrm{G}$, $\gamma_1 = 67° \pm 3°$, $\phi_1 = 114° \pm 2°$, $f \sim 0.94$ for the standard component and $v_2 = 11 \pm 2\,\mathrm{km\,s^{-1}}$, $B_2 = 1424 \pm 300\,\mathrm{G}$, $\gamma_2 = 23° \pm 20°$, $\phi_2 = 81° \pm 51°$, $f \sim 0.06$ for the magnetic one. The inferred stray-light is $\alpha \sim 5\%$. The uncertainties associated to the parameters of the second component were obtained with SIR and verified with the sensitivity analysis explained at the end of Section 4.2.

tion of the He I red component, of Fig. 5(b). Bear in mind that the multi-component profiles were only found in the photosphere; there is no signature of these highly Doppler shifted components in the chromospheric He I 10830 Å profiles. The atypical Si I profiles contain information about a strongly redshifted component that the standard SIR inversions cannot pick out. The conspicuous signature present in Stokes *V* calls for a two-atmosphere inversion that can provide some insights into the nature of this shifted component. Such inversions were performed on those specific profiles where this signature was visually detected. The following properties were inferred:

1. The atypical Stokes *V* profiles appear at, or very close to, the PIL, i.e., where the magnetic field lines are mainly horizontal (see inclinations inferred from the standard single-component silicon inversions, γ_{Si} in Fig. 5(d)).
2. From the two-component SIR inversions we inferred: (1) a dominant transverse component with a filling factor in the range of $f_1 \in [0.87, 0.98]$ and inclinations with respect to the LOS $\gamma_1 \in [68°, 95°]$. This is the component that is most similar to that retrieved by the standard inversions. (2) A second component with smaller filling factors, $f_2 \in [0.02, 0.13]$, oriented more parallel to the LOS, with inclinations $\gamma_2 \in [21°, 58°]$.
3. The inferred Doppler maps show that the dominant transverse component has velocities in the range of $v_1 \in [-0.1, 0.5]$ $\mathrm{km\,s^{-1}}$ while the longitudinal one, with smaller filling factors, has downward velocities $v_2 \in [6.2, 11.9]$ $\mathrm{km\,s^{-1}}$. It is clearly a supersonic downflowing component.
4. In Fig. 5, all the detected atypical Stokes *V* profiles had a second component with the same polarity than the first one, except for the group of points between $y = [11'', 13'']$ (area 1 in Fig. 5(c)) which had a second component with opposite polarity to that of the first one. Note, however, that the dominant polarity, being highly transverse, is very much prone to polarity changes due to projection effects.

Table 4. Mean LOS inclinations ($<\gamma>$) and velocities ($<v>$) inferred from the two-component inversions of the Si I line. The different areas are marked in Fig. 5(c). σ stands for the standard deviation and # is the number of pixels averaged in each area.

Area	Comp.	$<\gamma>$ (°)	σ_γ (°)	$<v>$ ($\mathrm{km\,s^{-1}}$)	σ_v ($\mathrm{km\,s^{-1}}$)	# (px)
1	1	94.6	1.4	−0.126	0.135	25
	2	57.7	51.5	11.890	8.867	
2	1	76.3	2.3	0.351	0.034	3
	2	20.7	20.2	4.699	2.439	
3	1	68.5	6.5	0.496	0.315	32
	2	43.7	18.1	7.595	2.278	
4	1	72.7	11.8	0.355	0.256	85
	2	28.4	17.4	9.632	2.795	
5	1	78.7	3.5	0.250	0.113	18
	2	49.4	20.4	6.190	2.919	

The multiple component profiles were grouped in five separate areas. Since the properties of the dominant and of the redshifted components differ in each of these areas, a separate statistical study for them has been carried out. The five areas are marked in Fig. 5(c). Table 4 summarizes the mean LOS inclinations ($<\gamma>$) and velocities ($<v>$), for both components, in the five areas. The standard deviation (σ) of both quantities, as well as the number of pixels used for the statistics (#), are also listed. As stated before, the second component is completely

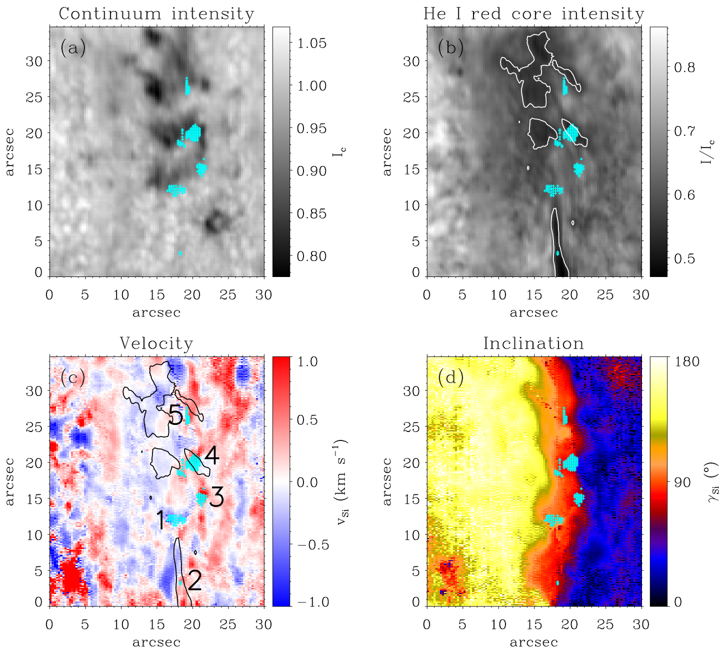

Fig. 5. (a) The continuum intensity image show pores and orphan penumbrae at the PIL. (b) The absorption in helium (red core) clearly shows the spine in the lower part of the image and a diffuse filament in the upper part. (c) LOS velocity map inferred from the standard single-component inversions of SIR. The marked areas (1–5) correspond to the two-component Stokes *V* profiles (the average inclinations and velocities for these areas are presented in Table 4). (d) LOS inclinations from the single-component inversions. In all maps, the cyan colored crosses mark the positions where two-component profiles were detected.

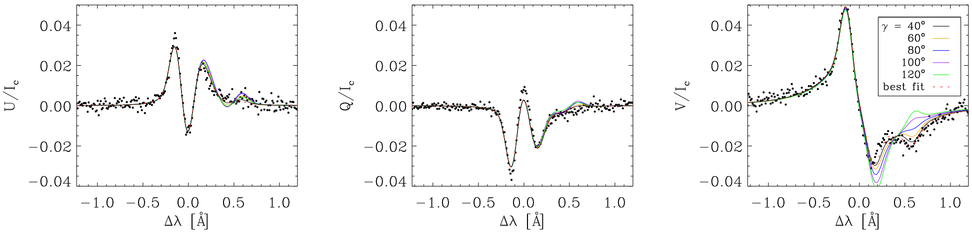

Fig. 6. Dots represent the observed Si I Stokes *U*, *Q*, and *V* profiles (same as Fig. 4). The overplotted synthetic profiles were computed using different magnetic field inclination angles for the second component, that varied between $\gamma \in [40°, 120°]$. The test was performed by varying the magnetic field inclination of the second component and keeping the remaining atmospheric parameters (which came from the best fit of the SIR inversion) fixed. The dotted red line shows the best matching profile, whose corresponding atmospheric parameters are shown in the caption of Fig. 4.

dominated by magnetic field line inclinations which are more longitudinally orientated. These inclinations, however, vary substantially within each area (note the large values of the standard deviation σ_γ for Comp. 2 in Table 4). In these atypical cases, the inversion code provides considerable uncertainties associated with the atmospheric parameters, something that should be expected since this redshifted component has a small effect on the observed profiles, as reflected by its low filling factor (mostly < 0.1). However, a clear tendency for smaller inclinations, i.e., more vertically oriented field lines, is seen in all five areas.

Given the small amplitude of the signatures that this component leaves on the emergent Stokes profiles, the question is raised of how reliable the inversions are. To address this question, we performed the following test: We selected several pixels with multilobed Stokes *V* signals and used the atmospheres resulting from the two-component inversions to synthesize sets of Stokes profiles. For each model atmosphere, several different realizations of the synthesis, with different values of the inclinations and azimuths of the second component, were carried out (the first component was kept unchanged). Figure 6 shows one example of the synthetic Stokes *Q*, *U*, and *V* profiles (Stokes *I* showed no changes and was therefore not presented) with different inclinations, between 40° and 120°. Stokes *Q* and *U* present minor changes in their shape that are just above the noise level and therefore not conclusive. However, the changes in inclination substantially affected the resulting Stokes *V* profiles. It is apparent from Fig. 6 that the most likely inclination is far from being transverse. In fact, the best fit (dotted red line) yields an inclination of $\gamma = 22.9° \pm 20°$. We also carried out the same test changing the azimuth. Stokes *Q* and *U* were only slightly affected by these variations, again within the noise level, while Stokes *V* was completely insensitive to the changes. This shows

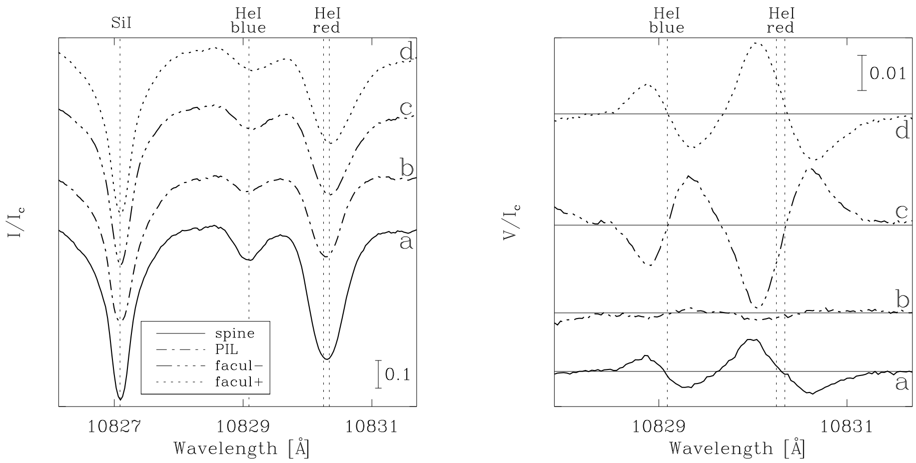

Fig. 7. *Left*: averaged intensity profiles I/I_c of four selected positions of the map acquired on July 5 between 13:39-13:58 UT. Each profile is marked with a character (a–d) which indicates its position in Fig. 2. Note the shifted red wing of the blended He I red component for the two facular profiles indicating the presence of more than one component contributing to the line formation. *Right:* the corresponding helium Stokes V/I_c profiles to the intensity profiles shown on the *left* panel. The solid lines along the x-axis indicate $V/I_c = 0$ for each profile. The dotted vertical lines, in both panels, mark the position of the line cores of the involved ions.

that while the inclination of the redshifted component is well established (and that it is more vertical than the dominant, transverse, component), the value of its azimuth is highly uncertain.

4.3. Ubiquitous downflows around the PIL in the helium velocity maps

As mentioned above, the velocities inferred from the He I inversions outside the PIL (in the faculae) are ubiquitously dominated by downflows on both days (see the lower panels of Fig. 3). This was largely unexpected, so it is important to understand what signature in the spectral profiles made MELANIE infer these downflows. Figure 7 shows four representative Stokes I and V profiles from different areas of the map taken between 13:39–13:58 UT on July 5. They correspond to: (a) the spine, (b) the PIL, (c) the negative and (d) the positive polarities within the faculae. The locations of pixels a–d are marked in Fig. 2. The dotted vertical lines, in Fig. 7, mark the centers of the line cores at rest. In the *lefthand* panel, the intensity spectra comprise the photospheric Si I line and the He I triplet. The cores of the four silicon intensity profiles are almost perfectly centered at their rest wavelengths. However, while the He I triplet profiles of the spine and the PIL are also approximately at rest, the two facular profiles are clearly redshifted. It is also of interest that the red wing of the He I red component of the facular profiles is stretched away from the line core. This, together with the fact that the profiles are not symmetric, indicates that more than one atmospheric component was involved in the line formation process, and that one of these components harbors distinct downflows. The redshift in the helium red component of the facular regions is also seen in their Stokes V profiles (c and d) in the *righthand* panel of Fig. 7. As expected, profile (b) has almost no Stokes V signal since it is located at the PIL, where the transverse fields dominate.

It is, thus, clear that the facular profiles seen in the chromosphere are substantially redshifted. A possible explanation for this is given in Sect. 5. To quantify the general trend of the facular velocities found in our data sets we did averages only taking into account those pixels which had photospheric inclinations close to longitudinal ($\gamma_{\rm Si} < 25°$ and $\gamma_{\rm Si} > 155°$). Note that the inclinations we used are the ones inferred from the Si I 10827 Å inversions, whereas the velocities correspond to the ones obtained from the He I 10830 Å inversions. This criterion ideally distinguishes the points belonging to the faculae (having mainly longitudinal fields at photospheric heights, Martinez Pillet et al. 1997) from those of other areas, such as the PIL or outside the faculae. The mean velocities found in the faculae, for all maps (July 3 and 5), were in the range of $v_{\rm He}^{\rm fac} \sim 1.4 - 1.8\,{\rm km\,s^{-1}}$. The standard deviations associated to these velocities were typically around $\sigma = 1.0 - 1.4\,{\rm km\,s^{-1}}$, and the number of points used for the statistics of each map was between 300 – 400. As mentioned above, since these He I intensity profiles are likely to comprise more than one component, multi-component inversions in this spectral region (e.g., Lagg et al. 2007; Sasso et al. 2011) might reveal slightly stronger downflows in the faculae.

4.4. Time series

A time series with the slit fixed over the PIL was acquired on July 5, approximately between $x \sim 18'' - 20''$ on the *righthand* panel of Fig. 2. The velocities shown in Fig. 8 were retrieved from the standard Si I inversions. Time is represented along the x-axis while the y-axis shows the spatial direction along the slit. In the lower half of the figure, the photospheric 5 minute oscillation is unequivocal. This corresponds to the area below the spine. There is an apparent phase shift of the oscillation pattern, starting at $y \sim 15''$. This shift coincides with the beginning of the orphan penumbrae. The single most striking finding from this figure was the continuous downflow seen between $y \sim 23'' - 25''$ (dark red pattern) throughout the whole time range, with which not even the photospheric oscillation pattern interfered.

The Stokes V profiles were carefully inspected one by one along the slit every minute. This was done in order to find the atypical multilobed Stokes V profiles defined in Sect. 4.2. As in Fig. 5, the cyan crosses in Fig. 8 represent the location of the detected atypical Stokes V profiles. From this figure it is obvious that the lifetime of the supersonic downflow was at least as long as our time series (19 minutes). We take this time to be a lower limit but it might, in fact, be much longer, since this supersonic downflow was not an isolated event. Other strong downflows have been detected on all maps from July 5 (albeit not continuously), starting from 7:36 until 14:51 UT.

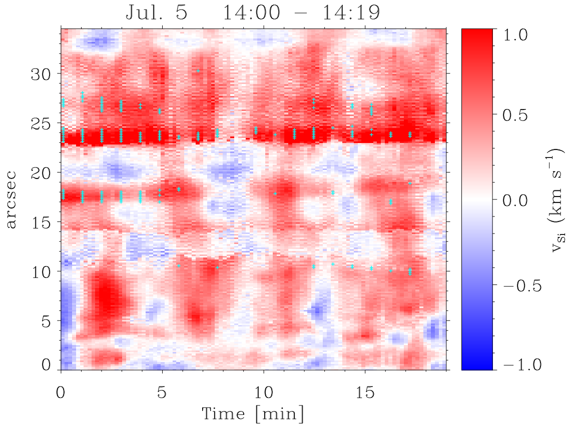

Fig. 8. Photospheric velocity time evolution. The time series was taken with the slit fixed on top of the PIL (between $x \sim 18''-20''$ in the second column of Fig. 2). The velocities were inferred from the "standard" Si I 10827 Å inversions. The cyan-colored crosses mark the positions of the two-component profiles.

5. Discussion

In this paper, we have investigated the line-of-sight velocities inferred from chromospheric and photospheric spectropolarimetric inversions of the Stokes profiles measured in and below an active region filament. The aim of this study, together with the results of Paper I, is to clarify the formation and evolution of this AR filament. In Paper I we reported that the magnetic field configuration of the spine of the filament is compatible with a flux rope topology (on July 3, and also in the spine portion of July 5). Furthermore, the orphan penumbral region of July 5, was also likely to be the imprint of a flux rope, but with its axis sitting low in the photosphere. These results are supported by recent magnetic field extrapolations of the same filament by Yelles Chaouche et al. (2012) who, for July 5, also deduced the presence of a flux rope structure whose axis lay below the formation height of the He I 10830 Å lines. Our AR filament is, therefore, extremely low-lying.

The next question that needs to be addressed is the mechanism by which flux ropes in AR filaments are formed. First of all, at the time of the observing run, the filament had already reached the chromosphere. However, on July 5, the low-lying magnetic structure and the newly appeared pores and orphan penumbrae indicated that new flux had emerged between the two days of observation. This flux was mainly horizontal due to its proximity to the polarity inversion line, as reported in Paper I. Thus, we placed special emphasis on the study of the photospheric LOS velocities associated with these transverse fields, i.e., inferred from what we called the silicon "magnetic" inversions, which provided information similar to that of the Dopplergrams of the magnetic component presented by Okamoto et al. (2009) and Lites et al. (2010). There is a very good agreement among the velocities from all maps of July 5 (see Table 3). All the maps but one pointed to an upward movement of the photospheric transverse fields, with average velocities between $< v_{\rm Si}^{\rm mag} >= -0.21$ and $-0.28\,{\rm km\,s^{-1}}$, the last map being the exception, where slower upward motions ($\sim -0.10\,{\rm km\,s^{-1}}$) are shown. These velocities agree surprisingly well with the ones presented by Okamoto et al. (2009) ($-0.30 \pm 0.20\,{\rm km\,s^{-1}}$). However, when carrying out "standard" inversions, (weighting all four Stokes parameters in the inversion equally) the average inferred velocities were close to zero or positive (downflows), with values between $< v_{\rm Si} >= 0.02 - 0.11\,{\rm km\,s^{-1}}$ and $0.21\,{\rm km\,s^{-1}}$ for the last map. Note that the differences between both inversions is, on average, of around $0.3\,{\rm km\,s^{-1}}$. This is indeed a small number. It corresponds to 11 mÅ or, equivalently, a sixth of the spectral resolution. The fact that we obtain velocities that are more redshifted when we weight Stokes I and V equally in the inversion indicates that a longitudinal component harboring downflows is present, to some degree, in all pixels. While no evidence for this is provided here, we hypothesize that the same chromospheric downflow that is observed almost everywhere in He I has an impact on the Si I data, producing slightly more redshifted values when all Stokes parameters are equally weighted in the inversion code.

In the chromosphere above the orphan penumbrae, the retrieved mean LOS velocities are dominated by downflows in the range of $< v_{\rm He} >= 0.18 - 0.55\,{\rm km\,s^{-1}}$. Nevertheless, these averaged velocities need to be interpreted with caution since the helium velocity maps of Fig. 3 clearly show localized upflows and slower downward motions at the PIL (inside the green contours). These upward motions at the PIL reach velocities of about $-1\,{\rm km\,s^{-1}}$ in all the maps of July 5. A continuous upflow of mass, lasting at least $\sim$ 7 hours, is detected at some locations of the PIL. Since helium traces the upper part of the flux rope (whose axis is lying below, in the photosphere), these localized upflows strongly suggest that the material is being pushed upwards by the magnetic field lines of the top of the flux rope (similar to what is seen in the simulations by Martínez-Sykora et al. 2008). This is in agreement with previous simulations of flux rope emergence (e.g., Fan 2001; Manchester et al. 2004; Archontis et al. 2004; Fan 2009), where only the upper field lines are able to rise and expand in the corona, leaving the main body of the flux tube behind. This process is driven by the so-called Parker instability. This interpretation would lead to plasma drainage wherever the field lines are not horizontal or dipped, and, hence, would explain the photospheric downflows close to the PIL. Sometimes, the downflows at the orphan penumbrae produce atypical multi-lobed Stokes V profiles. Examples of these were found in some areas near the PIL (see Fig. 5). Two-component inversions of these Stokes V profiles yielded mainly supersonic speeds, in the range of $6 - 12\,{\rm km\,s^{-1}}$, for the redshifted component. Similar strong downflows have been detected in the past (e.g., Martinez Pillet et al. 1994; Lites et al. 2002; Shimizu et al. 2008) and have also been found in numerical models of emerging flux regions (Cheung et al. 2008). The case described by Martinez Pillet et al. (1994) is particularly relevant to this paper because it describes a downflow below an AR filament, similar to the ones studied here. Magnetic reconnection is one of the proposed mechanisms to cause these supersonic downflows as suggested from the simulations of Cheung et al. (2008). In our data sets, this could only have taken place in the photosphere which is where we see them clearly. The long periods of time (tens of minutes) during which the redshifted flows persist basically unaltered, almost rule out any link with a fast process such as reconnection. The downflows might also be interpreted as a combination of plasma draining from the flux rope's body during its emergence process at the photosphere and/or the continuation of the ubiquitous chromospheric downflows.

The filament formation model of van Ballegooijen & Martens (1989) would expect horizontal field lines submerging at the PIL after a magnetic reconnection event (van Ballegooijen & Mackay 2007). While strong downflows in our observations are clearly detected at several positions along the PIL, they are never co-spatial with transverse magnetic fields. The inclinations retrieved from the inversions of the atypical Stokes *V* profiles, showed that the second component (the strongly redshifted one) was much more longitudinally orientated ($\gamma_2 \in [21^\circ, 58^\circ]$) than the first one ($\gamma_1 \in [68^\circ, 95^\circ]$) (see more details in Table 4). Our test inversions support the reliability of these results (see Fig. 6). Therefore, we can safely say that our AR filament presents no evidence of submerging horizontal field lines, thus, challenging some features of the aforementioned models.

Let us consider now the spine of the filament, which was seen in the middle of the FOV on July 3 and only in its lower part on July 5. This portion of the filament is what we would call a classical case of AR filament, "classical" meaning that it has a thin elongated shape presenting a flux rope topology and is located in the chromosphere (it is perfectly discernible in the He I absorption image of Fig. 2). There is a distinct difference between the chromospheric LOS velocities of both days. On July 3, the spine is completely dominated by upflows which perfectly trace the transverse fields (see black contour in the *lower left* panel of Fig. 3). The average upward velocity inside this black contour was $< v_{\rm He} >\sim -0.24\,{\rm km\,s^{-1}}$. On July 5, however, the spine is not as strongly blueshifted, characteristic that continues throughout the day (see Fig. 3). Downflows in the range of $< v_{\rm He} >\sim 0.81$ and $1.09\,{\rm km\,s^{-1}}$, are detected in the ~ 7 hours between the first and last maps. We interpret this result as a halt in the rise of the filament's axis. This event makes the spine area be dominated by the same ubiquitous chromospheric downflows that are seen in the rest of the FOV.

The photospheric motions of the spine on July 3 show the same trend as the chromospheric ones, with average upflows of the transverse fields of $< v_{\rm Si}^{\rm mag} >\sim -0.15\,{\rm km\,s^{-1}}$. We interpret this as a coordinated upflow of the entire flux rope. This is compatible with the flux rope emergence simulations, in which the whole structure is very low-lying. On July 5, the transverse fields begin the day moving upwards $< v_{\rm Si}^{\rm mag} >= -0.19\,{\rm km\,s^{-1}}$, but after ~ 2 hours they seem to stop, still remaining at rest by the end of the observing run, four hours later.

We found ubiquitous downflows in the chromosphere, on both sides of the polarity inversion line. This was consistent throughout all of our observations. The average line-of-sight velocity in the faculae, for all maps, was $1.6\,{\rm km\,s^{-1}}$ with a dispersion of $\sim 1.2\,{\rm km\,s^{-1}}$. We hypothesize that these downflows are a manifestation of the so-called *coronal rain*. This phenomenon occurs when plasma condenses in the corona and then flows along coronal loops, down into active regions (Tandberg-Hanssen 1995). So far, however, our knowledge of this process is still rather poor (but see Antolin & Rouppe van der Voort 2012). Recent studies reveal that the velocities found in coronal rain are in a range between $20 - 120\,{\rm km\,s^{-1}}$ (Antolin et al. 2010; Antolin & Verwichte 2011; Antolin & Rouppe van der Voort 2012). This is much faster than the velocities obtained from our data (Fig. 3), although our measurements correspond to lower heights. There is a strong possibility that more than one atmospheric component, along the line-of-sight, contributes to the He I 10830 Å triplet formation. This can be deduced from the shape of the red wings of the intensity profiles in the faculae (*lefthand* panel; Fig. 7). However, the signature is weak and, hence, it is unclear whether strong downflows, such as those reported by previous authors in the He I triplet ($\sim 42\,{\rm km\,s^{-1}}$, e.g., Muglach et al. 1997; Schmidt et al. 2000; Lagg et al. 2007), would be inferred in a multi-component analysis. Another explanation could be that material is falling from the slowly rising flux rope structure on July 3, or from the expanding field lines above the orphan penumbrae on July 5, following vertical magnetic field lines (in a similar way as the draining of rising loops proposed by Lagg et al. 2007). However, these processes can also be considered to be different manifestations of the coronal-rain phenomenon.

6. Conclusions

For the sake of clarity we divided the study of the AR filament into two parts, the main distinction between them being the height at which the filament axis lies. The first part corresponds to the spine (seen mainly on July 3, and also in the lower half of the FOV on July 5), where the filament axis lies in the chromosphere. The second corresponds to the diffuse filament (seen only in the upper half of the FOV on July 5), which sits above the orphan penumbrae and pore regions, and has a much lower-lying filament axis. In this latter case, the helium 10830 Å only traces the upper part of the flux rope, as explained in Paper I. The main conclusions of this study are:

1. On July 3, the LOS velocities inferred from the helium and "magnetic" silicon inversions (that trace the behavior of the horizontal magnetic fields) in the *spine* region, show generalized upflows, which we interpret to represent the emergence of the flux rope structure as a whole. Two days later, on July 5, the spine shows downflows in the chromosphere, similar to those seen elsewhere in the facular region. Yet the photospheric velocities in this region present upflows for the first few hours of the day that drop to velocities close to zero towards the end of the observing run.
2. On July 5, in the chromosphere, above the orphan penumbrae, the LOS velocities are on average redshifted. This redshift is, however, smaller than the dominant redshift seen in the facular region. Indeed, blueshifted patches are present along the PIL in all data sets. We propose that the blueshifted patches seen in the chromosphere are due to field lines which expand from the lower-lying flux rope into the chromosphere, similar to what is found in the flux rope emergence simulations (e.g., Martínez-Sykora et al. 2008). The photospheric transverse field lines along the orphan penumbrae are clearly moving upwards. This is consistent in all seven data sets. Therefore the sheared field lines (the flux rope axis) are rising.
3. Atypical multilobed Stokes *V* profiles were found in the photosphere near the PIL. Two-component inversions of these profiles revealed localized supersonic downflows in the strongly redshifted component. These downflows last for at least 19 minutes, ruling out any episodic origin. Furthermore, the retrieved magnetic fields associated with this component are oriented along (or very close to) the line of sight. Therefore, we cannot identify this component with submerging loops that harbor horizontal fields as in the models from van Ballegooijen & Martens (1989) and van Ballegooijen & Mackay (2007). It is also important to point out that the number of detected two-component profiles was only a small percentage of the total number of points inside the PIL (12 %), which, on average, showed an upward motion of the transverse fields.

4. Almost ubiquitous redshifts of the chromospheric He I 10830 Å triplet, with average downflows of $\sim 1.6\,\mathrm{km\,s^{-1}}$ and a dispersion of $\sim 1.2\,\mathrm{km\,s^{-1}}$, were found in the faculae in all data sets.

The global picture resulting from the Doppler shifts studied in this paper can be summarized as follows. AR faculae are immersed in a global rainfall of mass from the upper layers, as indicated by the redshifted He I line. We have tentatively associated this redshift with coronal rain. This process has no evident counterpart in the photosphere, being some localized supersonic downflows the only possible candidate. In this environment, the transverse field lines (including the filament axis observed either in the chromosphere or in the photosphere) display upflows. The only case where this does not hold true is that of the chromospheric spine region on July 5. In this area, only the global downflow is observed.

As we have learned from the simulations, the process of flux rope emergence through the photosphere is not an easy one and will often be aborted. We propose that this is what might have happened on July 5 at the spine region. Note, however, that the rest of the filament for this day displayed clear upflows at both heights. All in all, the present study supports the scenario of an emerging flux rope from below the photosphere. Vector magnetograms, as well as LOS velocities in the photosphere and chromosphere, agree with the proposed scenario. Whether or not this emergence process is common to all active region filaments, or at least to those that present a photospheric manifestation (orphan penumbrae), needs to be proven by using further multi-wavelength and multiheight observations.

There are some limitations in this work that need to be considered. First, an important observational gap on July 4 exists. Data from that day would have contributed to a better understanding of the inferred magnetic structure observed on July 5. Another limitation to this work is the small field of view of the polarimeter that we had at the time of the observations (nowadays the slit is twice as large). This work has proved that there is an imperative need for multi-wavelength instruments and larger FOVs in order to understand the formation process and evolution of AR filaments. It is crucial to have magnetic field information of at least two heights, e.g., in the photosphere and in the chromosphere, to carry out a simultaneous and co-spatial analysis of the evolution of the filament.

The flux rope that constitutes the studied AR filament is extremely low-lying, especially the portion observed on the second day. This result makes it hard for the filament formation models that build flux ropes in the corona by reconnection (e.g., van Ballegooijen & Martens 1989; DeVore & Antiochos 2000) to reproduce the scenario that we observe. In particular, the large scale submergence of photospheric transverse field lines is not observed in our data. While a rather complete picture of the evolution of this AR filament (favoring a flux rope emergence from below the photosphere) has come out of this series of papers, we would like to stress that the formation process of AR filaments in general could differ, maybe substantially, from this case.

Appendix A: Velocity calibration

In order to obtain LOS velocities on an absolute scale, our Doppler shifts have to be calibrated to high precision and corrected for the systematic effects introduced by the Earth's rotation, the orbital motion of Earth around the Sun, the solar rotation, as well as for the solar gravity redshift.

The final accuracy and precision have to be high enough to be able to measure typical photospheric Doppler shifts which, in the case of the Si I line, correspond to velocities in the range of few hundred $\mathrm{m\,s^{-1}}$. Since our spectral range comprises two telluric H_2O lines, we can use these to calculate our sampling (Å per pixel). A Gaussian function with six terms was fit to the deepest part of these lines in our data in order to determine the position of their centers. The difference, Δx, is the distance between both lines in pixel units. The same process was carried out on the Fourier Transform Spectrometer (FTS) spectrum (Kurucz et al. 1984) from the Kitt Peak National Observatory, obtaining $\Delta\lambda = 1.873$ Å for the distance between both lines. The spectral sampling is merely calculated by dividing $\Delta\lambda/\Delta x$. This was done for each map using the average spectrum from a small non-magnetic region (containing about 1000 pixels). The mean spatial sampling of all maps is 11.035 ± 0.010 mÅ/px. Ideally, the sampling should always be the same. It can be theoretically calculated using the specifications of the telescope and of the spectrograph. A comparison with the theoretical sampling (11.240 mÅ/px) reveals that the calibration delivered a slightly smaller value, but not too different.

We are now able to construct the wavelength array using the calculated spectral sampling and a telluric line whose central wavelength is known, as a reference. According to the solar spectrum atlas of Swensson et al. (1970), the telluric line closest to the He I triplet has a wavelength of 10832.120 Å, although the authors also provide another value: 10832.150 Å. However, when we calculate the line center position using the Gaussian fit to the FTS spectrum we find a wavelength of 10832.099 Å. Note that the wavelengths of the FTS atlas are not corrected for the gravity shift. This is perfectly adequate for telluric lines, which are, indeed, not affected by it. Other wavelength values, differing slightly from those mentioned previously, can also be found in the literature. These discrepancies led us to make our own estimate for the center wavelength of the H_2O telluric line. The process, explained in Appendix B, results in a wavelength of 10832.108 Å. This value is supported by the work of Breckinridge & Hall (1973), who inferred a wavelength of 10832.109 Å with an accuracy approaching ±1 mÅ.

The newly constructed wavelength array is referred to a terrestrial reference frame, that does not account for any relative orbital motions. We followed the calibration procedures presented in Appendix A of Martinez Pillet et al. (1997), and references therein, adapted to the Observatorio del Teide, to obtain absolute line-of-sight velocities. Line shifts due to Earth's rotation, orbital motion of Earth around the Sun and solar rotation have been corrected. In the same way, the gravitational redshift, $\Delta\lambda_{\mathrm{G}} = (GM_{\odot}/R_{\odot}c^2)\lambda$ (which translates into 23 mÅ for this spectral range), was also corrected in our calibration. The effect of convective blueshift has been studied for the photospheric Si I line, however, after reviewing the literature and studying the response function to various physical perturbations of this line, we concluded that the correction is rather negligible owing to the formation height of the Si I line, which happens at a considerable height ($\log\tau \sim -2$) above the surface.

Appendix B: Determination of a new telluric line wavelength

As mentioned in the previous appendix, the literature quotes several different values for the central wavelength (λ_{T}) of the H_2O telluric line next to the He I triplet. We calibrated our spectrum using this telluric line as a reference, but the resulting velocity maps were clearly shifted to the red (when using λ_T = 10832.120 Å) or to the blue (when using λ_T = 10832.099 Å). This is, we found systematic photospheric redshifts or blueshifts (depending on the wavelength used for the calibration) in the faculae, where velocities are expected to be around zero (see Fig. 12 in Martinez Pillet et al. 1997, where high filling factor faculae show no velocity shift). Shifts of the same order of magnitude were found when compared to new data from a recent observing campaign in 2010 with the Tenerife Infrared Polarimeter at the VTT. We attribute this inconsistency to an incorrect value of the central wavelength of the telluric line and therefore we corrected its wavelength using the following method: we took three flat fields from our 2010 campaign with TIP-II (August 21 and 22); two from the morning and one from the afternoon. All of the flat fields were taken at disk center in the quiet sun, with a random circular movement of the telescope pointing of up to 50″. These maps were then used as input data for the standard reduction procedure including flat field, dark current and polarimetric calibration corrections (Collados 1999, 2003). The spectral sampling for each flat field was inferred using the same procedure described in Appendix A. Using λ_T = 10832.120 Å as the reference telluric line, a mean redshift of the Si I line of $\Delta\lambda \sim 0.0117$ Å was found. As mentioned above, this line is not expected to show any convective blueshift due to its formation height. Also no redshifts are expected at disk center. Thus, this systematic redshift was subtracted from the λ_T = 10832.120 Å telluric line, yielding a new wavelength of $\lambda_\mathrm{T}^\mathrm{NEW}$ = 10832.108 Å. With the new reference, the average photospheric facular velocity for all maps resulted in ~ -0.06 km s^{-1}. Since the faculae observed here are very compact and have large filling factors (typically, higher than 50%), this value is expected to be zero. We thus conclude that the systematic effects of our velocity calibration are smaller than 60 m s^{-1} or around 2 mÅ.

Acknowledgements. This work has been partially funded by the Spanish Ministerio de Educación y Ciencia, through Project No. AYA2009-14105-C06-03 and AYA2011-29833-C06-03. Financial support by the European Commission through the SOLAIRE Network (MTRN-CT-2006-035484) is gratefully acknowledged. This paper is based on observations made with the VTT operated on the island of Tenerife by the KIS in the Spanish Observatorio del Teide of the Instituto de Astrofísica de Canarias. The National Center for Atmospheric Research (NCAR) is sponsored by the National Science Foundation (NSF). B. Ruiz Cobo helped with the support and implementation of the SIR code and is gratefully acknowledged.

References

Antolin, P. & Rouppe van der Voort, L. 2012, ApJ, 745, 152
Antolin, P., Shibata, K., & Vissers, G. 2010, ApJ, 716, 154
Antolin, P. & Verwichte, E. 2011, ApJ, 736, 121
Archontis, V., Moreno-Insertis, F., Galsgaard, K., Hood, A., & O'Shea, E. 2004, A&A, 426, 1047
Babcock, H. W. & Babcock, H. D. 1955, ApJ, 121, 349
Bard, S. & Carlsson, M. 2008, ApJ, 682, 1376
Borrero, J. M., Bellot Rubio, L. R., Barklem, P. S., & del Toro Iniesta, J. C. 2003, A&A, 404, 749
Breckinridge, J. B. & Hall, D. N. B. 1973, Sol. Phys., 28, 15
Chae, J., Park, H.-M., & Park, Y.-D. 2007, Journal of Korean Astronomical Society, 40, 67
Cheung, M. C. M., Schüssler, M., Tarbell, T. D., & Title, A. M. 2008, ApJ, 687, 1373
Collados, M. 1999, in Astronomical Society of the Pacific Conference Series, Vol. 184, Third Advances in Solar Physics Euroconference: Magnetic Fields and Oscillations, ed. B. Schmieder, A. Hofmann, & J. Staude, 3–22
Collados, M., Lagg, A., Díaz Garcí A, J. J., et al. 2007, in Astronomical Society of the Pacific Conference Series, Vol. 368, The Physics of Chromospheric Plasmas, ed. P. Heinzel, I. Dorotovič, & R. J. Rutten, 611–+
Collados, M. V. 2003, in Presented at the Society of Photo-Optical Instrumentation Engineers (SPIE) Conference, Vol. 4843, Society of Photo-Optical Instrumentation Engineers (SPIE) Conference Series, ed. S. Fineschi, 55–65
Demoulin, P., Malherbe, J. M., Schmieder, B., & Raadu, M. A. 1987, A&A, 183, 142
DeVore, C. R. & Antiochos, S. K. 2000, ApJ, 539, 954
Fan, Y. 2001, ApJ, 554, L111
Fan, Y. 2009, ApJ, 697, 1529
Ioshpa, B. A. & Obridko, V. N. 1999, in ESA Special Publication, Vol. 448, Magnetic Fields and Solar Processes, ed. A. Wilson & et al., 497
Kuckein, C., Centeno, R., Martínez Pillet, V., et al. 2009, A&A, 501, 1113
Kuckein, C., Martínez Pillet, V., & Centeno, R. 2012, A&A, 539, A131
Kupka, F., Piskunov, N., Ryabchikova, T. A., Stempels, H. C., & Weiss, W. W. 1999, A&AS, 138, 119
Kurucz, R. L., Furenlid, I., Brault, J., & Testerman, L. 1984, Solar flux atlas from 296 to 1300 nm, ed. Kurucz, R. L., Furenlid, I., Brault, J., & Testerman, L.
Lagg, A., Woch, J., Solanki, S. K., & Krupp, N. 2007, A&A, 462, 1147
Lin, Y., Engvold, O., Rouppe van der Voort, L., Wiik, J. E., & Berger, T. E. 2005, Sol. Phys., 226, 239
Lites, B. W., Kubo, M., Berger, T., et al. 2010, ApJ, 718, 474
Lites, B. W., Low, B. C., Martinez Pillet, V., et al. 1995, ApJ, 446, 877
Lites, B. W., Socas-Navarro, H., Skumanich, A., & Shimizu, T. 2002, ApJ, 575, 1131
Mackay, D. H., Karpen, J. T., Ballester, J. L., Schmieder, B., & Aulanier, G. 2010, Space Sci. Rev., 151, 333
MacTaggart, D. & Hood, A. W. 2010, ApJ, 716, L219
Malherbe, J. M., Schmieder, B., Ribes, E., & Mein, P. 1983, A&A, 119, 197
Manchester, IV, W., Gombosi, T., DeZeeuw, D., & Fan, Y. 2004, ApJ, 610, 588
Martinez Pillet, V., Lites, B. W., & Skumanich, A. 1997, ApJ, 474, 810
Martinez Pillet, V., Lites, B. W., Skumanich, A., & Degenhardt, D. 1994, ApJ, 425, L113
Martínez-Sykora, J., Hansteen, V., & Carlsson, M. 2008, ApJ, 679, 871
Martres, M.-J., Mein, P., Schmieder, B., & Soru-Escaut, I. 1981, Sol. Phys., 69, 301
Martres, M.-J., Rayrole, J., & Soru-Escaut, I. 1976, Sol. Phys., 46, 137
Mein, P. 1977, Sol. Phys., 54, 45
Muglach, K., Schmidt, W., & Knoelker, M. 1997, Sol. Phys., 172, 103
Murray, M. J., Hood, A. W., Moreno-Insertis, F., Galsgaard, K., & Archontis, V. 2006, A&A, 460, 909
Okamoto, T. J., Tsuneta, S., Lites, B. W., et al. 2008, ApJ, 673, L215
Okamoto, T. J., Tsuneta, S., Lites, B. W., et al. 2009, ApJ, 697, 913
Ruiz Cobo, B. & del Toro Iniesta, J. C. 1992, ApJ, 398, 375
Sasso, C., Lagg, A., & Solanki, S. K. 2006, A&A, 456, 367
Sasso, C., Lagg, A., & Solanki, S. K. 2011, A&A, 526, A42+
Schmidt, W., Muglach, K., & Knölker, M. 2000, ApJ, 544, 567
Schmieder, B., Chandra, R., Berlicki, A., & Mein, P. 2010, A&A, 514, A68+
Schmieder, B., Malherbe, J. M., Simon, G., & Poland, A. I. 1985, A&A, 153, 64
Shimizu, T., Lites, B. W., Katsukawa, Y., et al. 2008, ApJ, 680, 1467
Socas-Navarro, H. 2001, in Astronomical Society of the Pacific Conference Series, Vol. 236, Advanced Solar Polarimetry – Theory, Observation, and Instrumentation, ed. M. Sigwarth, 487–+
Socas-Navarro, H., Trujillo Bueno, J., & Landi Degl'Innocenti, E. 2004, ApJ, 612, 1175
Swensson, J. W., Benedict, W. S., Delbouille, L., & Roland, G. 1970, Memoires of the Societe Royale des Sciences de Liege, 5
Tandberg-Hanssen, E., ed. 1995, Astrophysics and Space Science Library, Vol. 199, The nature of solar prominences
van Ballegooijen, A. A. & Mackay, D. H. 2007, ApJ, 659, 1713
van Ballegooijen, A. A. & Martens, P. C. H. 1989, ApJ, 343, 971
von der Lühe, O., Soltau, D., Berkefeld, T., & Schelenz, T. 2003, in Presented at the Society of Photo-Optical Instrumentation Engineers (SPIE) Conference, Vol. 4853, Society of Photo-Optical Instrumentation Engineers (SPIE) Conference Series, ed. S. L. Keil & S. V. Avakyan, 187–193
Welsch, B. T. & Fisher, G. H. 2012, ArXiv e-prints
Yelles Chaouche, L., Cheung, M. C. M., Solanki, S. K., Schüssler, M., & Lagg, A. 2009, A&A, 507, L53
Yelles Chaouche, L., Kuckein, C., Martínez Pillet, V., & Moreno-Insertis, F. 2012, ApJ, 748, 23

6

Conclusions and future work

This thesis presents an observational study of a solar active region filament. The study was carried out mainly analyzing full Stokes spectropolarimetric data sets in the 10830 Å spectral region, acquired with the Tenerife Infrared Polarimeter at the VTT in Tenerife. Inversions of the chromospheric He I 10830 Å triplet and the photospheric Si I 10827 Å line have been performed using a Milne-Eddington and a LTE inversion code, respectively. Further analysis of the evolution of this active region has been fulfilled using images from different ground based and space-borne instruments / telescopes: MDI (SOHO), TRACE, DOT, Big Bear Solar Observatory, and VSM (SOLIS). Magnetic field extrapolations complemented the observational results.

6.1 Conclusions

The main scientific conclusions drawn from this work are:

- We have inferred the largest magnetic field strength values in active region filaments ever detected before. The Stokes profiles of the filament were dominated by the Zeeman effect and field strengths around 600-700 G are inferred. Longitudinal fields are in the range of 100-200 G, in agreement with past measurements. Therefore, AR filaments have much stronger magnetic fields than expected in the past. This result was confirmed by three different techniques (magnetograph analysis, ME inversions, and PCA inversions). Strong magnetic fields of the same order of magnitude as the ones presented in this thesis were inferred afterwards from spectropolarimetric inversions by Xu et al. (2012) (600–800 G) and from extrapolations by Guo et al. (2010) (~ 700 G), thus confirming our results.

- The magnetic structure and evolution of the observed AR filament is in agreement with a flux rope emergence scenario from below the photosphere. Further observations need to be carried out to confirm if this scenario is common to all AR filaments. However, this study supports earlier observations presented by Okamoto et al. (2008, 2009) and Lites et al. (2010), who found a photospheric signature compatible with an emerging flux rope below an AR filament. The recent work by Xu et al. (2012) also favors the emergence of a flux rope that generated an AR filament.

- The magnetic structure of an AR filament has been inferred for the first time simultaneously in the chromosphere and in the photosphere. In the chromosphere we observe the filament's axis (spine) and a normal polarity configuration that corresponds to the top of the flux rope. At the same time, in the photosphere we observe an inverse polarity configuration (bottom of flux rope) and the spine (see Fig. 6.1).

- The extremely low-lying spine of the filament, which is seen in the photosphere, leads to the creation of an orphan penumbrae. We propose that orphan penumbrae are systematically indicative of flux ropes that have emerged at the PIL of active regions.

- Thoroughly inferred and absolutely calibrated Doppler velocities (along the line-of-sight) show that the filament axis is moving predominantly upwards in the photosphere and in the chromosphere.

- Photospheric transverse magnetic fields also show upward motions along the PIL. This contradicts filament formation models that show downward motions of the transverse component of $\vec{B}$ at the PIL, such as the one presented by van Ballegooijen and Martens (1989). These models generate the flux rope via magnetic reconnection processes in the corona.

- An ubiquitous systematic downflow (redshift), of 1.6 $\mathrm{km\,s^{-1}}$ on average, was detected in the chromosphere surrounding the filament (in the faculae). The origin of this redshift is unknown.

- Concentrated supersonic downflows detected in the photosphere along the PIL might be the counterpart of the chromospheric downflows. Magnetic reconnections are short-lived events. Therefore, reconnection seems to not be the origin of these supersonic downflows that last for at least $\sim$ 19 minutes without interruption.

- A new wavelength for the telluric line closest to the He I 10830 Å triplet red component has been determined: 10832.108 Å. This wavelength agrees well with a historical value (10832.109 Å) proposed by Breckinridge and Hall (1973). We propose that from now on the scientific community uses our inferred wavelength and rejects other alternative values that have been recently used.

- NLFF field extrapolations taking the Si I 10827 Å and the He I 10830 Å vector magnetograms as boundary values, confirm the flux rope topology deduced from the observations.

- The photospheric extrapolations, in combination with the chromospheric vector magnetograms, allow to give an average formation height of the He I 10830 Å triplet: 1.4 Mm above the solar surface in these particular observations.

- In the context of the 180° ambiguity, the selected solution of the azimuth in the observations is confirmed by the magnetic field extrapolations. Hence, a new method

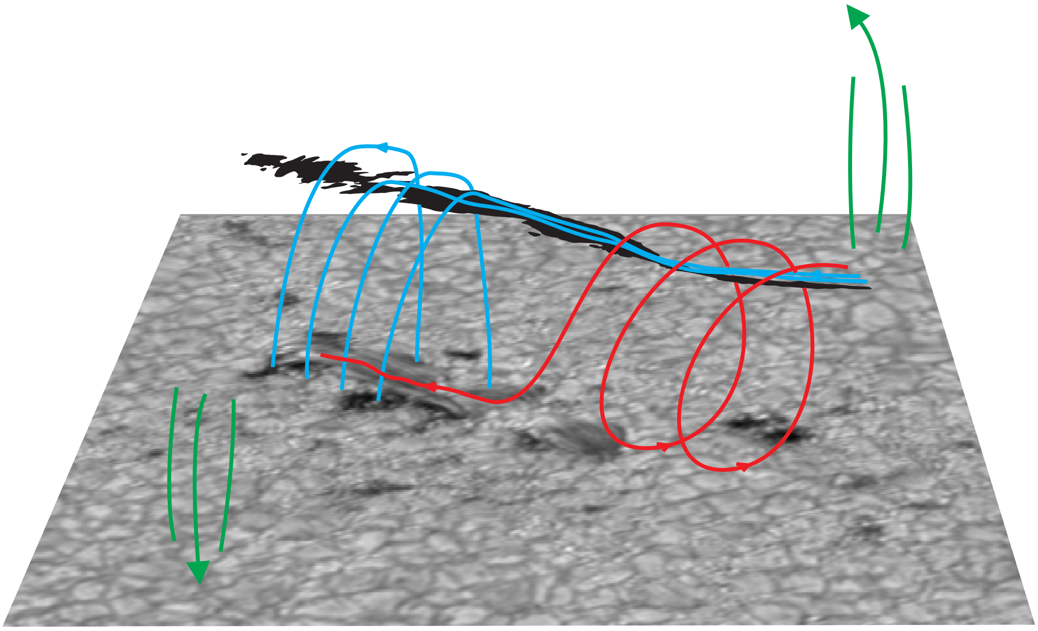

Figure 6.1 Cartoon showing the inferred magnetic structure of the AR filament. The surface corresponds to a continuum image of the DOT. The red field lines are representative of what we inferred from the Si I 10827 Å vector magnetic field whereas the light blue lines represent the He I 10830 Å vector magnetic field. The filament is outlined by the black structure taken from the Hα image of the DOT. Green field lines on both sides of the filament represent the fields in the positive (upward arrow) and negative (downward arrow) faculae.

to solve the 180° ambiguity, when vector magnetograms are available at two heights, has been developed.

6.2 Future work

The results presented in this thesis have given rise to new questions that should be addressed in the future.

Firstly, we have not been lucky with the many observing campaigns that we had along the duration of this thesis (not only due to weather conditions, but also because of the long and “well-know” solar minimum between cycles 23–24). AR filament observations are extremely scarce in the literature and therefore are a promising target in the near future to test old (and new) filament formation models. Especially, multi-layer observations involving different spectral lines that map several heights are required. New space-borne telescopes, such as SDO, and future ground based facilities, such as GREGOR, ATST, and EST, will perfectly complement the various available telescopes and substantially improve our understanding of filaments. In particular, the question of whether all AR filaments have a photospheric counterpart underneath, i.e., orphan penumbrae, is of interest. The strong magnetic fields firstly presented in this study need to be further confirmed with new observations.

Secondly, a detailed analysis of the orphan penumbrae phenomenon needs to be carried out. These features, originally mentioned by Zirin and Wang (1991), seem to have been forgotten by the solar community. In our study, orphan penumbrae are directly related to the emergence of the flux rope. Hence, flux emergence along the PIL of decaying active regions might trigger the formation of AR filaments.

Finally, the intriguing facular downflows observed everywhere in the chromosphere need to be clarified. Are they found in all faculae independently of their evolutionary stage or are they only found adjacent to AR filaments? As mentioned at many points throughout this thesis, the origin of this downflow might be coronal rain. However, the inferred velocities of our data sets are much slower than the ones expected from coronal rain, which are about one order of magnitude higher. It is therefore not clear that these ubiquitous downflows are the chromospheric manifestation of the coronal rain. Consequently, they need to be thoroughly analyzed in the future.

There are of course many more questions regarding AR filaments that need to be answered. Among others, are AR filaments formed in a different way than the quiescent ones? Where does the filament's plasma come from? Is it lifted up from the photosphere into the chromosphere by a specific physical mechanism? Or is the filament channel filled by plasma due to condensation? These are all open questions that need to be addressed and will maintain filaments as a puzzling topic for many more decades to come.

7

Conclusiones y trabajo futuro

En esta tesis se desarrolla un estudio observacional de un filamento solar en una region activa (RA). El estudio se ha llevado a cabo principalmente analizando datos espectropolarimétricos de los cuatro parámetros de Stokes, adquiridos con el polarímetro TIP acoplado al telescopio VTT en Tenerife, en la region espectral de 10830 Å. Para llevar a cabo esta investigación se realizaron inversiones del triplete cromosférico del He I 10830 Å usando un código de inversion que opera con la aproximación de Milne-Eddington (ME), así como de la línea fotosférica del Si I 10827 Å, usando un código que supone ETL. El análisis de la evolución de la RA se ha completado usando imágenes obtenidas de diferentes instrumentos / telescopios terrestres y espaciales: MDI (SOHO), TRACE, DOT, el observatorio solar de Big Bear, y VSM (SOLIS). Los resultados observacionales se complementaron con extrapolaciones del campo magnético.

7.1 Conclusiones

A continuación se presentan las principales conclusiones científicas que se han obtenido en esta tesis:

- Los valores del campo magnético que hemos obtenido son, hasta el momento, los valores más fuertes detectados en filamentos en regiones activas. Los perfiles de Stokes encontrados en el filamento están dominados por el efecto Zeeman y el campo magnético deducido alcanza los 600-700 G. Los campos longitudinales alcanzan valores entre 100-200 G, lo cual concuerda con estudios anteriores. Por lo tanto, y al contrario de lo esperado, los filamentos en RAs poseen campos magnéticos muy fuertes. Hemos comprobado la fiabilidad de este resultado usando diferentes técnicas y todas ellas han confirmando la presencia de fuertes campos magnéticos (análisis de magnetógrafo, inversiones ME e inversiones de PCA). Recientemente se han encontrado campos magnéticos fuertes en otros filamentos en RAs, del mismo orden de magnitud que los presentados en esta tesis, a partir de inversiones espectropolarimétricas realizadas por Xu et al. (2012) (600–800 G) y de extrapolaciones llevadas a cabo por Guo et al. (2010) ($\sim$ 700 G). Teniendo en cuenta esto, podemos decir que nuestros resultados han sido confirmados también por otros autores.

- La historia evolutiva de este filamento en RA concuerda con la emergencia de líneas de campo magnético en forma de hélice desde debajo de la fotosfera. Esta historia evolutiva debe ser confirmada por nuevas observaciones para comprobar si este proceso es común a todos los filamentos en RAs. Este estudio apoya observaciones anteriores de Okamoto et al. (2008, 2009) y Lites et al. (2010), que encontraron evidencias fotosféricas compatibles con la emergencia de campos helicoidales debajo de un filamento en una RA. El trabajo recientemente publicado por Xu et al. (2012) también apoya la emergencia de campos helicoidales que dan lugar a la formación de un filamento en una RA.

- Por primera vez se ha deducido la estructura magnética de un filamento en una RA simultáneamente en la cromosfera y fotosfera. En la cromosfera observamos el eje del filamento y una configuración de polaridad normal que representa la parte superior de la hélice. Al mismo tiempo, en la fotosfera se observa una configuración de polaridad inversa (correspondiente a la parte inferior de la hélice) y el eje del filamento (ver Fig. 7.1).

- Las penumbras huérfanas que se observan en la fotosfera son creadas por el eje del filamento que se encuentra extremadamente bajo en la atmósfera solar. Proponemos que las penumbras huérfanas son siempre indicios de la existencia de campos magnéticos helicoidales que han emergido en líneas de inversión de polaridad (LIP) fotosféricas de regiones activas.

- Se han deducido y calibrado rigurosamente las velocidades Doppler a lo largo de la línea de visión en una escala absoluta. El análisis de estas velocidades revela que, predominantemente, el eje del filamento asciende en la fotosfera y cromosfera.

- En la fotosfera, los campos magnéticos transversales muestran también movimientos ascendentes a lo largo de la LIP. Este resultado contradice algunos modelos de formación de filamentos, por ejemplo, el modelo presentado por van Ballegooijen y Martens (1989), que encuentran campos transversales en sentido descendente en la LIP. Estos modelos crean campos helicoidales en la corona a través de reconexión magnética.

- En la fácula cromosférica, alrededor del filamento, se detectan sistemáticamente, y de manera omnipresente, velocidades en sentido descendente (corrimientos al rojo) con un valor promedio de $1.6\,\mathrm{km\,s^{-1}}$. El origen de este corrimiento al rojo es aún desconocido.

- En la fotosfera se encuentran agrupaciones puntuales, a lo largo de la LIP, con velocidades supersónicas en sentido descendente que podrían ser la manifestación fotosférica de las velocidades descendentes encontradas en la fácula cromosférica. Debido a que el fenómeno de reconexión magnética es un proceso rápido, éste no parece ser el causante de estas velocidades supersónicas ya que la duración de éstas es de al menos ~ 19 minutos sin interrupción.

- Se ha deducido una nueva longitud de onda, 10832.108 Å, para la línea telúrica más próxima a la componente roja del triplete de He I 10830 Å. Este valor se aproxima mucho a otro valor histórico, 10832.109 Å, propuesto por Breckinridge y Hall (1973). Proponemos que, a partir de ahora, la comunidad científica use la longitud de onda determinada en esta tesis y rechace otros valores alternativos que se han usado recientemente.

- Se han realizado extrapolaciones magnéticas, bajo la aproximación no lineal y libre de fuerzas (NLFFF por sus siglas en inglés), tomando los magnetogramas vectoriales de Si I 10827 Å y He I 10830 Å como condiciones de contorno. Estas extrapolaciones confirman la topología en forma de hélice de las líneas de campo deducida a partir de las observaciones.

- La combinación de las extrapolaciones desde la fotosfera con los magnetogramas vectoriales de la cromosfera ha permitido calcular para estas observaciones una altura de formación promedia del triplete de He I 10830 Å cuyo valor es 1.4 Mm por encima de la superficie solar.

- Se ha propuesto un nuevo método para resolver la ambigüedad de los 180° mediante las extrapolaciones magnéticas, siempre y cuando se disponga de magnetogramas vectoriales a dos alturas diferentes. Dicho método confirma la solución del acimut elegida a través de las observaciones.

7.2 Trabajo futuro

Tras los resultados presentados en esta tesis han surgido nuevas preguntas.

En primer lugar, no hemos tenido suerte con las diferentes campañas de observación llevadas a cabo a lo largo de esta tesis (y no solamente debido a las condiciones meteorológicas desfavorables sino también por la larga duración del "conocido" mínimo solar entre los ciclos solares 23 y 24). Dado que se encuentran muy pocas observaciones de filamentos en RAs en la literatura, nuevas observaciones de estos fenómenos solares serán un objetivo prometedor en el futuro cercano para comprobar la validez de modelos viejos (y nuevos) de formación de filamentos. En concreto, se requieren observaciones a múltiples alturas y con diferentes líneas espectrales. Para aumentar nuestro conocimiento sobre los filamentos solares, los nuevos telescopios espaciales, por ejemplo SDO, y futuras instalaciones terrestres como GREGOR, ATST y EST, complementarán a la perfección los telescopios existentes hoy en día. Es de especial interés determinar si todos los filamentos en RAs tienen un homólogo fotosférico debajo, es decir, una penumbra huérfana en la fotosfera. Los campos magnéticos fuertes que se han encontrado por primera vez en filamentos de RAs en esta tesis deben ser confirmados por nuevas observaciones.

En segundo lugar, se debería hacer un análisis detallado del fenómeno de las penumbras huérfanas, observadas originalmente por Zirin and Wang (1991) y aparentemente olvidadas por la comunidad solar. En nuestro estudio hemos visto penumbras huérfanas que están directamente relacionadas con la emergencia de campos magnéticos helicoidales. Por lo tanto, es posible que la emergencia de flujo a lo largo de la LIP de regiones activas en fase de decaimiento pueda dar lugar a la formación de filamentos en RAs.

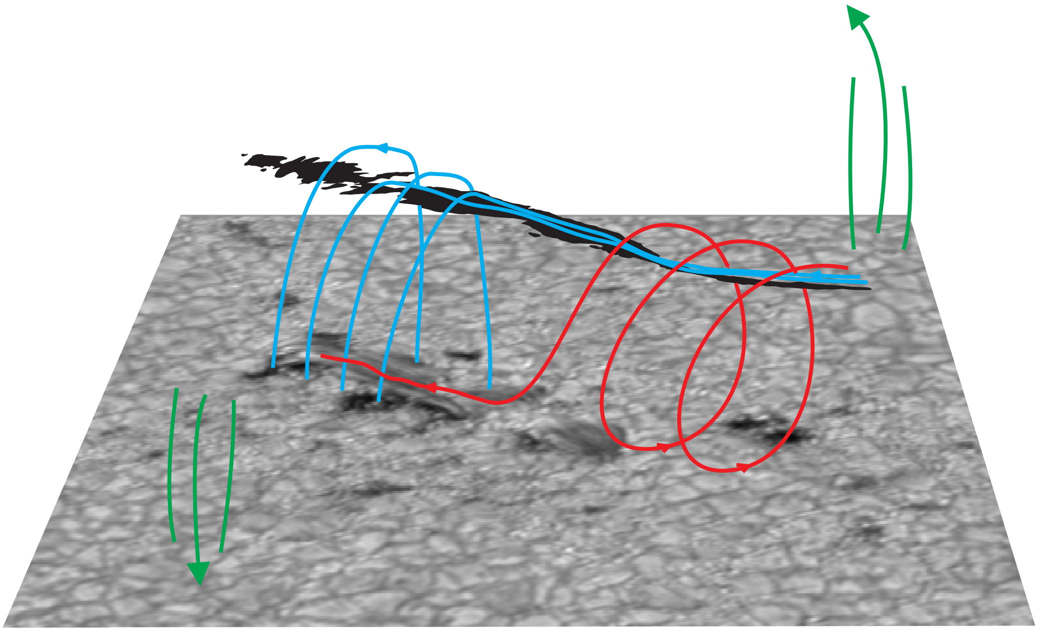

Figure 7.1 El dibujo representa la estructura magnética deducida para el filamento en RA. La superficie gris corresponde a una imagen del Sol en la banda del continuo obtenida con el DOT. Las líneas rojas representan las líneas de campo magnético deducidas del vector de campo magnético de Si I 10827 Å mientras que las azules representan el vector de campo magnético obtenido del análisis de He I 10830 Å. El filamento está representado por una estructura negra, encima de la superficie, recortada de una imagen de Hα del DOT. Las líneas verdes verticales a ambos lados del filamento representan las líneas de campo en la fácula de polaridad positiva (flecha hacia arriba) y de polaridad negativa (flecha hacia abajo).

Finalmente, es necesario clarificar y entender el origen del intrigante y omnipresente corrimiento al rojo observado en la cromosfera de la fácula. ¿Se encuentra en todas las fáculas independientemente del estado evolutivo de la RA o solamente se encuentra cerca de los filamentos en RAs? Como ya se ha mencionado a lo largo de esta tesis, el origen podría ser la lluvia coronal, pero nuestras velocidades son mucho más lentas que las ligadas al fenómeno de la lluvia coronal (aproximadamente en un orden de magnitud). Por lo tanto, no está claro que el corrimiento al rojo facular sea la manifestación cromosférica de la lluvia coronal. Se debería llevar a cabo un análisis detallado de este fenómeno.

Obviamente hay más preguntas sin resolver relacionadas con los filamentos en RAs. Entre otras: ¿es el proceso de formación de filamentos en RAs el mismo que el que da lugar a los filamentos de Sol en calma? ¿de dónde viene el plasma que forma los filamentos?, ¿existe un mecanismo físico que eleve el plasma desde la fotosfera hasta la cromosfera?, o por el contrario, ¿es la condensación del plasma el mecanismo responsable de que se llene el canal del filamento? Todas estas preguntas siguen sin resolverse por lo que el fenómeno de los filamentos solares seguirá siendo un tema interesante y con trabajo por delante para las próximas décadas.

Bibliography

Amari, T., Luciani, J. F., Mikic, Z., and Linker, J.: 1999, *ApJ* **518**, L57

Andretta, V. and Jones, H. P.: 1997, *ApJ* **489**, 375

Antiochos, S. K., Dahlburg, R. B., and Klimchuk, J. A.: 1994, *ApJ* **420**, L41

Anzer, U.: 1989, in E. R. Priest (ed.), *Dynamics and Structure of Quiescent Solar Prominences*, Vol. 150 of *Astrophysics and Space Science Library*, pp 143–166

Anzer, U. and Heinzel, P.: 2007, *A&A* **467**, 1285

Archontis, V., Moreno-Insertis, F., Galsgaard, K., Hood, A., and O'Shea, E.: 2004, *A&A* **426**, 1047

Archontis, V. and Török, T.: 2008, *A&A* **492**, L35

Asensio Ramos, A. and Manso Sainz, R.: 2011, *ApJ* **731**, 125

Asensio Ramos, A., Manso Sainz, R., Martínez González, M. J., Viticchié, B., Orozco Suárez, D., and Socas-Navarro, H.: 2012, *ApJ* **748**, 83

Asensio Ramos, A., Trujillo Bueno, J., and Landi Degl'Innocenti, E.: 2008, *ApJ* **683**, 542

Asplund, M., Nordlund, Å., Trampedach, R., Allende Prieto, C., and Stein, R. F.: 2000, *A&A* **359**, 729

Athay, R. G. and Johnson, H. R.: 1960, *ApJ* **131**, 413

Athay, R. G., Querfeld, C. W., Smartt, R. N., Landi Degl'Innocenti, E., and Bommier, V.: 1983, *Sol. Phys.* **89**, 3

Auer, L. H., House, L. L., and Heasley, J. N.: 1977, *Sol. Phys.* **55**, 47

Aulanier, G. and Demoulin, P.: 1998, *A&A* **329**, 1125

Aulanier, G. and Démoulin, P.: 2003, *A&A* **402**, 769

Aulanier, G., DeVore, C. R., and Antiochos, S. K.: 2002, *ApJ* **567**, L97

Aulanier, G., DeVore, C. R., and Antiochos, S. K.: 2006, *ApJ* **646**, 1349

Avrett, E. H., Fontenla, J. M., and Loeser, R.: 1994, in D. M. Rabin, J. T. Jefferies, & C. Lindsey (ed.), *Infrared Solar Physics*, Vol. 154 of *IAU Symposium*, pp 35–+

Babcock, H. W. and Babcock, H. D.: 1955, *ApJ* **121**, 349

Balasubramaniam, K. S., Keil, S. L., and Tomczyk, S.: 1997, *ApJ* **482**, 1065

Bard, S. and Carlsson, M.: 2008, *ApJ* **682**, 1376

Barklem, P. S., Piskunov, N., and O'Mara, B. J.: 2000, *A&AS* **142**, 467

Beck, C., Rezaei, R., and Fabbian, D.: 2011, *A&A* **535**, A129

Bommier, V., Landi Degl'Innocenti, E., Leroy, J.-L., and Sahal-Brechot, S.: 1994, *Sol. Phys.* **154**, 231

Bommier, V., Sahal-Brechot, S., and Leroy, J. L.: 1981, *A&A* **100**, 231

Borrero, J. M., Bellot Rubio, L. R., Barklem, P. S., and del Toro Iniesta, J. C.: 2003, *A&A* **404**, 749

Borrero, J. M., Tomczyk, S., Kubo, M., Socas-Navarro, H., Schou, J., Couvidat, S., and Bogart, R.: 2011, *Sol. Phys.* **273**, 267

Breckinridge, J. B. and Hall, D. N. B.: 1973, *Sol. Phys.* **28**, 15

Canou, A. and Amari, T.: 2010, *ApJ* **715**, 1566

Cartledge, N. P., Titov, V. S., and Priest, E. R.: 1996, *Astrophysical Letters and Communications* **34**, 89

Casini, R., López Ariste, A., Tomczyk, S., and Lites, B. W.: 2003, *ApJ* **598**, L67

Centeno, R., Trujillo Bueno, J., Uitenbroek, H., and Collados, M.: 2008, *ApJ* **677**, 742

Chae, J., Park, H., and Park, Y.: 2007, *Journal of Korean Astronomical Society* **40**, 67

Chae, J., Yun, H. S., Sakurai, T., and Ichimoto, K.: 1998, *Sol. Phys.* **183**, 229

Cheung, M. C. M., Schüssler, M., Tarbell, T. D., and Title, A. M.: 2008, *ApJ* **687**, 1373

del Toro Iniesta, J. C.: 2003, *Introduction to Spectropolarimetry*

del Toro Iniesta, J. C., Tarbell, T. D., and Ruiz Cobo, B.: 1994, *ApJ* **436**, 400

Demoulin, P.: 1998, in D. F. Webb, B. Schmieder, & D. M. Rust (ed.), *IAU Colloq. 167: New Perspectives on Solar Prominences*, Vol. 150 of *Astronomical Society of the Pacific Conference Series*, p. 78

Demoulin, P. and Priest, E. R.: 1989, *A&A* **214**, 360

DeVore, C. R. and Antiochos, S. K.: 2000, *ApJ* **539**, 954

Elmore, D. F., Lites, B. W., Tomczyk, S., Skumanich, A. P., Dunn, R. B., Schuenke, J. A., Streander, K. V., Leach, T. W., Chambellan, C. W., and Hull, H. K.: 1992, in D. H. Goldstein & R. A. Chipman (ed.), *Society of Photo-Optical Instrumentation Engineers (SPIE) Conference Series*, Vol. 1746 of *Society of Photo-Optical Instrumentation Engineers (SPIE) Conference Series*, pp 22–33

Engvold, O.: 1976, *Sol. Phys.* **49**, 283

Fan, Y.: 2001, *ApJ* **554**, L111

Fan, Y.: 2009, *ApJ* **697**, 1529

Fontenla, J. M., Avrett, E. H., and Loeser, R.: 1993, *ApJ* **406**, 319

Foukal, P.: 1971, *Sol. Phys.* **19**, 59

Gary, G. A.: 1989, *ApJS* **69**, 323

Georgoulis, M. K., LaBonte, B. J., and Metcalf, T. R.: 2004, *ApJ* **602**, 446

Goldberg, L.: 1939, *ApJ* **89**, 673

Gray, D. F.: 1992, *The observation and analysis of stellar photospheres.*

Guo, Y., Schmieder, B., Démoulin, P., Wiegelmann, T., Aulanier, G., Török, T., and Bommier, V.: 2010, *ApJ* **714**, 343

Hale, G. E. and Ellerman, F.: 1903, *Publications of the Yerkes Observatory* **3**, 1

Harvey, J. and Hall, D.: 1971, in R. Howard (ed.), *Solar Magnetic Fields*, Vol. 43 of *IAU Symposium*, p. 279

Harvey, J. W.: 1969, *Ph.D. thesis*, UNIVERSITY OF COLORADO AT BOULDER.

Harvey, J. W. and Tandberg-Hanssen, E.: 1968, *Sol. Phys.* **3**, 316

Heinzel, P. and Anzer, U.: 2006, *ApJ* **643**, L65

Hindman, B. W., Haber, D. A., and Toomre, J.: 2006, *ApJ* **653**, 725

Hirayama, T.: 1971, *Sol. Phys.* **17**, 50

Hirayama, T.: 1985, *Sol. Phys.* **100**, 415

Huggins, W.: 1868, *Royal Society of London Proceedings Series I* **17**, 302

Jing, J., Yuan, Y., Wiegelmann, T., Xu, Y., Liu, R., and Wang, H.: 2010, *ApJ* **719**, L56

Jordan, C.: 1975, *MNRAS* **170**, 429

Kim, I. S., Nikolsky, G. M., Koutchmy, S., and Stellmacher, G.: 1982, *A&A* **114**, 347

Kippenhahn, R. and Schlüter, A.: 1957, *ZAp* **43**, 36

Klimchuk, J. A.: 1990, *ApJ* **354**, 745

Kuperus, M. and Raadu, M. A.: 1974, *A&A* **31**, 189

Kupka, F., Piskunov, N., Ryabchikova, T. A., Stempels, H. C., and Weiss, W. W.: 1999, *A&AS* **138**, 119

Labrosse, N., Heinzel, P., Vial, J.-C., Kucera, T., Parenti, S., Gunár, S., Schmieder, B., and Kilper, G.: 2010, *Space Sci. Rev.* **151**, 243

Lagg, A., Woch, J., Krupp, N., and Solanki, S. K.: 2004, *A&A* **414**, 1109

Landi Degl'Innocenti, E.: 1982, *Sol. Phys.* **77**, 285

Landi Degl'Innocenti, E.: 1992, *Magnetic field measurements*, pp 71–+

Landi Degl'Innocenti, E. and Landolfi, M.: 1982, *Sol. Phys.* **77**, 13

Landi Degl'Innocenti, E. and Landolfi, M. (eds.): 2004, *Polarization in Spectral Lines*, Vol. 307 of *Astrophysics and Space Science Library*

Landolfi, M. and Landi Degl'Innocenti, E.: 1996, *Sol. Phys.* **164**, 191

Leroy, J. L.: 1977, *A&A* **60**, 79

Leroy, J. L.: 1978, *A&A* **64**, 247

Leroy, J. L.: 1989, in E. R. Priest (ed.), *Dynamics and Structure of Quiescent Solar Prominences*, Vol. 150 of *Astrophysics and Space Science Library*, pp 77–113

Leroy, J. L., Bommier, V., and Sahal-Brechot, S.: 1983, *Sol. Phys.* **83**, 135

Leroy, J. L., Bommier, V., and Sahal-Brechot, S.: 1984, *A&A* **131**, 33

Leroy, J. L., Ratier, G., and Bommier, V.: 1977, *A&A* **54**, 811

Lin, H., Penn, M. J., and Kuhn, J. R.: 1998, *ApJ* **493**, 978

Lin, Y., Engvold, O., Rouppe van der Voort, L., Wiik, J. E., and Berger, T. E.: 2005, *Sol. Phys.* **226**, 239

Lin, Y., Soler, R., Engvold, O., Ballester, J. L., Langangen, Ø., Oliver, R., and Rouppe van der Voort, L. H. M.: 2009, *ApJ* **704**, 870

Lites, B., Casini, R., Garcia, J., and Socas-Navarro, H.: 2007, *Mem. Soc. Astron. Italiana* **78**, 148

Lites, B. W.: 2005, *ApJ* **622**, 1275

Lites, B. W., Keil, S. L., Scharmer, G. B., and Wyller, A. A.: 1985, *Sol. Phys.* **97**, 35

Lites, B. W., Kubo, M., Berger, T., Frank, Z., Shine, R., Tarbell, T., Title, A., Okamoto, T. J., and Otsuji, K.: 2010, *ApJ* **718**, 474

Lites, B. W. and Low, B. C.: 1997, *Sol. Phys.* **174**, 91

Lites, B. W., Low, B. C., Martinez Pillet, V., Seagraves, P., Skumanich, A., Frank, Z. A., Shine, R. A., and Tsuneta, S.: 1995, *ApJ* **446**, 877

Lockyer, J. N.: 1868, *Royal Society of London Proceedings Series I* **17**, 91

López Ariste, A.: 2002, *ApJ* **564**, 379

López Ariste, A. and Aulanier, G.: 2007, in P. Heinzel, I. Dorotovic, & R. J. Rutten (ed.), *The Physics of Chromospheric Plasmas*, Vol. 368 of *Astronomical Society of the Pacific Conference Series*, p. 291

López Ariste, A., Aulanier, G., Schmieder, B., and Sainz Dalda, A.: 2006, *A&A* **456**, 725

López Ariste, A., Casini, R., Paletou, F., Tomczyk, S., Lites, B. W., Semel, M., Landi Degl'Innocenti, E., Trujillo Bueno, J., and Balasubramaniam, K. S.: 2005, *ApJ* **621**, L145

Low, B. C.: 1996, *Sol. Phys.* **167**, 217

Low, B. C. and Hundhausen, J. R.: 1995, *ApJ* **443**, 818

Lyot, B.: 1937, *L'Astronomie* **51**, 203

Mackay, D. H., Karpen, J. T., Ballester, J. L., Schmieder, B., and Aulanier, G.: 2010, *Space Sci. Rev.* **151**, 333

MacTaggart, D. and Hood, A. W.: 2010, *ApJ* **716**, L219

Magara, T.: 2004, *ApJ* **605**, 480

Malherbe, J. M., Schmieder, B., Ribes, E., and Mein, P.: 1983, *A&A* **119**, 197

Maltby, P., Avrett, E. H., Carlsson, M., Kjeldseth-Moe, O., Kurucz, R. L., and Loeser, R.: 1986, *ApJ* **306**, 284

Malville, J. M.: 1968, *Sol. Phys.* **5**, 236

Manchester, IV, W., Gombosi, T., DeZeeuw, D., and Fan, Y.: 2004, *ApJ* **610**, 588

Martin, S. F.: 1973, *Sol. Phys.* **31**, 3

Martin, S. F.: 1990, in V. Ruzdjak & E. Tandberg-Hanssen (ed.), *IAU Colloq. 117: Dynamics of Quiescent Prominences*, Vol. 363 of *Lecture Notes in Physics, Berlin Springer Verlag*, pp 1–44

Martin, S. F.: 1998, *Sol. Phys.* **182**, 107

Martin, S. F., Bilimoria, R., and Tracadas, P. W.: 1994, in R. J. Rutten & C. J. Schrijver (ed.), *Solar Surface Magnetism*, p. 303

Martin, S. F., Lin, Y., and Engvold, O.: 2008, *Sol. Phys.* **250**, 31

Martinez Pillet, V.: 1992, *Sol. Phys.* **140**, 207

Mártinez Pillet, V., Collados, M., Sánchez Almeida, J., González, V., Cruz-Lopez, A., Manescau, A., Joven, E., Paez, E., Diaz, J., Feeney, O., Sánchez, V., Scharmer, G., and Soltau, D.: 1999, in T. R. Rimmele, K. S. Balasubramaniam, & R. R. Radick (ed.), *High Resolution Solar Physics: Theory, Observations, and Techniques*, Vol. 183 of *Astronomical Society of the Pacific Conference Series*, p. 264

Martínez-Sykora, J., Hansteen, V., and Carlsson, M.: 2008, *ApJ* **679**, 871

Mein, P. and Mein, N.: 1991, *Sol. Phys.* **136**, 317

Merenda, L., Trujillo Bueno, J., Landi Degl'Innocenti, E., and Collados, M.: 2006, *ApJ* **642**, 554

Metcalf, T. R.: 1994, *Sol. Phys.* **155**, 235

Metcalf, T. R., Leka, K. D., Barnes, G., Lites, B. W., Georgoulis, M. K., Pevtsov, A. A., Balasubramaniam, K. S., Gary, G. A., Jing, J., Li, J., Liu, Y., Wang, H. N., Abramenko, V., Yurchyshyn, V., and Moon, Y.-J.: 2006, *Sol. Phys.* **237**, 267

Milkey, R. W., Heasley, J. N., and Beebe, H. A.: 1973, *ApJ* **186**, 1043

Moon, Y.-J., Wang, H., Spirock, T. J., Goode, P. R., and Park, Y. D.: 2003, *Sol. Phys.* **217**, 79

Murray, M. J., Hood, A. W., Moreno-Insertis, F., Galsgaard, K., and Archontis, V.: 2006, *A&A* **460**, 909

Neukirch, T.: 2005, in D. E. Innes, A. Lagg, & S. A. Solanki (ed.), *Chromospheric and Coronal Magnetic Fields*, Vol. 596 of *ESA Special Publication*

Nikolsky, G. M., Kim, I. S., Koutchmy, S., and Stellmacher, G.: 1984, *A&A* **140**, 112

Okamoto, T. J., Tsuneta, S., Lites, B. W., Kubo, M., Yokoyama, T., Berger, T. E., Ichimoto, K., Katsukawa, Y., Nagata, S., Shibata, K., Shimizu, T., Shine, R. A., Suematsu, Y., Tarbell, T. D., and Title, A. M.: 2008, *ApJ* **673**, L215

Okamoto, T. J., Tsuneta, S., Lites, B. W., Kubo, M., Yokoyama, T., Berger, T. E., Ichimoto, K., Katsukawa, Y., Nagata, S., Shibata, K., Shimizu, T., Shine, R. A., Suematsu, Y., Tarbell, T. D., and Title, A. M.: 2009, *ApJ* **697**, 913

Paletou, F. and Aulanier, G.: 2003, in J. Trujillo-Bueno & J. Sanchez Almeida (ed.), *Astronomical Society of the Pacific Conference Series*, Vol. 307 of *Astronomical Society of the Pacific Conference Series*, p. 458

Paletou, F., López Ariste, A., Bommier, V., and Semel, M.: 2001, *A&A* **375**, L39

Parker, E. N.: 1955, *ApJ* **121**, 491

Pneuman, G. W.: 1983, *Sol. Phys.* **88**, 219

Povel, H. P.: 1998, in R. E. Schielicke (ed.), *Astronomische Gesellschaft Meeting Abstracts*, Vol. 14 of *Astronomische Gesellschaft Meeting Abstracts*, p. 7

Press, W. H., Flannery, B. P., and Teukolsky, S. A.: 1986, *Numerical recipes. The art of scientific computing*

Priest, E. R.: 2000, *Solar magneto-hydrodynamics.*

Priest, E. R., Hood, A. W., and Anzer, U.: 1989, *ApJ* **344**, 1010

Querfeld, C. W., Smartt, R. N., Bommier, V., Landi Degl'Innocenti, E., and House, L. L.: 1985, *Sol. Phys.* **96**, 277

Ramelli, R., Bianda, M., Trujillo Bueno, J., Merenda, L., and Stenflo, J. O.: 2006, in R. Casini & B. W. Lites (ed.), *Astronomical Society of the Pacific Conference Series*, Vol. 358 of *Astronomical Society of the Pacific Conference Series*, p. 471

Ruiz Cobo, B. and del Toro Iniesta, J. C.: 1992, *ApJ* **398**, 375

Rust, D. M.: 1967, *ApJ* **150**, 313

Rust, D. M. and Kumar, A.: 1994, *Sol. Phys.* **155**, 69

Rutten, R. J., Hammerschlag, R. H., Bettonvil, F. C. M., Sütterlin, P., and de Wijn, A. G.: 2004, *A&A* **413**, 1183

Sahal-Brechot, S., Bommier, V., and Leroy, J. L.: 1977, *A&A* **59**, 223

Sainz Dalda, A., Martínez-Sykora, J., Bellot Rubio, L., and Title, A.: 2012, *ApJ* **748**, 38

Sasso, C., Lagg, A., Solanki, S. K., Aznar Cuadrado, R., and Collados, M.: 2007, in P. Heinzel, I. Dorotovic, & R. J. Rutten (ed.), *The Physics of Chromospheric Plasmas*, Vol. 368 of *Astronomical Society of the Pacific Conference Series*, p. 467

Scharmer, G. B., Bjelksjo, K., Korhonen, T. K., Lindberg, B., and Petterson, B.: 2003, in S. L. Keil & S. V. Avakyan (ed.), *Society of Photo-Optical Instrumentation Engineers (SPIE) Conference Series*, Vol. 4853 of *Society of Photo-Optical Instrumentation Engineers (SPIE) Conference Series*, pp 341–350

Schmieder, B., Chandra, R., Berlicki, A., and Mein, P.: 2010, *A&A* **514**, A68+

Schmieder, B., Raadu, M. A., and Wiik, J. E.: 1991, *A&A* **252**, 353

Schrijver, C. J., De Rosa, M. L., Metcalf, T. R., Liu, Y., McTiernan, J., Régnier, S., Valori, G., Wheatland, M. S., and Wiegelmann, T.: 2006, *Sol. Phys.* **235**, 161

Secchi, F.: 1872, *MNRAS* **32**, 226

Shine, R., Gerola, H., and Linsky, J. L.: 1975, *ApJ* **202**, L101

Smith, S. F.: 1968, in K. O. Kiepenheuer (ed.), *Structure and Development of Solar Active Regions*, Vol. 35 of *IAU Symposium*, p. 267

Smith, S. F. and Ramsey, H. E.: 1967, *Sol. Phys.* **2**, 158

Socas-Navarro, H.: 2001, in M. Sigwarth (ed.), *Advanced Solar Polarimetry – Theory, Observation, and Instrumentation*, Vol. 236 of *Astronomical Society of the Pacific Conference Series*, pp 487–+

Socas-Navarro, H., Trujillo Bueno, J., and Landi Degl'Innocenti, E.: 2004, *ApJ* **612**, 1175

Socas-Navarro, H., Trujillo Bueno, J., and Ruiz Cobo, B.: 2000, *ApJ* **530**, 977

Stenflo, J. O.: 2002, in J. Trujillo-Bueno, F. Moreno-Insertis, & F. Sánchez (ed.), *Astrophysical Spectropolarimetry*, pp 55–100

Stix, M.: 2002, *The sun: an introduction*

Tandberg-Hanssen, E.: 1970, *Sol. Phys.* **15**, 359

Tandberg-Hanssen, E.: 1974, *Geophysics and Astrophysics Monographs* 12

Tandberg-Hanssen, E. (ed.): 1995, *The nature of solar prominences*, Vol. 199 of *Astrophysics and Space Science Library*

Tandberg-Hanssen, E.: 1998, in D. F. Webb, B. Schmieder, & D. M. Rust (ed.), *IAU Colloq. 167: New Perspectives on Solar Prominences*, Vol. 150 of *Astronomical Society of the Pacific Conference Series*, p. 11

Tandberg-Hanssen, E. and Malville, J. M.: 1974, *Sol. Phys.* **39**, 107

Thevenin, F.: 1989, *A&AS* **77**, 137

Thompson, III, W. I. and Billings, D. E.: 1967, *ApJ* **149**, 269

Trujillo Bueno, J.: 2001, in M. Sigwarth (ed.), *Advanced Solar Polarimetry – Theory, Observation, and Instrumentation*, Vol. 236 of *Astronomical Society of the Pacific Conference Series*, p. 161

Trujillo Bueno, J.: 2006, in R. Ramelli, O. Shalabiea, I. Saleh, & J. O. Stenflo (ed.), *Solar Physics and Solar Eclipses (SPSE 2006)*, pp 77–92

Trujillo Bueno, J., Landi Degl'Innocenti, E., Collados, M., Merenda, L., and Manso Sainz, R.: 2002, *Nature* **415**, 403

Tupman, G. L.: 1872, *MNRAS* **33**, 105

van Ballegooijen, A. A. and Mackay, D. H.: 2007, *ApJ* **659**, 1713

van Ballegooijen, A. A. and Martens, P. C. H.: 1989, *ApJ* **343**, 971

Vernazza, J. E., Avrett, E. H., and Loeser, R.: 1981, *ApJS* **45**, 635

Wiegelmann, T.: 2004, *Sol. Phys.* **219**, 87

Wiehr, E. and Stellmacher, G.: 1991, *A&A* **247**, 379

Xu, Z., Lagg, A., Solanki, S., and Liu, Y.: 2012, *ApJ* **749**, 138

Yan, Y., Deng, Y., Karlický, M., Fu, Q., Wang, S., and Liu, Y.: 2001, *ApJ* **551**, L115

Yelles Chaouche, L., Cheung, M. C. M., Solanki, S. K., Schüssler, M., and Lagg, A.: 2009, *A&A* **507**, L53

Yi, Z., Engvold, O., and Keil, S. L.: 1991, *Sol. Phys.* **132**, 63

Zirin, H.: 1975, *ApJ* **199**, L63

Zirin, H.: 1988, *Astrophysics of the sun*

Zirin, H. and Severny, A.: 1961, *The Observatory* **81**, 155

Zirin, H. and Wang, H.: 1991, *Advances in Space Research* **11**, 225

Zirker, J. B., Engvold, O., and Martin, S. F.: 1998, *Nature* **396**, 440

Zirker, J. B. and Koutchmy, S.: 1990, *Sol. Phys.* **127**, 109

List of Figures

List of Tables

Agradecimientos

Con la finalización de esta tesis se cierra un capítulo de mi vida que sin duda me ha aportado mucho. He conocido a mucha gente nueva durante esta etapa pero lo más importante es que la gente “de siempre” ha seguido estando a mi lado. Para comenzar me gustaría agradecer a la persona más importante de mi vida, mi novia (futura esposa) Gaby, el día a día que hemos compartido. Siempre has estado ahí para los momentos buenos y no tan buenos. Me has dado apoyo y cariño. Me siento muy afortunado de tenerte en mi vida y no pienso soltarte. Agradezco a mis padres, Bernd y Veronika, por haberme dado la posibilidad de estudiar la carrera que yo quería y haberme dado toda la libertad para desarrollar mi carrera profesional. Aunque no seamos muy expresivos a la hora de expresar los sentimientos quiero que sepan que les quiero mucho. No me puedo olvidar de mis suegros, Jorge y Susana, que siempre han estado ahí para lo que hiciese falta y que han cuidado de Gaby mientras yo estaba de viaje.

Una vez acabado con los agradecimientos familiares, hay muchísimas personas que me gustaría nombrar porque todos ellos han contribuido a que me sintiese muy cómodo en mi lugar de trabajo. Comienzo por mi despacho original, donde no me olvido de mi compañera Luisa, que se sentaba a mi izquierda (al lado de la ventana) y le gustaba mantener las ventanas del despacho cerradas (efecto sauna). A mi compañera que se sentaba a mi derecha que nunca llegué a conocer pero le agradezco que pudiera expandir mis apuntes y cosas hacia una buena parte de su mesa durante casi cuatro años. Detrás mío se sentaba mi compi de solar Tobías y la chica que hacía los mejores postres del IAC, Inés. A ambos les he cogido mucho cariño durante la tesis. Por último me falta Manu, que tras la marcha de todos los demás compañeros ha compartido conmigo el despacho durante casi un año. Nos hemos entendido de maravilla y tenemos puntos de vista muy parecidos. A mis nuevos compañeros de despacho: Paulo, Jorge, Tanausu, Marja y Bartosz no les puedo agradecer mucho porque han revolucionado el despacho que hasta el momento en que ellos llegaron era muy tranquilo. Incluso como regalo de bienvenida me han tirado el café de la cafetera sobre mis apuntes. Pero que sepan que a pesar de todo al final les cogí cariño.

Aunque seamos astrofísicos con muchísimas ganas de trabajar, hay vida fuera del despacho. Es ahí donde entran en juego personas como Nayra, Miriam, Judit, Julio, el famoso Jesús, Jorge, Peter, Mireia, Anna, Pepa, Pio, Trini, . . . que siempre han estado ahí para una charlita o un mini (o no tan mini) descanso. Adalito, que no me olvido de ti, que también entrabas a nuestro despacho y conversabas (gritabas) con nosotros efusivamente. Elisa y Ariadna, compañeras de desayuno y buenas amigas. Julio, Jesús, Elisa y Sebas, gracias por ser mis guías para llegar a depositar la tesis que tienen en vuestras manos. Debería haber una asignatura de tres créditos para abordar todo lo relacionado con el depósito de la tesis.

Un poquito más lejos del despacho tengo que agradecer la buena acogida que ha tenido la iniciativa de hacer deporte los miércoles en la cancha del IAC. Estoy contento de dejar atrás un grupo aficionado al voleibol que se reúne todos los miércoles (Inés, Tobías y Manu han sido directamente responsables junto a mi de dicha iniciativa). Un abrazo muy especial a mis compis de volei: Gaby, Manu, Sebas, Karla, Judit, Nicola, Inés, Tobías, Lotfi, Alberto, Carlos, Stefano, Edgar, Hannu, . . . Ha sido de los mejores momentos de desconexión de los problemas de la vida diaria, especialmente cuando salíamos a jugar en arena de playa.

Alejándome ya de lo que es el área de trabajo, he compartido muchas horas de los fines de semana con mis amigos de La Laguna. Les aseguro que jugando al Galáctica y al Bang! se puede desconectar perfectamente de los problemas de la tesis. Gracias amigos: Javi, Juan Antonio, Elisa, Ángel, Miguel, Dan, Jeza, Sara, Jorge, Judit, Peter, Pio y como no Gaby.

Y para acabar no quiero dejar de dar las gracias a mis directores de tesis: Valentín y Rebecca. Recuerdo bien que Valentín tardó un par de días en aceptarme como su estudiante de doctorado. Creo que ha valido la pena, ¿no? Los dos me han enseñado muchas cosas a lo largo de estos años (no solamente en el campo de la física solar) y me han dado la oportunidad de viajar mucho. Sin ustedes esta tesis no hubiese sido posible. Gracias.